Mathematical Problems in Engineering

Dynamics, Control, and Management of Renewable Energy Systems

Lead Guest Editor: Kai Wang
Guest Editors: Xiufeng Liu, Licheng Wang, Yaping Fu, Huajun Dong, and Jinyan Song

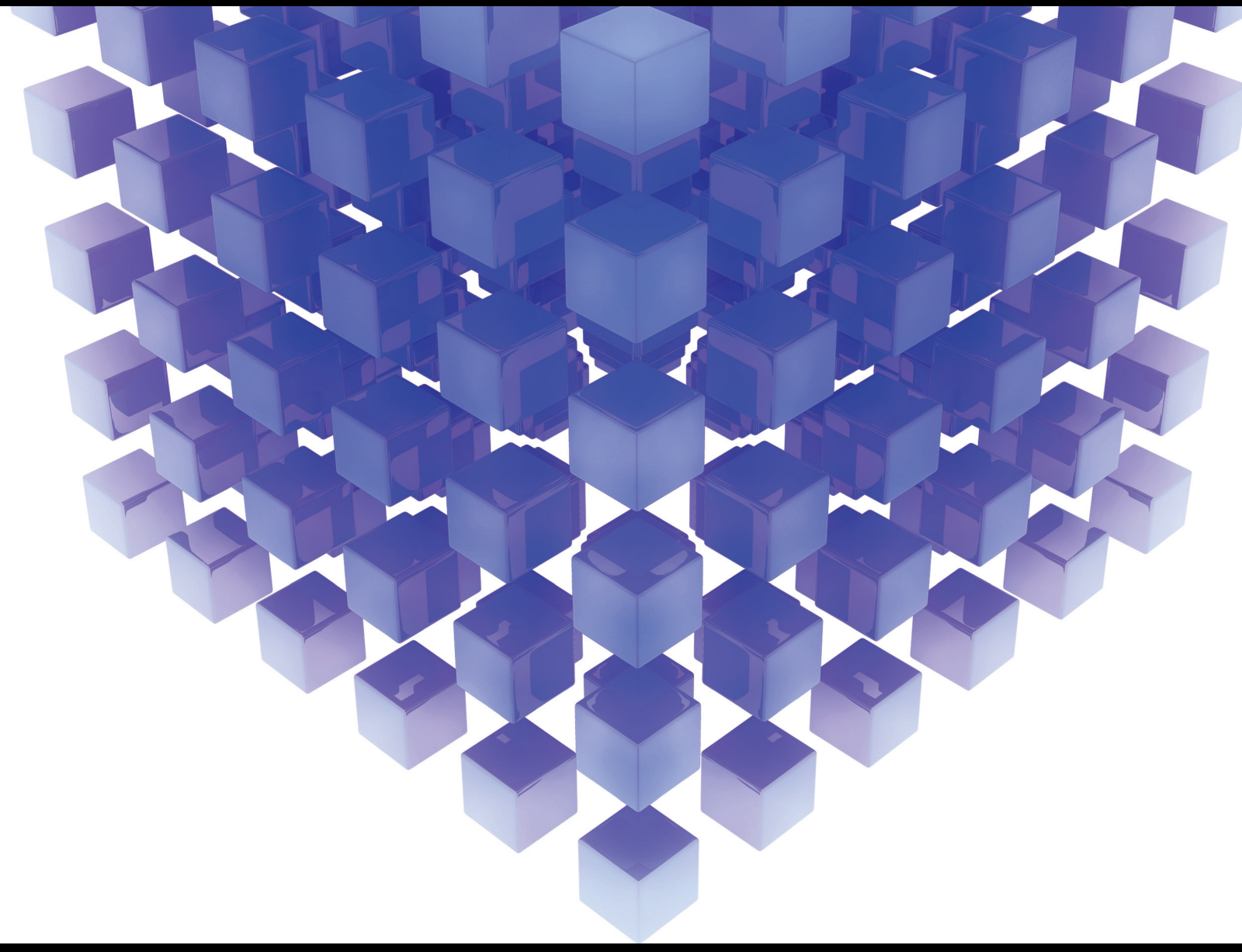

Dynamics, Control, and Management of Renewable Energy Systems

Mathematical Problems in Engineering

Dynamics, Control, and Management of Renewable Energy Systems

Lead Guest Editor: Kai Wang
Guest Editors: Xiufeng Liu, Licheng Wang, Yaping Fu, Huajun Dong, and Jinyan Song

Chief Editor

Academic Editors

Contents

Hindawi
Mathematical Problems in Engineering
Volume 2021, Article ID 6672656, 11 pages
https://doi.org/10.1155/2021/6672656

Research Article

Decomposition Analysis of Green Technology Innovation from Green Patents in China

Aiping Chen and Huiying Chen

College of Economics and Management, Shandong University of Science and Technology, Qingdao, Shandong 266590, China

Correspondence should be addressed to Aiping Chen; skd992057@sdust.edu.cn

Received 30 October 2020; Revised 15 April 2021; Accepted 21 April 2021; Published 4 May 2021

Academic Editor: Jinyan Song

Green technology innovation is essential to promoting not only the construction of ecological civilization but also the fundamental means of achieving sustainable development. Taking research and development (R&D) investment, CO_2 emissions, and other related factors into account, this study constructed an extended logarithmic mean Divisia index (LMDI) decomposition model for the change in the number of green technology patent applications to quantify the contribution of each driving factor based on green patent applications data in China from 2000 to 2017. The results indicated that economic scale, R&D efficiency, R&D reaction, and green patent share play positive roles in promoting green patent applications in China, among which R&D efficiency is the most significant contributor. By contrast, carbon intensity plays a dampening role. The conclusions of this study could provide a theoretical foundation for China to formulate targeted green technology innovation management policies, promotion measures, and related R&D strategies.

1. Introduction

Climate change and CO_2 emissions mitigation have drawn global attention in recent years. Human beings have made considerable efforts to mitigate the impact of climate change and environmental degradation [1–3]. Documents such as the *United Nations Framework Agreement on Climate Change*, *Kyoto Protocol*, and *Paris Protocol* have emphasized the importance of CO_2 emissions reduction in the fight against climate change. Technological innovation is key to driving energy saving and CO_2 emission reduction, and this idea has gained a wide societal consensus [4–6]. The theme of World Intellectual Property Day 2020 was *Innovate for a Green Future*, which stressed on innovation being crucial to creating a greener tomorrow. Climate change has far-reaching effects for everyone, and innovation in green technology sectors will be vital to address this global challenge successfully [7, 8].

Growth in energy markets slowed in line with weaker economic growth in 2019. China was the exception, with its energy consumption accelerating in 2019. China was by far the biggest driver of energy, accounting for more than three-quarters of net global growth in 2019 [9]. The nation was still the country with the world's highest CO_2 emissions, however, accounting for 28.8%. As the largest CO_2 emitter, the nation has more and more challenges in CO_2 emission reduction and sustainable development. As a result, China plays a crucial role in tackling climate change. China has made an ambitious aim to have CO_2 emissions peak before 2030 and achieve carbon neutrality before 2060.

Figure 1 shows the trend of China's annual gross domestic product (GDP) growth rate and CO_2 emissions from 2000 to 2019. China's GDP growth rate increased annually until 2007; however, it dramatically slowed in 2008 because of the worldwide financial crisis. After 2008, the nation's GDP growth rate gradually decreased. The bars illustrate CO_2 emissions from 2000 to 2019 in China. Notably, CO_2 emissions have continued to grow despite the reduced economic growth rate since 2008. As China is facing restraints on its resources and the environment, how to balance the relationship between environmental protection and economic development is especially important [5, 10–12].

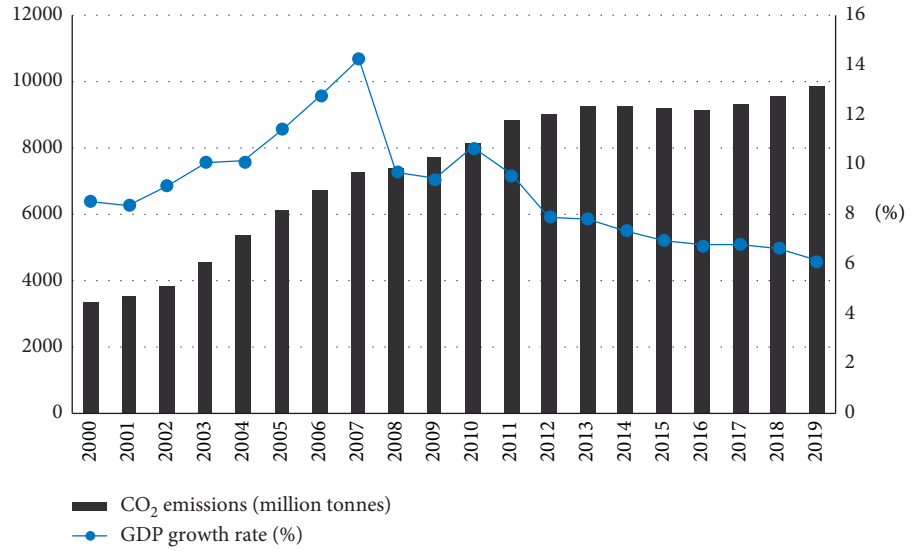

Figure 1: Trends of GDP growth rate and CO_2 emissions in China in 2000–2019. Data source: China Statistical Yearbook (2020) and BP Statistical Review of World Energy (2020).

Green technology innovation helps balance the relationship between environmental protection and economic development; however, it is also key to building a sustainable society, which is becoming more important around the globe, especially in China [7, 13–15].

In fact, it was a weak sustainable development model until the 12th Five-Year-Plan period in China was released, which, for the first time, focused on the concept of strong sustainability. Green growth was popular afterwards including the advocacy of green innovation [16]. China has introduced the new development concepts for the 13th Five-Year Plan, which has placed "innovative" and "green" development in an important position. The focus of innovative development is to address the issue of growth drivers, whereas the focus of green development is to address the issue of harmony between humankind and nature. China has transformed its economy from a high-speed growth stage to a high-quality development stage, and the organic combination of innovation-driven and green development is a critical way to achieve high-quality development. As a crucial method in promoting the construction of ecological civilization and green development, green technology innovation has both technology spillovers and environmental externalities in China. Under the principles of innovative and green development, exploring the driving factors of green technology innovation is of marked significance to promote the development of green technology and the formulation of related policies.

The purpose of this paper is to explore the determinants of green patent applications in China from 2000 to 2017 through the logarithmic mean Divisia index (LMDI) analysis framework. Our study not only examines the influencing factors of green patent applications in China but also evaluates the effects of CO_2 emissions and the efficiency of R&D expenditure.

The remainder of this paper is arranged as follows. Section 2 reviews the relevant and informative literature. Section 3 explains the LMDI decomposition method and data source. Section 4 covers the empirical results from the decomposition analysis of green technology patent applications in China. Finally, Section 5 comes to conclusions and proposes policy implications.

2. Literature Review

Braun first proposed the concept of green technology [17]. With the increasingly severe problems of global climate change and environmental degradation, more scholars have begun to pay attention to green technology innovation. These studies have focused on the definition and mode of green technology innovation and its motivation, efficiency, and influencing factors. The research scope of these studies has involved the country level, industrial level, or firm level [4, 18–23]. In terms of factors affecting green technology innovation, numerous scholars have studied the impact of environmental regulations on green technology innovation and drawn valuable conclusions [24, 25]. Most conclusions are consistent with the Porter hypothesis viewpoint [26], which suggests that the environmental regulation has a positive role in promoting green technology innovation [27–30]. Some scholars' conclusions, however, are inconsistent with the Porter hypothesis [31, 32]. Their studies found that (1) environmental regulations will have an inhibitory effect on enterprises' competitiveness, and (2) such regulations will have only a tenuous promotional effect on green technology innovation. In addition to the influence of environmental regulation factors, some scholars consider the impact of alternative factors—economic development level, R&D investment, CO_2 emissions, and government subsidies—on green technology innovation [3, 33–37]. However, the relationship between CO_2 emissions and R&D investment in green technologies has rarely been discussed.

The measurement of green technology innovation includes three primary indicators: the amount of R&D,

number of green patents, and green total-factor productivity; these represent the input, output, and performance of green technology innovation, respectively. Since Lanjouw and Mody [29] first introduced patent data into the study of green technology innovation, research in this field has reached constructive results [33, 38–40]. To explore the effect of green technologies, patent data has been used [41–44]. However, because of incomplete green patent statistics, studies on technological innovation based on China's green patents are still limited [3, 18, 33, 44, 45]. Fujii used patent data combined with the LMDI method to study the determinants of green technology inventions in China from the 9th Five-Year Plan to the 12th Five-Year Plan and focused on analyzing the differences in green technology development priorities during each five-year plan [44]. Chen and Lin made a decomposition analysis of patenting in renewable energy technologies from an extended LMDI approach based on three Chinese five-year-plan periods [46].

From the perspective of research methods, decomposition analysis has been widely utilized to quantify the variations in energy consumption and CO2 emissions. There are primarily two categories of the decomposition approach: structure decomposition analysis (SDA) and index decomposition analysis (IDA). SDA is widely used in revealing the role of structure change [47]. IDA can be implemented using either the Laspeyres index or the Divisia index. Ang proposed the logarithmic mean Divisia index (LMDI) method [47]. In contrast, the LMDI method does not produce unexplained residual terms, handles zero values, and is easy to conduct for comparative studies [49]. Because of its merits, the LMDI method is widely applied in energy and environmental science to address issues such as climate change and energy security [10, 48, 50–52]. In general, the LMDI method is rarely used to decompose green patent counts. Based on patent data, researchers have applied the extended LMDI method to study green chemical [43], biological [35], food waste management [53], fishery [54], and artificial intelligence technologies [21]. Cho and Sohn not only used LMDI decomposition to evaluate the impact of changes in CO_2 emissions on green R&D investment and related patents but also compared the primary factors driving green patent applications in France, Germany, Italy, and the United Kingdom [42]. Fujii and Managi applied the LMDI method to study China's sustainable green technology; the study considered the decomposed factors, including the priority of specific green technology, share of green patents, R&D share, and GDP scale [44].

Although countless efforts have been made to explore the factors influencing green technology innovation, this study highlights a few gaps in the literature. First, the majority of previous studies have focused on environmental regulations; however, little attention has been paid to the CO_2 emissions and R&D activities factors. Second, most of the previous literature has centered on the presentation of econometric results but has rarely applied the patent decomposition method. Most importantly, much of the previous research has investigated green technologies in developed countries but rarely discussed them in developing countries.

To fill in the previously mentioned gaps, this paper identifies the central drivers behind China's green technology innovation and focuses on CO_2 emissions and R&D activities based on an extended LMDI decomposition analysis. Moreover, this paper evaluates China's underlying policies and implemented measures and discusses the role of R&D activities in green technology innovation.

Our study's contributions are as follows. First, we extend the LMDI by introducing CO_2 emissions and R&D activities into green technology patent decomposition study. Second, we discuss the decomposition results through two ways: time-series decomposition analysis and period-wise decomposition analysis, which may provide a lot of new information for policy makers. In this regard, this study can provide insights for formulating different policies.

3. Methodology and Data

The LMDI method can be used for either multiplicative or additive decompositions [47]. Although the two decomposition forms' results are different, the same conclusions can be drawn in regard to analyzing influencing factors. In this study, we used the additive LMDI method because it is easy to examine the number of green patent application changes influenced by each factor.

Through expanding the Kaya identity [55] and highlighting the influence of carbon emissions and R&D activities on green technology innovation, this paper builds an additive LMDI decomposition model to decompose the influencing determinants of green technology innovation output change in China. We use this method to study the driving factors of green technology innovation because it can wholly decompose the changes in green technology innovation into five factors—economic scale, carbon emission intensity, R&D response, R&D efficiency, and green patent shares—and can effectively avoid problems, such as endogeneity, which may arise when using regression analysis.

3.1. Model Construction. As opposed to previous studies, this paper takes carbon emission intensity, R&D response, and R&D efficiency as essential factors of the extended LMDI decomposition framework. There are no definite study conclusions about the time lag between environmental changes and R&D investment changes. To achieve the goals of the *Kyoto Protocol* or *Paris Protocol*, countries often determine the amount of R&D investment in the current year based on the previous year's CO_2 emission level. Some studies consider a one-year time lag between R&D investment and CO_2 emissions [42]. Besides considering the impact of GDP on R&D investment, this study includes the one-year time lag of GDP and CO_2 emissions in the decomposition model as driving factors of green technology innovation.

In related studies, the indicators for measuring green technology innovation output included chiefly new product sales revenue and green patent quantity; however, new product sales revenue is more suitable for the enterprise level, and the impact of factors such as marketing strategies

on sales revenue cannot be excluded. Therefore, this study uses the number of green patent applications as a measurement of green technology innovation. Patents are also closely related to R&D activities. Some studies have shown that a time lag of approximately one to two years exists between R&D investment and patent applications [55–57], while other studies have found that a strong correlation lies between patent applications and R&D investments with a very little lag. In particular, a study by Brunnermeier and Cohen has shown there is no time difference between R&D investment and environmental patent applications [48]; therefore, this study does not consider the time lag between them.

We applied a patent decomposition analysis approach to identify the driving factors associated with green patent applications. Based on the existing literature [37, 46] and combined with the actual situation of green development in China, we used five indicators to decompose green patents. The detailed process of the patent decomposition method is expressed as follows:

$$P_{\mathrm{GREEN}t} = \mathrm{GDP}_{(t-1)} \times \frac{\mathrm{CO}_{2(t-1)}}{\mathrm{GDP}_{(t-1)}} \times \frac{\mathrm{R\&D}_t}{\mathrm{CO}_{2(t-1)}} \times \frac{P_{\mathrm{TOTAL}t}}{\mathrm{R\&D}_t} \times \frac{P_{\mathrm{GREEN}t}}{P_{\mathrm{TOTAL}t}}, \tag{1}$$

where P_{GREEN} is the number of green patent applications; GDP denotes the gross domestic product; CO_2 is carbon emissions; R&D is a research and development investment; P_{TOTAL} is the total number of patent applications.

Subsequently, (1) is further simplified as follows:

$$P_{\mathrm{GREEN}_t} = G_{(t-1)} \times I_{(t-1)} \times R_t \times E_t \times S_t, \tag{2}$$

where G is the gross domestic product, which indicates the economic scale; I is the intensity of carbon emissions, which indicates CO_2 emissions per unit of GDP; R is the R&D reaction, which shows the response of R&D expenditures with the changes in CO_2 emissions; E is R&D efficiency, which indicates the green patent output per unit of R&D input; S is defined as the total number of green patent applications divided by the total number of patent applications, which yields the share of green patent applications. This indicator shows the direction of technological innovation. The higher the proportion, the more apparent the green tendency of technological innovation. Equation (2) explains that the number of green patent applications is affected by economic scale, CO_2 emission intensity, R&D reaction, R&D efficiency, and green patent share.

According to the LMDI additive decomposition, the changes in the number of green patent applications from the base year B to a target year T can be represented as follows:

$$\Delta P_{\mathrm{GREEN}} = P^T_{\mathrm{GREEN}} - P^B_{\mathrm{GREEN}} = \Delta P_{\mathrm{gdp}} + \Delta P_{\mathrm{int}} + \Delta P_{\mathrm{rea}} + \Delta P_{\mathrm{eff}} + \Delta P_{\mathrm{str}}. \tag{3}$$

Equation (3) denotes that the change in the number of green patent applications can be decomposed into economic scale effect (ΔP_{gdp}), carbon emission intensity effect (ΔP_{int}), R&D reaction effect (ΔP_{rea}), R&D efficiency effect (ΔP_{eff}), and green patent share effect (ΔP_{str}), which, respectively, indicate the contribution value of each factor to the change of green patent applications. If the decomposition effect is a positive value, then, it will have a favorable driving impact on the green technology innovation output. If it is a negative value, then, it exerts a negative impact on green technology innovation output.

The LMDI decomposition method includes an additive version and a multiplicative version that produces similar results. In this paper, we applied the additive decomposition method for decomposing changes in the number of green patent applications. The calculation process is shown as follows:

$$\begin{aligned}
\Delta P_{\mathrm{gdp}} &= \omega_i \ln\left(\frac{G^{T-1}}{G^{B-1}}\right),\\
\Delta P_{\mathrm{int}} &= \omega_i \ln\left(\frac{I^{T-1}}{I^{B-1}}\right),\\
\Delta P_{\mathrm{rea}} &= \omega_i \ln\left(\frac{R^{T}}{R^{B}}\right),\\
\Delta P_{\mathrm{eff}} &= \omega_i \ln\left(\frac{E^{T}}{E^{B}}\right),\\
\Delta P_{\mathrm{str}} &= \omega_i \ln\left(\frac{S^{T}}{S^{B}}\right),
\end{aligned} \tag{4}$$

where ω_i is the estimated weight, which is the conventional processing method of the additive LMDI approach, and this weight is defined as

$$\omega_i = \frac{P^T_{\mathrm{GREEN}} - P^B_{\mathrm{GREEN}}}{\ln P^T_{\mathrm{GREEN}} - \ln P^B_{\mathrm{GREEN}}}. \tag{5}$$

Following the decomposition approach, we also apply contribution rate analysis to further study the changing impact of drivers of the green patent over time. The contribution rate of each driving force is calculated by the following equations:

$$\begin{aligned}
CR_{\mathrm{gdp}} &= \frac{\Delta P_{\mathrm{gdp}}}{\Delta P_{\mathrm{GREEN}}} \times 100\%,\\
CR_{\mathrm{int}} &= \frac{\Delta P_{\mathrm{int}}}{\Delta P_{\mathrm{GREEN}}} \times 100\%,\\
CR_{\mathrm{rea}} &= \frac{\Delta P_{\mathrm{rea}}}{\Delta P_{\mathrm{GREEN}}} \times 100\%,\\
CR_{\mathrm{eff}} &= \frac{\Delta P_{\mathrm{eff}}}{\Delta P_{\mathrm{GREEN}}} \times 100\%,\\
CR_{\mathrm{str}} &= \frac{\Delta P_{\mathrm{str}}}{\Delta P_{\mathrm{GREEN}}} \times 100\%.
\end{aligned} \tag{6}$$

3.2. Data. To apply the previously mentioned additive form of the LMDI method, we collected the necessary data related to GDP, CO_2 emissions, R&D expenditure, and patent data. Patent data usually include two types: patent applications and patent grants. Patent application data can reflect inventors' R&D activities and R&D strategies, and patent grant data represent the number of qualifying patent applications that are primarily used to examine the diffusion of technologies. Because patent grants are often granted long after the submission of the patent application, patent grant data can easily cause information distortion and are subject to human factors, such as differences between patent agencies in various countries, which causes uncertainty. Therefore, we use patent application data as the measurement of green technology innovation. Green patent application data come from the China National Intellectual Property Administration (CNIPA) patent search and analysis system. According to the international patent classification number corresponding to the World Intellectual Property Organization's (WIPO) list of green technologies, China's green patent invention and green utility model patents are counted to obtain the data on green patent applications from 2000 to 2017. China's R&D investment data and the total number of patent applications are taken from the China Statistical Yearbook on Science and Technology (2001–2018). To correspond to the green patent statistics, total patent data include the number of patent applications for green patent invention and green utility model patents. The R&D investment data include R&D expenditures of R&D institutions, universities, and large- and medium-sized industrial enterprises. The CO_2 emission data were compiled using the BP Statistical Review of World Energy (2001–2018), and the GDP data come from the China Statistical Yearbook (2001–2018). R&D expenditures and GDP were deflated based on the 2000 price to eliminate the influence of price fluctuations and make the yearly indicators comparable.

As previously mentioned, to reflect the time lag, however, the GDP and CO_2 emissions values used were from 1999 to 2016. The data used, including the R&D expenditure and related patent application data, referred to the interval from 2000 to 2017.

4. Results and Discussion

4.1. Trends of Green Patent Applications in China. Figure 2 shows the number and share of green patent applications in China from 2000 to 2017. During this period, the number of green patent applications in China increased by 52.16 times. It has maintained an especially rapid growth since 2010. Economic growth has gradually slowed in China after the 2008 financial crisis, but the number of green patent applications maintains a relatively fast-growing trend. Although the proportion of green patents to total patent applications is not high, it has increased from 4.87% in 2000 to 8.31% in 2017, indicating clear growth potential.

4.2. LMDI Analysis. In general, there are two types of decomposition analysis mode: the period-wise manner and the time-series manner. The period-wise manner compares indices between the first and last years of a given period without considering the details during different periods. Time-series analysis can compare the indices on an annual basis. To better analyze the influencing factors of green technology innovations, we employed the period-wise and time-series forms to study the driving factors that can change the number of green patent applications in China.

4.2.1. Period-Wise Decomposition Analysis. We analyzed the five determinants of green patent applications from 2000 to 2017. Following the five-year plan in China, we subdivided the study period into four intervals of five years and one period of one year, 2016-2017. The determinants of green patent applications and their relative contribution value and contribution rate are presented in Table 1 and Figure 3.

As shown in Table 1, the number of green patent applications in China dramatically increased by 238,473 from 2000 to 2017, especially in 2011–2015 (12th Five-Year Plan) and 2016-2017. Overall, economic activity, R&D reaction, R&D efficiency, and green patent share played promoting roles in the increased number of green patent applications from 2000 to 2017. Among the positive effects, the R&D efficiency factor is the dominant factor, and economic activity is the second most important factor affecting green patent applications. By contrast, carbon emission intensity played a negative role in the increased number of green patent applications.

Differences exist in various intervals. We applied the contribution rate to investigate each factor's contribution degree. As shown in Figure 3, the contribution rate fluctuated during the study period of 2000–2017. During 2000–2005, the contribution rate of the R&D reaction effect was negative, indicating an inhibiting effect on the increased number of green patent applications in comparison with other positive drivers. By contrast, the carbon emission intensity effect was positive in this period. Nevertheless, from 2006 to 2017, the carbon emission intensity effect played a negative role, and the R&D reaction effect played a promoting role in the increased number of green patent applications. Besides the 2016-2017 period, the green patent share had a significant contribution to the change in green patent applications, accounting for 61.44%.

4.2.2. Time-Series Decomposition Analysis. Compared with the period-wise decomposition, using the time-series mode to decompose the change factors of green technology patent applications year by year can provide more detailed information. Table 2 shows the time-series decomposition results of the changes in the number of green patent applications in 2000–2017.

The results show that all influencing factors contributed differently to the change in green patent applications in various years and grew involved in largely disparate influence with respect to time series. Based on the results in Table 2, further analysis of the change in influence factors based on China's actual situation was conducted as follows.

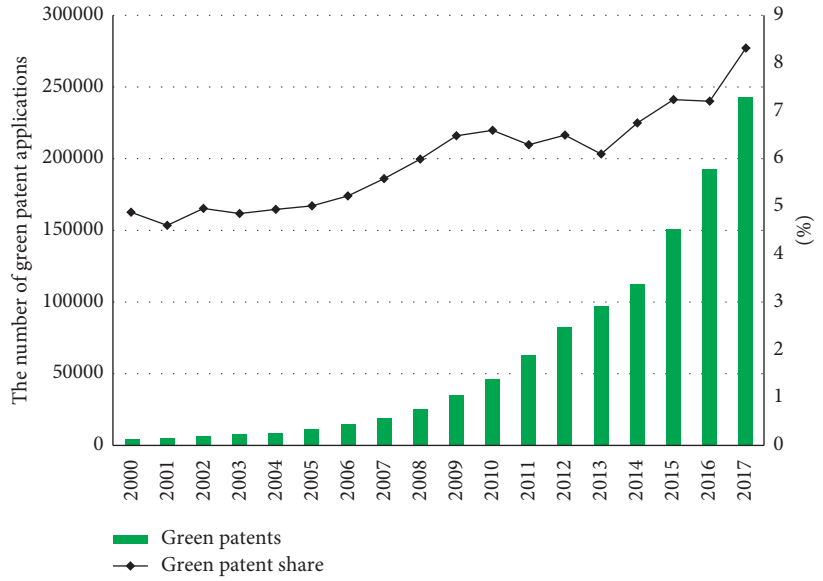

Figure 2: Trends of green technology patent application in China in 2000–2017. Data source: China and Global Patent Examination Inquiry from the CNIPA.

Table 1: Period-wise decomposition results of green patent applications in China in 2000–2017.

Effect	5-year intervals				Full period
	2000–2005	2006–2010	2011–2015	2016-2017	2000–2017
ΔP_{gdp}	3320.52	11955.35	31372.04	14054.50	91669.06
ΔP_{int}	320.23	−5516.17	−18759.84	−15373.43	−30566.62
ΔP_{rea}	−121.15	4998.94	16346.27	15779.27	29674.96
ΔP_{eff}	3300.80	13544.22	45270.81	5080.47	115686.95
ΔP_{str}	205.59	6419.66	14046.73	31136.19	32008.65
ΔP_{GREEN}	7026	31402	88276	50677	238473

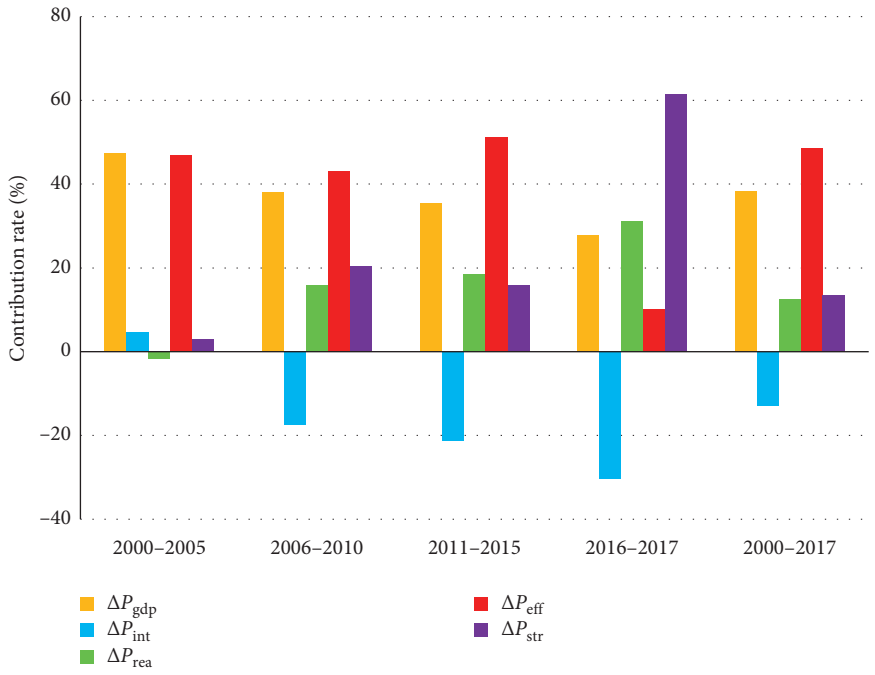

Figure 3: The contribution rate of each factor in the changes in the number of green patent applications in China during different periods.

Table 2: Year-by-year decomposition analysis results of green patent applications in China in 2000–2017.

Year	Economic activity		CO_2 emission intensity		R&D reaction		R&D efficiency		Green patent share		Total
	ΔP_{gdp}	CR_{gdp} (%)	ΔP_{int}	CR_{int} (%)	ΔP_{rea}	CR_{rea} (%)	ΔP_{eff}	CR_{eff} (%)	ΔP_{str}	CR_{str} (%)	Δ_{Green}
2000-2001	391.4	85.1	−293.4	−63.8	284.5	61.9	351.4	76.4	−274.0	−59.6	460
2001-2002	458.6	30.5	−187.4	−12.5	229.8	15.3	582.5	38.7	420.6	28.0	1504
2002-2003	630.2	43.5	−0.7	−0.1	60.1	4.2	909.4	62.8	−151.1	−10.4	1448
2003-2004	797.1	103.4	581.2	75.4	−573.6	−74.4	−180.7	−23.4	146.9	19.1	771
2004-2005	972.8	34.2	674.9	23.7	−556.3	−19.6	1604.7	56.4	146.9	5.2	2843
2005-2006	1414.1	45.3	335.0	10.7	−183.1	−5.9	1029.3	32.9	529.7	17.0	3125
2006-2007	1982.0	51.4	−480.2	−12.5	699.3	18.1	539.0	14.0	1117.8	29.0	3858
2007-2008	2876.2	44.4	−1124.5	−17.3	253.7	3.9	2942.4	45.4	1536.2	23.7	6484
2008-2009	2748.5	28.1	−2187.2	−22.4	2105.9	21.5	4785.9	48.9	2329.9	23.8	9783
2009-2010	3613.7	32.0	−1852.2	−16.4	2291.0	20.3	6555.8	58.1	668.7	5.9	11277
2010-2011	5438.6	32.9	−2532.3	−15.3	1992.7	12.0	14176.3	85.6	−2517.3	−15.2	16558
2011-2012	6541.9	33.2	−832.2	−4.2	−228.8	−1.2	11941.1	60.6	2274.1	11.6	19696
2012-2013	6801.9	46.7	−4935.6	−33.9	4852.7	33.4	13410.4	92.2	−5578.3	−38.3	14551
2013-2014	7835.2	51.7	−5016.6	−33.1	4531.6	29.9	−2728.9	−18.0	10523.8	69.5	15145
2014-2015	9198.6	23.7	−9396.5	−24.2	8908.9	22.9	21062.4	54.2	9110.7	23.4	38884
2015-2016	11398.3	27.5	−12310.2	−29.7	11990.3	29.0	31135.7	75.2	−805.1	−1.9	41409
2016-2017	14054.5	27.7	−15373.4	−30.3	15779.3	31.1	5080.5	10.0	31136.2	61.4	50677

(1) Economic Scale Effect. Innovation and economic development complement each other. Innovation is an important driving force for economic growth. An increase in the level of economic development can provide a better environment and better conditions for technology innovation. Green technology innovation needs economic support. Generally speaking, the higher the level of economic development, the greater the amount of R&D investment, and the more the innovation output. China became the third-largest economy in the world in 2007 and the second largest in 2011, but growth has recently slowed. The decomposition results show that the economic scale has a significant positive role in promoting green technology innovation output, with an average contribution rate of 32.35%. As shown by the orange line in Figure 4, significant differences lie in the level of economic scale effect. In 2004-2005, the contribution rate of economic scale effect on green patent applications sharply decreased, which may be a byproduct of the 2003 SARS outbreak. Due to the impact of the 2008 financial crisis, China's economic development has slowed; this has since reduced the impact of economic development on the number of China's green technology patent applications.

(2) Carbon Emission Intensity Effect. Looking at Table 2, carbon emission intensity has a negative impact on green patent applications, except in the periods of 2003-2004, 2004-2005, and 2005-2006 (demonstrated by the blue line in Figure 4). In particular, the carbon emission intensity effect accounted for a reduction of approximately 33.9% in patent applications in 2012-2013. To date, China has become the country with the largest carbon emissions rate in the world. China must control its CO_2 emissions and reduce its carbon emissions intensity to achieve its low-carbon development goal.

(3) R&D Reaction Effect. R&D reaction refers to the response of R&D activities to changes in CO_2 emissions. With the promulgation and implementation of China's environmental regulation measures, CO_2 emissions control has become an important measure. To achieve energy conservation and emission reduction targets, investment funds for R&D continue to increase, thereby promoting green technology innovation output. Since the 12th Five-Year Plan (2011–2015) espcially—with the country's attention turned towards climate change, environmental issues, and determination of CO_2 emission targets—green technology innovation has been significantly affected. According to the decomposition results in Table 2, the R&D reaction effect is generally positive, except in the periods of 2003-2004, 2004-2005, 2005-2006, and 2011-2012.

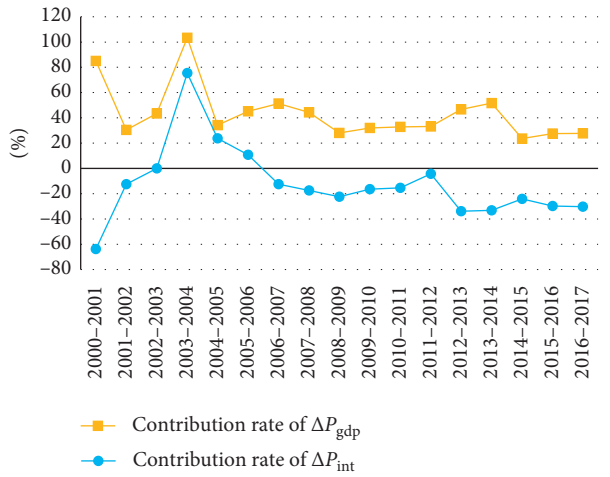

Figure 4: The trend of contribution rate of economic scale and carbon emissions intensity factors to China's green patent applications increase from 2000 to 2017.

(4) R&D Efficiency Effect. The decomposition results show that the R&D efficiency effect is the dominant driving force

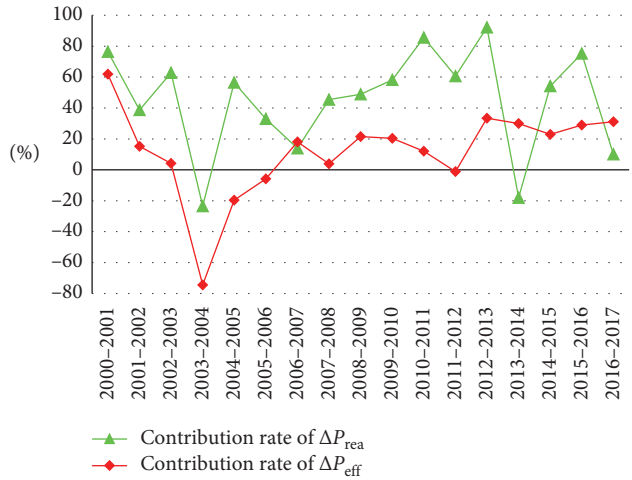

Figure 5: The trend of contribution rate of R&D activities factors to China's green technology innovation output from 2000 to 2017.

for the change in green patent applications, with a high contribution rate of 47.47%. Table 2 presents that the increase in R&D efficiency from 2000 to 2001 on green patents was only 351.4 and that the contribution value from 2015 to 2016 was as high as 31,135.7, indicating that China has continuously improved its R&D efficiency in the past ten years. The contribution rate of R&D efficiency to the change in green patents from 2003 to 2004 is negative; both innovation activities and innovation efficiency were affected, where the 2003 SARS outbreak might also have had an influence. The downwind pressure on China's economic development may have caused the negative effect of R&D efficiency in 2013-2014. Although the effect of R&D efficiency fluctuated during the study period, it showed an overall upward trend, indicating that the efficiency of green technology innovation in China was consistently improving. R&D investment was more effectively used, which also benefits from a series of technological innovation incentive policies that China implemented.

Notably, R&D effects (i.e., R&D reaction effect and R&D efficiency effect) played a dominant role in the increased number of green patent applications. Figure 5 demonstrates that the two effects' contribution rate shows approximately the same trend. Therefore, increasing investment in R&D activities and improving R&D efficiency are of substantial significance to improving the output of green technology innovation in China.

(5) Green Patent Share Effect. The green patent share effect also plays a positive role in promoting green technology innovation. Although the effects of green patents fluctuated during the study period (and even showed negative values in specific years), the overall trend was upward. The maximum value was 10523.8 in 2013-2014, and the minimum value was 146.9 in 2004-2005. This indicates that the proportion of green technology innovation output was increasing with the rising market demand for green technology products and the growing importance of green technology innovation.

5. Conclusions and Implications

5.1. Conclusions. This study has examined the main influencing factors contributing to green patent applications in China from 2000 to 2017. We developed the extended LMDI method to decompose and analyze the contributions of the main influencing factors, which include economic scale, carbon emission intensity, R&D reaction, R&D efficiency, and green patent share factors. The main conclusions are as follows.

First, taking the number of green patent applications as an indicator for green innovation output and based on the statistical data from 2000 to 2017, the number of green patent applications in China showed an upward trend—especially after 2010, maintaining rapid growth.

Second, the results of the LMDI additive decomposition based on the period-wise manner indicate that all of the factors, except the carbon emission intensity effect, are positive factors on the growth of China's green patent applications. Of these positive factors, the R&D efficiency effect and economic scale effect contribute the most to the growth of China's green technology patents. Among the positive and negative effects, R&D efficiency and carbon emission intensity effect are the most prominent, which indirectly reflects modern climate change and environmental deterioration; that is, improving R&D efficiency and reducing carbon emissions are important measures to promote China's green technology innovation.

Third, the year-by-year decomposition analysis results show that all influencing factors contributed differently to the change in green patent applications in various years and grew involved in largely disparate influence with respect to time series. In most years, carbon emission intensity has a negative impact on green patent applications. Notably, the contribution rate of R&D reaction effect and R&D efficiency effect shows approximately the same trend, and the two effects played a dominant role in the increased number of green patent application.

5.2. Policy Implications. From the previously mentioned findings, we can better understand the trend of China's green technology innovation and clarify the importance of carbon emissions, R&D efficiency, economic development, and other factors for green technology innovation. We can then formulate targeted management policies, governance measures, and R&D strategies. Based on these conclusions, we propose the following policy recommendations.

First, China must accelerate the construction of a market-oriented green technology innovation system and promote the development of green technology innovation activities. With increasingly prominent domestic environmental problems and the ongoing pressure of international climate negotiations (e.g., *Kyoto Protocol* and *Paris Agreement*), international green competition is likely to change the current national comparative advantage. To solve practical problems, undertake international obligations, and enhance international competitiveness, China must accelerate the construction of a market-oriented green

technology innovation promotion system. In May 2019, the National Development and Reform Commission and the Ministry of Science and Technology jointly issued the Guiding Opinions on the Construction of Market-Oriented Green Technology Innovation System. This was the first instance in which China published opinions on how to construct a system for green technology innovation, and the system is of considerable value. The system suggested the government formulate a series of policies to guide, stimulate, and guarantee (1) green technology innovation, such as financial measures as well as science and technology policies and the popularization and application of achievements; (2) policies to encourage green production and the green transformation and upgrading of industries; and (3) green financial policies and green import and export policies to stimulate innovation subjects' enthusiasm and to improve the quality of green innovation.

Second, China should increase investment in green technology R&D to improve R&D efficiency. This study demonstrates that R&D factors, especially R&D efficiency, are important factors affecting the output of green technology innovation. Although China's R&D investment has been increasing in recent years due to its large-scale market, the investment is too scattered, and most enterprises' R&D expenditure is relatively low. Therefore, the government should increase R&D investment related to the environment and designate relevant incentive mechanisms so that enterprises can actively become the source of R&D funds and the main body of implementation.

Third, China needs to improve environmental regulatory policies and accelerate innovation in environmental regulatory tools. As opposed to previous studies, which mainly considered the impact of environmental regulation on green technology innovation, this study included carbon emissions in the decomposition framework of innovation output in the green technology department. The study found the intensity of carbon emissions inhibited the output of green technology innovation. Therefore, China still must strengthen environmental regulation, reduce carbon emission intensity, and balance environmental protection and economic development. Enterprises should be encouraged to carry out green technology innovation by further improving environmental regulation policies, innovating environmental regulation tools, and using diversified environmental regulation methods. At the same time, China should pay attention to strengthening the cooperation between environmental regulation policy tools and relevant policies (such as finance and innovation policies).

Finally, China must strengthen the protection of intellectual property rights. The primary objectives are to take the strictest measures to protect intellectual property rights, reduce the risk of infringement on enterprises' R&D investment, maintain and protect the achievements and benefits of enterprise green technology innovation, and fully mobilize enterprise enthusiasm for green technology innovation.

We believe the novel decomposition analysis applied in this study is useful for understanding changes in green patent application activities in China. Additionally, a comparison of carbon intensity effect, R&D reaction effect, and R&D intensity effect are helpful for understanding the influencing factors of green technology innovation. A limitation of this study is the difficulty of clarifying the effects of policies and subsidies on green technology innovation activities. Therefore, further research is needed to develop a research framework to consider the previously mentioned factors. In addition, the green patent includes numerous types of green technologies; thus, further studies are needed to consider various green patent classifications.

Data Availability

The data used to support the findings of this study are available from the corresponding author upon request.

Conflicts of Interest

The authors declare that there are no conflicts of interest regarding the publication of this paper.

References

[1] Q. Wang and S. Wang, "Decoupling economic growth from carbon emissions growth in the United States: the role of research and development," *Journal of Cleaner Production*, vol. 234, pp. 702–713, 2019.

[2] B. H. Hall and C. Helmers, "Innovation and diffusion of clean/green technology: can patent commons help?" *Journal of Environmental Economics and Management*, vol. 66, no. 1, pp. 33–51, 2013.

[3] H.-H. Qiu and J. Yang, "An assessment of technological innovation capabilities of carbon capture and storage technology based on patent analysis: a comparative study between China and the United States," *Sustainability*, vol. 10, no. 3, pp. 877–920, 2018.

[4] Å. Lindman and P. Söderholm, "Wind energy and green economy in Europe: measuring policy-induced innovation using patent data," *Applied Energy*, vol. 179, pp. 1351–1359, 2016.

[5] Y. Ma, Q. Zhang, and Q. Yin, "Influence of environmental management on green process innovation: comparison of multiple mediating effects based on routine replication," *International Journal of Environmental Research and Public Health*, vol. 16, no. 22, p. 4346, 2019.

[6] J.-F. Dong, Q. Wang, C. Deng, X.-M. Wang, and X.-L. Zhang, "How to move China toward a green-energy economy: from a sector perspective," *Sustainability*, vol. 8, no. 4, p. 337, 2016.

[7] W. Fang, L. Tang, P. Cheng, and N. Ahmad, "Evolution decision, drivers and green innovation performance for collaborative innovation center of ecological building materials and environmental protection equipment in Jiangsu province of China," *International Journal of Environmental Research and Public Health*, vol. 15, no. 11, pp. 2365–2419, 2018.

[8] R. Nikzad and G. Sedigh, "Greenhouse gas emissions and green technologies in Canada," *Environmental Development*, vol. 24, pp. 99–108, 2017.

[9] BP, *Statistical Review of World Energy, 2020*, BP, London, UK, 69th edition, 2020.

[10] J. Liu, Q. Yang, Y. Zhang, W. Sun, and Y. Xu, "Analysis of CO_2 emissions in China's manufacturing industry based on

extended logarithmic mean division index decomposition," *Sustainability*, vol. 11, no. 1, p. 226, 2019.

[11] C. Xia, Y. Li, Y. Ye, Z. Shi, and J. Liu, "Decomposed driving factors of carbon emissions and scenario analyses of low-carbon transformation in 2020 and 2030 for Zhejiang province," *Energies*, vol. 10, no. 11, pp. 1747–1816, 2017.

[12] S. Zhang, F. Yang, C. Liu et al., "Study on global industrialization and industry emission to achieve the 2°C goal based on MESSAGE model and LMDI approach," *Energies*, vol. 13, no. 4, p. 825, 2020.

[13] Q. Du, X. Lu, Y. Li, M. Wu, L. Bai, and M. Yu, "Carbon emissions in China's construction industry: calculations, factors and regions," *International Journal of Environmental Research and Public Health*, vol. 15, no. 6, p. 1220, 2018.

[14] F. Dong, J. Li, Y.-J. Zhang, and Y. Wang, "Drivers analysis of CO_2 emissions from the perspective of carbon density: the case of Shandong province, China," *International Journal of Environmental Research and Public Health*, vol. 15, no. 8, p. 1762, 2018.

[15] W. Wang, Y. Li, L. Li, L. Wang, and K. Wang, "SnO_2/TiO_2 nanocomposite prepared by pulsed laser deposition as anode material for flexible quasi-solid-state lithium-ion batteries," *International Journal of Electrochemical Science*, vol. 15, no. 12, pp. 11709–11722, 2020.

[16] Z. Li, W. Yang, C. Wang, Y. Zhang, and X. Yuan, "Guided high-quality development, resources, and environmental forcing in China's green development," *Sustainability*, vol. 11, no. 7, p. 1936, 2019.

[17] E. Braun and D. Wield, "Regulation as a means for the social control of technology," *Technology Analysis & Strategic Management*, vol. 6, no. 3, pp. 259–272, 1994.

[18] D. Zhang, Z. Rong, and Q. Ji, "Green innovation and firm performance: evidence from listed companies in China," *Resources, Conservation and Recycling*, vol. 144, pp. 48–55, 2019.

[19] L. J. Aaldering, J. Leker, and C. H. Song, "Competition or collaboration? - analysis of technological knowledge ecosystem within the field of alternative powertrain systems: a patent-based approach," *Journal of Cleaner Production*, vol. 212, pp. 362–371, 2019.

[20] CIPO, *Patented Inventions in Climate Change Mitigation Technologies*, CIPO, Canada, 2017.

[21] H. Fujii and S. Managi, "Trends and priority shifts in artificial intelligence technology invention: a global patent analysis," *Economic Analysis and Policy*, vol. 58, pp. 60–69, 2018.

[22] W. Kai, L. Li, T. Zhang, and Z. Liu, "Nitrogen-doped graphene for supercapacitor with long-term electrochemical stability," *Energy*, vol. 70, pp. 612–617, 2014.

[23] K. Wang, W. Wang, L. Wang, and L. Li, "An improved SOC control strategy for electric vehicle hybrid energy storage systems," *Energies*, vol. 13, no. 20, p. 5297, 2020.

[24] M.-Y. Hsu, "Green patent: promoting innovation for environment by patent system," in *Proceedings of the PICMET '07 - 2007 Portland International Conference on Management of Engineering & Technology*, pp. 2491–2497, Portland, OR, USA, August 2007.

[25] T. Stucki, "Which firms benefit from investments in green energy technologies? - the effect of energy costs," *Research Policy*, vol. 48, no. 3, pp. 546–555, 2019.

[26] M. E. Porter and C. V. D. Linde, "Toward a new conception of the environment-competitiveness relationship," *Journal of Economic Perspectives*, vol. 9, no. 4, pp. 97–118, 1995.

[27] N. Johnstone, I. Haščič, and D. Popp, "Renewable energy policies and technological innovation: evidence based on patent counts," *Environmental and Resource Economics*, vol. 45, no. 1, pp. 133–155, 2010.

[28] D. Acemoglu, P. Aghion, and D. Hémous, "The environment and directed technical change in a North-South model," *Oxford Review of Economic Policy*, vol. 30, no. 3, pp. 513–530, 2014.

[29] J. O. Lanjouw and A. Mody, "Innovation and the international diffusion of environmentally responsive technology," *Research Policy*, vol. 25, no. 4, pp. 549–571, 1996.

[30] P. Aghion, A. Dechezleprêtre, D. Hémous, R. Martin, and J. van Reenen, "Carbon taxes, path dependency, and directed technical change: evidence from the auto industry," *Journal of Political Economy*, vol. 124, no. 1, pp. 1–51, 2016.

[31] R. D. Simpson and R. L. Bradford, "Taxing variable cost: environmental regulation as industrial policy," *Journal of Environmental Economics and Management*, vol. 30, no. 3, pp. 282–300, 1996.

[32] J. A. Frankel, A. K. Rose, R. Kopp et al., "Manufacturing : what does the evidence tell Us ?" *The Economics of International Trade and the Environment*, vol. 87, pp. 85–91, 1991.

[33] Q. Wang, J. Qu, B. Wang, P. Wang, and T. Yang, "Green technology innovation development in China in 1990-2015," *Science of the Total Environment*, vol. 696, p. 134008, 2019.

[34] Y.-C. Pan, X.-Y. Liang, Y. Xiong, and J.-H. Ma, "Game analysis of green technology implementation with green consumption preference considered under cap-and-trade scheme," in *Proceedings of the DEStech Transactions on Computer Science and Engineering*, pp. 290–295, Xi'an, China, June 2018.

[35] H. Fujii, K. Yoshida, and K. Sugimura, "Research and development strategy in biological technologies: a patent data analysis of Japanese manufacturing firms," *Sustainability*, vol. 8, no. 4, p. 351, 2016.

[36] V. Costantini, F. Crespi, and A. Palma, "Characterizing the policy mix and its impact on eco-innovation: a patent analysis of energy-efficient technologies," *Research Policy*, vol. 46, no. 4, pp. 799–819, 2017.

[37] W. Kai, F. Xiao, P. Jinbo, R. Jun, D. Chongxiong, and L. Liwei, "State of charge (SOC) estimation of lithium-ion battery based on adaptive square root Unscented Kalman Filter," *International Journal of Electrochemical Science*, vol. 15, pp. 9499–9516, 2020.

[38] E. Maasoumi, A. Heshmati, and I. Lee, "Green innovations and patenting renewable energy technologies," *Empirical Economics*, vol. 60, pp. 1–26, 2020.

[39] S.-J. Ahn and H. Y. Yoon, "'Green chasm' in clean-tech for air pollution: patent evidence of a long innovation cycle and a technological level gap," *Journal of Cleaner Production*, vol. 272, p. 122726, 2020.

[40] A. Fabrizi, G. Guarini, and V. Meliciani, "Green patents, regulatory policies and research network policies," *Research Policy*, vol. 47, no. 6, pp. 1018–1031, 2018.

[41] B. Escobar Andrae and N. Arellano Escudero, "Green innovation from the global south: renewable energy patents in Chile, 1877€"1910," *Business History Review*, vol. 93, no. 2, 2019.

[42] J. H. Cho and S. Y. Sohn, "A novel decomposition analysis of green patent applications for the evaluation of R & D efforts to reduce CO_2 emissions from fossil fuel energy consumption," *Journal of Cleaner Production*, vol. 193, pp. 290–299, 2018.

[43] H. Fujii, "Decomposition analysis of green chemical technology inventions from 1971 to 2010 in Japan," *Journal of Cleaner Production*, vol. 112, pp. 4835–4843, 2016.

[44] H. Fujii and S. Managi, "Decomposition analysis of sustainable green technology inventions in China," *Technological Forecasting and Social Change*, vol. 139, pp. 10–16, 2019.

[45] W. Kai, L. Liwei, X. Wen et al., "Electrodeposition synthesis of PANI/MnO_2/graphene composite materials and its electrochemical performance," *International Journal of Electrochemical Science*, vol. 12, pp. 8306–8314, 2017.
[46] Y. Chen and B. Lin, "Decomposition analysis of patenting in renewable energy technologies: from an extended LMDI approach perspective based on three Five-Year Plan periods in China," *Journal of Cleaner Production*, vol. 269, p. 122402, 2020.
[47] B. W. Ang, "Decomposition analysis for policymaking in energy:," *Energy Policy*, vol. 32, no. 9, pp. 1131–1139, 2004.
[48] S. B. Brunnermeier and M. A. Cohen, "Determinants of environmental innovation in US manufacturing industries," *Journal of Environmental Economics and Management*, vol. 45, no. 2, pp. 278–293, 2003.
[49] B. W. Ang, "The LMDI approach to decomposition analysis: a practical guide," *Energy Policy*, vol. 33, no. 7, pp. 867–871, 2005.
[50] P. Yang, X. Liang, and P. J. Drohan, "Using Kaya and LMDI models to analyze carbon emissions from the energy consumption in China," *Environmental Science and Pollution Research*, vol. 27, no. 21, pp. 26495–26501, 2020.
[51] P. M. De Oliveira-De Jesus, J. J. Galvis, D. Rojas-Lozano, and J. M. Yusta, "Multitemporal LMDI index decomposition analysis to explain the changes of ACI by the power sector in Latin America and the Caribbean between 1990-2017," *Energies*, vol. 13, no. 9, p. 2328, 2020.
[52] H. Lei, X. Xia, C. Li, and B. Xi, "Decomposition analysis of wastewater pollutant discharges in industrial sectors of China (2001-2009) using the LMDI I method," *International Journal of Environmental Research and Public Health*, vol. 9, no. 6, pp. 2226–2240, 2012.
[53] H. Fujii and Y. Kondo, "Decomposition analysis of food waste management with explicit consideration of priority of alternative management options and its application to the Japanese food industry from 2008 to 2015," *Journal of Cleaner Production*, vol. 188, pp. 568–574, 2018.
[54] H. Fujii, Y. Sakakura, A. Hagiwara, J. Bostock, K. Soyano, and Y. Matsushita, "Research and development strategy for fishery technology innovation for sustainable fishery resource management in north-east Asia," *Sustainability*, vol. 10, no. 1, p. 59, 2018.
[55] Y. Kaya, *Impact of Carbon Dioxide Emission Control on GNP Growth: Interpretation of Proposed Scenarios IPCC Energy and Industry Subgroup*, Response Strategies Working Group, Paris, France, 1990.
[56] T. D. Corsatea, "Technological capabilities for innovation activities across Europe: evidence from wind, solar and bioenergy technologies," *Renewable and Sustainable Energy Reviews*, vol. 37, pp. 469–479, 2014.
[57] M. Kondo, "R & D dynamics of creating patents in the Japanese industry," *Research Policy*, vol. 28, no. 6, pp. 587–600, 1999.

Hindawi
Mathematical Problems in Engineering
Volume 2021, Article ID 6635749, 10 pages
https://doi.org/10.1155/2021/6635749

Research Article

An Adaptive Memetic Algorithm for Dynamic Electric Vehicle Routing Problem with Time-Varying Demands

Na Wang,[1] Yihao Sun,[2] and Hongfeng Wang[2]

[1]*Department of Basic Computer and Mathematics, Shenyang Normal University, Shenyang 110034, China*
[2]*College of Information Science and Engineering, Northeastern University, Shenyang 110819, China*

Correspondence should be addressed to Hongfeng Wang; hfwang@mail.neu.edu.cn

Received 29 October 2020; Revised 21 January 2021; Accepted 22 February 2021; Published 4 March 2021

Academic Editor: Kai Wang

Dynamic electric vehicle routing problem (DEVRP) is an extension of the electric vehicle routing problem (EVRP) into dynamic logistical transportation system such that the demand of customer may change over time. The routing decision of DEVRP must concern with the driving range limitation of electric vehicle (EV) in a dynamic environment since both load degree and battery capacity are variable according to the time-varying demands. This paper proposes an adaptive memetic algorithm, where a special encoding strategy, an adaptive local search operator, and an economical random immigrant scheme are employed in the framework of evolutionary algorithm, to solve DEVRP efficiently. Numeric experiments are carried out upon a series of test instances that are constructed from a stationary VRP benchmark. The computational results show that the proposed algorithm is more effective in finding high-quality solution than several peer algorithms as well as significant in improving the capacity of the routing plan of EVs in dynamic transportation environment.

1. Introduction

In recent years, electric vehicles (EVs) have begun to widely apply into the logistical transportation systems due to their advantages of energy consumption and low pollution [1]. For example, there are about 2000 EVs, accounting for 10% in total, which are operated by the French electricity distribution company ENEDIS in 2016. However, EVs usually have a short driving range of 100–150 miles due to the technology bottleneck of battery [2]. Furthermore, the energy consumption of EVs is varied with the load degree, the speed, and even the road slope that may cause their driving range to be significantly lower [3]. In reality, the logistical transportation systems are often dynamic. For example, the request of a new customer arrives dynamically or the demand of an old customer can change over time. When deciding the route plan of an EV fleet in these dynamic environments, the influence of dynamic load degree upon the driving range must be considered due to the time-varying delivery requests. Figure 1 illustrates the route execution of a single EV in a dynamic logistical transportation system. Before an EV leaves the depot O time t_0, an initial route plans to visit the currently known requests (A, B, C, D, E). While EV executes its route, a new request X arrives at time t_1 and the initial route is adjusted to fulfill it. However, the increased load by new arrival request X limits the driving range of EV that causes its inevitable return to depot O once for recharging. Finally, the real executed route of EV is (A, B, C, X, O, D, E). Therefore, the routing plan of EVs in dynamic logistical transportation system becomes distinctively different from the traditional vehicle routing problem (VRP) in the literature as we will demonstrate throughout this paper.

In this paper, a special dynamic electric VRP (DEVRP) is investigated for the optimal routing plan of a fleet of EVs so that they can serve a set of customers with time-varying demands while minimizing the total driving distance of EVs. Obviously, DEVRP can be regarded as an extension of electric VRP (EVRP) into dynamic transport environment. Recently, a lot of researchers have begun to focus on EVRPs due to the wide application of EVs in the logistical transportation field [4–9]. Schneider et al. [10] studied an EVRP with time windows and changing stations in order to minimize the total travel distance by a homogenous EV fleet. Felipe et al. [11] proposed

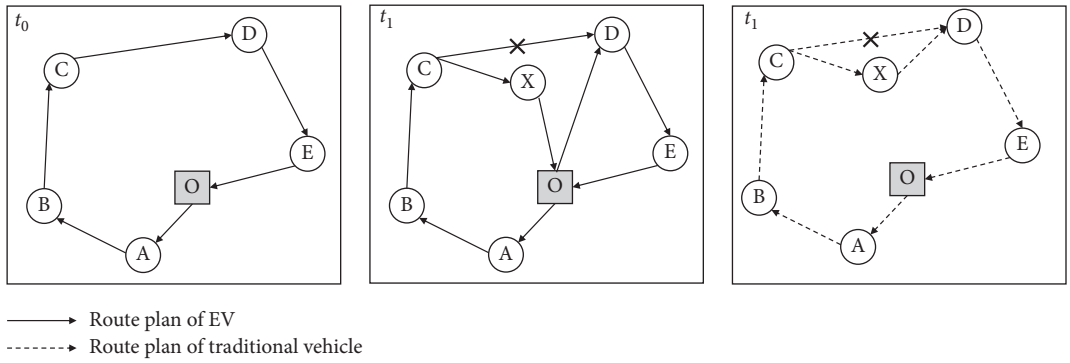

Figure 1: Example of dynamic EV routing.

several heuristics that were constructed within the framework of simulated annealing algorithm for an EVRP with multiple charging technologies and partial recharges. Goeke and Schneider [12] considered a full charging policy with a linear charging function approximation in the routing problem of a mixed electric and conventional vehicle fleet. Lin et al. [13] discussed the effect of vehicle load on battery consumption in EVRP. Keskin and Çatay [14] investigated the application of an adaptive large neighborhood search algorithm for an EVRP that allowed partial recharging. Montoya et al. [15] designed a hybrid metaheuristic for EVRP, in which the battery-charge level was defined as a nonlinear function of the charging time. Zhang et al. [16] utilized an ant colony algorithm for solving an EVRP with the objective of minimizing the energy consumption of EVs. Jie et al. [17] presented a two-echelon capacitated EVRP with battery swapping stations and utilized a hybrid algorithm that combined column generation and adaptive large neighborhood search to determine the delivery strategy under battery consumption limitations. It is noticeable that the current relevant literature on EVRP were concerned with the recharging operations of EVs along their route or the utilization efficiency of battery during the transport course. However, most researches only considered EVRPs as static optimization problems; that is, all customer demands were given as constant. As shown by the example in Figure 1, rerouting an EV must consider the influence of its driving range with load degree once a new customer demand arrives, which is not involved if a traditional vehicle is used.

According to the method proposed by Pillac et al. [18], there are four categories of VRPs. The first is the static and deterministic VRP, where all input is known beforehand and vehicle routes do not change once they are in execution [19]. The second is the static and stochastic VRP, which is characterized by input partially known as random variables (Gendreau et al.) [20]. The third is the dynamic and deterministic VRP, where part or all of the input is unknown and revealed dynamically during the design or execution of the routes [21]. The final is the dynamic and stochastic VRP that has part or all of the input unknown and revealed the exploitable stochastic knowledge dynamically during the execution of the routes [22].

The investigated problem in this paper belongs to the third category; however, the routing algorithm of DEVRP is significantly complicated due to the influence of EVs' driving range varying with their load degree in dynamic environment. For DEVRP, an effective optimization algorithm should track these environmental changes and adapt the best routing scheme of an EV fleet to the changes accordingly. Therefore, we will investigate the applications of an adaptive memetic algorithm (MA) for DEVRP in this paper. The contributions of this study can be summarized as follows:

(i) We extend EVRP into dynamic delivery transport environment, which is more general and practical, and present a special DEVRP, where the driving range of EV is limited by the variable load degree according to the time-varying demand requests.

(ii) We propose an adaptive MA method to solve the investigated DEVRP. The proposed method introduces a special individual representation strategy, an adaptive local search (LS) operator, and an economical random immigrant scheme into the framework of evolutionary algorithm (EA).

(iii) We validate the performance of the proposed method using a series of test instances constructed from a stationary VRP benchmark.

The rest of this paper is outlined as follows. Section 2 formally provides the investigated DEVRP. Section 3 describes the proposed MA method in detail. Section 4 constructs DEVRP test suites from a stationary VRP benchmark and evaluates empirically the performance of the proposed MA for DEVRPs. The final section concludes this paper with discussions on future works.

2. Problem Definition

In this section, we provide a formal description of the DEVRP, in which a homogenous fleet of EVs start from a single depot and deliver the goods to a set of customers. Each EV has a fixed load capacity and limited driving range. While EV is traveling, the battery charge level decreases proportionally with the distance traversed and the current load degree. All EVs must return to the depot for the battery recharging. The demands of customers may change during the design stage. As a consequence, the delivery routes may have to be revised to accommodate the corresponding changes of demands.

Let $I = \{1, \ldots, n\}$ be the set of nodes representing the customers and 0 a node representing the depot. Each customer has a time-varying demand q_i^t over the design horizon $[t, T]$ with $t > 0$. The DEVRP is defined on a directed and complete graph $G = (V, A)$, where $V = \{0\} \cup I$ and $A = \{(i, j): i, j \in V, i \neq j\}$ represents the set of arcs connecting vertices of V. Each arc (i, j) has two associated nonnegative values: a travel distance d_{ij} and a battery consumption b_{ij}. All EVs have a battery of capacity Q and a maximal load capacity $C_{\max}$. Note that b_{ij} can be calculated by the following formulation:

$$b_{ij} = \frac{q_{\text{cur}} - q_{\text{emp}}}{q_{\text{ful}} - q_{\text{emp}}} \cdot e_f \cdot d_{ij}, \tag{1}$$

where e_f represents the engine efficiency of EV, and q_{cur}, q_{ful}, and q_{emp} represent the load degrees with the current, full, and empty statuses of EV on arc (i, j), respectively.

The additional assumptions in the investigated DEVRP are given as follows:

(1) Each EV starts with the full-battery capacity from the depot

(2) Each EV route ends at the depot

(3) Each customer node is visited once by only an EV route

(4) Driving speed on each arc is constant

(5) The battery is recharged to full each time after returning to the depot

(6) No time window constraint is considered for the delivery service and the battery recharging

The purpose of DEVRP investigated in this paper is to decide an optimal delivery route plan so as to minimize the total travel distance of EVs as well as adapting to the time-varying demands of customers during the design stage. Considering that the traditional exact or approximation methods for large-scale VRPs are not very exciting, an adaptive memetic algorithm will be proposed for solving this problem efficiently and the detailed algorithmic designs will be given in the next section.

3. Proposed MA Method for DEVRP

3.1. General Framework of MA. In the EA community, MA can be regarded as a hybrid metaheuristic method inspired by Darwinian principles of natural evolution and Dawkins' notion of a meme, defined as a unit of cultural evolution that is capable of local refinements. Within the framework of a MA, EA operators are responsible for global rough search and LS operators (an LS is also called a meme) are used for local refinement. Due to the advantage of maintaining an efficient balance between exploration and exploitation, MAs have been successfully used to solve a lot of complex optimization problems [23–26]; however, they are rarely considered for dynamic optimization problems [27, 28].

The proposed MA in this paper is a class of EA-based hybrid metaheuristic, which can be expressed by the pseudocode in Figure 2, where pop_size, *pc*, and *pm* are the population size, crossover probability, and mutation probability, respectively. Within this MA, a population of pop_size chromosomes are generated randomly and then evaluated at the initialization step. Then, an elite chromosome, i.e., the chromosome with the best fitness, is improved by an LS operator. At each subsequent generation, the chromosomes undergo a binary tournament selection, where two chromosomes are selected randomly from the current population and the best one is taken for one parent, and the selected chromosome undergoes an order crossover (OX) operation with a probability *pc*. After crossover is executed, a 2-OPT mutation operator is performed for each newly generated offspring chromosome with a probability *pm*. Then, the pop_size best chromosomes among all the parents and offspring are selected to proceed into the next generation, and an elite chromosome in the newly generated population is refined in the LS operation. If the immigrant scheme is used, a certain number of immigrants are generated randomly and replace the worst chromosomes in the current population in order to improve the exploration capacity of MA in dynamic environment.

```
begin
  parameterize (pop_size, pc, pm);
  t = 0;
  initializePopulation (P(0));
  evaluatePopulation (P(0));
  if the LS method is used then
    elite = selectForLocalSearch (P(0));
    execute the LS operation upon elite;
  repeat
    P'(t) = selectForReproduction (P(t));
    P''(t) = crossover (P'(t));
    mutate (P''(t));
    evaluatePopulation (P''(t));
    P (t + 1) = selectForSurvival (P''(t) ∪ P(t));
    if the LS method is used then
      elite = selectForLocalSearch (P(t));
      execute the LS operation upon elite;
    if the immigrant scheme is used then
      immigrate a number of random chromosomes into P (t + 1);
    t = t + 1;
  until a stop condition is met
end.
```

Figure 2: Framework of the proposed MA for DEVRP.

3.2. Individual Representation. How to express a chromosome using a proper encoding method is a basic work when designing an MA for VRP. A good representation scheme can help the algorithm obtain high-quality solutions easily, while an improper representation may make it hard for an algorithm to achieve even feasible solutions.

Prins [29] proposed a simple and effective encoding scheme of GA for VRP, where each chromosome is defined as a sequence of N customer nodes, just like in most GAs for traveling salesman problem (TSP). This encoding scheme can be viewed as a giant tour performed by one vehicle of infinite

capacity if only the same vehicle performs all trips one by one. Then, an optimal split procedure can partition a given chromosome into the best VRP solution. Based on this encoding mechanism, we develop a permutation encoding scheme in MA for the investigated DEVRP. Note that the evaluation of a chromosome is time-costing since the splitting procedure, as shown in Figure 3, is known as an exact algorithm in $O(N)$. Thus, the evaluation number will be considered as the time index in the proposed MA for DEVRP in this paper.

3.3. Local Search. In many heuristic methods for the routing problems, the inverse operation, where two nodes are selected from a segment which is reversed, is often employed as the local move technique, as shown in Figure 4. The quality of a neighbor generated by executing one inversion can be estimated by a parameter Δ, which is calculated by the formula $\Delta = (ac + b\ d) - (ab + c\ d)$. Obviously, the smaller the value of Δ is, the higher the quality of the new generated solution is.

In the original inversion scheme, the sequence between two different nodes chosen randomly in a single tour is reversed. Since there are existing multiple tours in the VRP solution, the inversion can be divided into two ways: single-tour-based inversion (SI) and multiple-tour-based inversion (MI). The former starts from choosing a single tour and reverses the sequence between two different nodes in the chosen tour. In the latter, the tours are not considered in isolation, and paths and nodes are allowable to exchange between different tours.

An example of SI and MI is presented in Figure 5, where node 3 and node 6 are selected from single (SI) and multiple (MI) tours and the sequence between them is reversed. It is easy to see that SI can always help a solution s make a single-tour local improvement, which means that one local move in SI always occurs in a smaller area around s, and MI can perform one move in a wider range upon s. Obviously, each local move makes a biased search and hence may be efficient for some classes of problems but not for others. Therefore, how to develop an efficient LS operator and avoid utilizing inappropriate local move becomes a very important issue.

Here, we design an adaptive LS (ALS) method for the investigated DEVRP according to an effective learning mechanism [30] in order to utilize SI and MI operators efficiently. In our proposed ALS method, SI and MI are both allowed to work together and selected by probability to generate a neighbor of an individual at every step of an LS operation on every iteration of the algorithm. In order to obtain the advantages of both of them during different periods when they are effective, an adaptive learning strategy is used to adjust their execution probabilities according to the improvement each inversion operator has achieved on every LS step.

Let p_{si} and p_{mi} denote the probabilities of applying SI and MI to generate a neighbor of an individual that is used for local search, respectively; $p_{si} + p_{mi} = 1$. At the start of this strategy, p_{si} and p_{mi} are both set to 0.5, which means giving a fair competition chance to each inversion operator. As each inversion move always makes a biased search, the inversion operator which produces more improvements should be given a greater selection probability. Let η denote the improvement

$V_0 = 0$;
for $i = 1$ **to** n **do** $V_i = +\infty$ **endfor**
for $i = 1$ **to** n **do**
  $load = 0$; $cost = 0$; $dist = 0$; $j = i$;
  repeat
    $load = load + q_j$;
    if $i = j$ **then**
      $dist = d_{0,S_j} + d_{S_j,0}$; $cost = b_{0,S_j} + b_{S_j,0}$;
    else
      $dist = dist\text{-}d_{S_{j-1},0} + d_{S_{j-1},S_j} + d_{S_j,0}$;
      $cost = cost\text{-}b_{S_{j-1},0} + b_{S_{j-1},S_j} + b_{S_j,0}$;
    enif
    if $(load <= C_{max})$ **and** $(cost <= Q)$ **then**
      if $V_{i-1} + dist < V_j$ **then**
        $V_j = V_{i-1} + dist$;
        $P_j = i\text{-}1$;
      endif
      $j = j + 1$;
    endif
  until $(j > n)$ **or** $(load > C_{max})$ **or** $(cost > Q)$
endfor
Denotations:
S: a sequence vector of visiting n customers;
P: a label vector of EVs.

Figure 3: Algorithm for the splitting procedure.

degree of the selected individual when one inversion operator is used to refine it and η can be calculated by

$$\eta = \frac{f_{\text{imp}} - f_{\text{ini}}|}{f_{\text{ini}}}, \tag{2}$$

where f_{imp} is the final fitness of the selected individual for the local refinement after executing one LS operation and f_{ini} is its initial fitness before the local refinement. At each generation, the degree of improvement of each inversion operator is calculated when a predefined number of iterations is achieved, and then p_{si} and p_{mi} are recalculated to proceed with the local improvement in the next generation.

Suppose $\eta_{si}(t)$ and $\eta_{mi}(t)$, respectively, denote the total improvement of SI and MI at generation t. Their selection probabilities $p_{si}(t+1)$ and $p_{mi}(t+1)$ at generation $(t+1)$ can be calculated orderly by the following formulae:

$$\begin{aligned} p_{si}(t+1) &= p_{si}(t) + \delta \cdot \eta_{si}(t), \\ p_{mi}(t+1) &= p_{mi}(t) + \delta \cdot \eta_{mi}(t), \\ p_{si}(t+1) &= \frac{p_{si}(t+1)}{p_{si}(t+1) + p_{mi}(t+1)}, \\ p_{mi}(t+1) &= 1 - p_{si}(t+1), \end{aligned} \tag{3}$$

where δ signifies the relative influence of the degree of the improvement on the selection probability. The proposed

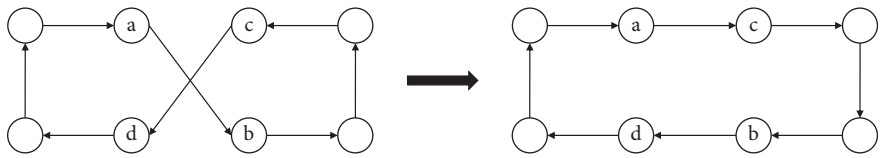

Figure 4: An example of inversion operator.

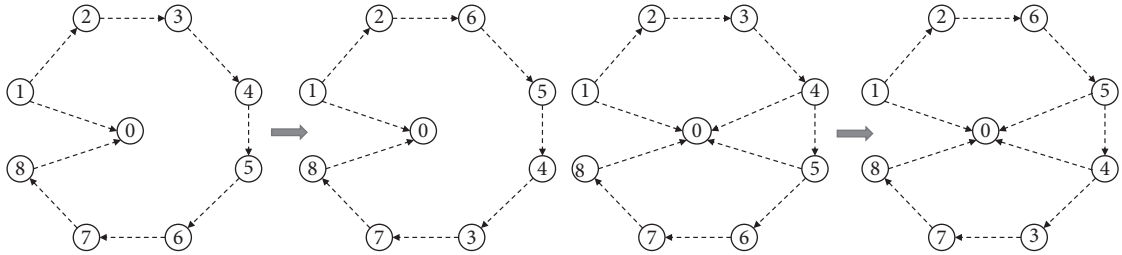

Figure 5: An example of SI and MI operators.

inverse-based LS operator can be expressed by the pseudocode in Figure 6.

From Figure 6, it can be seen that SI and MI are used to generate a certain number of s's neighbors, which compose a neighbor set S, by probability. For each neighbor s' in S, the corresponding value of $\Delta(s, s\prime)$ is calculated to estimate the effect of this local move. It is noticeable that the quality of s' is only estimated by the value of $\Delta(s, s\prime)$ rather than its fitness $f(s\prime)$, which differs from the general LS method as shown in Figure 1. This is because that the evaluation of fitness is too time-consuming (see the relevant description in Section 2.1), while the total evaluation number in each generation is always limited. Finally, the best neighbor s^* with the smallest value of Δ would be evaluated and replace s if its fitness is lower than $f(s)$.

3.4. Increasing Population Diversity. The major problem when EAs are applied for dynamic optimization problems is that the converging population cannot adapt to the changing environments. The random immigrant scheme, where the population is partially replaced by the new-generated chromosomes at every generation, is a simple and efficient scheme for EAs in dynamic environments since it can introduce a constant diversity into the population [31, 32]. Obviously, it is more helpful to migrate random chromosomes into a converging population than a spread-out one. Thus, it is not necessary to always inject a constant number of random chromosomes into the population at every generation.

Here, we propose an economical random immigrant scheme for the proposed MA, where the immigrant ratio ri of every generation can be calculated based on the value of a population diversity index ξ. The index ξ can be calculated as follows:

$$\xi = \min\left\{\frac{\left|f_{\text{ave}} - f_{\text{best}}\right|}{f_{\text{ave}}}, 1\right\}, \tag{4}$$

where f_{best} and f_{ave} are the best and average fitness among the fitness values of the population, respectively. The index ξ is a fitness-based measurement of population diversity, and it can be seen as a measurement of the convergence degree of an algorithm. If $\xi \longrightarrow 1$, there is a high population diversity and therefore the algorithm is far from convergence; if $\xi \longrightarrow 0$, there is a low population diversity, which means that the convergence is approaching.

With the definition of ξ, the immigrant ratio ri can be calculated by the following formula:

begin
  if p_{si} and p_{mi} are not initialized **then**
    set $p_{si} = p_{mi} = 0.5$;
  set $\eta_{si} = \eta_{mi} = 0$;
  for i=1 **to** ls_size **do**
    set $S = \emptyset$ and $ns = 0$;
    while $(ns \leq max\_ns)$ **do**
      if $random() < p_{si}$ **then** //SI is selected
        generate a neighbor s' of s using SI operator;
      else // MI is selected
        generate a neighbor s' of s using MI operator;
      calculate $\Delta(s, s')$;
      $S = S \cup \{s'\}$;
      $ns = ns + 1$;
    endwhile
    find a solution s^* with the smallest value Δ of in S;
    evaluate $f(s^*)$;
    if $f(s^*) < f(s)$ **then** $s = s^*$;
    update η_{si} and η_{mi};
  endfor
  recalculate p_{si} and p_{mi};
end.
Denotations:
max_ns: the maximal allowable value of |S| per generation;
$random()$: a pseudo-random number between 0 and 1;
$\Delta(s, s')$: the corresponding value of Δ when s moving to s'.

Figure 6: Pseudocode for the ALS method.

With the definition of ξ, the immigrant ratio ri can be calculated by the following formula:

$$ri = \min\{\alpha \cdot (1 - \xi) \cdot (ri\_\max - ri\_\min) + ri\_\min, ri\_\max\}, \tag{5}$$

where $ri\_\max$ and $ri\_\min$ are, respectively, the predefined maximum and minimum value of ri and are preset constant to control the decreasing or increasing speed of ri. From this formula, it is easy to understand that less random immigrants could be introduced into the population in the presence of higher diversity (i.e., when $\xi \longrightarrow 1$) as a result of $ri \longrightarrow ri\_\min$. However, when the population is converging (i.e., when $\xi \longrightarrow 0$), $ri \longrightarrow ri\_\max$, which increases the level of random immigrants with a great degree.

4. Experimental Study

4.1. Dynamic Test Environment. In this section, the behaviors of investigated algorithms are examined on a series of DEVRPs which are constructed based on an instance from VRPLIB (http://comopt.ifi.uni-heidelberg.de/software/TSPLIB95/). In the basic VRP instance eil51, one depot node and $N = 50$ customer nodes are defined by the points in the plane and the cost for each edge (i, j) is the Euclidean distance between node i and node j. For each EV, the maximal load capacity is set to 160 and the capacity of battery is set to 20 kWh.

According to the generated method of dynamic optimization problems by Wang et al. [33], the dynamics of DEVRPs is defined as follows: every τ generations, the demands of $\rho \times N$ customers change according to a random Gaussian variable. More formally, a change of a single customer can be described as follows:

$$q_i(t) = \min\{\max\{q_{\min}, 15 + 8 \cdot N(0,1)\}, q_{\max}\}, \tag{6}$$

where $q_i(t)$ denotes the demand of customer i at time t, $q_{\max} = 160$ and $q_{\min} = 1$ denote the allowable maximum and minimum demand of a customer, respectively, and $N(0,1)$ denotes a normal distribution random number in $(0,1)$. In fact, $q_{\max}$ is equal to the capacity of an EV, while $q_{\min}$ is set to 1 in order to ensure that the demand of each customer is nonnegative. Moreover, the mean demand and variance of all customers is 15 and 8, respectively, in the original data set. According to this constructing method, the parameter τ controls the speed of changes while $\rho \in (0.1, 1.0)$ controls the severity of changes. A bigger ρ means more severe changes while a smaller τ means more frequent changes.

In this study, the change speed parameter τ is set to 50, 100, and 200, respectively, which means that the environment changes very fast, in the moderate speed, and slowly, respectively. The change severity parameter ρ is set to 0.1, 0.5, and 1.0, respectively, in order to examine the performance of algorithms in dynamic environments with different severities: from slight change $\rho = 0.1$ to moderate variation $\rho = 0.5$ to intense change $\rho = 1.0$. In order to study the behavior of algorithms in randomly changing environment, we also set ρ to be a random number uniformly distributed in $(0.0, 1.0)$, i.e., $\rho =$ rand. In total, a series of 12 different dynamic problems are constructed from each stationary test problem. The dynamics parameter settings are summarized in Table 1.

Table 1: The index table for dynamic parameter settings.

τ	Environmental dynamic index			
50	1	2	3	4
100	5	6	7	8
200	9	10	11	12
$\rho \longrightarrow$	0.1	0.5	1.0	rand

4.2. Experimental Design. Experiments are carried out in order to study the major features of our proposed MAs and to compare their performance with several other peer algorithms. The following abbreviations represent the algorithms considered in this paper.

(1) SGA: A simple GA
(2) SGAr: A simple GA with restart from scratch whenever the environment changes
(3) RIGA: SGA with the traditional random immigrants' scheme
(4) MA-Inverse: MA with the simple reverse-based LS operator
(5) MA-Swap: MA with the simple swap-based LS operator
(6) MA-Insert: MA with the simple insert-based LS operator
(7) MA-ALS: MA with our proposed ALS operator
(8) MAr-ALS: MA-ALS with a simple restart scheme
(9) RIMA-ALS: MA with the ALS operator and our proposed economical random immigrant scheme

The following parameters are used in all algorithms: the population size (pop_size) is set to 100 for all MAs, but is set to 120 for SGA, SGAr, and RIGA because the LS operation in MAs may be executed by $ls\_\text{size} = 20$ steps per generation. It is easy to see that the total number of evaluations per generation is always 120 for all algorithms. The order crossover probability pc equals 0.8 and the inversion mutation probability pm is set to 0.2 for all GAs and MAs. The specific parameters in our proposed algorithms are set as follows: $\alpha = 1.0$, $ri\_\max = 0.1$, and $ri\_\min = 0.01$ for the random immigrant scheme, while $\Delta = 0.98$, $ls\_\text{size}\,1 = 5$, and $ls\_\text{size}\,2 = 5$ in the ALS operator.

For each experiment of an algorithm on a test problem, 30 independent runs were executed with the same set of random seeds. For each run of an algorithm on a DOP, 10 environmental changes were allowed and the best-of-generation fitness was recorded per generation. The overall offline performance of an algorithm is defined as the best-of-generation fitness averaged across the number of total runs and then averaged over the data gathering period, as formulated below:

$$\overline{F}_{BG} = \frac{1}{G} \sum_{i=1}^{G} \left(\frac{1}{R} \sum_{j=1}^{R} F_{BG_{ij}} \right), \tag{7}$$

where G is the number of generations i.e., $G = 10 \cdot \tau$, $R = 30$ is the total number of runs, and $F_{BG_{ij}}$ is the best-of-generation fitness of generation i of run j.

4.3. Experimental Study on the Effect of LS Operators. In the experimental study on LS operators, we investigate the performance of MAs with different LS operators, with the aim of examining the effect of our proposed operator in Section 3. In particular, five different algorithms, including MA-ALS, MA-Inverse, MA-Swap, MA-Insert, and SGA, are tested on the stationary instance of DEVRP. For each run of an algorithm on each problem, the maximum allowable number of generations was set to 200. The experimental results are shown in Figure 7, where the data were also averaged over 30 runs.

From Figure 7, it can be seen that the performance of four MAs is always better than that of SGA on the stationary EVRP. This is because the LS operators can improve the performance of an algorithm significantly. The similar results have been obtained by many researchers. It is noticeable that the behavior of different MAs is different during the running course. MA-Insert, MA-Inverse, and MA-Swap significantly outperform SGA at the early iterative stage of running the algorithms, while their behavior becomes a little disappointing at the late iterative stage. However, MA-ALS almost performs much better than other algorithms on the whole course of running. This is because three different LS operators are employed and selected to execute local improvements for an individual with an adaptive mechanism in MA-ALS. Obviously, our proposed LS operator, which combines the features of two inverse operation in an adaptive learning strategy, can improve the individual more efficiently than each of the three single LS operators. The result that MA-ALS outperforms significantly other algorithms shows the efficiency of the proposed ALS operator.

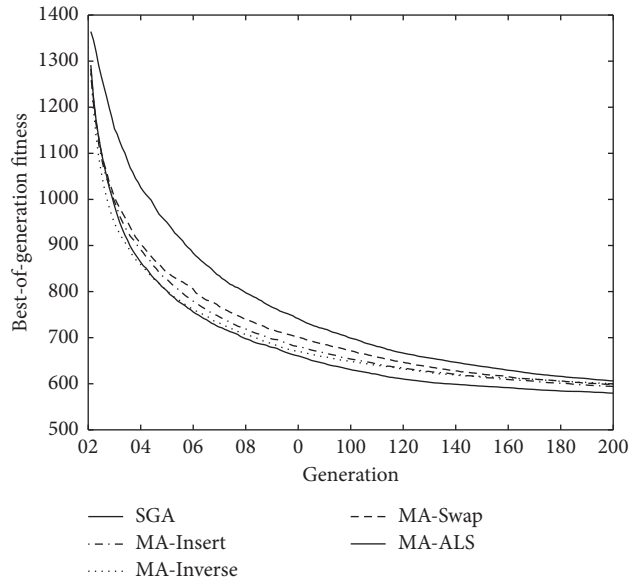

Figure 7: Experimental results of MAs with different LS operators on the stationary problem.

4.4. Experimental Study on the Performance of MAs on DEVRPs. In the experiments on DEVRPs constructed in Table 1, we attempt to compare the performance of our proposed algorithm RIMA-ALS with some other peer algorithms, including SGAr, RIGA, MA-ALS, and MAr-ALS described in Section 4.2.

The experimental results with respect to the overall offline performance are presented in Table 2 and plotted in Figure 8. The corresponding statistical results of comparing algorithms by the one-tailed t-test with 58 degrees of freedom at a 0.05 level of significance are given in Table 3. In Table 3, the t-test results regarding Alg. 1 − Alg. 2 are shown as "$s+$," "$s-$," "+," or "−" when Alg. 1 is significantly better than, significantly worse than, insignificantly better than, or insignificantly worse than Alg. 2, respectively. From Table 2, Table 3, and Figure 8, several results can be observed and are analyzed below.

First, RIMA-ALS significantly outperforms other peer algorithms on most DEVRPs, as indicated in the relevant t-test results in Table 3. This result validates our expectation of the proposed MA for solving DEVRPs. In RIMA-ALS, the ALS operator can make a sufficient exploitation for the best-fitness chromosome. Many researches in the literature often utilize the LS technique to refine each chromosome in the current population. This is too costly or impossible for an MA in dynamic environments considering that the total cost per iteration in terms of evaluations is always limited. The ALS operator is only applied for the best-fitness chromosome in our proposed algorithm and can always help the algorithm keep tracking a changing high-quality solution, which is obviously feasible, especially on real-world applications. Moreover, the population is also introduced a certain degree of diversity by the economical random immigrant scheme, which can help the algorithm adapt well to environmental changes, especially when the environment is subject to significant changes. More relevant analysis on the effect of the operators in RIMA-ALS will be explained in the late experimental analysis.

Second, MAr-ALS performs much worse than MA-ALS and RIGA, but it is better than SGAr on all dynamic problems. Given the perfect restart scheme, MAr-ALS does not reuse any information from the past population, but only restarts to search the equivalent problem from a random initial state when an environmental change occurs. It is easy to understand that MAs or GAs with the restart scheme always take too much cost to reachieve the high-fitness solutions. The result that MAr-ALS significantly underperforms MA-ALS and RIGA on DEVRPs indicates the importance of reusing the useful information in the past population for MA in dynamic environments. The reason why MAr-ALS outperforms SGAr lies in that the ALS operator can help the algorithm obtain the high-fitness solution more quickly, which has been obtained in the experiment in the last section.

Third, MA-ALS always performs well on most DEVRPs, even outperforms RIMA-ALS on DEVRP when $\tau = 200$ and $\rho = 0.1$. This happens because that a new environment is close to the previous one when the value of ρ is very small. It is much advantageous to execute sufficient exploitation for the elite chromosome in the current population when a slight environmental change occurs in terms of severity. When ρ increases to 0.5 or 1.0, MA-ALS is significantly

Table 2: Experimental results of all peer algorithms on DEVRPs.

Dynamics		Algorithms				
τ	ρ	SGAr	RIGA	MA-ALS	MAr-ALS	RIMA-ALS
50	0.1	1026.93 ± 7.05	659.91 ± 15.15	616.16 ± 17.85	872.54 ± 10.28	610.53 ± 11.79
50	0.5	1022.74 ± 8.74	654.29 ± 12.97	616.40 ± 16.78	872.31 ± 10.55	608.07 ± 15.39
50	1.0	1023.24 ± 7.80	660.73 ± 13.88	621.13 ± 14.89	872.15 ± 8.97	612.98 ± 11.96
50	rand()	1022.43 ± 9.44	659.25 ± 20.74	616.70 ± 13.86	871.43 ± 9.34	606.87 ± 12.21
100	0.1	891.90 ± 8.14	613.56 ± 14.70	585.51 ± 15.45	777.13 ± 9.32	584.08 ± 12.20
100	0.5	892.85 ± 7.17	606.41 ± 10.91	589.58 ± 10.59	776.26 ± 6.86	582.60 ± 10.81
100	1.0	892.03 ± 6.72	610.34 ± 9.08	586.30 ± 12.12	771.01 ± 11.20	581.57 ± 11.15
100	rand()	893.47 ± 10.15	607.56 ± 12.51	588.22 ± 10.51	774.04 ± 9.83	583.07 ± 10.67
200	0.1	766.86 ± 8.25	586.05 ± 12.56	566.39 ± 9.74	687.77 ± 8.47	566.78 ± 12.63
200	0.5	765.06 ± 6.99	581.79 ± 13.65	566.90 ± 8.96	688.89 ± 9.67	566.41 ± 13.10
200	1.0	766.04 ± 6.46	582.32 ± 7.53	569.22 ± 7.30	686.49 ± 6.17	564.33 ± 9.02
200	rand()	767.29 ± 6.76	585.65 ± 9.15	567.11 ± 10.42	685.89 ± 8.56	566.82 ± 11.36

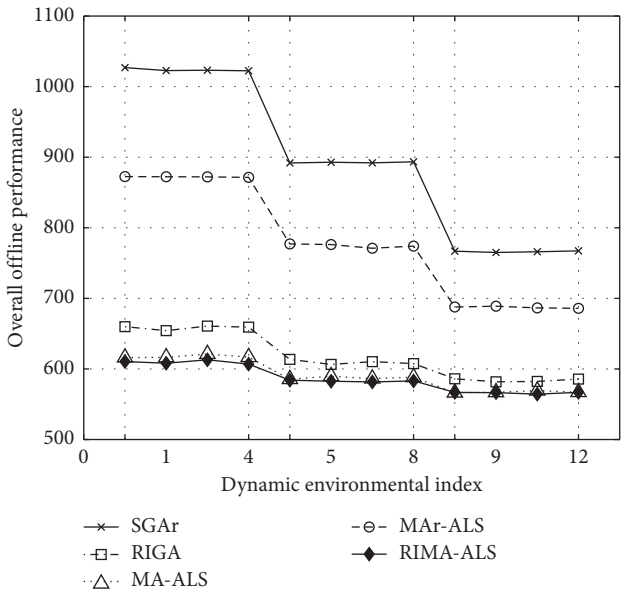

Figure 8: Experimental results of all GAs and MAs on DEVRPs.

Table 3: The t-test results of comparing algorithms regarding the overall offline performance.

t-test result	DEVRP instances			
$\tau = 50$, $\rho \Longrightarrow$	0.1	0.5	1.0	Rand()
RIMA-ALS–MAr-ALS	$s+$	$s+$	$s+$	$s+$
RIMA-ALS–MA-ALS	$+$	$s+$	$s+$	$s+$
RIMA-ALS–RIGA	$s+$	$s+$	$s+$	$s+$
MAr-ALS–MA-ALS	$s-$	$s-$	$s-$	$s-$
MAr-ALS–RIGA	$s-$	$s-$	$s-$	$s-$
MAr-ALS–SGAr	$s+$	$s+$	$s+$	$s+$
MA-ALS–RIGA	$s+$	$s+$	$s+$	$s+$
RIGA–SGAr	$s+$	$s+$	$s+$	$s+$
$\tau = 100$, $\rho \Longrightarrow$	0.1	0.5	1.0	rand()
RIMA-ALS–MAr-ALS	$s+$	$s+$	$s+$	$s+$
RIMA-ALS–MA-ALS	$+$	$s+$	$s+$	$s+$
RIMA-ALS–RIGA	$s+$	$s+$	$s+$	$s+$
MAr-ALS–MA-ALS	$s-$	$s-$	$s-$	$s-$
MAr-ALS–RIGA	$s-$	$s-$	$s-$	$s-$
MAr-ALS–SGAr	$s+$	$s+$	$s+$	$s+$
MA-ALS–RIGA	$s+$	$s+$	$s+$	$s+$

Table 3: Continued.

t-test result	DEVRP instances			
RIGA–SGAr	$s+$	$s+$	$s+$	$s+$
$\tau = 200$, $\rho \Rightarrow$	0.1	0.5	1.0	rand()
RIMA-ALS–MAr-ALS	$s+$	$s+$	$s+$	$s+$
RIMA-ALS–MA-ALS	$-$	$s+$	$s+$	$s+$
RIMA-ALS–RIGA	$s+$	$s+$	$s+$	$s+$
MAr-ALS–MA-ALS	$s-$	$s-$	$s-$	$s-$
MAr-ALS–RIGA	$s-$	$s-$	$s-$	$s-$
MAr-ALS–SGAr	$s+$	$s+$	$s+$	$s+$
MA-ALS–RIGA	$s+$	$s+$	$s+$	$s+$
RIGA–SGAr	$s+$	$s+$	$s+$	$s+$

beaten by RIMA-ALS, which shows the necessity of maintaining the sufficient population diversity for MAs in dynamic environments. Since it is usually not possible to judge the strength and weakness of an environmental change in advance, the proposed random immigrant scheme is a good choice when MAs are applied for DOPs; notice that RIMA-ALS always performs better than MA-ALS on all DEVRPs when ρ = rand.

Finally, the environmental parameters affect the performance of algorithms. The performance of all algorithms increases when the value of τ increases from 50 to 100 to 200. When τ becomes larger, algorithms have more time to find better solutions before the next change. However, the performance of algorithms hardly changes with the increasing or decreasing of the value of ρ.

5. Conclusion

In this paper, an adaptive MA is proposed for addressing a special DEVRP that is characterized by the time-varying customer demands during the route design stage, under the consideration of the influence of the variable load degree upon the driving range of EVs. In the proposed MA method, there are three major algorithmic schemes. The first is to develop a splitting procedure to translate an individual with simple permutation-based representation to a solution of DEVRP. The second is to propose an ALS operator that utilizes two different inverse-based LS operations, that is, SI and MI, in an adaptive cooperation way. The last is to employ an economical random immigrant scheme to maintain a sufficient population diversity for the proposed algorithm to adapt well to the changing environment.

From the experimental results based on a series of DEVRPs, which are constructed from a stationary instance of VRP, the following conclusions can be drawn on the dynamic test problems. Firstly, MAs with the ALS operator enhanced by the suitable diversity technique can exhibit a better performance in solving DEVRPs. For most test problems, RIMA-ALS, which hybridizes GA with the ALS operator and the economical random immigrant scheme, outperforms other peer algorithms. Secondly, the ALS operator can help the algorithm execute a robust local refinement since it employs multiple LS operators via an adaptive cooperation mechanism. In our experiments, MA-ALS performs much better than other MAs with a single LS operator for the stationary instance of VRP. Thirdly, maintaining a sufficient population diversity and reusing the past information efficiently are both important for MAs in dynamic environments. For most DEVRPs, RIMA-ALS always performs better than MA-ALS and MAr-ALS, while MA-ALS outperforms MAr-ALS. Finally, the environmental parameter can affect the performance of algorithms. In our experiments, algorithms perform better with the increase of the frequency of changes, while the influence of the severity of change seems very limited. Generally speaking, the experimental results indicate that the proposed algorithm, where an EA is hybridized with the ALS operator and an economical random immigrant scheme, seems a good optimizer for DEVRPs.

For the future work, it is straightforward to examine the performance of our proposed algorithm for more DEVRP instances. For example, a mixed fleet of EVs or multiple charging stations can be considered in DEVRPs. Another interesting research topic is to investigate the effect of hybridizing the other LS operations, such as those especially used for EVRPs, within this adaptive learning way. In addition, it is also valuable to carry out the sensitivity analysis on the effect of parameters, e.g., α, Δ, etc., on the performance of the proposed algorithm in the future.

Data Availability

The data used to support the findings of this study are available within the article.

Conflicts of Interest

The authors declare that they have no conflicts of interest.

Acknowledgments

This work was supported in part by the National Natural Science Foundation of China under Grant nos. 61703290 and 71671032, the Natural Science Fund Guidance Program of Liaoning Province under Grant no. 2019-ZD-0478, and the Fundamental Research Funds for the Central Universities under Grant no. N180408019.

References

[1] P. R. Kleindorfer, A. Neboian, A. Roset, and S. Spinler, "Fleet renewal with electric vehicles at La Poste," *Interfaces*, vol. 42, no. 5, pp. 465–477, 2012.

[2] S. Pelletier, O. Jabali, and G. Laporte, "Battery electric vehicles for goods distribution: a survey of vehicle technology, market penetration, incentives and practices," Technical Report CIRRELT-2014-43, CIRRELT, Montreal, Canada, 2014.

[3] C. De Cauwer, J. Van Mierlo, and T. Coosemans, "Energy consumption prediction for electric vehicles based on real-world data," *Energies*, vol. 8, no. 8, pp. 8573–8593, 2015.

[4] A. Artmeier, J. Haselmayr, M. Leucker, and M. Sachenbacher, "The optimal routing problem in the context of battery-powered electric vehicles," in *Proceedings of the 2nd International Workshop on Constraint Reasoning and Optimization for Computational Sustainability*, Bologna, Italy, June 2010.

[5] R. G. Conrad and M. A. Figliozzi, "The recharging vehicle routing problem," in *Proceedings of the 2011 Industrial Engineering Research Conference*, Reno, NV, USA, May 2011.

[6] S. Erdoğan and E. Miller-Hooks, "A green vehicle routing problem," *Transportation Research Part E*, vol. 48, no. 1, pp. 100–114, 2012.

[7] S. Pelletier, O. Jabali, and G. Laporte, "50th anniversary invited article-goods distribution with electric vehicles: review and research perspectives," *Transportation Science*, vol. 50, no. 1, pp. 3–22, 2016.

[8] A. Afroditi, M. Boile, S. Theofanis, E. Sdoukopoulos, and D. Margaritis, "Electric vehicle routing problem with industry constraints: trends and insights for future research," *Transportation Research Procedia*, vol. 3, pp. 452–459, 2014.

[9] G. Hiermann, J. Puchinger, S. Ropke, and R. F. Hartl, "The electric fleet size and mix vehicle routing problem with time windows and recharging stations," *European Journal of Operational Research*, vol. 252, no. 3, pp. 995–1018, 2016.

[10] M. Schneider, A. Stenger, and D. Goeke, "The electric vehicle-routing problem with time windows and recharging stations," *Transportation Science*, vol. 48, no. 4, pp. 500–520, 2014.

[11] Á. Felipe, M. T. Ortuño, G. Righini, and G. Tirado, "A heuristic approach for the green vehicle routing problem with multiple technologies and partial recharges," *Transportation Research Part E: Logistics and Transportation Review*, vol. 71, no. 1, pp. 111–128, 2014.

[12] D. Goeke and M. Schneider, "Routing a mixed fleet of electric and conventional vehicles," *European Journal of Operational Research*, vol. 245, no. 1, pp. 81–99, 2015.

[13] J. Lin, W. Zhou, and O. Wolfson, "Electric vehicle routing problem," *Transportation Research Procedia*, vol. 12, pp. 508–521, 2016.

[14] M. Keskin and B. Çatay, "Partial recharge strategies for the electric vehicle routing problem with time windows," *Transportation Research Part C: Emerging Technologies*, vol. 65, pp. 111–127, 2016.

[15] A. Montoya, C. Guéret, J. E. Mendoza, and J. G. Villegas, "The electric vehicle routing problem with nonlinear charging function," *Transportation Research Part B: Methodological*, vol. 103, pp. 87–110, 2017.

[16] S. Zhang, Y. Gajpal, S. S. Appadoo, and M. M. S. Abdulkader, "Electric vehicle routing problem with recharging stations for minimizing energy consumption," *International Journal of Production Economics*, vol. 203, pp. 404–413, 2018.

[17] W. Jie, J. Yang, M. Zhang, and Y. Huang, "The two-echelon capacitated electric vehicle routing problem with battery swapping stations: formulation and efficient methodology," *European Journal of Operational Research*, vol. 272, no. 3, pp. 879–904, 2019.

[18] V. Pillac, M. Gendreau, C. Guéret, and A. L. Medaglia, "A review of dynamic vehicle routing problems," *European Journal of Operational Research*, vol. 225, no. 1, pp. 1–11, 2013.

[19] G. Laporte, "Fifty years of vehicle routing," *Transportation Science*, vol. 43, no. 4, pp. 408–416, 2009.

[20] M. Gendreau, G. Laporte, and R. Séguin, "Stochastic vehicle routing," *European Journal of Operational Research*, vol. 88, no. 1, pp. 3–12, 1996.

[21] P. Jaillet and M. R. Wagner, "Generalized online routing: new competitive ratios, resource augmentation, and asymptotic analyses," *Operations Research*, vol. 56, no. 3, pp. 745–757, 2008.

[22] N. Secomandi and F. Margot, "Reoptimization approaches for the vehicle-routing problem with stochastic demands," *Operations Research*, vol. 57, no. 1, pp. 214–230, 2009.

[23] A. E. Fallahi, C. Prins, and R. Wolfler Calvo, "A memetic algorithm and a tabu search for the multi-compartment vehicle routing problem," *Computers & Operations Research*, vol. 35, no. 5, pp. 1725–1741, 2008.

[24] H. Wang, Y. Fu, M. Huang, G. Q. Huang, and J. Wang, "A NSGA-II based memetic algorithm for multiobjective parallel flowshop scheduling problem," *Computers & Industrial Engineering*, vol. 113, pp. 185–194, 2017.

[25] H. Wang, M. Huang, and J. Wang, "An effective metaheuristic algorithm for flowshop scheduling with deteriorating jobs," *Journal of Intelligent Manufacturing*, vol. 30, no. 7, pp. 2733–2742, 2019.

[26] H. Wang, I. Moon, S. Yang, and D. Wang, "A memetic particle swarm optimization algorithm for multimodal optimization problems," *Information Sciences*, vol. 197, pp. 38–52, 2012a.

[27] H. Wang, D. Wang, and S. Yang, "A memetic algorithm with adaptive hill climbing strategy for dynamic optimization problems," *Soft Computing*, vol. 13, no. 8-9, pp. 763–780, 2009.

[28] H. Wang, S. Yang, W. H. Ip, and D. Wang, "A memetic particle swarm optimisation algorithm for dynamic multimodal optimisation problems," *International Journal of Systems Science*, vol. 43, no. 7, pp. 1268–1283, 2012b.

[29] C. Prins, "A simple and effective evolutionary algorithm for the vehicle routing problem," *Computers & Operations Research*, vol. 31, no. 12, pp. 1985–2002, 2004.

[30] Y. S. Ong and A. J. Keane, "Meta-lamarckian learning in memetic algorithms," *IEEE Transactions on Evolutionary Computation*, vol. 8, no. 2, pp. 99–110, 2004.

[31] S. Yang, "Genetic algorithms with memory- and elitism-based immigrants in dynamic environments," *Evolutionary Computation*, vol. 16, no. 3, pp. 385–416, 2008.

[32] S. Yang, Y. S. Ong, and Y. Jin, *Evolutionary Computation in Dynamic and Uncertain Environments*, Springer-Verlag, Berlin, Germany, 2007.

[33] H. Wang, S. Yang, W. H. Ip, and D. Wang, "A particle swarm optimization based memetic algorithm for dynamic optimization problems," *Natural Computing*, vol. 9, no. 3, pp. 703–725, 2010.

Hindawi
Mathematical Problems in Engineering
Volume 2021, Article ID 6643223, 11 pages
https://doi.org/10.1155/2021/6643223

Research Article

An Improved Active Damping Method Based on Single-Loop Inverter Current Control for LCL Resonance in Grid-Connected Inverters

Xiaofeng Wan,[1] **Xiaohua Ding**,[1] **and Hailin Hu**[2]

[1]*School of Information Engineering, Nanchang University, Nanchang 330031, Jiangxi Province, China*
[2]*School of Electrical Engineering and Automation, Jiangxi University of Science and Technology, Ganzhou 341000, Jiangxi Province, China*

Correspondence should be addressed to Xiaofeng Wan; xfwan@ncu.edu.cn

Received 30 October 2020; Revised 21 January 2021; Accepted 17 February 2021; Published 3 March 2021

Academic Editor: Licheng Wang

This paper investigates active damping of LCL filter resonance in grid-connected inverters with only inverter current feedback control, since it only needs to sample one current to realize both current control and inverter protection. The traditional single-loop inverter current control (SLICC) can damp the LCL filter resonance actively. However, if the control delay is considered in digital control, the system stability will depend on the ratio of the LCL resonance frequency f_{res} to the sampling frequency f_s, and the valid damping region is only up to $f_s/6$. Considering that the design region of the LCL resonance frequency f_{res} is up to $f_s/2$, the system can easily become unstable due to the LCL resonance frequency shifting. Thus, this paper proposes an improved active damping method based on SLICC, including the asymmetric regular sampling method and delay compensation method. The improved sampling method minimizes the control delay without introducing a switching ripple, and the delay compensation method further compensates for the delay effect. With a proper parameter design, the upper limit of the valid damping region is extended up to $f_s/2$, which can cover all the possible resonance frequencies, and it has inherent robustness against grid-impedance variation. Finally, a few simulations in MATLAB/SIMULINK and experiments based on a 6 kW prototype are performed to verify the theoretical analysis.

1. Introduction

Recently, the renewable energy distributed generation technique is attracting more and more attention, to deal with the increasing concern of the exhaustion of fossil fuels and the environmental pollution. Grid-connected inverters are the key devices to connect the distributed systems to the power grid [1]. As the grid-connected inverter is controlled by the pulse width modulation (PWM), the output current contains an amount of switching harmonics. The LCL filter is widely used due to its better attenuation capability of the switching harmonics and cost advantage compared with L filter. However, the LCL filter is a third-order low-damping system, which challenges the stability of the whole system [2].

In order to stabilize the system, a variety of active damping techniques without power losses have been developed. Generally, the traditional active damping techniques can be classified into two modes based on whether an additional sensor is needed, except for the essential sensors of the control current and grid voltage: the single-loop and the multiloop feedback control. The multiloop feedback control methods introduce additional damping terms into the current control loop by sensing additional variables, such as capacitor current [3–6] or capacitor voltage [7]. Due to their flexible and efficient implementation, these methods have been widely used. However, requiring additional sensors increases the hardware cost and affects the system's reliability. Alternatively, a state observer can be used to simplify the system hardware effectively [8, 9], but it is sensitive to system parameter uncertainties and variations [10].

Simultaneously, the single-loop feedback control methods can avoid these problems and have increasingly been studied in [11–25], including inverter current control and grid current control. In [11], it is first pointed out that the inverter current contains capacitor current component so that the inverter current control can promise stable operation. Moreover, inverter current control is beneficial to the instantaneous overcurrent protection for the inverter, which is more convenient to be implemented and popular in industrial applications [12]. But good damping can be achieved only when the resonance frequency is low enough. In order to increase the damping, an active damping inner loop control is introduced. It is implemented by extracting the high-frequency components of the inverter current or grid current to simulate the capacitor current [13–15], and the first-order High Pass Filter (HPF) is the most popular filter. However, when the control current is the grid current, it may not be able to introduce sufficient damping since the high-frequency components have been filtered by the filter capacitor, which might result in the need to compromise between the resonance frequency offset and the resonance suppression ability [16].

On the other hand, the control delay is introduced in the digital control implementation process, and it has a significant influence on all active damping techniques [17–19]. The system stability will depend on the ratio of the LCL resonance frequency f_{res} to the sampling frequency f_s. For the single-loop feedback control without active damping inner loop or the multiloop feedback control, the critical frequency is $f_s/6$ [17, 18], while it can increase to $f_s/3$ at most when adopting the active damping inner loop [20]. Thus, the LCL resonance frequency must be away from the critical frequency to enhance the system damping. Unfortunately, considering the potential variation of the grid inductance, the LCL resonance frequency may shift to the critical frequency; thus, the system stability cannot be promised [21–23]. Hence, how to decrease the control delay and increase the critical frequency is a research focus in recent years.

The control delay is reduced by adjusting the sampling instant [17] or multisampling [12], but the sampling instant may be no longer the switching instant of the power tube. It is easy to introduce the switching frequency harmonics into the control loop and deteriorate the system stability [16]. Alternatively, the filter-based methods are presented in [24–26]. By inserting a digital filter in the forward path, the frequency characteristics around the LCL resonance frequency can be changed. But such a solution relies on the accuk6rate filter parameters; the variation of grid inductance may greatly affect the system stability. Thus, it is very difficult to enhance the system stability only by reducing the control delay or introducing digital filters. Therefore, in [22], a robust method including the double-sampling double-loading (DSDL) mode and a lead grid current control part is proposed, and a similar method based on the inverter current control is proposed [16]. The DSDL mode minimizes the control delay and the lead control part further compensates for the delay effect. However, the active damping inner loop can be equivalent to a second-order filter since a first-order HPF is in series with a first-order lead control part in it. Thus, the order of the system control is increased. The amplitude and phase characteristics of high-order filters vary more sharply and widely, making the parameters design more difficult [15].

In this paper, an improved SLICC is proposed. This method extends the valid damping region up to $f_s/2$, improving the system stability margin greatly without increasing the control algorithm complexity and system cost. And it has inherent robustness against grid-impedance variation. The remainder of this paper is organized as follows. In Section 2, the control scheme and the mathematical model of a three-phase grid-connected inverter with an LCL filter are presented at first. The equivalent impedance model of the SLICC considering the control delay is established, and the detailed system stability analysis is given in Section 3. In Section 4, an improved SLICC for extending the valid damping region up to $f_s/2$ is proposed. Moreover, a step-by-step parameter design procedure is presented. Section 5 shows the simulations and experimental results and Section 6 summarizes the conclusions.

2. System Modeling and Description

Figure 1 shows the circuit diagram and control scheme of a three-phase grid-connected inverter with an LCL filter and a constant DC voltage source U_{dc}, where C is the filter capacitor and L_1 and L_2 are the filter inductance of the inverter side and the grid side, respectively. Considering the worst-case condition, where no passive damping of the resonance exists and the system becomes more unstable, the parasitic series resistances of its filter inductor and filter capacitor are all neglected here. u_g is the grid voltage, and it has been assumed as balanced, which then allows per-phase diagrams to be used for analysis. i_1 and i_2 are the inverter and grid current, respectively. In this paper, to reduce the impact on the low-frequency stability of the system, the synchronous reference frame phase-locked loop (SRF-PLL) with low bandwidth has been employed to synchronize the inverter to the point of common coupling (PCC) voltage [20].

The overall control structure for per-phase based on SLICC is depicted in Figure 2. For simplicity, the equivalent gain of the inverter is set to 1. $G_{\text{PR}}(s)$ is the current controller, whose notation is given as follows [10]:

$$G_{\text{PR}}(s) = K_p + \frac{2K_r\omega_i s}{s^2 + 2\omega_i s + \omega_0^2}, \tag{1}$$

where K_p and K_r are the proportional and resonance gains, respectively, ω_i is the bandwidth of the resonance term, and ω_0 is the grid fundamental angular frequency.

Generally, the digital signal processor (DSP) is introduced to control the grid-connected inverter, and the most common mode for PWM is the single-update mode. Thus, the computation and PWM delays should be considered. Specifically, $G_{d1}(s)$ represents the computation delay, which is one sampling period in the traditional sampling scheme. $G_{d2}(s)$ is the PWM delay, caused by the zero-order hold (ZOH) effect. Thus, the total delay in the system can be expressed as [17]

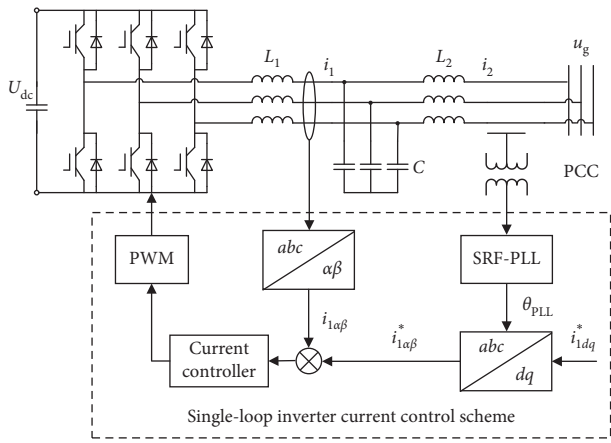

Figure 1: Three-phase grid-connected inverter with an LCL filter.

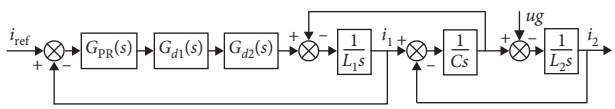

Figure 2: Per-phase control diagram with SLICC strategy.

$$G_d(s) = e^{-1.5sT_s}, \tag{2}$$

where T_s is the sampling cycle of the digital control system.

$G_{\mathrm{LCL}}(s)$ is the transfer function of the LCL filter under SLICC strategy, as shown in the following equation:

$$G_{\mathrm{LCL}}(s) = \frac{L_2 C s^{21} + 11}{L_1 L_2 C s^3 + (L_1 + L_2)s}. \tag{3}$$

3. Impedance-Based Analysis

This section generalizes the physical circuit property of the SLICC by presenting an impedance-based analysis [27]. For demonstrating circuit properties realized by SLICC, the control diagram is redrawn as in Figure 3(a) by sensing the voltage of the inverter-side inductance instead of the inverter current, and the equivalent circuit of LCL filter can be shown as Figure 3(b). This informs that the SLICC is equivalent to a virtual impedance $Z_v(s)$ connected in series with the inverter-side inductance. The expression of $Z_v(s)$ can be written as

$$Z_v(s) = G_{\mathrm{PR}}(s) e^{-1.5sT_s}. \tag{4}$$

Thus, the equivalent virtual impedance $Z_v(s)$ can be shaped by varying $G_{\mathrm{PR}}(s)$ and $G_d(s)$. Since the resonance term of $G_{\mathrm{PR}}(s)$ mainly affects the frequency characteristics of the system at the fundamental frequency [19], the equivalent virtual impedance $Z_v(s)$ is simplified as $K_p e^{-1.5sT_s}$ for simplicity.

If the control delay $G_d(s)$ is neglected, the equivalent virtual impedance is a constant positive resistance with a value of K_p, which damps the LCL resonance peak. Therefore, the SLICC can provide inherent damping to stabilize the system [18].

When the control delay $G_d(s)$ is incorporated, the frequency expression of the equivalent virtual impedance is yielded as

$$\begin{aligned} Z_v(j\omega) &= K_p(\cos 1.5\,\omega T_s - j \sin 1.5\,\omega T_s) \\ &= R_v(\omega) + jX_v(\omega). \end{aligned} \tag{5}$$

It shows that the control delay changes the constant positive resistance to a virtual impedance which is composed of resistance and reactance, whose frequency characteristics are shown in Figure 4, and f_s is the sampling frequency. The equivalent virtual resistance $R_v(\omega)$ could be positive or negative depending on the frequency range, whose critical frequency f_R is $f_s/6$. Similarly, the equivalent virtual reactance $X_v(\omega)$ could be inductive or capacitive and its critical frequency f_X is $f_s/3$. The negative $R_v(\omega)$ will add open-loop right-half-plane (RHP) poles to the system, introducing a nonminimum-phase closed-loop behavior to the system, which can impair the overall system stability and robustness [20]. The existence of $X_v(\omega)$ will shift the LCL resonance frequency f_{res} [16]. As the damping effect, that is, stability of system, is determined by $R_v(\omega)$ [22], the critical stable frequency of the traditional digital control system adopting SLICC is $f_s/6$. When the actual LCL resonance frequency f_{res} is up to $f_s/6$, the system will be unstable due to the lack of necessary damping for the LCL resonance peak. Therefore, the control delay $G_d(s)$ plays a decisive role in the stability of digital control system.

To identify the critical frequency f_R of $R_v(\omega)$ when the control delay varies, $G_d(s)$ can be rewritten as $e^{-\lambda sT_s}$ (normally $0 < \lambda \le 1.5$). When $R_v(\omega)$ is assumed to zero, it leads to

$$\cos(\lambda \cdot 2\pi x) = 0, \tag{6}$$

where x is the ratio of the critical frequency f_R to the sampling frequency f_s.

Figure 5 shows the relationship between x and λ according to (6). As shown in Figure 5, the critical frequency gradually increases as the control delay decreases. In particular, when the control delay decreases to $e^{-0.5sT_s}$, the critical frequency reaches the upper limit of the LCL resonance frequency design value, that is, $f_s/2$. That is, if the control delay can be reduced to $e^{-0.5sT_s}$, the system stability can be ensured with the SLICC within the design range of the LCL resonance frequency.

Due to the inherent characteristics of the digital control system, reducing the control delay to $e^{-0.5sT_s}$ can only be realized by increasing the sampling frequency. In this case, the sampling frequency should be increased to three times its original value [12]. However, it may lead to problems that introduce the switch ripple into the control loop and multiple intersections between the modulated wave and the carrier [3]. That makes the method impractical.

4. Proposed Active Damping Method

Based on the above discussions, there is a need to decrease the control delay and compensate for its side effects. In this section, an improved active damping method based on SLICC is proposed, which includes the asymmetric regular

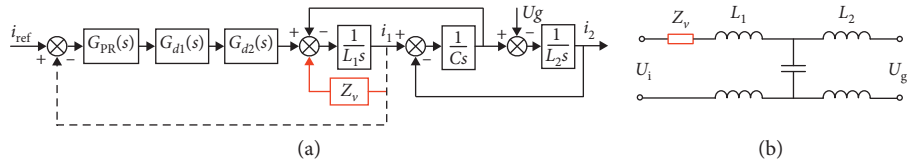

Figure 3: Equivalent control diagram and circuit of control diagram with SLICC strategy.

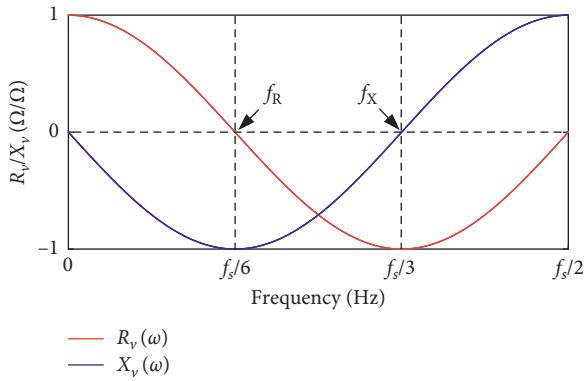

Figure 4: Frequency-domain characteristics of $R_v(\omega)$ and $X_v(\omega)$.

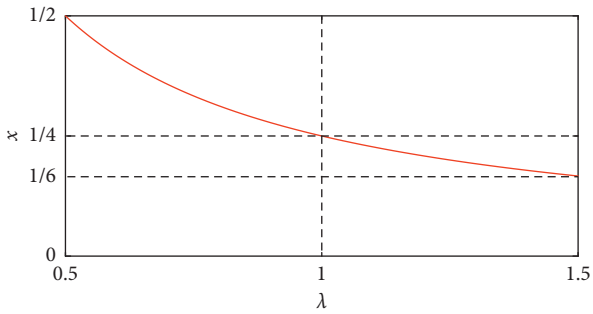

Figure 5: Relationship between x and λ.

sampling method and the delay compensation method. The proposed active damping method can extend the valid damping region up to $f_s/2$, improving the system stability and robustness. The traditional SLICC has inherent robustness against grid-impedance variation, since the grid-impedance decreases the LCL resonance frequency [18]. The proposed active damping method can inherit this feature due to no additional active damping inner loop in the control loop.

4.1. Asymmetric Regular Sampling Method. In the digital control system, in order to avoid the influence of switching noise, the signal sampling and update are operated at the peak or valley of the triangular carrier. The sampling signals are sent to the DSP; then the modulation waveform is obtained by calculating these signals with the control algorithm. Meanwhile, to avoid the phenomenon of multiple intersections between the modulation waveform and the triangular carrier, the calculated modulation waveform is updated at the next sampling instant, as shown in Figure 6(a). The computation delay is the duration between sampling instant of the signal and update instant of the corresponding calculated modulation waveform, which is equal to e^{-sT_s}. The PWM is often modeled as a ZOH, so the PWM delay is considered as half of the sampling period, which is equal to $e^{-0.5sT_s}$. Thus, the total control delay in the control loop is $e^{-1.5sT_s}$.

In order to directly reduce the control delay, the asymmetric regular sampling method is adopted, as shown in Figure 6(b). Instead of sampling and updating the signals one time in a control period, this method samples and updates twice time, which means that the signal sampling and update are operated at the peak and valley of the triangular carrier. Since the sampling frequency and update frequency are both doubled, the control delay is reduced to $e^{-0.75sT_s}$, without changing the switching frequency and introducing the switching ripple. It is worth mentioning that, since the sampling frequency is doubled, this method requires a higher precision current sensor.

4.2. Analysis and Design of Delay Compensation Method. As shown in Figure 5, when the control delay is $e^{-0.75sT_s}$, the critical frequency of the equivalent virtual resistance is around $f_s/3$. In this section, the delay compensation method is further introduced to compensate for the delay effect, realizing $f_R \geq (f_s/2)$ and ensuring that the system has a sufficient stability margin at f_{res}.

Considering that the controller needs to be discretized, the simplest form of the delay compensator can be expressed as [22]

$$G_{C1} = \frac{1}{1 + e^{-0.5ksT_s}}, \tag{7}$$

where $k = 1, 2, \ldots, m$. Since the sampling frequency has doubled, the minimum delay in the control loop is $e^{-0.5sT_s}$. Then the equivalent virtual impedance can be expressed as

$$\begin{aligned} Z_{v1}(j\omega) &= K_P \frac{e^{-0.75sT_s}}{1 + e^{-0.5ksT_s}}\Big|_{s=j\omega} \\ &= \frac{K_p\left(A_1(\omega) + jB_1(\omega)\right)}{C_1(\omega)} \\ &= R_{v1}(\omega) + jX_{v1}(\omega), \end{aligned} \tag{8}$$

where

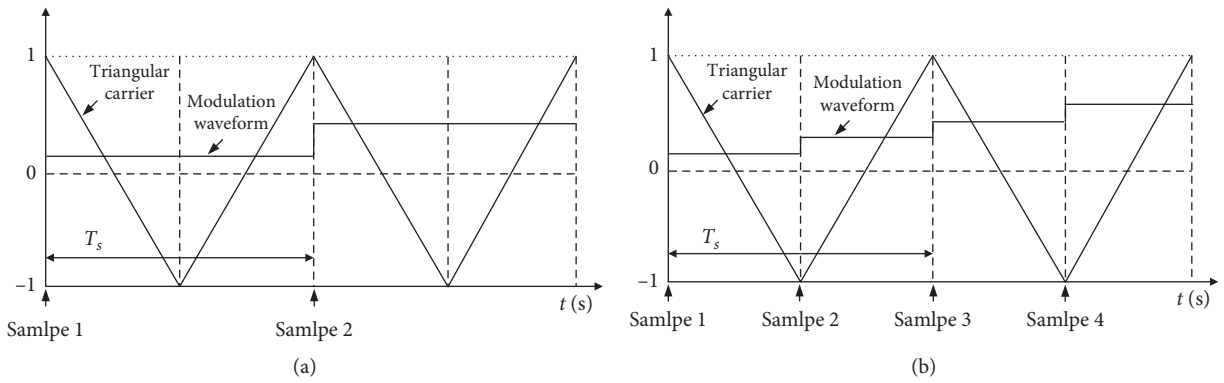

Figure 6: Implementation principle of different sampling method. (a) Symmetry regular sampling method. (b) Asymmetric regular sampling method.

$$\begin{cases} A_1(\omega) = \cos 0.75\,\omega T_s\,(1 + \cos 0.5\,k\omega T_s) + \sin 0.75\,\omega T_s \sin 0.5\,k\omega T_s, \\ B_1(\omega) = \cos 0.75\,\omega T_s \sin 0.5\,k\omega T_s + \sin 0.75\,\omega T_s\,(1 + \cos 0.5\,k\omega T_s), \\ C_1(\omega) = 2 + 2\cos 0.5\,k\omega T_s. \end{cases} \tag{9}$$

In order to ensure $f_R \geq (f_s/2)$, the equivalent virtual resistance should be positive within the interval of $(0, (f_s/2)]$; thus, the constraints are derived as

$$\begin{cases} A_1(\omega) > 0, C_1(\omega) > 0, & f \in (0, 0.5 f_s), \\ A_1(\omega) \geq 0, C_1(\omega) > 0, & f = 0.5 f_s. \end{cases} \tag{10}$$

Therefore, k is within the interval of $[1, 2)$. Figure 7 shows the frequency-domain characteristics of $R_{v1}(\omega)$ and $X_{v1}(\omega)$ with different k values. As can be seen in Figure 7, when $k = 1$, $R_{v1}(\omega)$ decreases as the frequency increases and decreases to 0 at $f_s/2$. That means there is no damping at $f_s/2$, and the more the LCL resonance frequency f_{res} closer to $f_s/2$, the smaller the stability margin. However, the LCL resonance frequency f_{res} can be designed close to $f_s/2$, and the change of the filter inductance L and the filter capacitor C may shift the actual LCL resonance frequency toward $f_s/2$, worsening the system stability margin.

In contrast, when $k = 1.5$, $R_{v1}(\omega)$ stays constant within the interval of $(0, f_s/2]$, which means the system has a sufficient stability margin whatever the LCL resonance frequency f_{res} is. However, $k = 1.5$ cannot be implemented in digital control system, and the only practical case would be $k = 1$. Nevertheless, the main goal of the above analysis is that there is a value that can satisfy the delay compensation requirements. As illustrated in [4, 21, 22], the delay compensation method works through compensating the lagging phase. Thus, we can mimic the delay compensator G_{C1} by the lead compensator.

Figure 8 shows the Bode diagram of the delay compensator G_{C1} for different k ($k = 1, 1.5$). The leading phases at $f_s/2$ are 45° and around 66°, respectively. Apparently, the leading phase at $f_s/2$ when $k = 1.5$ is much larger than it when $k = 1$ that is why the system can be more stable when $k = 1.5$. To compare the performance of the lead compensator with the delay compensator, the leading phases at $f_s/2$ are the same; that is, $\theta_1 = 45°$ and $\theta_2 = 66°$. And the

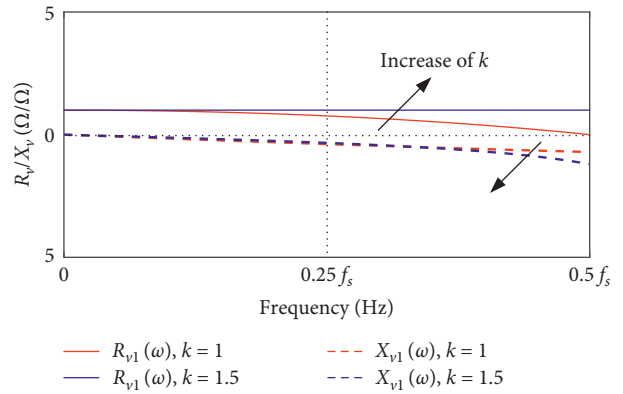

Figure 7: Frequency-domain characteristics of $R_{v1}(\omega)$ and $X_{v1}(\omega)$ with different k values.

attenuation of the transmission coefficient of the open loop is fully compensated, as shown in Figure 8. The form of the compensator can be expressed as [12]

$$G_{C2} = \frac{Ts + 1}{\alpha T s + 1}, \tag{11}$$

where α and T are

$$\begin{cases} \alpha = \dfrac{1 - \sin\theta}{1 + \sin\theta}, \\ T = \dfrac{1}{2\pi f \sqrt{\alpha}}. \end{cases} \tag{12}$$

Thus, the equivalent virtual impedance of the system can be expressed as

$$\begin{aligned} Z_{v2}(s) &= K_P G_{C2}|_{s=j\omega} \\ &= \frac{K_p\,(A_2(\omega) + jB_2(\omega))}{C_2(\omega)} \\ &= R_{v2}(\omega) + jX_{v2}(\omega), \end{aligned} \tag{13}$$

where

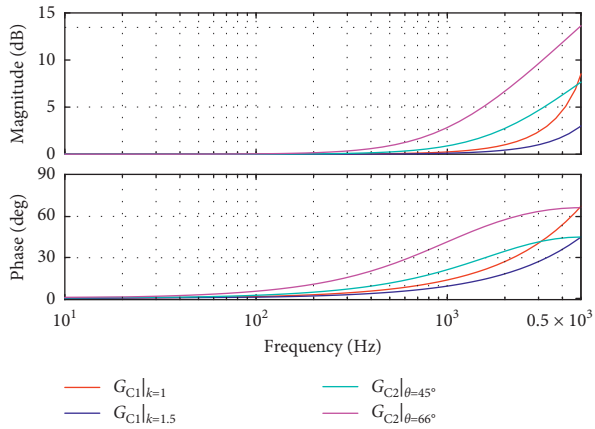

FIGURE 8: Bode diagram of G_{C1} and G_{C2} with different leading phases.

$$\begin{cases} A_2(\omega) = \left(1 + \alpha T^2 \omega^2\right)\cos 0.75\,\omega T_s + (1-\alpha)T\omega \sin 0.75\,\omega T, \\ B_2(\omega) = (1-\alpha)T\omega \cos 0.75\,\omega T_s - \left(1 + \alpha T^2 \omega^2\right)\sin 0.75\,\omega T_s, \\ C_2(\omega) = 1 + (\alpha T \omega)^2. \end{cases} \tag{14}$$

Figure 9(a) shows the frequency-domain characteristics of $R_{v1}(\omega)$ and $R_{v2}(\omega)$; Figure 9(b) shows the frequency-domain characteristics of $X_{v1}(\omega)$ and $X_{v2}(\omega)$. As can be seen from Figure 9(a), through the same leading phase at $f_s/2$, $R_{v2}(\omega)|_{\theta=45°}$ is always greater than $R_{v1}(\omega)|_{k=1}$ within the interval of $(0,\ f_s/2)$. This is because the lead compensator can provide a bigger leading phase. What is more, $R_{v2}(\omega)|_{\theta=45°}$ is greater than $R_{v1}(\omega)|_{k=1.5}$ within the interval of $(0,\ 0.4f_s)$, and the range can be extended to $(0,\ f_s/2)$ by increasing the leading phase. Thus, the system can achieve more effective damping when the lead compensator is introduced, and the parameters design procedure can be more flexible.

It is worth mentioning that $X_{v2}(\omega)|_{\theta=45°}$ is always greater than $X_{v1}(\omega)|_{k=1}$ within the interval of $(0,\ f_s/2)$, even greater than $X_{v1}(\omega)|_{k=1.5}$, as shown in Figure 9(b). And $X_{v2}(\omega)$ can be greater within high-frequency interval by increasing the leading phase θ. This is because of the amplitude amplification effect of the lead compensator, resulting in shifting the actual resonance frequency f_{res} toward $f_s/2$, decreasing the stability margin of the system. Thus, the leading phase θ should be designed carefully.

4.3. Design Guideline for the Proposed Active Damping Method. In this section, a step-by-step parameter design procedure considering the phase margin (PM) and the gain margin (GM) of the system is summarized as follows:

Step 1. Consider the requirements of the power level and the current limit of the inverter; the switching harmonic suppression ability, the filter inductances L_1 and L_2, and filter capacitance C are preliminarily determined [1].

Step 2. Set the cutoff frequency f_c according to the sampling frequency f_s, low-frequency harmonic suppression ability, and overshoot constraint. As reported in [10], to achieve an overshoot within the reasonable range, $f_0 < f_c < 4\% f_s$ is expected with PM_1 at f_c over 60°, where f_0 is the fundamental grid frequency.

Step 3. Specifically, K_p is related to f_c by [5]

$$K_p = 2\pi f_c (L_1 + L_2). \tag{15}$$

When PR controller is adopted, the magnitude of the loop gain at f_0 should be bigger than 75 dB, ensuring that the amplitude error is less 1% at the rated power [5]. Once f_c is specified, K_p and K_r can be determined.

Step 4. Draw the Bode diagram of the open-loop transfer function of the overall system with the asymmetric regular sampling method only. Generally, the PM_2 at f_{res} is expected within the interval of [30°, 60°], and GM > 5 dB is expected [5]. Then examine the actual PM_2 and GM. If the actual PM_2 or GM is not satisfied, go back to Step 3 and slightly decrease K_p and K_r.

Step 5. If the actual PM_2 or GM cannot be satisfied only by decreasing K_p and K_r, introduce the delay compensator and examine the actual PM_2 and GM. Go back to Step 3 and slightly decrease K_p and K_r if necessary.

Step 6. If the actual PM_2 or GM still cannot be satisfied, introduce the lead compensator and set the leading phase θ at $f_s/2$ to be $= \pi/4$. Go back to Step 3 and slightly decrease K_p and K_r if necessary. If it is not satisfied again, increase the leading phase according to the difference between the actual PM_2 and the preset value, and further slightly decrease K_p and K_r. If it is still not satisfied, go back to Step 1 and slightly decrease the LCL resonance frequency and repeat the other steps until the system stability requirements are met. The flowchart can be shown in Figure 10.

The parameters are designed according to the design procedure, as shown in Table 1. Figure 11 shows Bode diagram of the overall system with the designed parameters, and the stability requirements are satisfied, since $\text{PM}_1 = 70°$, $\text{PM}_2 = 31°$, and GM = 6.5 dB.

5. Simulation and Experiment Results

5.1. Simulation Results. To verify the above analysis and the proposed active damping method, a simulation model based on Figure 1 is built in the MATLAB/SIMULINK, and the main system parameters are shown in Table 1.

For verifying the analysis of the critical frequency of the SLICC, the LCL resonance frequency f_{res} is selected as $0.24 f_s$ by intentionally increasing the filter capacitance C to 9.4 μF. Figure 12 shows the simulated grid current for this case. As shown in Figure 12(a), when f_{res} is bigger than the critical frequency of the traditional SLICC, that is, $f_s/6$, the system cannot be stabilized. After decreasing the control delay by adopting the asymmetric regular sampling method, the system can be stabilized while the grid current still

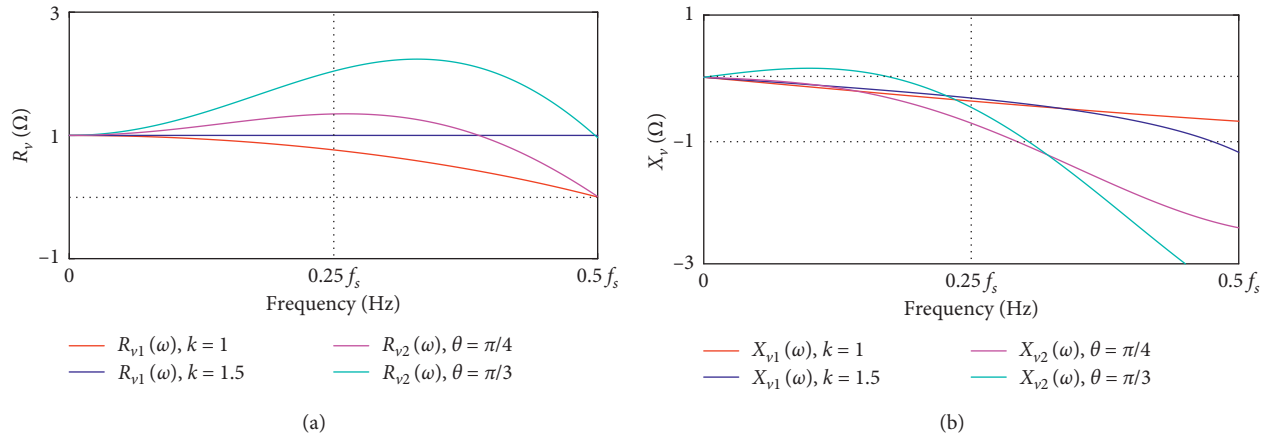

Figure 9: Frequency-domain characteristics of the equivalent virtual impedance with different leading phases. (a) $\mathbf{R_{v1}}(\omega)$ and $\mathbf{R_{v2}}(\omega)$; (b) $\mathbf{X_{v1}}(\omega)$ and $\mathbf{X_{v2}}(\omega)$.

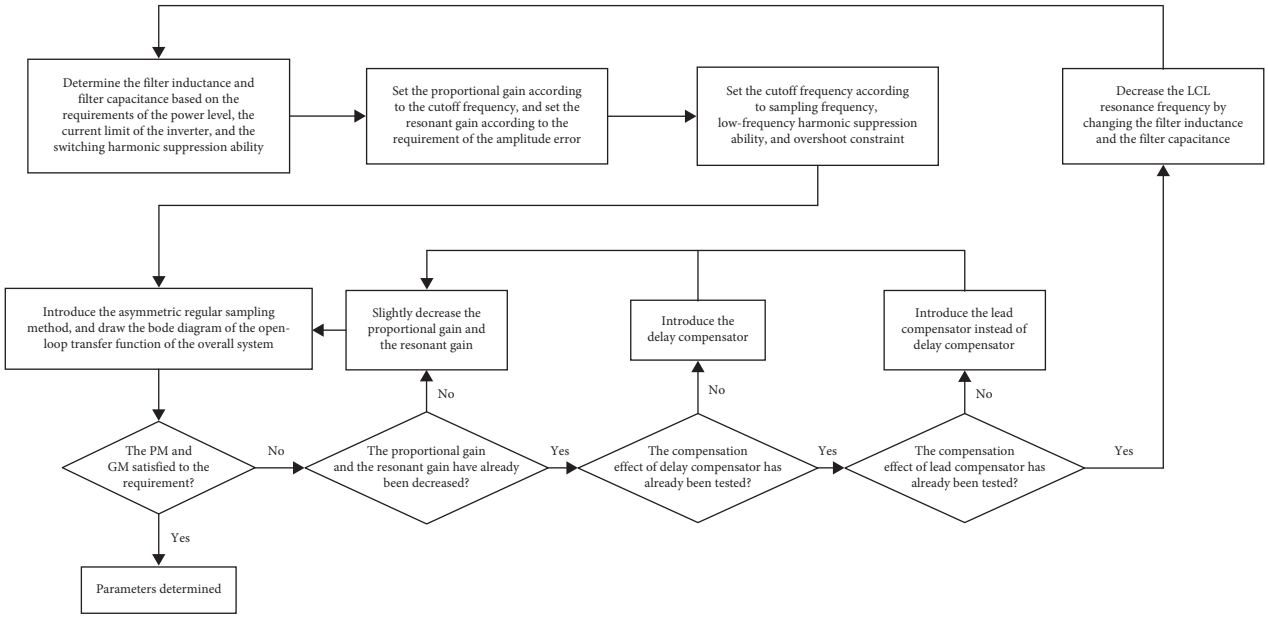

Figure 10: The flowchart of the step-by-step parameter design procedure.

Table 1: System simulation parameters.

Parameter/unit	Value
L_1/mH	2
L_2/mH	0.6
C/uF	4.7
f_s/kHz	10
f_0/Hz	50
U_{dc}/V	750
u_g/V	220
ω_i	π
K_p	10
K_r	1000
α	0.17
T	$7.7e-3$

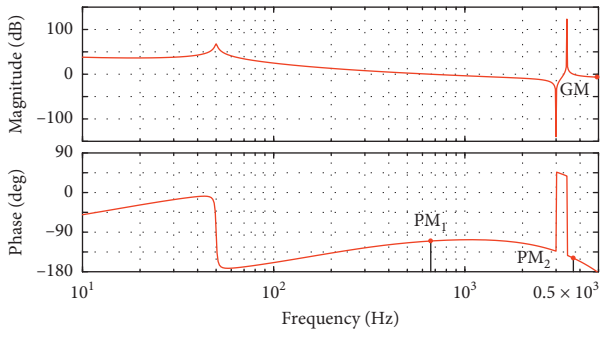

Figure 11: Bode diagram of the overall system.

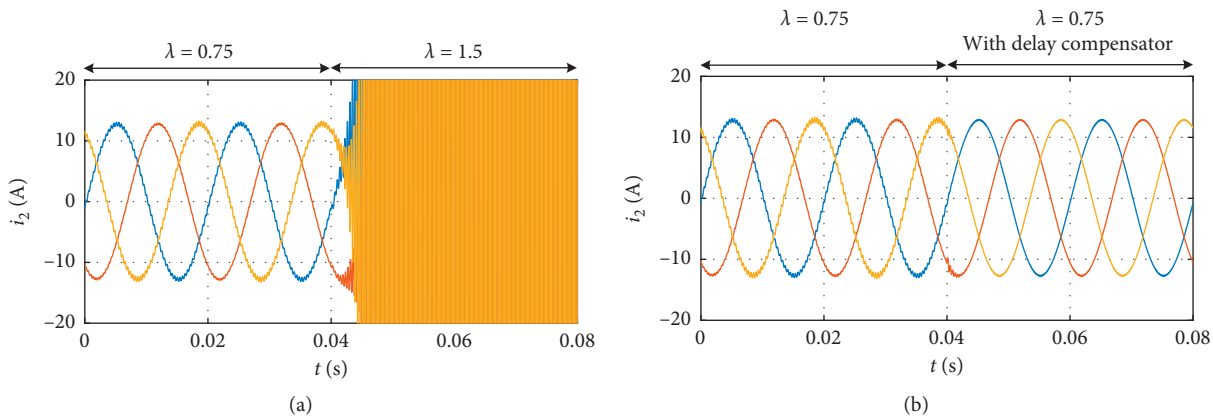

FIGURE 12: Simulation waveforms of the grid current when $f_{res} = 0.24\ f_s$ with different control strategies. (a) Only the asymmetric regular sampling method. (b) The proposed active damping method.

contains oscillation, indicating that the system stability margin is insufficient.

When further adopting the delay compensator, the current oscillation rapidly decays, indicating that the system stability margin has been increased, as shown in Figure 12(b). It is worth mentioning that, under this condition, there is little difference between the results of the delay compensator and the lead compensator (not shown in Figure 12). That means when the LCL resonance frequency f_{res} is relatively low, the system stability margin under the two methods has little difference, which is consistent with the analysis in Section 4.

When the filter capacitance C is regularly designed according to the design guidance, it equals 4.7 μF, as shown in Table 1. In this case, $f_{res} = 0.34\ f_s$, which is close to the critical frequency when the control delay decreases to $e^{-0.75sT_s}$, that is, around $f_s/3$. Figure 13 shows the simulated grid current for this case. With adopting the asymmetric regular sampling method, the control delay reduces to $e^{-0.75sT_s}$, and the system still cannot be stabilized, as shown in Figures 13(a) and 13(b).

The system can be stabilized when further adopting the delay compensator, as shown in Figure 13(a). However, the current still contains high resonance frequency harmonics, which makes the current cannot meet the requirements of total harmonic distortion (THD). Comparatively, when adopting the lead compensator, there is no obvious oscillation in the steady state, as shown in Figure 13(b). It indicates that, at a high level of the LCL resonance frequency, the system has a higher stability margin when adopting the lead compensator.

In addition, the robustness of the proposed active damping method is verified by shifting the LCL resonance frequency. Figure 14 shows the contrastive simulation results under the proposed method with the delay compensator and the lead compensator. The LCL resonance frequency reaches 0.4 f_s by decreasing the filter capacitor C to 75% designed value. The resonance frequency harmonics increase significantly with the delay compensator, as shown in Figure 14(a). Comparatively, with the implementation of the lead compensator, the resonance frequency harmonics increase slightly, as shown in Figure 14(b). Compared to the results shown in Figure 13, it indicates that the higher the resonance frequency, the greater the advantage of the lead compensator, verifying the effectiveness of the analysis and the proposed method.

5.2. Experiment Results. In order to verify the above simulation results, a 6 kW three-phase grid-connected inverter prototype is built in the laboratory, as shown in Figure 15. In practice, the PR controller is decomposed into a direct integrator and a feedback integrator, and they are discretized with a forward difference and backward difference separately [10]. The delay compensator and the lead compensator are discretized with Tustin transform with prewarping to match the frequency responses at f_{res} [5]. Thus, the discretized controller can be implemented in a TI TMS320F28335 DSP. The main system parameters are shown in Table 1.

Figure 16(a) shows the grid current with the asymmetric regular sampling method adopted only. Though the grid current contains large oscillation, the system can be stabilized when the actual LCL resonance frequency f_{res} is close to the critical frequency. That is because of the damping effects of the parasitic series resistances of the filter inductor and filter capacitor in the prototype, leading to the difference between Figures 13 and 16(a).

Figures 16(b) and 16(c) show the grid current with the delay compensator and the lead compensator, respectively. The system stability margin is improved after introducing the delay compensator, and the oscillation rapidly decays, as shown in

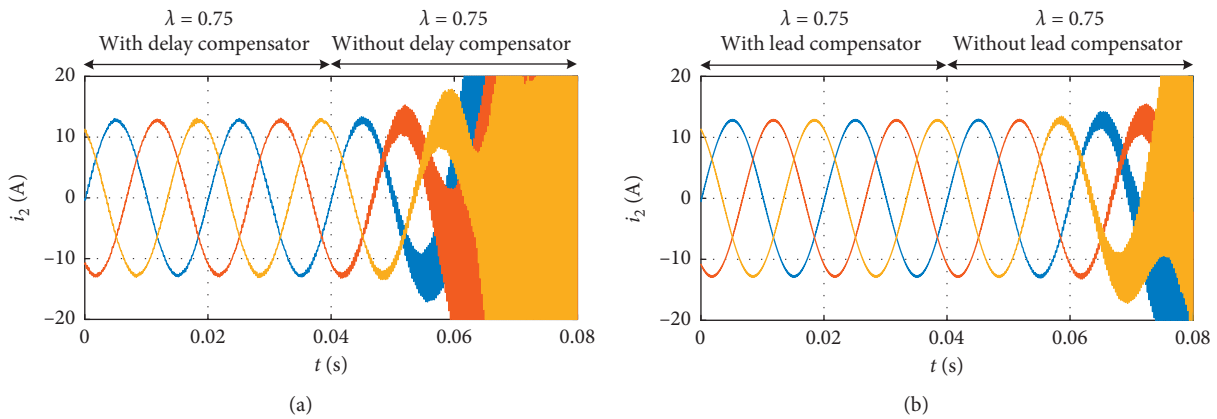

FIGURE 13: Simulation waveforms of the grid current when $f_{res} = 0.34\ f_s$ with the proposed active damping method. (a) Delay compensator. (b) Lead compensator.

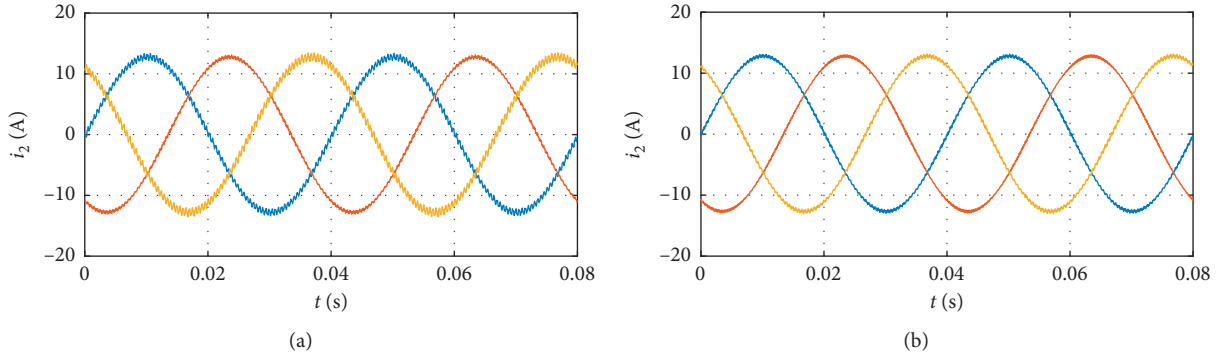

FIGURE 14: Simulation waveforms of the grid current with the proposed active damping method when C decreases. (a) Delay compensator. (b) Lead compensator.

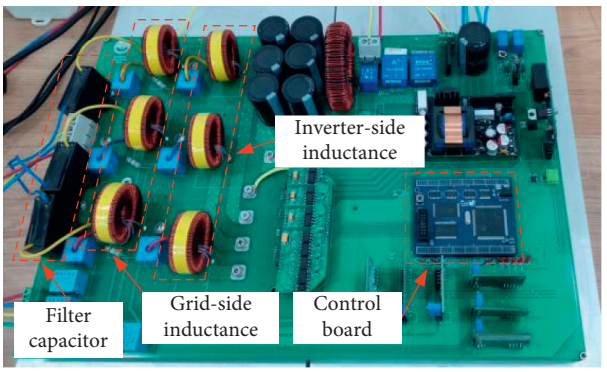

FIGURE 15: Photograph of the three-phase grid-connected inverter prototype.

Figure 16(b). But the resonance frequency harmonics still cannot meet the standards of THD. Comparatively, when adopting the lead compensator, there is no obvious oscillation in the steady state, as shown in Figure 16(c). It indicates that when the system has a high level of LCL resonance frequency, a higher stability margin can be achieved by adopting the lead compensator, verifying the effectiveness of the proposed method and the simulation results.

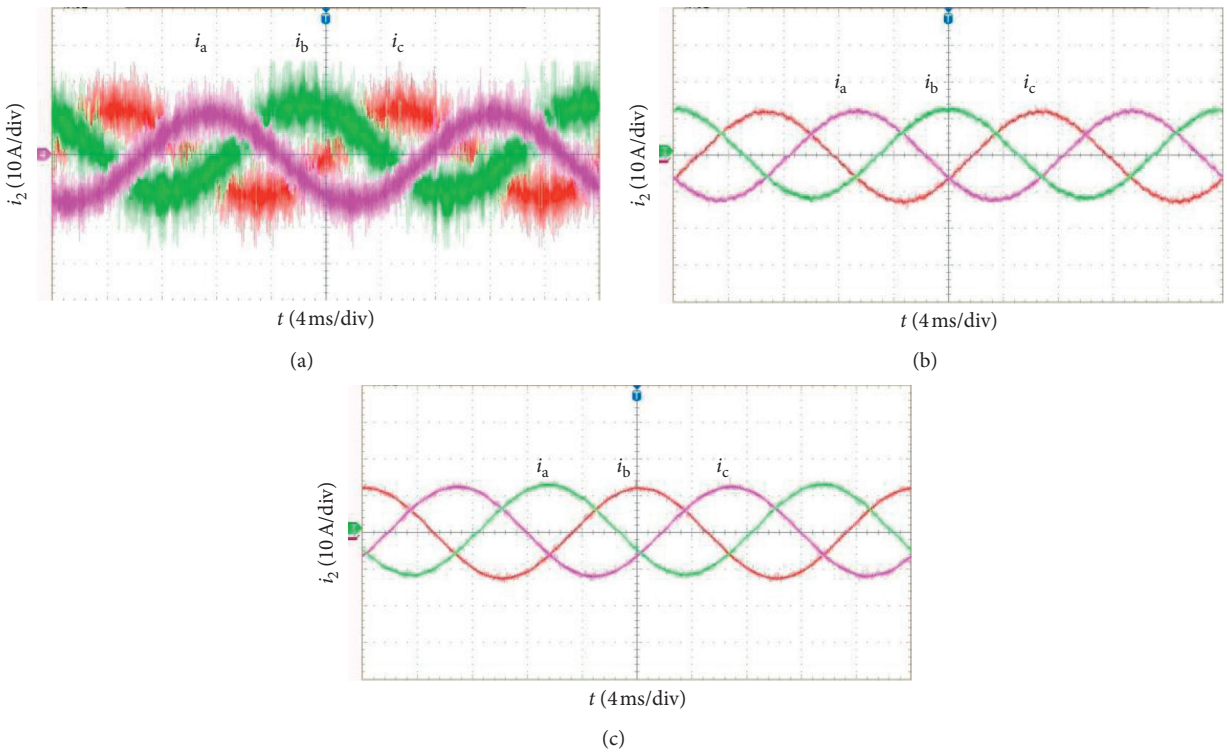

FIGURE 16: Experimental waveforms of the grid current when $f_{res} = 0.34\ f_s$ with different control strategies. (a) Only the asymmetric regular sampling method. (b) The proposed active damping method with the delay compensator. (c) The proposed active damping method with the lead compensator.

6. Conclusions

This paper studies active damping method for LCL-filtered three-phase grid-connected inverters based on SLICC. Through systematic impedance-based analyses, it has been shown that the control delay has changed the equivalent virtual resistance of the SLICC, and the critical frequency of the equivalent virtual resistance locates within the range of the LCL resonance frequency. To ensure the stability of the SLICC, an improved active damping method is proposed. The damping region is widened to $(0, f_s/2)$, which can cover all the possible resonance frequencies. A step-by-step design procedure considering the different resonance frequency range is also formulated. Particularly, the delay compensator may be unable to provide sufficient PM within the interval of high resonance frequency, and the lead compensator could further improve the system stability. The simulation and experimental results show the effectiveness of the proposed active damping method. To mimic the delay compensator more precisely when the control delay is equal to $e^{-0.75sT_s}$ is the future work.

Data Availability

The data that support the findings of this study are included within the article.

Conflicts of Interest

The authors declare no conflicts of interest regarding the publication of this paper.

Acknowledgments

This work was supported in part by the National Natural Science Foundation of China (no. 61563034), the International S&T Cooperation Program of China (no. 2014DFG72240), and the Higher School Science and Technology Floor Plan in Jiangxi Province under Grant no. KJLD14006.

References

[1] F. Blaabjerg, R. Teodorescu, M. Liserre, and A. V. Timbus, "Overview of control and grid synchronization for distributed power generation systems," *IEEE Transactions on Industrial Electronics*, vol. 53, no. 5, pp. 1398–1409, 2006.

[2] W. M. Wu, Y. Liu, Y. B. He, H. S.-H. Chung, M. Liserre, and F. Blaabjerg, "Damping methods for resonances caused by LCL-filter-based current-controlled grid-tied power inverters: an overview," *IEEE Trans. Power Electron.*vol. 32, no. 6, pp. 4395–4410, 2017.

[3] D. Pan, X. Ruan, C. Bao, W. Li, and X. Wang, "Capacitor-current-feedback active damping with reduced computation delay for improving robustness of LCL-type grid-connected inverter," *IEEE Transactions on Power Electronics*, vol. 29, no. 7, pp. 3414–3427, 2014.

[4] X. Li, X. Wu, Y. Geng, X. Yuan, C. Xia, and X. Zhang, "Wide damping region for LCL-type grid-connected inverter with an improved capacitor-current-feedback method," *IEEE Transactions on Power Electronics*, vol. 30, no. 9, pp. 5247–5259, 2015.

[5] Y. L. Ma, L. Xu, X. H. Wang, Y. Y. He, X. B. Ruan, and F. X. Liu, "Passivity-based design of capacitor-current-feedback active damping for lcl-filtered inverter considering computation delay reduction," in *Proceedings of the 2020 IEEE 11th International Symposium on Power Electronics for Distributed Generation Systems (PEDG)*, pp. 364–369, Dubrovnik, Croatia, September 2020.

[6] Z. Miao, W. Yao, and Z. Lu, "Single-cycle-Lag compensator-based active damping for digitally controlled LCL/LLCL-Type grid-connected inverters," *IEEE Transactions on Industrial Electronics*, vol. 67, no. 3, pp. 1980–1990, 2020.

[7] J. Jo, H. An, and H. Cha, "Stability improvement of current control by voltage feedforward considering a large synchronous inductance of a diesel generator," *IEEE Transactions on Industry Applications*, vol. 54, no. 5, pp. 5134–5142, 2018.

[8] B. Wang, Y. Xu, Z. Shen, J. Zou, C. Li, and H. Liu, "Current control of grid-connected inverter with LCL filter based on extended-state observer estimations using single sensor and achieving improved robust observation dynamics," *IEEE Transactions on Industrial Electronics*, vol. 64, no. 7, pp. 5428–5439, 2017.

[9] A. Mohammad, M. Alaa, and K. Muhieddin, "Current control and active damping for single phase LCL-filtered grid connected inverter," *Journal of Control Science and Engineering*, vol. 2020, Article ID 3164601, 12 pages, 2020.

[10] D. Pan, X. Ruan, X. Wang, H. Yu, and Z. Xing, "Analysis and design of current control schemes for LCL-type grid-connected inverter based on a general mathematical model," *IEEE Transactions on Power Electronics*, vol. 32, no. 6, pp. 4395–4410, 2017.

[11] Y. Tang, P. C. Loh, P. Wang, F. H. Choo, and F. Gao, "Exploring inherent damping characteristic of LCL-filters for three-phase grid-connected voltage source inverters," *IEEE Transactions on Power Electronics*, vol. 27, no. 3, pp. 1433–1443, 2012.

[12] X. Zhang, P. Chen, C. Yu, F. Li, H. T. Do, and R. Cao, "Study of a current control strategy based on multisampling for high-power grid-connected inverters with an LCL filter," *IEEE Transactions on Power Electronics*, vol. 32, no. 7, pp. 5023–5034, 2017.

[13] J. M. Xu, S. J. Xie, J. R. Kan, and L. Ji, "An improved inverter-side current feedback control for grid-connected inverters with LCL filters," in *Proceedings of the 9th International Conference on Power Electronics and ECCE Asia*, pp. 984–989, Seoul, South Korea, June 2015.

[14] M. Hanif, V. Khadkikar, W. Xiao, and J. L. Kirtley, "Two degrees of freedom active damping technique for LCL filter-based grid connected PV systems," *IEEE Transactions on Industrial Electronics*, vol. 61, no. 6, pp. 2795–2803, 2014.

[15] J. Xu, S. Xie, and T. Tang, "Active damping-based control for grid-connected LCL -filtered inverter with injected grid current feedback only," *IEEE Transactions on Industrial Electronics*, vol. 61, no. 9, pp. 4746–4758, 2014.

[16] L. Zhou, J. M. Guerrero, X. Zhou et al., "Inverter-current-feedback resonance-suppression method for LCL-type DG system to reduce resonance-frequency offset and grid-inductance effect," *IEEE Transactions on Industrial Electronics*, vol. 65, no. 9, pp. 7036–7048, 2018.

[17] J. M. Gonzalez, C. A. Busada, and J. A. Solsona, "A robust controller for a grid-tied inverter connected through an LCL filter," *IEEE Journal of Emerging and Selected Topics in Industrial Electronics*, vol. 2, no. 1, pp. 82–89, 2021.

[18] C. Zou, B. Liu, S. Duan, and R. Li, "Influence of delay on system stability and delay optimization of grid-connected inverters with LCL filter," *IEEE Transactions on Industrial Informatics*, vol. 10, no. 3, pp. 1775–1784, 2014.

[19] J. Wang, J. D. Yan, L. Jiang, and J. Zou, "Delay-dependent stability of single-loop controlled grid-connected inverters with LCL filters," *IEEE Transactions on Power Electronics*, vol. 31, no. 1, pp. 743–757, 2016.

[20] X. Wang, F. Blaabjerg, and P. C. Loh, "Grid-current-feedback active damping for LCL resonance in grid-connected voltage-source converters," *IEEE Transactions on Power Electronics*, vol. 31, no. 1, pp. 213–223, 2016.

[21] Z. Xin, X. Wang, P. C. Loh, and F. Blaabjerg, "Grid-current-feedback control for LCL-filtered grid converters with enhanced stability," *IEEE Transactions on Power Electronics*, vol. 32, no. 4, pp. 3216–3228, 2017.

[22] X. Zhou, L. Zhou, Y. Chen et al., "Robust grid-current-feedback resonance suppression method for LCL-type grid-connected inverter connected to weak grid," *IEEE Journal of Emerging and Selected Topics in Power Electronics*, vol. 6, no. 4, pp. 2126–2137, 2018.

[23] N. N. N. Nam, N.-D. Nguyen, C. Yoon, M. Choi, and Y. I. Lee, "Voltage sensorless model predictive control for a grid-connected inverter with LCL filter," *IEEE Transactions on Industrial Electronics*, vol. 1, p. 1, 2021.

[24] E. Rodriguez-Diaz, F. D. Freijedo, J. C. Vasquez, and J. M. Guerrero, "Analysis and comparison of notch filter and capacitor voltage feedforward active damping techniques for LCL grid-connected converters," *IEEE Transactions on Power Electronics*, vol. 34, no. 4, pp. 3958–3972, 2019.

[25] R. Pena-Alzola, M. Liserre, F. Blaabjerg, R. Sebastian, J. Dannehl, and F. W. Fuchs, "Systematic design of the lead-lag network method for active damping in LCL-filter based three phase converters," *IEEE Transactions on Industrial Informatics*, vol. 10, no. 1, pp. 43–52, 2014.

[26] W. Yao, Y. Yang, Y. Xu, F. Blaabjerg, S. Liu, and G. Wilson, "Phase reshaping via all-pass filters for robust LCL-filter active damping," *IEEE Transactions on Power Electronics*, vol. 35, no. 3, pp. 3114–3126, 2020.

[27] J. Sun, "Impedance-based stability criterion for grid-connected inverters," *IEEE Transactions on Power Electronics*, vol. 26, no. 11, pp. 3075–3078, 2011.

Hindawi
Mathematical Problems in Engineering
Volume 2021, Article ID 8879122, 11 pages
https://doi.org/10.1155/2021/8879122

Research Article

Energy Cooperation Optimization in Residential Microgrid with Virtual Storage Technology

Jun Tang,[1] Chen Yang,[1] Changsen Feng,[2] Junting Li,[1] Xiaowen Gu,[1] and Xuelei Jiang[1]

[1]*State Grid Suzhou Power Supply Company, Suzhou 215004, China*
[2]*College of Information Engineering, Zhejiang University of Technology, Hangzhou 310023, China*

Correspondence should be addressed to Changsen Feng; fcs@zjut.edu.cn

Received 25 September 2020; Revised 15 October 2020; Accepted 19 January 2021; Published 29 January 2021

Academic Editor: Omar Jacobo Santos Sanchez

The power balance of the tie-line is crucial to the stable operation of a community microgrid. This paper presents a power fluctuation smoothing method of the microgrid tie-line based on virtual energy storage technology. Firstly, the structure characteristics and the energy coupling mode of the combined heat and power system is systematically analyzed. Considering the operating characteristics of heat pumps, micro gas turbines, and buildings' heat storage characteristics, a virtual energy storage model is established. Secondly, the target power of the tie-line is determined with the storage state indexes into consideration. Subsequently, a power allocation strategy which takes into account the correction of equipment state mapping set is proposed to allocate the tie-line power fluctuations to heat pumps, micro gas turbines, and supercapacitors. Simulation results show this method can realize the coupling coordination between heat and power energy and ensure the smoothing effect of the power fluctuations. Meanwhile, the control flexibility of the combined heat and power system can be enhanced, and the microgrid's operating economy can be improved.

1. Introduction

Along with the popularization and application of renewable energy, the distributed power supply system composed of wind power and photovoltaic can form a user-oriented community microgrid [1–3]. During the past decade, the combined heat and power (CHP) system has gained increasing concerns and is regarded as the key of the community microgrid to meet users' multiple demands for electricity and heat [4, 5]. Renewable energy and traditional energy are collaboratively utilized to provide system optimization management and regulation in the community microgrid [6–8]. In the traditional mode, the community microgrid generally realizes the power balance of the tie-line through the configuration of battery energy storage to ensure the security operation of the system, but this will increase the operation cost due to the high price of the battery energy storage. Coordinated control of heat and power energy can smooth the tie-line's power fluctuations and realize multienergy supply and cascade utilization, and therefore the overall investment costs of the microgrid can be reduced [9–11].

At present, battery energy storage system (BESS) [12, 13] and supercapacitors [14, 15] are widely utilized in the energy cooperation optimization [16–18]. In [19], the optimal performance function is presented to obtain the control sequence of the BESS, while with the total electricity cost minimized and the battery's lifetime simultaneously extended. Hierarchical control, composed of centralized and distributed control mode, is proposed in [20] to minimize bus voltage deviation and maximize the utilization of the hybrid energy storage system's utilization capacities, respectively. Although the power fluctuations could be effectively smoothed by the BESS, its popularity is still limited by the high investment cost [21, 22].

Heat pumps, micro gas turbines, and other heating equipment can achieve coordinated control of heat and power energy through electric-thermal conversion and CHP technology, while with the power fluctuations of the tie-line smoothed and the thermal demand of the microgrid satisfied

[23, 24]. In [25], switching of switches state of heat pumps can effectively reduce the numbers of energy storage charge and discharge conversion and smooth power fluctuations of the microgrid tie-line. An electrothermal joint model, which aims at reducing the power fluctuations of the tie-line and the operating cost of the microgrid, is established in [26]. However, this condition does not consider the impact of heat production on user comfort. The above research mainly focuses on single heating equipment, and the deep coupling of heat and power energy demand further investigation. In order to furtherly explore the advantages of energy complementarity and collaborative control of the CHP system, it is necessary to comprehensively consider various types of heating equipment, and make full use of the flexibility of heat energy regulation to smooth the power fluctuations of the tie-line.

In the CHP system, the microgrid energy control centre increases/reduces the heat power to regulate the electric power of the heat pumps and the power output of the micro gas turbines, thus undertaking the smoothing power fluctuations of the tie-line. Due to the heat insulation effect of building walls, the response speed of indoor temperature to electric power changes is relatively slow. Thus, its heat storage characteristics can be compared to the charging/discharging characteristic of energy storage [27, 28].

Given this background, this paper is devoted to addressing the power fluctuations of microgrid tie-line considering the virtual energy storage. The structure of the community microgrid is introduced and virtual storage is modeled considering the characteristics of the CHP system and the heat storage characteristics of buildings. Also, the allocation strategy of power fluctuations of microgrid tie-line is presented to determine the output power of micro gas turbines, heat pumps, and supercapacitors, and therefore the power fluctuations smoothing can be realized and the comprehensive utilization efficiency of energy can be improved. The contributions could be summarized as follows:

The energy coupling mode of the CHP microgrid is analyzed.

The operating characteristics of heat pumps, micro gas turbines, and heat storage characteristics of buildings are elaborately analyzed, and then a virtual energy storage model is established.

A strategy for smoothing community microgrid tie-line power considering the virtual storage technology is presented.

A correction factor is designed to determine the final output power based on the equipment state mapping set.

The remainder of this paper is given as follows. Section 2 proposed the structure of the community microgrid, including the microelectricity network and microthermal network. In Section 3, the heat pumps, micro gas turbines, supercapacitor, and virtual energy storage are modeled. The tie-line's target power is determined in Section 4, and the allocation strategy of the target power of the tie-line is detailed in Section 5. The simulation results of the presented model are described in Section 6. The final section gives the conclusions.

2. System Structure of Community Microgrid

The community microgrid structure is depicted in Figure 1, which includes the microelectricity network and microthermal network. Distributed generation such as wind power and photovoltaic generate and input electric energy into the microelectricity grid, and supercapacitors are used to smooth the power fluctuations of the tie-line of the microgrid. The micro gas turbines input electric energy to the microelectricity network by burning natural gas and recycle the waste thermal energy through the absorption heat engine to generate heat and input it to the microthermal network, so as to realize the cogeneration of heat and power. Based on electric-thermal conversion technology, the heat pumps can convert low-quality thermal energy in the environment into high-quality thermal energy, in which part of electric energy is consumed by the heat exchanger and compressor and thermal energy are output to microthermal network. The electric energy and thermal energy are finally transmitted to the community to meet the demand for electric power and thermal energy on the user side. The power flow and heat flow are marked with green and red in Figure 1, respectively.

$$P_{\text{tie-line}}(t) = P_{\text{EL}}(t) + P_{\text{HP}}(t) + P_{\text{SC}}(t) - P_{\text{wind}}(t) - P_{\text{PV}}(t) - P_{\text{MT}}(t). \quad (1)$$

The electric power balance equation of community microgrid at time t is described in equation (1), where $P_{\text{tie-line}}(t)$ is defined as real-time power of tie-line at time t, and the value of energy flowing into the microgrid is positive and negative otherwise. $P_{\text{sc}}(t)$ represents the charging/discharging power of the supercapacitors at time t and is positive with charging and negative with discharging. $P_{\text{wind}}(t)$ and $P_{\text{pv}}(t)$ denote the output of wind power and photovoltaic at time t, respectively. $P_{\text{MT}}(t)$ and $P_{\text{HP}}(t)$ represent the power of micro gas turbines and heat pumps at time t, respectively. $P_{\text{EL}}(t)$ represents the load demand of the community at time t:

$$Q_{\text{TL}}(t) = Q_{\text{HP}}(t) + Q_{\text{MT}}(t). \quad (2)$$

The heat power balance equation is described in equation (2), where $Q_{\text{TL}}(t)$ represents heat demand power of users at time t in the microgrid and $Q_{\text{HP}}(t)$ and $Q_{\text{MT}}(t)$ denote the heat power of heat pumps and micro gas turbines at time t, respectively.

3. Modeling of Virtual Energy Storage

The air conditioning load is assumed as the heat demand in the microgrid. Since the user's demand for temperature is adjustable, the heat pumps and micro gas turbines can change heat demand to participate in the power smoothing of tie-line, which is similar to the charging/discharging characteristics of the energy storage system. Therefore, heat pumps and micro gas turbines can form a virtual storage system. The output can be adjusted to smooth power fluctuations of tie-line and ensure that the room temperature is reasonable.

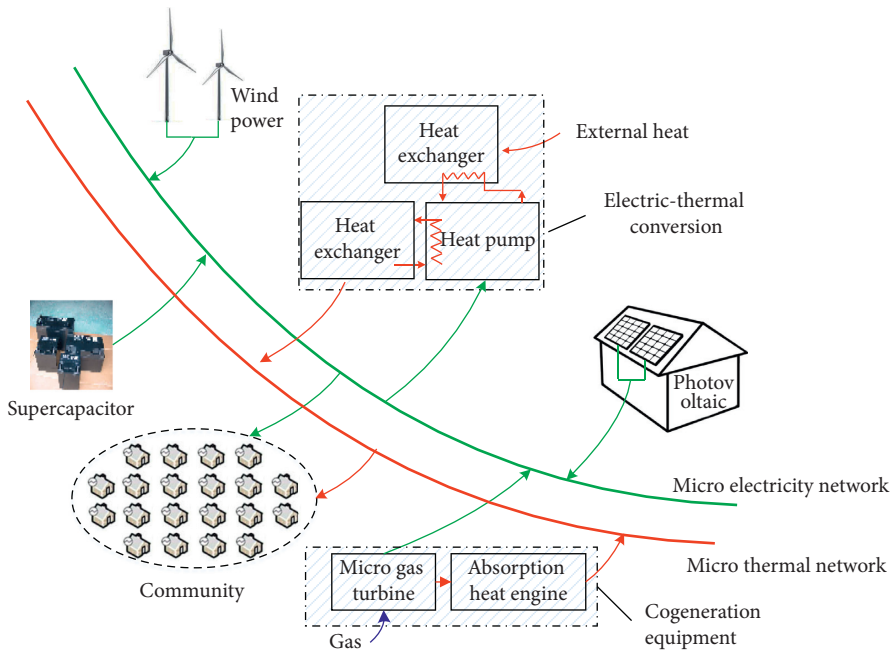

Figure 1: Energy flow in community microgrid combined with heat and power system.

3.1. Micro Gas Turbine. Under the condition of CHP cogeneration, the electric power and heat power of the micro gas turbine are shown as follows:

$$\begin{aligned} P_{\mathrm{MT}}(t) &= P_{\mathrm{gas}}(t) \times \eta_{\mathrm{MT}}, \\ Q_{\mathrm{MT}}(t) &= \gamma_{\mathrm{MT}} \times \eta_{\mathrm{heat}} \times P_{\mathrm{MT}}(t) \times \mathrm{COP}_{\mathrm{MT}}, \end{aligned} \tag{3}$$

where $P_{\mathrm{MT}}(t)$ and $Q_{\mathrm{MT}}(t)$ represent the electric power and heat power of the micro gas turbine at time t, respectively; $P_{\mathrm{gas}}(t)$ denotes the gas power injected into the micro gas turbine at time t; η_{MT} represents the power generation efficiency of the micro gas turbine; γ_{MT} and η_{heat} represent the cogeneration ratio and heat transfer efficiency of the micro gas turbine; and, COP_{MT} is the heating energy efficiency coefficient of the micro gas turbine.

3.2. Heat Pump. The heat pump can convert low-grade heat energy into high-grade heat energy by consuming a small amount of electric energy. The real-time power consumption of the heat pump changes correspondingly with the working fluid flow:

$$\begin{aligned} \mathrm{COP}_{\mathrm{HP}} &= \frac{Q_{\mathrm{HP}}}{P_{\mathrm{HP}}}, \\ Q_{\mathrm{HP}}(t) &= C_{\mathrm{HP}} \times \rho_{\mathrm{HP}} \times v(t) \times \Delta T_{\mathrm{HP}}, \end{aligned} \tag{4}$$

where $\mathrm{COP}_{\mathrm{HP}}$ is the heating energy efficiency coefficient of heat pump, C_{HP} and ρ_{HP} represent the specific heat and density of heat pump working fluid, $v(t)$ denotes the flow of heat pump working fluid at time t, and ΔT_{HP} is the temperature difference before and after one working cycle.

3.3. Super-capacitor. The state of charge (SOC) of the supercapacitors can be described as follows:

$$\begin{aligned} \mathrm{SOC}_{\mathrm{SC}}(t) &= \mathrm{SOC}_{\mathrm{SC}}(t-1) + \frac{P_{\mathrm{SC}}(t)}{E_{\mathrm{SC}}}, \\ \mathrm{SOC}_{\mathrm{SC\_min}} &\le \mathrm{SOC}_{\mathrm{SC}}(t) \le \mathrm{SOC}_{\mathrm{SC\_max}}, \end{aligned} \tag{5}$$

where $\mathrm{SOC}_{\mathrm{SC}}(t)$ represents the SOC of supercapacitors at time t, E_{SC} is the capacity of the supercapacitors, and $\mathrm{SOC}_{\mathrm{SC\_max}}$ and $\mathrm{SOC}_{\mathrm{SC\_min}}$ are the upper limit and lower limit of the SOC of supercapacitors, respectively.

3.4. Virtual Energy Storage. Based on the laws of thermodynamics [29, 30], the heat balance equation of the virtual energy storage system can be described as

$$\frac{\mathrm{d}Q}{\mathrm{d}t} = \rho \times C \times V \times \frac{\mathrm{d}T_{\mathrm{inside}}}{\mathrm{d}t}, \tag{6}$$

where Q represents the indoor heat, ρ and C are the air density and specific heat capacity of air, respectively; and V and T_{inside} represent the indoor air capacity and the indoor temperature, respectively.

Heat pumps and micro gas turbines provide heat to users, and the indoor heat is also related to heat transfer and heat radiation caused by indoor and outdoor temperature differences. Equation (6) can be furtherly expressed as

$$\begin{aligned}\rho \times C \times V \times \frac{\mathrm{d}T_{\text{inside}}}{\mathrm{d}t} &= Q_{\text{HP}}(t) + Q_{\text{MT}}(t) + (t) \times S_{\text{window}} \times k_S \\ &\quad + \left(k_{\text{wall}} \times S_{\text{wall}} + k_{\text{window}} \times S_{\text{window}}\right) \\ &\quad \times \left[T_{\text{outside}}(t) - T_{\text{inside}}(t)\right],\end{aligned} \tag{7}$$

where k_{wall} and k_{window} are heat transfer coefficients of wall and window [29], respectively; S_{wall} and S_{window} are the area of wall and window, respectively; $I(t)$ represents the solar radiation power at time t; k_s is the radiation coefficient, which is related to the glass material [1].

Suppose only a single type of heating equipment (e.g., heat pump) is applied to participate in smoothing power fluctuations. In that case, the tie-line's instantaneous power change will directly affect the heating equipment's heat power, causing the room temperature's instability on the user side. This control mode is accessible, but the control effect is not satisfying. Nevertheless, the cogeneration system in this paper includes two types of equipment, heat pumps and micro gas turbines. When the power fluctuations of the tie-line are positive, the heat pumps can undertake parts of the fluctuations component by increasing the compressor's power, and the rise of heat production causes the increase in room temperature on the user side. Simultaneously, the micro gas turbines can bear another part of power fluctuations by reducing natural gas injection power, and the drop in heat production can cause room temperature reduction (the analysis of tie-line power fluctuation being negative is similar). Through coordinated control of heat pumps and micro gas turbines, the range of room temperature variation on the user side is smaller and the effect of temperature control can be greatly enhanced. As a result, compared with a single type of heating equipment, the virtual energy storage composed of heat pumps and micro gas turbines has higher control flexibility and heating stability.

4. Determination of Target Power of Microgrid Tie-Line

The microgrid energy control centre comprehensively considers the real-time power of renewable energy, user load, and the state of supercapacitors and virtual energy storage and then determines the target power of the tie-line.

State indexes of virtual energy storage and supercapacitors are introduced to measure the ability of smoothing fluctuating power of the tie-line:

$$\begin{aligned}S_{\text{T}}(t) &= \frac{\left[T_{\text{inside}}(t) - T_{\text{inside0}}\right] \times 2}{T_{\text{inside\_max}} - T_{\text{inside\_min}}}, \\ S_{\text{SC}}(t) &= \frac{\left[\text{SOC}_{\text{SC}}(t) - \text{SOC}_{\text{SC0}}\right] \times 2}{\text{SOC}_{\text{SC\_max}} - \text{SOC}_{\text{SC\_min}}},\end{aligned} \tag{8}$$

where $S_{\text{T}}(t)$ and $S_{\text{SC}}(t)$ represent the state indexes of virtual energy storage and supercapacitors, respectively. $T_{\text{inside-max}}$ and $T_{\text{inside-min}}$ are the upper and lower limit of room temperature; T_{inside0} is the target reference value of room temperature, and the value is specified as $(T_{\text{inside-max}} + T_{\text{inside-min}})/2$ in this paper. Similarly, SOC_{SC0} represents the target reference value of the supercapacitors' SOC and the value is set as $(\text{SOC}_{\text{SC\_max}} + \text{SOC}_{\text{SC\_min}})/2$. It can be seen that the value range of both the virtual energy storage state index and the supercapacitors state index is $[-1, 1]$. When the value is close to 1, the energy release characteristic is strong, but the energy absorption characteristic is very weak. When the value is close to -1, it indicates that the energy absorption characteristic is robust, but the energy release characteristic is weak. When the energy storage state index is close to 0, it means that it has strong energy charging/discharging characteristics, which can be used as an ideal index of smoothing tie-line power.

The weighted sliding average filter algorithm is used to smooth the power fluctuations and determine the tie-line's target power. When the state index of virtual energy storage or supercapacitors is good, it means the capacity of charging/discharging is relatively strong, and the number of filtering should be increased correspondingly to improve the smoothing effect of power fluctuations. When the state index is poor, the number of filtering shall be decreased to reduce the smoothing effect of power fluctuations, so as to ensure that the virtual energy storage and supercapacitors are in an appropriate state:

$$N(t) = \left(2 - \left|S_{\text{SC}}(t-1) \times S_T(t-1)\right|\right) \times N_{\text{base}}, \tag{9}$$

where $N(t)$ is the number of sliding average filtering at time t and N_{base} is defined as the base value of sliding average filtering.

In order to improve the effectiveness of the sliding average filter algorithm for smoothing the power fluctuations of the tie-line, a weight factor is introduced to ensure the algorithm focuses more on the power near time t and weakens the power influence away from time t. The expression of the weight factor can be described as follows:

$$\beta(k) = 1 - \lambda \times \left(1 - \frac{k}{N}\right), \quad k = 1, 2, \ldots, N, \tag{10}$$

where $\beta(k)$ is the weight factor, λ is the slope of the weight factor, and the larger the value is, the more obvious the effect of weight factor is, that is, more emphasis is placed on the power of tie-line in the adjacent time t when filtering. In this paper, λ is taken as 0.5. The target power of the tie-line at time t can be expressed through the sliding average filter algorithm:

$$P_{\text{tie-line0}}(t) = \frac{\sum_{k=1,t=t-N+1}^{N,t} \beta(k) \times P_{\text{tie-line}}(t)}{\sum_{k=1}^{N} \beta(k)}, \tag{11}$$

where $P_{\text{tie-line0}}(t)$ represents the tie-line's target power at time t.

The flowchart of the sliding average filtering algorithm to determine the tie-line's target power of the microgrid at time t is shown in Figure 2.

5. Allocation Strategy of Power Fluctuations of Microgrid Tie-Line

After determining the tie-lines target power, the difference between real-time power and the tie-line's target power is the power fluctuations of tie-line, which should be smoothed by heat pumps, micro gas turbines, and supercapacitors. The power smoothing target of the microgrid tie-line at time t is shown in the following equation::

$$\begin{aligned} &P_{\text{tie-line}}(t) - P_{\text{tie-line0}}(t) \\ &\quad = P_{\text{SC}}(t) + P_{\text{HP}}(t) - P_{\text{HP},N}(t) - P_{\text{MT}}(t) + P_{\text{MT},N}(t) \\ &\quad = P_{\text{SC}}(t) + \Delta P_{\text{HP}}(t) - \Delta P_{\text{MT}}(t), \end{aligned} \tag{12}$$

where $P_{\text{tie-line0}}(t)$ is the target power of tie-line at time t; $\Delta P_{\text{HP}}(t)$ and $\Delta P_{\text{MT}}(t)$ represent the power component of the heat pumps and the micro gas turbines participating in smoothing the power fluctuations of the tie-line at time t, respectively; and $P_{\text{HP},N}(t)$ and $P_{\text{MT},N}(t)$ are the rated operating power of heat pumps and micro gas turbines at time t, respectively.

Supercapacitors have the fastest power response speed and can bear high-frequency components of power fluctuations. For the heating equipment in the cogeneration system, the heat pumps and micro gas turbines have a capacity margin for smoothing power: the heat pumps have the slowest power response speed and can bear the low-frequency components in the power fluctuations by regulating the compressor output [11]. The power response speed of the micro gas turbines is between the supercapacitors and the heat pumps, and therefore the micro gas turbines can undertake the intermediate-frequency components of power fluctuations by regulating the injection power of natural gas.

Firstly, according to the different power response speeds of heat pumps, micro gas turbines, and supercapacitors, the corresponding low-pass filtering time constant is determined and the preoutput components of heat pumps, micro gas turbines, and supercapacitors can be obtained, respectively. Secondly, considering the output constraints of heat pumps and micro gas turbines, the SOC of supercapacitors, and virtual energy storage state, the equipment state mapping set is introduced to carry out real-time equipment correction preoutput.

5.1. Preoutput Calculation Based on Low-Pass Filtering. The power fluctuations of the tie-line are firstly low-pass filtered to obtain the preoutput of the heat pump, which is the low-frequency component. Then, the remaining medium-high frequency power fluctuations are filtered similarly, and the preoutput of micro gas turbines and supercapacitors can be determined. The expressions of the preoutput of the heat pumps, micro gas turbines and supercapacitors are shown in the following equations:

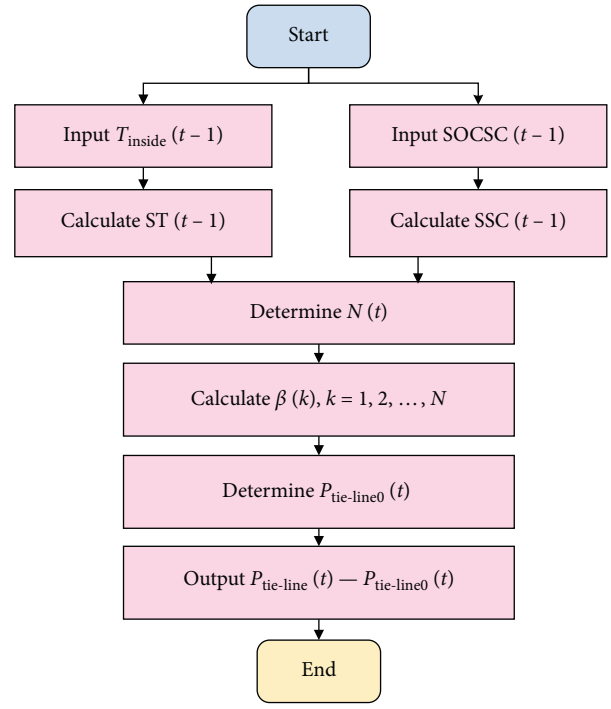

Figure 2: Flowchart of target power smoothing strategy.

$$\begin{aligned} \Delta P_{\text{HP\_ref}}(t) = &\frac{\lambda_{\text{HP}}}{\lambda_{\text{HP}} + \Delta t} \times \Delta P_{\text{HP\_ref}}(t-1) \\ &+ \frac{\Delta t}{\lambda_{\text{HP}} + \Delta t} \times \left[P_{\text{tie-line}}(t) - P_{\text{tie-line0}}(t)\right], \end{aligned} \tag{13}$$

$$\begin{aligned} \Delta P_{\text{MT\_ref}}(t) = &\frac{\lambda_{\text{MT}}}{\lambda_{\text{MT}} + \Delta t} \times \Delta P_{\text{MT\_ref}}(t-1) \\ &+ \frac{\Delta t}{\lambda_{\text{MT}} + \Delta t} \\ &\times \left[P_{\text{tie-line0}}(t) - P_{\text{tie-line}}(t) + \Delta P_{\text{HP\_ref}}(t)\right], \end{aligned} \tag{14}$$

$$\begin{aligned} P_{\text{SC\_ref}}(t) = &P_{\text{tie-line}}(t) - P_{\text{tie-line0}}(t) - \Delta P_{\text{HP\_ref}}(t) \\ &+ \Delta P_{\text{MT\_ref}}(t), \end{aligned} \tag{15}$$

where $\Delta P_{\text{HP\_ref}}$, $\Delta P_{\text{MT\_ref}}$, and $P_{\text{SC\_ref}}$ are the preoutput of the heat pumps, micro gas turbines, and supercapacitors, respectively. λ_{HP} and λ_{MT} are the filtering time constant of heat pumps and micro gas turbines, respectively. Δt is defined as the system sampling interval.

5.2. Preoutput Correction Based on State Mapping Set. The above preoutput calculation is based on the power response characteristics of heat pumps, micro gas turbines, and supercapacitors, without considering the virtual energy storage state and the SOC of supercapacitors. The equipment state mapping set and correction factor are introduced to modify the preoutput.

Input parameters of the heat pump state mapping set, the gas turbine state mapping set, and the supercapacitor state mapping set are shown in the following equations, respectively, and their values are per unit values:

$$x_{\mathrm{HP},1}(t) = \frac{\Delta P_{\mathrm{HP}}(t-1)}{P_{\mathrm{HP},N}}, \tag{16}$$

$$x_{\mathrm{HP},2}(t) = x_{\mathrm{MT},1}(t) = S_{\mathrm{T}}(t-1) = \frac{T_{\mathrm{inside}}(t-1) - T_{\mathrm{inside0}}}{\left(T_{\mathrm{inside\_max}} - T_{\mathrm{inside\_min}}\right)/2}, \tag{17}$$

$$x_{\mathrm{MT},2}(t) = \frac{\Delta P_{\mathrm{MT}}(t-1)}{P_{\mathrm{MT},N}}, \tag{18}$$

$$x_{\mathrm{SC},1}(t) = S_{\mathrm{SC}}(t-1) = \frac{\mathrm{SOC}_{\mathrm{SC}}(t-1) - \mathrm{SOC}_{\mathrm{SC0}}}{\left(\mathrm{SOC}_{\mathrm{SC\_max}} - \mathrm{SOC}_{\mathrm{SC\_min}}\right)/2}, \tag{19}$$

$$x_{\mathrm{SC},2}(t) = P_{\mathrm{tie-line}}(t) - P_{\mathrm{tie-line}}(t-1). \tag{20}$$

The heat pumps preoutput correction is based on the heat pumps' real-time running state and virtual energy storage state index. When the power fluctuations of the tie-line are positive, if $x_{\mathrm{HP},1}(t)$ is high, it indicates that the compressor's output is weak to increase and strong to decrease, so the correction factor should be reduced to avoid severe overload of the heat pumps; if $x_{\mathrm{HP},2}(t)$ is close to 1, that is, the room temperature is close to the allowed upper limit, at this time the compressor output should be cut down and the heat power of the heat pumps should be reduced to avoid room temperature exceeding the allowed upper limit. When the power fluctuations of the tie-line are negative, if $x_{\mathrm{HP},1}(t)$ is low, the compressor output reduction capacity is very weak, and the correction factor should be increased to avoid a light load of the heat pumps; and if the room temperature is close to the lower limit, the compressor output should be increased and the heat power of heat pumps should be increased to avoid room temperature exceeding the lower limit.

The micro gas turbines preoutput correction is based on the virtual energy storage state index and natural gas injection power state. When the power fluctuations are positive, if $x_{\mathrm{MT},2}(t)$ is high and the micro gas turbines have a strong lowering capacity, it is necessary to reduce the correction factor to avoid excessive natural gas injection power and if the virtual energy storage state index $x_{\mathrm{MT},1}(t)$ is close to 1, the heating power of the micro gas turbines should be reduced to avoid room temperature exceeding the allowed upper limit. The analysis of negative power fluctuations of the tie-line is similar.

The preoutput correction of the supercapacitors is based on the SOC and the power fluctuations of the tie-line. When the power fluctuations are positive, if $x_{\mathrm{SC},1}(t)$ is high, the correction factor should be reduced accordingly to reduce the supercapacitors' output, so as to avoid the SOC exceeding the allowed upper limit. Considering the supercapacitors' fast power response speed, if the positive fluctuation rate of the tie-line $x_{\mathrm{SC},2}(t)$ is large, the correction factor should be increased correspondingly to increase the output of the supercapacitors. The analysis of negative power fluctuations of the tie-line is similar.

Due to the space limit, this paper only presents the heat pump state mapping set when the power fluctuations of the tie-line are positive, as shown in Table 1. Input parameters $x_{\mathrm{HP},1}(t)$ are divided into 5 state intervals, [−0.1, −0.05), [−0.05, −0.02), [−0.02, 0.02], [−0.02, 0.02], (0.02, 0.05], (0.05, 0.1], and $x_{\mathrm{HP},2}(t)$ are divided into 3 state intervals, [−1, −0.5), [−0.5, 0.5], (0.5, 1], and can therefore map to 15 states. $\mu_{\mathrm{HP}}(t)$ is defined as the correction factor and $\Delta\mu_{\mathrm{HP}}(t)$ is the variation of the correction factor of heat pumps at time t compared with that at time $t-1$. Each state corresponds to a specific value of $\Delta\mu_{\mathrm{HP}}(t)$, of which the set of values are $\{-3\mu_0, -2\mu_0, -\mu_0, 0, \mu_0, 2\mu_0, 3\mu_0\}$, and μ_0 represents the unit basis of the correction factor and is a fixed constant. The expressions of $\mu_{\mathrm{HP}}(t)$ and $\Delta P_{\mathrm{HP}}(t)$ are shown in the following equations, respectively:

$$\mu_{\mathrm{HP}}(t) = \mu_{\mathrm{HP}}(t-1) + \Delta\mu_{\mathrm{HP}}(t), \tag{21}$$

$$\Delta P_{\mathrm{HP}}(t) = \left[1 + \mu_{\mathrm{HP}}(t)\right] \times \Delta P_{\mathrm{HP\_ref}}(t). \tag{22}$$

Similar to equation (22), the expressions of the corrected output component of micro gas turbines and supercapacitors are shown in the following equations, respectively:

$$\Delta P_{\mathrm{MT}}(t) = \left[1 + \mu_{\mathrm{MT}}(t)\right] \times \Delta P_{\mathrm{MT\_ref}}(t), \tag{23}$$

$$P_{\mathrm{SC}}(t) = \left[1 + \mu_{\mathrm{SC}}(t)\right] \times P_{\mathrm{SC\_ref}}(t). \tag{24}$$

To sum up, the smoothing community microgrid tie-line power procedure considering the virtual energy storage technology is shown in Figure 3. The target power of the tie-line can be determined by the weighted sliding average filtering algorithm. The preoutput components of heat pumps, micro gas turbines, and supercapacitors can be obtained through low-pass filtering, respectively. Considering the constraints of the equipment and the virtual energy storage state's running state, the correction factor is introduced to determine the final output based on the equipment state mapping set.

6. Case Study

The topology structure of the community microgrid is shown in Figure 4. The capacity of supercapacitors is 50 kWh, and the charging/discharging limit is 50 kW. The capacity of heat pumps and micro gas turbines is 50 kW and 100 kW, respectively. The target reference value of room temperature is 22°C. The daily power curve of microgrid equipment and environment temperature curve are displayed in Figures 5 and 6, respectively.

The power fluctuations smoothing results of the community microgrid are depicted in Figure 7(a). The comparison of target power output before and after smoothing is shown in Table 2. Referring to [31, 32], the day-ahead regulation reserve price is $15.68/MWh, and the regulation

Table 1: State mapping set of heat pumps ($P_{\text{tie-line}}(t) \geq 0$).

$x_{\text{HP},1}$	$x_{\text{HP},2}$		
	$[-1, -0.5)$	$[-0.5, 0.5]$	$(0.5, 1]$
$[-0.1, -0.05)$	$3\mu_0$	$2\mu_0$	μ_0
$[-0.05, -0.02)$	$2\mu_0$	μ_0	0
$[-0.02, 0.02]$	μ_0	0	$-\mu_0$
$(0.02, 0.05]$	0	$-\mu_0$	$-2\mu_0$
$(0.05, 0.1]$	$-\mu_0$	$-2\mu_0$	$-3\mu_0$

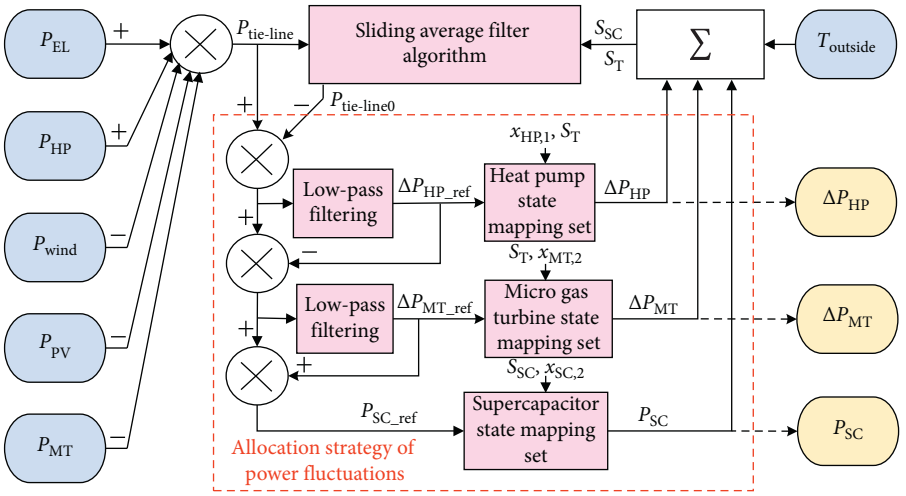

Figure 3: Structure of smoothing power fluctuations of the microgrid tie-line.

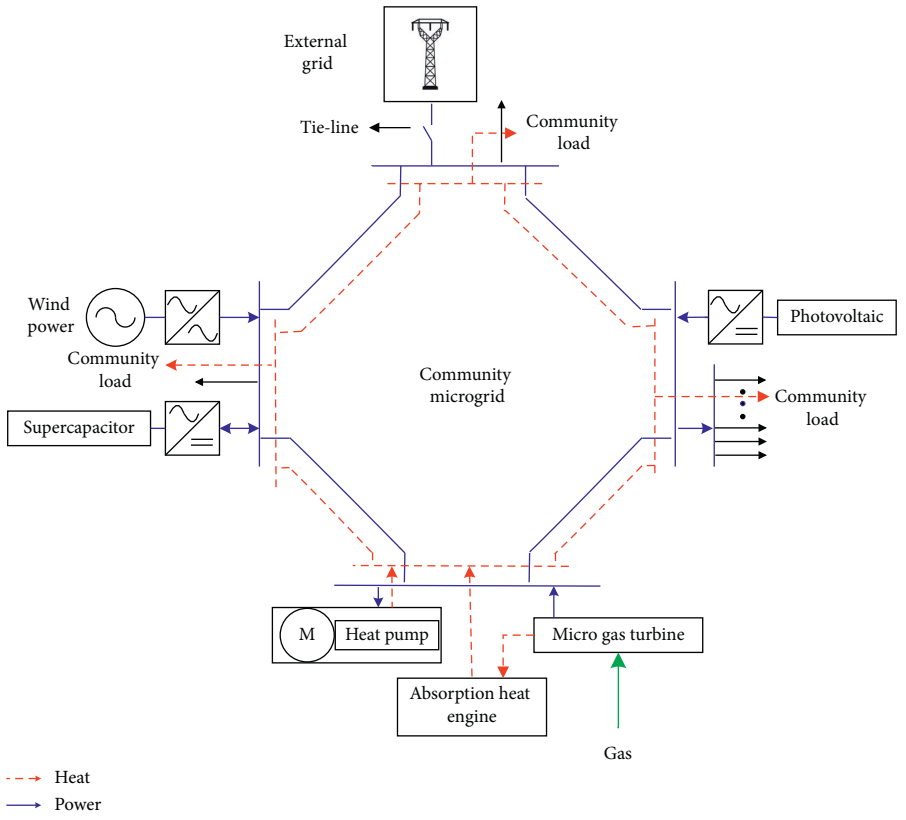

Figure 4: Topology of the community microgrid combined with heat and power system.

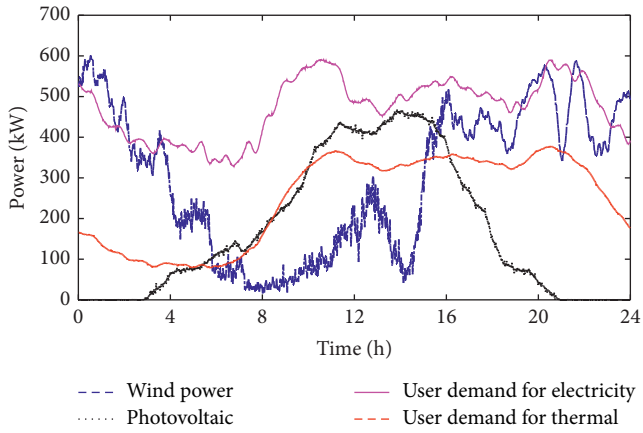

Figure 5: Daily power curves of the microgrid.

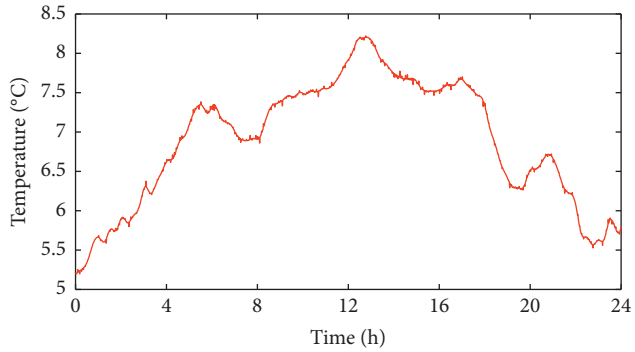

Figure 6: Temperature curve of the environment outside.

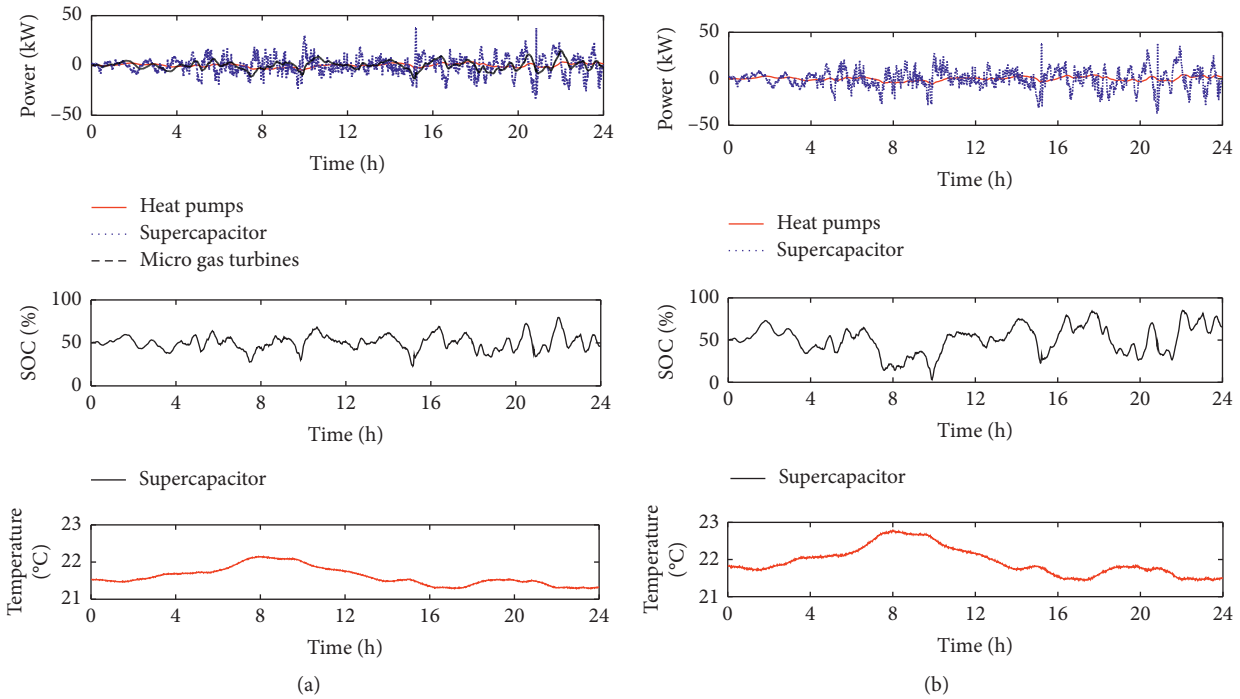

Figure 7: Power and SOC of microgrid equipment: (a) with micro gas turbine and (b) without micro gas turbine.

Table 2: Target power output before/after smoothing.

Parameter	Maximum rate of power change (kW/min)	Sum of power change rate (MW/min)	Regulation reserve cost per year (US dollar)
Before	121.93	7.83	746.87
After	8.34	1.83	174.55
Percentage decline (%)	86.1	76.6	76.6

reserve cost per year can be estimated, as shown in Table 2. After applying the micro gas turbines, heat pumps, and supercapacitors, the microgrid power output characteristics is greatly improved. Compared with supercapacitors' output characteristics, the heat pumps and micro gas turbines have a slower response speed and are used to compensate for the low-frequency and middle-frequency component of target power fluctuation, respectively. The supercapacitors bear the high-frequency of power fluctuations after being smoothed by heat pumps and micro gas turbines.

Comparatively, the target power curve when the micro gas turbines do not participate is displayed in Figure 7(b). Under this condition, the heat pumps compensate the low-frequency fluctuations component, while the supercapacitors undertake the high-frequency component. It can be found that the SOC of supercapacitors is very close to the allowable upper and lower limits of SOC. At this time, the supercapacitors' installed capacity should be increased correspondingly to improve the overall charging/discharging capacity of the cogeneration system to bear the target power fluctuation and extend the service life of the supercapacitors. In addition, by comparing the room temperature curves in Figures 7(a) and 7(b), it can be seen that the micro gas turbines can adjust the injection power of natural gas and correspondingly change the power to bear power fluctuations. Meanwhile, the effect of heat power on room temperature is opposite to that of heat pumps. Therefore, the range of room temperature variation on the user side is smaller and the temperature control effect is improved through the coordinated control of heat pumps and micro gas turbines.

The power smoothing effect of the community microgrid tie-line is shown in Figure 8. Based on the sliding average filtering algorithm, the target power of the tie-line is determined, and the preoutput of the micro gas turbine and heat pump is modified according to the state mapping table. It can be found from Figure 8 that the power smoothing effect of the tie-line is significantly improved with the cooperation of supercapacitors, heat pumps, and micro gas turbines. The more consistent the actual power of the tie-line is with the target power, the less reserve capacity the system needs and the better the economic benefit of the community microgrid is. The case study verifies the correctness and effectiveness of the power smoothing method for community microgrid tie-line with virtual energy storage.

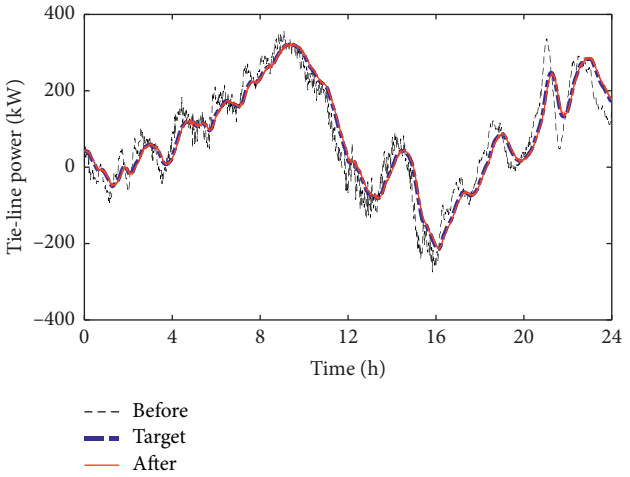

Figure 8: Smoothing effect of the tie-line power.

7. Conclusions

In this paper, a virtual energy storage model is established considering the heat storage capacity of buildings on the user side of the community microgrid, and a power smoothing method of community microgrid tie-line for cogeneration system is proposed. This method is no longer limited to single heating equipment, and coordinated control of heat pumps and micro gas turbines can smooth the power fluctuations more effectively and ensure the user side room temperature in a reasonable range. Coordination between the virtual energy storage and supercapacitors can achieve deep coupling between electric energy and thermal energy and reduce electric energy storage equipment's capacity cost. The coordination of heat pumps, micro gas turbines, and supercapacitors can significantly improve the energy control flexibility of microgrid and the comprehensive utilization efficiency of electricity, heat, and other energy.

Data Availability

The data used to support the study are available within the article.

Conflicts of Interest

The authors declare no conflicts of interest.

Acknowledgments

This work was supported by the World Class Urban Distribution Network Demonstration Project of Suzhou Historic District. This research was funded by State Grid Suzhou Power Supply Company.

References

[1] L. Igualada, C. Corchero, M. Cruz-Zambrano, and F.-J. Heredia, "Optimal energy management for a residential microgrid including a vehicle-to-grid system," *IEEE Transactions on Smart Grid*, vol. 5, no. 4, pp. 2163–2172, 2014.

[2] C. Feng, W. Liu, F. Wen, Z. Li, M. Shahidehpour, and X. Shen, "Expansion planning for active distribution networks considering deployment of smart management technologies," *IET Generation, Transmission & Distribution*, vol. 12, no. 20, pp. 4605–4614, 2018.

[3] L. Che, M. Shahidehpour, A. Alabdulwahab, and Y. Al-Turki, "Hierarchical coordination of a community microgrid with AC and DC microgrids," *IEEE Transactions on Smart Grid*, vol. 6, no. 6, pp. 3042–3051, 2015.

[4] X. Chen, C. Kang, M. O'Malley et al., "Increasing the flexibility of combined heat and power for wind power integration in China: modeling and implications," *IEEE Transactions on Power Systems*, vol. 30, no. 4, pp. 1848–1857, 2014.

[5] C. Feng, Z. Li, M. Shahidehpour, F. Wen, and Q. Li, "Stackelberg game based transactive pricing for optimal demand response in power distribution systems," *International Journal of Electrical Power & Energy Systems*, vol. 118, 2020.

[6] P. Shamsi, H. Xie, A. Longe et al., "Economic dispatch for an agent-based community microgrid," *IEEE Transactions on Smart Grid*, vol. 7, no. 5, pp. 2317–2324, 2015.

[7] C. Feng, Z. Li, M. Shahidehpour, F. Wen, W. Liu, and X. Wang, "Decentralized short-term voltage control in active power distribution systems," *IEEE Transactions on Smart Grid*, vol. 9, no. 5, pp. 4566–4576, 2017.

[8] P. Tian, X. Xiao, K. Wang et al., "A hierarchical energy management system based on hierarchical optimization for microgrid community economic operation," *IEEE Transactions on Smart Grid*, vol. 7, no. 5, pp. 2230–2241, 2015.

[9] K. Rahbar, C. C. Chai, and R. Zhang, "Energy cooperation optimization in microgrids with renewable energy integration," *IEEE Transactions on Smart Grid*, vol. 9, pp. 1482–1493, 2016.

[10] L. Wang, R. Yan, F. Bai, T. K. Saha, and K. Wang, "A distributed inter-phase coordination algorithm for voltage control with unbalanced PV integration in LV systems," *IEEE Transactions on Sustainable Energy*, vol. 11, no. 4, pp. 2687–2697, 2020.

[11] L. Wang, R. Yan, and T. K. Saha, "Voltage regulation challenges with unbalanced PV integration in low voltage distribution systems and the corresponding solution," *Applied Energy*, vol. 256, 2019.

[12] K. Wang, X. Feng, J. B. Pang, J. Ren, C. X. Duan, and L. W. Li, "State of charge (SOC) estimation of lithium-ion battery based on adaptive square root unscented kalman filter," *International Journal of Electrochemical Science*, vol. 15, no. 9, pp. 9499–9516, 2020.

[13] G.-T. Xia, C. Li, K. Wang, and L.-W. Li, "Structural design and electrochemical performance of PANI/CNTs and MnO2/CNTs supercapacitor," *Science of Advanced Materials*, vol. 11, no. 8, pp. 1079–1086, 2019.

[14] K. Wang, L. Li, T. Zhang, and Z. Liu, "Nitrogen-doped graphene for supercapacitor with long-term electrochemical stability," *Energy*, vol. 70, pp. 612–617, 2014.

[15] Y. Zhou, Y. Huang, J. Pang, and K. Wang, "Remaining useful life prediction for supercapacitor based on long short-term memory neural network," *Journal of Power Sources*, vol. 440, 2019.

[16] H. A. Aalami and S. Nojavan, "Energy storage system and demand response program effects on stochastic energy procurement of large consumers considering renewable generation," *IET Generation, Transmission & Distribution*, vol. 10, no. 1, pp. 107–114, 2016.

[17] Y. Zhou, Y. Wang, K. Wang et al., "Hybrid genetic algorithm method for efficient and robust evaluation of remaining useful life of supercapacitors," *Applied Energy*, vol. 260, pp. 114–169, 2020.

[18] F. Zhang, K. Meng, Z. Xu et al., "Battery ESS planning for wind smoothing via variable-interval reference modulation and self-adaptive SOC control strategy," *IEEE Transactions on Sustainable Energy*, vol. 8, pp. 695–707, 2016.

[19] Q. Wei, G. Shi, R. Song, and Y. Liu, "Adaptive dynamic programming-based optimal control scheme for energy storage systems with solar renewable energy," *IEEE Transactions on Industrial Electronics*, vol. 64, no. 7, pp. 5468–5478, 2017.

[20] J. Xiao, P. Wang, and L. Setyawan, "Hierarchical control of hybrid energy storage system in DC microgrids," *IEEE Transactions on Industrial Electronics*, vol. 62, no. 8, pp. 4915–4924, 2015.

[21] M. Zidar, P. S. Georgilakis, N. D. Hatziargyriou, T. Capuder, and D. Š.nd e, "Review of energy storage allocation in power distribution networks: applications, methods and future research," *IET Generation, Transmission & Distribution*, vol. 10, no. 3, pp. 645–652, 2016.

[22] C. Bu, F. Li, K. Yin, J. Pang, L. Wang, and K. Wang, "Research progress and prospect of triboelectric nanogenerators as self-powered human body sensors," *ACS Applied Electronic Materials*, vol. 2, no. 4, pp. 863–878, 2020.

[23] S. Kawachi, H. Hagiwara, J. Baba, K. Furukawa, E. Shimoda, and S. Numata, "Study on compensation of short term power fluctuation by use of heat pump air conditioning system based on real machine," *IEEJ Transactions on Power and Energy*, vol. 132, no. 1, pp. 77–85, 2012.

[24] P. S. Sauter, B. V. Solanki, C. A. Cañizares, K. Bhattacharya, and S. Hohmann, "Electric thermal storage system impact on northern communities' microgrids," *IEEE Transactions on Smart Grid*, vol. 10, no. 1, pp. 852–863, 2019.

[25] R. Wang, D. Wang, H. J. Jia et al., "A coordination control strategy of battery and virtual energy storage to smooth the micro-grid tie-line power fluctuations," *Proceedings of the CSEE*, vol. 20, pp. 5124–5134, 2015.

[26] L. Xu, G. Y. Yang, Z. Xu et al., "Combined scheduling of electricity and heat in a microgrid with volatile wind power," *Automation of Electric Power Systems*, vol. 35, no. 9, pp. 53–60, 2011.

[27] X. Jin, Y. Mu, H. Jia, J. Wu, T. Jiang, and X. Yu, "Dynamic economic dispatch of a hybrid energy microgrid considering building based virtual energy storage system," *Applied Energy*, vol. 194, pp. 386–398, 2017.

[28] X. Feng, Y. Zhang, L. Kang et al., "Integrated energy storage system based on triboelectric nanogenerator in electronic devices," *Frontiers of Chemical Science and Engineering*, pp. 1–13, 2020.

[29] C. Cristofari, R. Norvaišienė, J. L. Canaletti, and G. Notton, "Innovative alternative solar thermal solutions for housing in conservation-area sites listed as national heritage assets," *Energy and Buildings*, vol. 89, pp. 123–131, 2015.

[30] A. Buonomano and A. Palombo, "Building energy performance analysis by an in-house developed dynamic simulation code: an investigation for different case studies," *Applied Energy*, vol. 113, pp. 788–807, 2014.

[31] L. Rodríguez-Guerrero, O. Santos-Sánchez, and S. Mondié, "A constructive approach for an optimal control applied to a class of nonlinear time delay systems," *Journal of Process Control*, vol. 40, pp. 35–49, 2016.

[32] L. Lu, F. Wen, Y. Xue, and J. Kang, "Economic analysis of ancillary service provision by plug-in electric vehicles," *Automation of Electric Power Systems*, vol. 37, pp. 43–49, 2013.

Hindawi
Mathematical Problems in Engineering
Volume 2021, Article ID 6634278, 10 pages
https://doi.org/10.1155/2021/6634278

Research Article

Adaptive Droop Control of a Multibus DC Microgrid Based on Consensus Algorithm

Mingche Li, Jiangwei Fan, and Lihui Qiao

School of New Energy and Power Engineering, Lanzhou Jiaotong University, Lanzhou 730070, China

Correspondence should be addressed to Mingche Li; xiaowish913@126.com

Received 27 October 2020; Revised 11 December 2020; Accepted 22 December 2020; Published 18 January 2021

Academic Editor: Licheng Wang

The main control objective of a DC microgrid with a multibus structure is to stabilize the bus voltage and maintain the power balance of the whole system. An adaptive droop control strategy for multibus DC microgrid based on consensus algorithm is proposed. It is based on platform multiagent system, which is realized by network protocol. Under the condition of a weak communication network, the bus at all levels can realize regional power autonomy through packet consensus protocol. A hybrid simulation platform composed of Jade, MacSimJX, and Simulink is built to verify the effectiveness of the control strategy.

1. Introduction

Nowadays, microgrid is one of the most innovative fields in the power industry. Future microgrid can be used as an energy balance unit of distribution network and as independent power grid to supply community. DC microgrid has the advantages of less conversion times and simple control structure at the same time. It is not necessary to track the phase and frequency of voltage, and the eddy current loss and reactive power compensation in transmission process are not required, which is a more ideal solution for a microgrid system based on new energy generation.

DC bus voltage is the only indicator reflecting the power balance in DC microgrid [1]. Therefore, the important goal of DC microgrid control is to balance the input and output power of the system through the coordinated control of the whole system, thus maintaining the stability of DC bus voltage. The energy coordinated control method based on DC bus signal proposed in reference [2] can only achieve basic power and energy distribution. The DC Bus Signal (DBS) control method cannot achieve ideal power distribution effect because the bus voltage varies with the operating point, the line impedance is unknown, or the distribution is inhomogeneous [3]. However, the point-to-multipoint centralized communication control has strict requirements on the real time performance of the communication network, and its structure is not suitable for the DC microgrid system with microsources and scattered loads. Therefore, the distributed multiagent (MA) consensus and coordination control based on sparse communication network and point-to-point has attracted more and more attention [4]. In 2004, olfati saber first systematically proposed the theoretical framework of a multiagent network consensus problem and gave the basic form of consensus control protocol [5]. Then, Ren and Beard [5] studied the consensus problem of directed weighted networks with fixed topology and switched topology and pointed out that when the system topology contains directed spanning tree, the system can achieve consistency. Compared with literature [6], this conclusion is less conservative. Then, a lot of research and analysis show that the performance of the consensus algorithm is closely related to the connectivity of the network topology. The authors of [4, 7–10] studied the correlation between the connectivity of the communication network and the control gain and the algorithm boundary weight in the microgrid. Among the studies, literature [4] analyzed the limitations of traditional noncommunication control, proposed an adaptive droop control strategy based on discrete consensus, and realized high-precision load distribution and voltage regulation by taking the average voltage difference of the whole network as

the consensus optimization goal. The authors of [7, 8, 11] studied the application of consensus algorithm in DC microgrid clusters connected by shared common connection points (PCC), including the implementation of consensus algorithm in the average output current of each microgrid unit and the acquisition of core bus voltage. Literature [9] obtained the global information of the total injected power of nodes and the total number of control terminals participating in optimization, calculated the power and voltage reference values of the local converter station satisfying the specific objective function, and realized the global autonomous decentralized control.

The abovementioned research on DC microgrid consensus is based on a single bus structure, and its optimal control objective is unique. For the regional DC microgrid power supply system in island mode, the double-layer bus structure carries out the high-voltage and low-voltage hierarchical design for the single bus structure, which improves the security and compatibility of low-voltage equipment power supply [12], which is more practical than the single bus structure. Reference [13] proposed a coordinated control strategy for the dual bus DC microgrid. According to the voltage signals of the two buses, the coordinated control strategy and energy management scheme for each microsource and energy converter between the two buses were formulated. However, due to its dependence on the bus voltage signal to judge the working state of the system, high-precision power distribution could not be achieved.

Yu et al. first studied the group consensus problem of distributed multiagent [14] and obtained some conditions and criteria to ensure the system to achieve group consistency. Through comparative experiments, it was shown that the information interaction among subsystems in the multiagent system can accelerate the convergence speed of the consensus of each subsystem. At the same time, reference [15] studied the grouping consensus problem of multiagent based on discrete time. This is of positive significance to the research on the consensus control of DC microgrid with multibus structure. On this basis, a group consensus control strategy based on multibus DC microgrid is proposed in this paper. Compared with the traditional single bus structure consensus control strategy, it enhances the system compatibility and power allocation optimization ability.

2. Hierarchical Control of a Multibus DC Microgrid

2.1. The Problems in the Droop Control without Line Resistance. The Thevenin equivalent model of the double-bus six-node DC microgrid is shown in Figure 1. The traditional control equation of resistive droop is as follows [4]:

$$U_{oi} = U_{ref} - R_{di} I_{oi}, \quad i = 1, 2, \ldots, n_{ode}, \tag{1}$$

where $U_{oi}$is the output voltage of the converter; U_{ref} is the reference value of the output voltage; I_{oi} is the output current; R_{di} is the control coefficient of resistance droop; and n_{ode} is the total number of nodes. The intermediate energy converter is considered as an ideal energy transmission unit, and it can be seen from equation (1) that to achieve regional power autonomy of the multibus, the output power of the converter should be distributed proportionate to its rated power, and the output voltage and current of each node should meet the following relation:

$$\frac{I_{oi}}{I_{oj}} = \frac{R_{linej} + R_{dj}}{R_{linei} + R_{di}} = n_{i-j}, \quad i \neq j, \tag{2}$$

where $n_{i-j}$is the rated power ratio of the converter i and j; R_{linei}, R_{linej} is the i and j equivalent line impedance between the converter, corresponding port, and PCC point; Figure 1 shows the equivalent line impedance between high- and low-voltage buses. It can be seen that when the impedance of the line is complex, the fixed resistive droop control coefficient cannot always meet equation (2), and when the output power of the microsource increases, the output voltage may exceed the limit of ±5% bus voltage variation.

2.2. Hierarchical Control of Multibus Coordination. The traditional resistive droop control has inherent contradiction between voltage regulation and load proportion distribution, so it is necessary to adjust the control parameters twice, that is, hierarchical control of a DC microgrid.

In this paper, the coordinated layered control of multibus is divided into two layers, namely, equipment level control and system level control, as shown in Figure 2, where, i_{hi}, i_{li} and v_{DChi}, v_{DCli} are the sampling values of the current and voltage at the terminals of the high- and low-voltage bus converters. ΔU_{hi} and ΔU_{li} are the difference between the output voltage state variable of the converter corresponding to the high- and low-voltage bus and the average value of the subnet. In order to avoid the circulating current between nodes in the network and the microsource can adapt to the load power output, the main goal of secondary regulation is to monitor the output voltage and current of each microsource in real time and adjust its output according to the load capacity of the microsource; at the same time, the high-voltage and low-voltage DC buses are each other's hot standby microsources, and they can adjust the power of each other under the premise of surplus capacity making timely supplement.

When adjusting the voltage, the microsource in the network should be adjusted to the average voltage of the high- and low-voltage subnetworks synchronously, as shown in the following equation:

$$\Delta U = U_{ref} - \frac{1}{n} \sum_{i=1}^{n_s} U_{oi}, \tag{3}$$

where n_s is the total number of nodes corresponding to the subnet.

On this basis, the resistive droop coefficient is changed by the load capacity of each microsource, and its output current is distributed proportionally.

When the number of system nodes increases, it becomes difficult to calculate the target control parameters of quadratic coordination. Compared with centralized control,

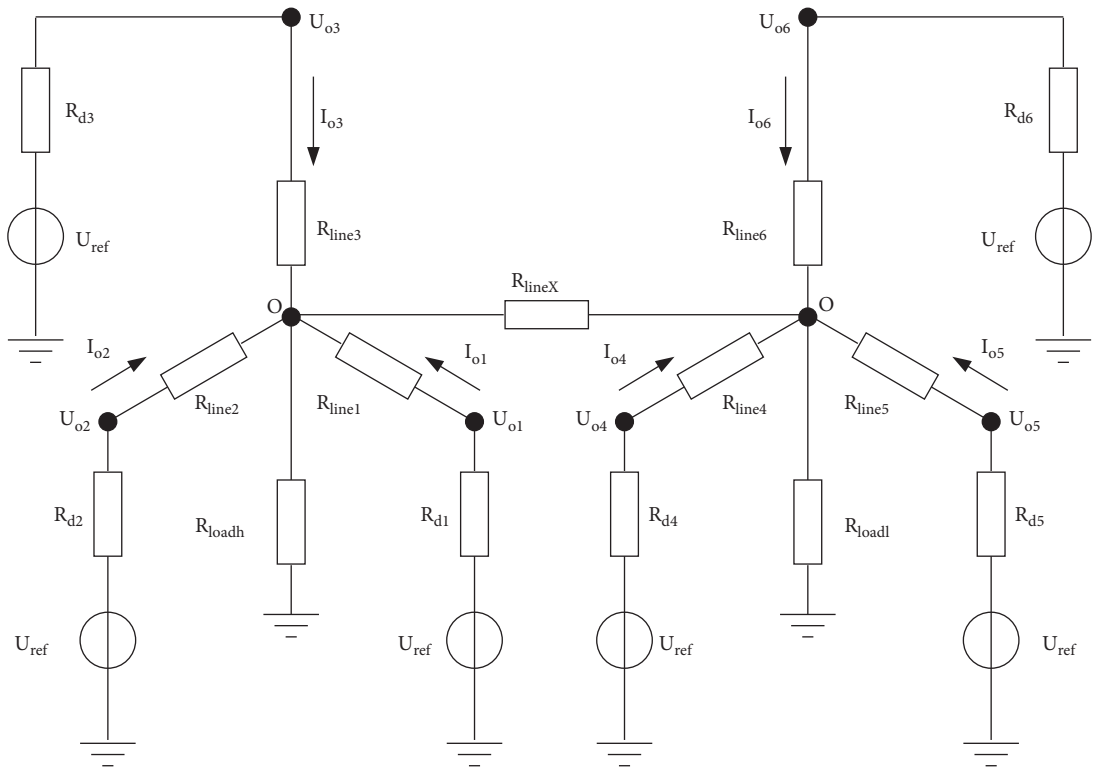

Figure 1: Equivalent model of a DC microgrid with two buses.

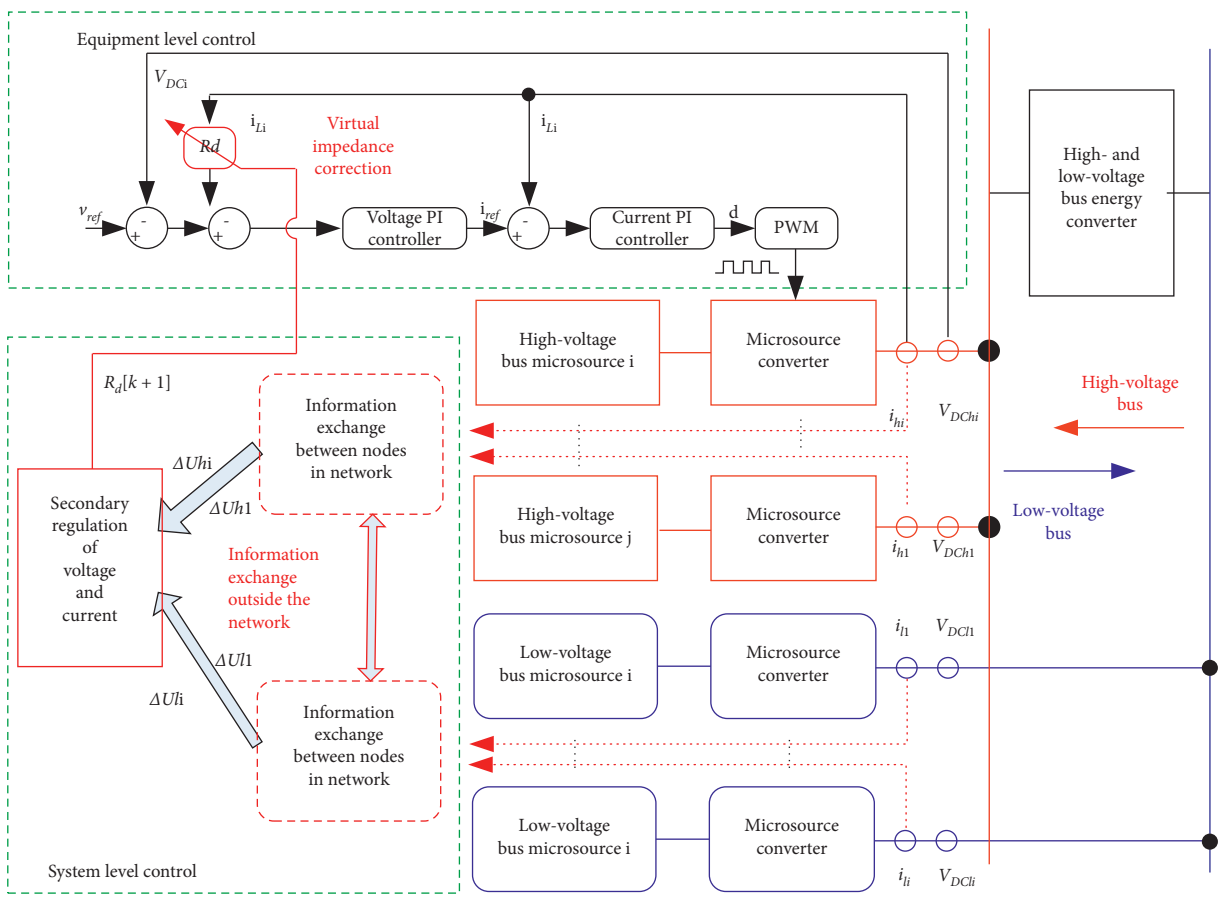

Figure 2: Hierarchical control structure of a DC microgrid with two buses.

distributed control can share the computing pressure of a multinode control system. Therefore, the discrete grouping consensus algorithm is applied in this paper to synchronously calculate the voltage and current control quantities required by high- and low-voltage DC busbars, and the correction quantity of the resistance droop coefficient satisfying each microsource is obtained through the information interaction within and between networks.

3. Discrete Group Consensus Algorithm

In the multiagent coordination control, in order to ensure that the target tasks can be distributed and coordinated, the state of all agents needs to be consistent at all times. However, under the influence of environment, state, and even time, the consistent state value of the system will change accordingly. In addition, when multiple different tasks are coordinated by multiple agents, different consistent results will appear, which is the problem of multiagent grouping consensus algorithm. In reference [14], a first-order linear multiagent group consensus protocol is formulated based on the assumption of degree balance. However, due to the strict assumption that the communication equivalent effect is 0 in internetwork communication, it is not practical. Reference [15] weakens the assumption and no longer requires the communication equivalent effect to be 0, but it needs new node adjacency weights and assumptions, which still has great limitations. Literature [16], on the basis of its research, formulates a continuous system grouping consensus protocol that is not limited by the abovementioned assumptions, but does not consider the discrete case. Due to the inherent discrete characteristics of data transmission in agent communication and the asynchronous communication mechanism of the Java Agent development framework (JADE), the following discrete packet consensus protocol is considered to be applied in the implementation of the system.

In the first-order discrete multiagent bipartite network with $n+m$ agents, n agents and m agents belong to two different consensus convergence values, and their corresponding nodes belong to two independent system subgraphs G_1 and G_2, respectively. The system equation is as follows [18]:

$$\dot{x}_i[k+1] = \dot{x}_i[k] + u_i[k], \quad i = 1, 2, \ldots, n+m, \tag{4}$$

where $x_i[k]$ and $u_i[k]$ are, respectively, the state value and control input of the ith agent at time k. The discrete packet control protocol applied is as follows:

$$u_i[k] = \begin{cases} \alpha\left[\sum_{v_j \in N_{1i}} a_{ij}\left(x_j[k] - x_i[k]\right) + \sum_{v_j \in N_{2i}} a_{ij} x_j[k]\right], & \forall i, j \in G_{L1}, \\ \alpha\left[\sum_{v_j \in N_{2i}} a_{ij}\left(x_j[k] - x_i[k]\right) + \sum_{v_j \in N_{1i}} a_{ij} x_j[k]\right], & \forall i, j \in G_{L2}, \end{cases} \tag{5}$$

where a_{ij} is the corresponding element of the system adjacency matrix; $G_{L1} = \{1, 2, \ldots, n\}$and $G_{L2} = \{n+1, n+2, \ldots, n+m\}$ are the node sequence sets contained in the submatrix of the system Laplacian matrix, which comes from the 2 subsystems described in the division diagram [17], respectively, and the corresponding node set is N_{1i} and N_{2i}, respectively. α is the system control gain; $\sum_{v_j \in N_{\theta i}} a_{ij}(x_j[k] - x_i[k])(\theta = 1, 2)$ represents the interaction between nodes in the subsystem; $\sum_{v_j \in N_{\theta i}} a_{ij} x_j[k](\theta = 1, 2)$ represents the combined influence from other grouped nodes.

For the multiagent network system equation (4), applying the packet control protocol equation (5), the following equation can be obtained:

$$x[k+1] = \begin{bmatrix} I_n - \alpha L_1 & \alpha \boldsymbol{\Omega}_1 \\ \alpha \boldsymbol{\Omega}_2 & I_m - \alpha L_2 \end{bmatrix} x[k], \tag{6}$$

$$\begin{cases} \boldsymbol{\Omega}_1 = \begin{bmatrix} a_{1(n+1)} & a_{1(n+2)} & \cdots & a_{1(n+m)} \\ a_{2(n+1)} & a_{2(n+2)} & \cdots & a_{2(n+m)} \\ \vdots & \vdots & & \vdots \\ a_{n(n+1)} & a_{n(n+2)} & \cdots & a_{n(n+m)} \end{bmatrix}, \\ \boldsymbol{\Omega}_2 = \begin{bmatrix} a_{(n+1)1} & a_{(n+1)2} & \cdots & a_{(n+1)n} \\ a_{(n+2)1} & a_{(n+2)2} & \cdots & a_{(n+2)n} \\ \vdots & \vdots & & \vdots \\ a_{(n+m)1} & a_{(n+m)2} & \cdots & a_{(n+m)n} \end{bmatrix}. \end{cases} \tag{7}$$

In equation (6), L_1 and L_2 are Laplacian matrices corresponding to subgraphs G_1 and G_2 and I_n and I_m are the corresponding dimensional identity matrices. The same assumptions as in reference [19] are adopted:

Assumption 1: for all nodes i in subgraph G_1, $\sum_{j=n+1}^{n+m} a_{ij} = 0$ is satisfied; for all nodes j in subgraph G_2, $\sum_{j=1}^{n} a_{ij} = 0$ is satisfied

Assumption 2: both system subgraphs G_1 and G_2 have directed spanning trees corresponding to them

In the actual control system, the convergence performance of the consensus algorithm is an important performance index of the control strategy. In the single-objective consensus discrete control system, the value of the boundary weight ε is determined by the maximum and submaximum eigenvalues of the Laplacian matrix L_s of the system, which is a necessary condition for the fast convergence of the consensus algorithm, as shown in the following equation:

$$\varepsilon = \frac{2}{\lambda_1(L_s) + \lambda_{n-1}(L_s)}. \tag{8}$$

For the discrete grouping consensus algorithm shown in equation (5), the corresponding control gain α determines whether the system can achieve consistency, as well as fast. It can be obtained by solving the Linear Matrix Inequality (LMI) of the error system based on the topological structure of the system, as shown in the following equations [20]:

$$\begin{bmatrix} \mathbf{P} & \left(I_{n+m-2} + \alpha\mathbf{F}\right)^T \\ I_{n+m-2} + \alpha\mathbf{F} & \mathbf{P}^{-1} \end{bmatrix} \succ 0_{2(n+m-2)\times(n+m-2)}, \tag{9}$$

$$\mathbf{F} = \begin{bmatrix} -L_1 & \mathbf{\Omega}_1 \\ \mathbf{\Omega}_2 & -L_2 \end{bmatrix}, \tag{10}$$

where $\mathbf{P}$ is a positive definite matrix and has $\mathbf{P} \in \mathbb{R}^{(n+m-2)\times(n+m-2)}$.

4. Adaptive Droop Control Based on Group Consensus Algorithm

4.1. The Overall Architecture of the Control Strategy. In this paper, each unit in the DC microgrid is regarded as an independent agent. Meanwhile, each subsystem can utilize the autonomy and inspiration of the MA system itself to adapt to the control requirements of the decentralized and complex DC microgrid.

During the execution of the control strategy, each agent monitors the output voltage and current of its power unit in real time and collects the information needed by the control. The high-voltage and low-voltage bus agents interact with each other in their own network and obtain the secondary control commands of voltage and current required by each agent through the group consensus algorithm. At the same time, the information exchange between bus boundary nodes can optimize the secondary control performance of the whole system and initiate energy exchange proposal when the power of high- and low-voltage buses is unbalanced. In addition, the system still has the consistent and universal "plug and play" feature, which makes adaptive adjustment when the system topology changes. The equipment level control is responsible for the autonomous regulation of voltage and current, which is completed by the PI controller, as shown in the following equation:

$$\begin{cases} d = \left(\dfrac{K_{\mathrm{ic}}}{s} + K_{\mathrm{pc}}\right)\left(I_{\mathrm{ref}} - I_i\right), \\ \\ I_{\mathrm{ref}} = \left(\dfrac{K_{\mathrm{iv}}}{s} + K_{\mathrm{pv}}\right)\left(V_{\mathrm{ref}} - V_i - I_i R_d\right), \end{cases} \tag{11}$$

where s is the Laplacian operator; d is the PWM duty ratio; I_{ref} is the reference value of current; V_{ref} is the voltage reference value; K_{ic} and K_{pc} are current PI controller parameters; K_{iv} and K_{pv} are voltage PI controller parameters; and R_d is the control coefficient of resistive droop.

Resistive droop control can lead to better current distribution and system damping, but fixed resistive droop coefficient R_d cannot bring accurate current distribution. Therefore, the group consensus algorithm is introduced into the system level control to adaptively adjust the resistive droop coefficient by obtaining the average current of the whole network and the average voltage difference of the buses at all levels, so as to realize high-precision load distribution and voltage regulation of the whole network.

4.2. Consensus Iteration of Network Voltage Restoration. The control of resistive droop will inevitably bring about the drop of output voltage of the microsource. Therefore, the adaptive algorithm should first consider the recovery of high- and low-voltage bus voltages. This requires the voltage data of each agent in each subnet to be acquired and processed separately by the group consensus algorithm. The local pressure difference can be obtained from the following equation:

$$\Delta U_i = U_{\mathrm{ref}} - U_{\mathrm{oi}}. \tag{12}$$

Among them, ΔU_i is the local voltage difference of the microsource and U_{oi} is the output voltage of the microsource.

The local pressure difference is used as the initial value in the agent and the local pressure difference state variables of

high- and low-voltage buses are updated by the following equation:

$$\begin{cases} \Delta U_{\mathrm{hi}}[k] = \alpha\left[\sum_{v_j \in N_{\mathrm{hi}}} a_{ij}\left(\Delta U_{\mathrm{hj}}[k] - \Delta U_{\mathrm{hi}}[k]\right) + \sum_{v_j \in N_{li}} a_{ij}\Delta U_{\mathrm{hj}}[k]\right], & \forall i \in L_h, \\ \Delta U_{\mathrm{li}}[k] = \alpha\left[\sum_{v_j \in N_{\mathrm{li}}} a_{ij}\left(\Delta U_{\mathrm{lj}}[k] - \Delta U_{\mathrm{li}}[k]\right) + \sum_{v_j \in N_{hi}} a_{\mathrm{ij}}\Delta U_{\mathrm{lj}}[k]\right], & \forall i \in L_l. \end{cases} \tag{13}$$

After several iterations, the local pressure difference state variables of each agent will converge to the average local pressure difference $\Delta U_h[\infty]$ and $\Delta U_l[\infty]$ of the high- and low-voltage bus, respectively.

4.3. Correction of the Droop Coefficient. Because the rated power of the microsource is not the same and its ability to provide external current is also quite different under different working conditions, after obtaining the average pressure difference of each subnet, the output of each microsource should be adjusted according to its load capacity. Equation (14) is used to calculate the per-unit value of each microsource:

$$I_i^* = \frac{I_i}{I_{iN}}, \tag{14}$$

where I_{iN} is the current rating of the ith microsource. Similar to voltage consensus iterations, information is exchanged through neighbor nodes. According to equation (15), the current control reference values of high- and low-voltage bus $I_{h\_\mathrm{ref}}^*$ and $I_{l\_\mathrm{ref}}^*$ are calculated:

$$\begin{cases} I_{h\_\mathrm{ref}}^*[k] = \alpha\left[\sum_{v_j \in N_{\mathrm{hi}}} a_{ij}\left(I_{\mathrm{hj}}^*[k] - I_{\mathrm{hi}}^*[k]\right) + \sum_{v_j \in N_{\mathrm{li}}} a_{ij} I_{\mathrm{hj}}^*[k]\right], & \forall i \in L_h, \\ I_{l\_\mathrm{ref}}^*[k] = \alpha\left[\sum_{v_j \in N_{\mathrm{li}}} a_{ij}\left(I_{\mathrm{lj}}^*[k] - I_{\mathrm{li}}^*[k]\right) + \sum_{v_j \in N_{\mathrm{hi}}} a_{ij} I_{\mathrm{lj}}^*[k]\right], & \forall i \in L_l. \end{cases} \tag{15}$$

Also, the resistive droop coefficient R_d of the corresponding microsource is updated accordingly:

$$R_d[k+1] = \frac{U_N - U_{\mathrm{oi}}[k]}{I_i^*[k] I_{iN} U_N}, \tag{16}$$

where $R_d[k+1]$ is the coefficient of resistive droop at the $k+1$th calculation; $U_{\mathrm{oi}}[k]$ and $I_i^*[k]$ are the actual output voltage and output current per-unit value of the corresponding high-low voltage bus microsource during the kth calculation. I_{iN} is the output current rating of the microsource. U_N is the bus voltage rating.

5. Simulation and Analysis

In this paper, a hybrid simulation platform based on JADE, MacSimJX, and Simulink is established to verify the effectiveness of the proposed control strategy. The structure of the microgrid is shown in Figure 3. JADE can build a real MA environment in the local area network. It uses the standard agent communication language ACL (Agent Communication Language) to realize the interaction of the contract network between agents [17]. The five microsource agents are located in two computers in the local area network, and they are interconnected through the TCP/IP protocol of multiple virtual machine terminals. An island DC microgrid model containing 3 high-voltage microsources MGH1-MGH3, 2 low-voltage microsources MGL1 and MGL2, and 3 constant power loads is built in Simulink, and it communicates with JADE through the MacSimJX interface. Each microsource works in the maximum power point tracking mode, and the high- and low-voltage bus voltages are set to 380 V and 48 V, respectively. The system parameters are shown in Table 1.

5.1. Performance Analysis of Agent Group Consensus Algorithm. The communication topology of each agent in Figure 3 is shown in Figure 4. Assuming that the

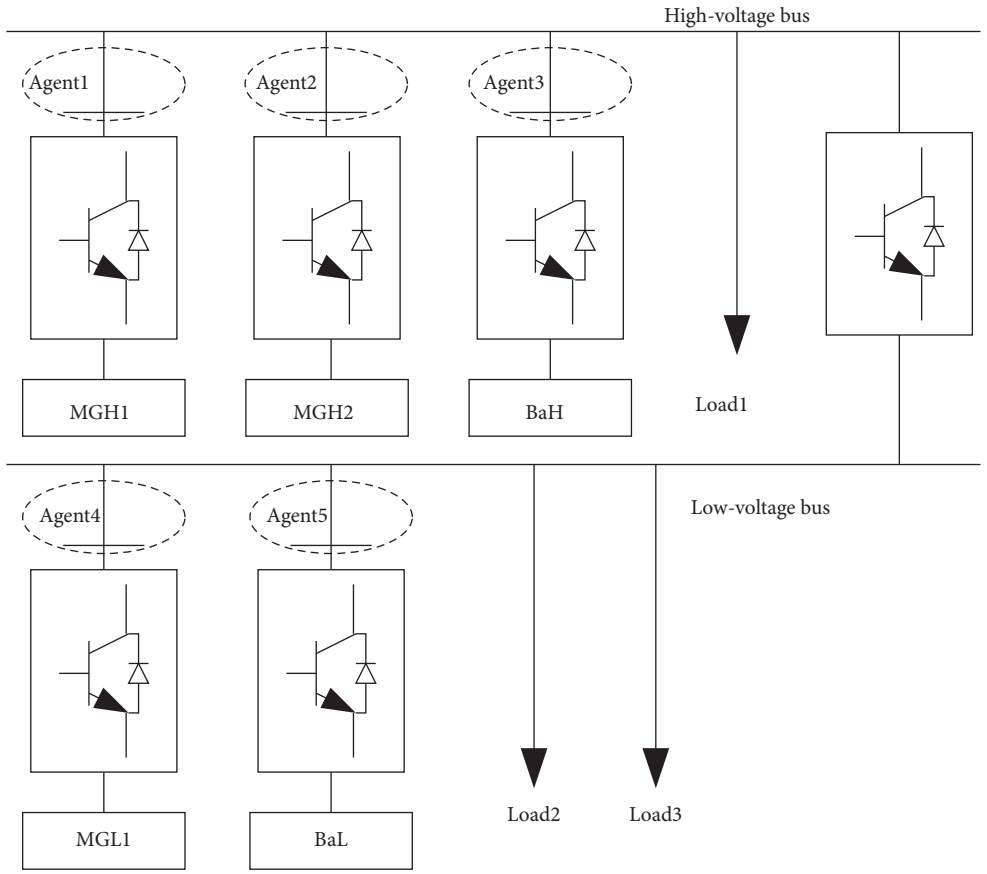

Figure 3: Structure of a DC microgrid with two buses.

Table 1: Parameters of a DC microgrid.

Microsource	Line impedance/Ω	Output voltage/V	Output current/A
MGH1	0.2	383	8.55
MGH2	0.3	379	8.43
MGH3	0.4	375	7.91
MGL1	0.2	50	20.35
MGL2	0.5	46	20.06

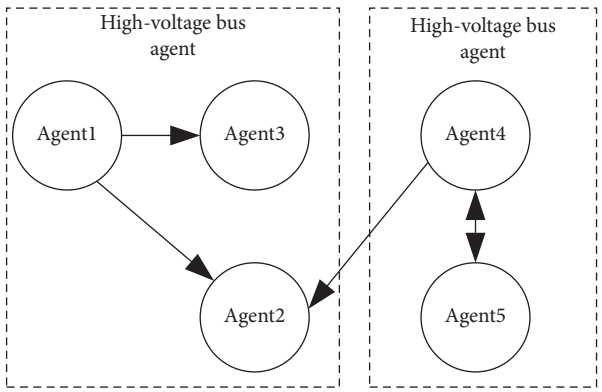

Figure 4: Communication topology structure of agents.

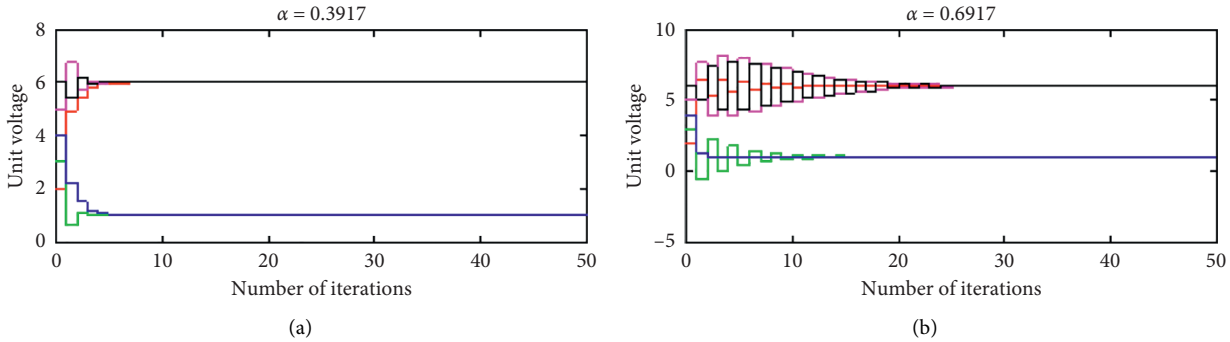

Figure 5: Performance of group consensus algorithm with different control gains. (a) $\alpha = 0.3917$. (b) $\alpha = 0.6917$.

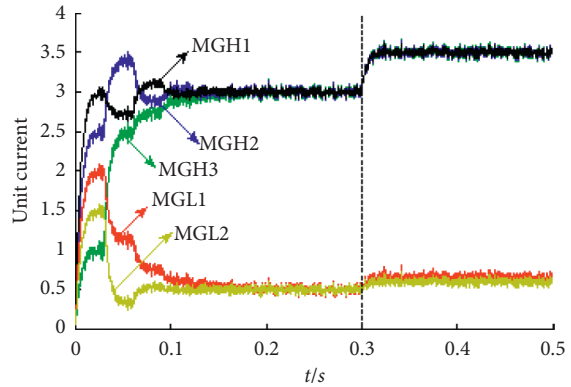

Figure 6: Output currents of microsources with high load disturbance.

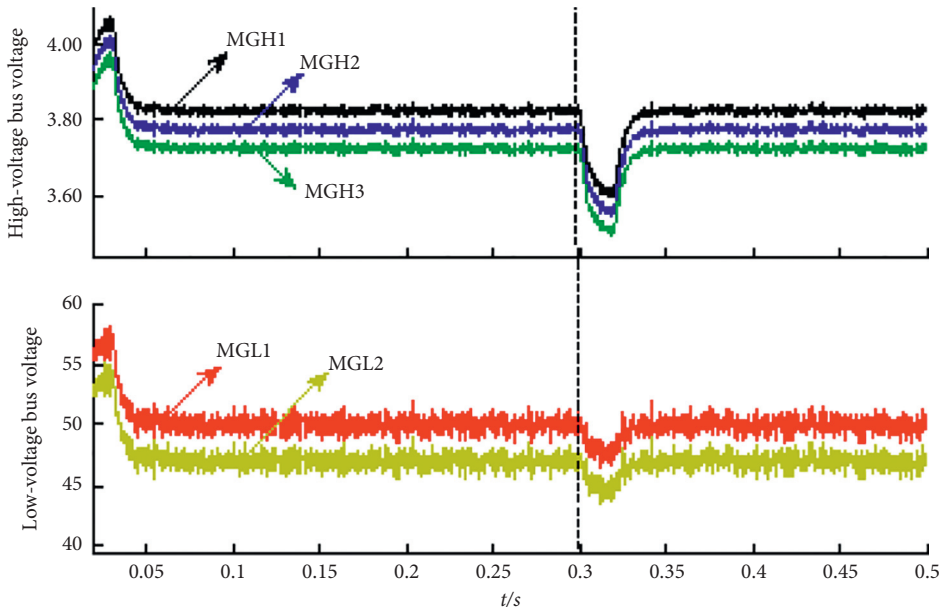

Figure 7: Output voltages of microsources with high load disturbance.

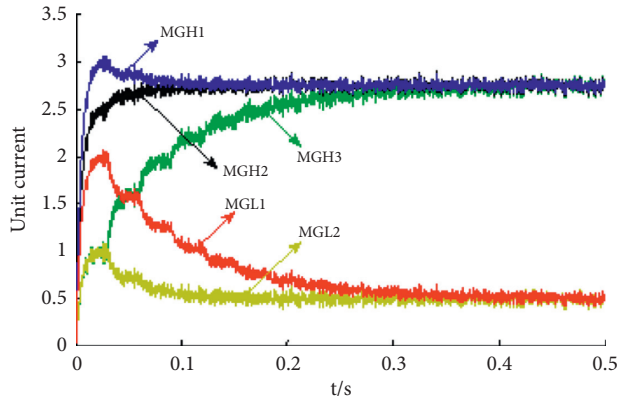

Figure 8: Output currents of microsources with network communication failure.

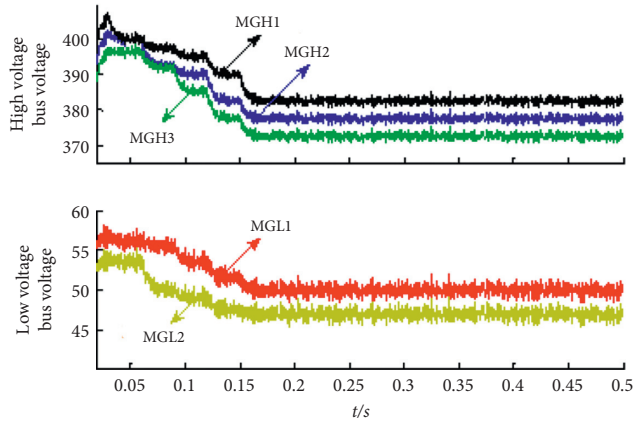

Figure 9: Output voltages of microsources with network communication failure.

communication weights are all 1, the Laplacian matrix of each subnet can be obtained as

$$\mathbf{L}_1 = \begin{bmatrix} 0 & -1 & -1 \\ 0 & 2 & 0 \\ 0 & 0 & 1 \end{bmatrix}, \quad \mathbf{L}_2 = \begin{bmatrix} 1 & -1 \\ -1 & 1 \end{bmatrix}. \tag{17}$$

From equations (6), (7), (9), and (10), combined with the Cone-Complementarity Linearization (CCL) algorithm, the system control gain $\alpha = 0.3917$ can be obtained. The convergence characteristics of the consensus algorithm under different control gains are as shown in Figure 5. It can be seen from the simulation results that when α deviating from the optimal solution, the number of iterations of voltage consensus convergence increases significantly, resulting in a decrease in algorithm performance. Among them, the α partial largeness makes the stability of the system worse, and even the consensus convergence cannot be achieved.

5.2. Load Disturbance Analysis. The high-voltage bus of the original system of the DC microgrid has a load of 7 kW, and the low-voltage bus has a load of 1 kW. The redundant power of the system's high-voltage bus is 2.1 kW during normal operation. The load disturbance analysis is that the high-voltage bus suddenly increases the load of 3 KW.

When the sudden load increase is greater than the redundant load capacity of the high-voltage bus, the output current and voltage of the microsource are as shown in Figures 6 and 7, respectively. The high- and low-voltage bus converters work in Boost mode, and the low-voltage bus energy supplements the high-voltage bus. The system reaches power balance in 0.35 s, and the voltage returns to the rated level.

5.3. Communication Failure Analysis. Intranetwork communication failure conditions have been described in literature [19]; here, we consider the case of internetwork communication failures. When the communication link between the two subnets is disconnected, that is, when both, as in equation (6), Ω_1 and Ω_2 are zero matrixes, the system microsource current and voltage are as shown in Figures 8 and 9, respectively. In the absence of boundary node communication, the proportional distribution of the power of the high- and low-voltage buses of the system under the same control gain takes more time; the bus voltage recovery is also affected by the same effect, and it takes 0.17 s to recover to the rated level.

6. Conclusions

This paper proposes a distributed collaborative control strategy for an island DC microgrid based on group consensus, and the conclusions are as follows:

(a) The performance of the grouped discrete consensus algorithm under the action of different control gains is quite different, and the CCL algorithm can quickly and accurately determine the gain value suitable for the system.

(b) The application of the group discrete consensus algorithm can make each subsystem achieve their respective consensus convergence faster and has positive significance for the correction control of the secondary current and voltage of the island DC microgrid with a multibus structure.

(c) The system as a whole and each subnet has the "plug and play" feature of distributed power. When the system power changes suddenly, the distributed power in the group communicates through neighbor nodes, the distributed power outside the group communicates through internetwork nodes, and the power needs in the network are proportionally borne by its own ability, which improves the adaptability and reliability of the overall system.

Data Availability

The data used to support the findings of this study are available from the corresponding author upon request.

Conflicts of Interest

The authors declare that there are no conflicts of interest.

Acknowledgments

This work was financially supported by the Youth Program of Lanzhou Jiaotong University and Energy Internet Technology "Tianyou Innovation Team" support plan.

References

[1] Y. Wang, L. Zhang, H. Li et al., "Hierarchical coordinated control of wind turbine-based DC micro-grid," *in Proceedings of the CSEE*, vol. 33, no. 4, pp. 16–24, 2013.

[2] X. Chen, M. Shi, H. Sun et al., "Distributed cooperative control and stability analysis of multiple DC electric springs in a DC microgrid," *IEEE Transactions on Industrial Electronics*, vol. 65, no. 7, 11 pages, 2018.

[3] X. Li, C. Wang, L. Guo et al., "Key technologies of DC microgrids: an overview," *Proceedings of the CSEE*, vol. 36, no. 1, pp. 2–17, 2016.

[4] L. Ü Zhenyu, Z. Wu, X. Dou et al., "An adaptive droop control for the islanded DC microgrid based on discrete consensus algorithm," *Proceedings of the CSEE*, vol. 35, no. 17, pp. 4397–4407, 2015.

[5] W. Ren and R. W. Beard, "Consensus seeking in multiagent systems under dynamically changing interaction topologies," *IEEE Transactions on Automatic Control*, vol. 50, no. 5, pp. 655–661, 2005.

[6] R. Olfati-Saber and R. M. Murray, "Consensus problems in networks of agents with switching topology and time-delays," *IEEE Transactions on Automatic Control*, vol. 49, no. 9, pp. 1520–1533, 2004.

[7] L. Meng, T. Dragicevic, J. C. Vasquez et al., "Modeling and sensitivity analysis of consensus algorithm based distributed hierarchical control for DC microgrids," *IEEE Transactions on Smart Grid*, vol. 7, no. 3, pp. 1504–1515, 2015.

[8] L. Meng, T. Dragicevic, J. C. Vasquez et al., "Modeling and sensitivity analysis of consensus algorithm based distributed hierarchical control for DC microgrids," in *Applied Power Electronics Conference and Exposition*, pp. 342–349, IEEE, Charlotte, NC, USA, March 2015.

[9] M. Han, X. U. Dong, L. Wan et al., "Consensus algorithm based decentralized autonomous control of hybrid multi-terminal direct current system," *Automation of Electric Power Systems*, vol. 40, no. 12, pp. 130–136, 2016.

[10] S. Sahoo, J. C.-H. Peng, A. Devakumar, S. Mishra, and T. Dragicevic, "On detection of false data in cooperative DC microgrids-a discordant element approach," *IEEE Transactions on Industrial Electronics*, vol. 67, no. 8, pp. 6562–6571, 2020.

[11] R. Zhang, B. Hredzak, and T. Morstyn, "Distributed control with virtual capacitance for the voltage restorations, state of charge balancing, and load allocations of heterogeneous energy storages in a DC datacenter microgrid," *IEEE Transactions on Energy Conversion*, vol. 34, no. 3, pp. 1296–1308, 2019.

[12] X. Yan, Y. Wang, X. Wang et al., "Parallel control based on dynamic consistency for distributed micro-sources," *Electric Power Automation Equipment*, vol. 37, no. 4, pp. 17–21, 2017.

[13] C. Ren, Y. Zhao, X. Han et al., "Coordination control of DC microgrid with two DC buses," *High Voltage Engineering*, vol. 42, no. 7, pp. 2166–2173, 2016.

[14] J. Yu and L. Wang, "Group consensus of multi-agent systems with directed information exchange," *International Journal of Systems Science*, vol. 43, no. 2, pp. 334–348, 2012.

[15] H. Zhao and J. H. Park, "Group consensus of discrete-time multi-agent systems with fixed and stochastic switching topologies," *Nonlinear Dynamics*, vol. 77, no. 4, pp. 1297–1307, 2014.

[16] C. Tan, G.-P. Liu, and G.-R. Duan, "Group consensus of networked multi-agent systems with directed topology," *IFAC Proceedings Volumes*, vol. 44, no. 1, pp. 8878–8883, 2011.

[17] F. Bellifemine, *Developing Multi-Agent Systems with JADE*, National Defense Industry Press, Beijing, China, 2013.

[18] R. Diestel, *Graph theory*, Higher Education Press, Beijing, China, 4th edition, 2013.

[19] W. Gu, S. Xue, Y. Wang et al., "Finite-time consensus based distributed cooperative control for DC microgrids," *Automation of Electric Power Systems*, vol. 40, no. 24, pp. 49–56, 2016.

[20] J. Yu and L. Wang, "Group consensus of multi-agent systems with undirected communication graphs," in *Asian Control Conference*, pp. 105–110, IEEE, Hong Kong, China, August 2009.

Hindawi
Mathematical Problems in Engineering
Volume 2021, Article ID 6693690, 11 pages
https://doi.org/10.1155/2021/6693690

Research Article

Simultaneous Unknown Input and State Estimation for the Linear System with a Rank-Deficient Distribution Matrix

Yu Hua,[1] **Na Wang**,[1,2] **and Keyou Zhao**[1]

[1]*College of Automation, Qingdao University, Qingdao 266071, China*
[2]*Shandong Key Laboratory of Industrial Control Technology, Qingdao University, Qingdao 266071, China*

Correspondence should be addressed to Na Wang; wangnaflcon@126.com

Received 30 October 2020; Accepted 21 December 2020; Published 4 January 2021

Academic Editor: Jinyan Song

The classical recursive three-step filter can be used to estimate the state and unknown input when the system is affected by unknown input, but the recursive three-step filter cannot be applied when the unknown input distribution matrix is not of full column rank. In order to solve the above problem, this paper proposes two novel filters according to the linear minimum-variance unbiased estimation criterion. Firstly, while the unknown input distribution matrix in the output equation is not of full column rank, a novel recursive three-step filter with direct feedthrough was proposed. Then, a novel recursive three-step filter was developed when the unknown input distribution matrix in the system equation is not of full column rank. Finally, the specific recursive steps of the corresponding filters are summarized. And the simulation results show that the proposed filters can effectively estimate the system state and unknown input.

1. Introduction

The traditional Kalman filter [1] and its extension can recursively estimate the state of the linear system with process noise and measurement noise. The time-domain recursive filter brings greater convenience for continuously processing input data, so it can play a more important role in control theory and engineering. The Kalman filter requires the noise to be stationary white noise, but this supposition is sometimes not feasible because unknown input may not be white noise and cannot be measured.

In the fields of environmental monitoring [2] and disturbance suppression [3, 4], the system equation or output equation contains unknown input owing to environmental impacts and improper selection of model parameters. In recent decades, the problem of state estimation with unknown input has received extensive attention.

For continuous-time systems, the necessary and sufficient conditions for the existence of optimal state filters have been established [5–7]. Furthermore, the steps to reconstruct unknown input are also quite complete [8, 9]. For the state estimation problem of discrete-time systems, an early solution was to add an unknown input vector to the system state vector. Then, the Kalman filter was used to estimate the augmented state. However, the scenarios of using this solution are limited to that the dynamical evolution of unknown input is known [10, 11]. In order to reduce computation costs of the augmented state filter, Friedland [11] proposed the two-stage Kalman filter in which the state estimation and unknown input estimation are decoupled. Although this filter has been successfully applied in some instances, it is still limited to the requirement that the dynamic evolution of unknown input is available. When the unknown input only affects the system equation, Kitanidis [5] developed an optimal recursive state filter which can estimate the system state without prior knowledge of the unknown input. And the stability and convergence conditions of the above filter were raised by Darouach and Zasadzinski [12]. Further, Darouachet al. [13] extended this filter. So, the filter is valid when unknown input is directly feedthrough to the output equation; that is, the unknown input affects both the system equation and output equation.

Although the above methods can get the estimation value of the system state, they all ignore obtaining the

estimation value of unknown input, which is necessary in some practical applications.

Hsieh [14] established a robust two-stage Kalman filter (RTSKF). For systems without direct feedthrough of unknown input to output, it can give the joint state and unknown input estimation. But the optimality of the unknown input estimation has not been proven. Furthermore, Gillijns and De Moor [15] proposed a recursive three-step filter (RTSF), which gave a proof that the unknown input estimation is optimal. And the form of the unknown input estimation obtained by RTSF is consistent with that of RTSKF. On the other hand, Gillijns and De Moor [16] extended RTSF so that it is still valid for linear discrete-time systems with direct feedthrough.

Despite the fact that the above filters can solve the problem of simultaneously estimating system state and unknown input, they are based on a precondition: the distribution matrix of unknown input must be of full column rank.

For systems with direct feedthrough, if the distribution matrix of unknown input in output equation is not of full column rank, Cheng et al. [17] presented an unbiased minimum-variance state estimation (UMVSE). This method transforms the output equation by singular value decomposition of the distribution matrix. Then UMVSE is applied to address the problem of state estimation for the new system. However, this method omitted the estimation of unknown input. Hsieh [18] used an extension of RTSF (ERTSF) to estimate the unknown input and state under the assumption that the distribution matrix is not of full column rank, but some parameters in ERTSF were obtained by experience. This paper put forward the novel recursive three-step filter with direct feedthrough (NRTSF-DF) which can give estimation value of the state and unknown input under the same assumption. And compared with ERTSF, the parameter of NRTSF-DF can be exactly obtained. For systems without direct feedthrough, the problem of filter design with unknown input still exists though there are few related literature studies about it. Similar to NRTSF-DF, the novel recursive three-step filter (NRTSF) is proposed in this paper. The novel filters can achieve a simultaneous estimation of the system state and unknown input under the condition that the unknown input distribution matrix is not of full column rank.

In recent years, the research of estimating system state with unknown input is concentrated on nonlinear systems. Based on the EKF structure, the filters estimating the state of the nonlinear system were designed in [19, 20]. Furthermore, by making some improvements on UKF [21], study [22] obtained the filter with RTSF form. And the filter can estimate the state and unknown input simultaneously.

This paper is organized as follows: in Section 2, the problem is formulated. Section 3 deals with the design of the optimal filter for the system with direct feedthrough, and the specific structure of NRTSF-DF is summarized. Next, the optimal filter for the system without feedthrough is established in Section 4. The structure of NRTSF is also obtained. Finally, Section 5 demonstrates the effectiveness of the proposed filters through simulation.

2. Problem Formulation

Consider the linear discrete-time-varying system:

$$x_k = A_{k-1}x_{k-1} + G_{k-1}d_{k-1} + w_{k-1}, \tag{1}$$

$$y_k = C_k x_k + H_k d_k + v_k, \tag{2}$$

where $x_k \in R^n$ is the state vector, $d_k \in R^m$ is an unknown input vector, and $y_k \in R^p$ is the measurement. The process noise $w_k \in R^n$ and the measurement noise $v_k \in R^p$ are assumed to be mutually uncorrelated, zero-mean, white random signals with known covariance matrices, $Q_k = E[w_k w_k^T] \geq 0$, and $R_k = E[v_k v_k^T] > 0$, respectively. The time-varying matrices A_k, G_k, C_k, and H_k are known with an appropriate dimension. Throughout the paper, the conditions that (A_k, G_k) is observable and that x_0 is independent of w_k and v_k are satisfied. And the unbiased estimate $\widehat{x}_0 = E(x_0)$ with $P_0^x = E[(x_0 - \widehat{x}_0)(x_0 - \widehat{x}_0)^T]$ is known.

The optimal filtering problem of the above system is to obtain the unbiased optimal filtering sequence of unknown input $\{\widehat{d}_{0|0}, \ldots, \widehat{d}_{k|k}\}$ and state $\{\widehat{x}_{0|0}, \ldots, \widehat{x}_{k|k}\}$ recursively based on the initial estimate $\widehat{x}_0$, the covariance matrix P_0^x, and the sequence of measurement $\{y_0, y_1, \ldots, y_k\}$. If $H_k = 0$, the system is transformed into a linear discrete-time-varying system without direct feedthrough of unknown input to output. Then, the corresponding optimal filtering problem is transformed to obtain the unbiased optimal filtering sequence of unknown input $\{\widehat{d}_{0|1}, \ldots, \widehat{d}_{k-1|k}\}$ and state $\{\widehat{x}_{0|0}, \ldots, \widehat{x}_{k|k}\}$ under the corresponding conditions.

3. NRTSF-DF

The RTSF proposed by Steven Gilljins in [16] can solve the state and unknown input estimation problem of linear system (1)-(2) while $\operatorname{rank}(H_k) = m, k = 0, 1, \ldots$. When the unknown input distribution matrix in the output equation is not of full column rank, that is, $\operatorname{rank}(H_k) = r_k < m$, we consider a NRTSF-DF design method. The following is the derivation process.

If $\operatorname{rank}(H_k) = r_k \leq m$, perform full rank decomposition:

$$H_k = \overline{H}_k T_k, \tag{3}$$

where $\overline{H}_k \in R^{p \times r_k}, T_k \in R^{r_k \times m}$, and $\operatorname{rank}(\overline{H}_k) = \operatorname{rank}(T_k) = r_k$. The full rank decomposition steps are given in Appendix.

Defining the virtual unknown input by $\overline{d}_k = T_k d_k$, then $H_k d_k = \overline{H}_k \overline{d}_k$. If the estimation value of $\overline{d}_k$ is expressed as $\widehat{\overline{d}}_{k|k}$, the minimal norm estimation value of unknown input d_k is

$$\widehat{d}_{k|k} = T_k^+ \widehat{\overline{d}}_{k|k}, \tag{4}$$

where T_k^+ is the Moore–Penrose inverse of T_k. Then, original output equation (2) is rewritten as

$$y_k = C_k x_k + \overline{H}_k \overline{d}_k + v_k, \tag{5}$$

where $\overline{d}_k \in R^{r_k}$ is the virtual unknown input vector.

Based on the system state equation (1) and output equation (5), we consider NRTSF-DF of the form

$$\widehat{x}_{k|k-1} = A_{k-1}\widehat{x}_{k-1|k-1} + G_{k-1}\widehat{d}_{k-1|k-1}, \tag{6}$$

$$\widehat{\overline{d}}_{k|k} = \overline{M}_k\left(y_k - C_k\widehat{x}_{k|k-1}\right), \tag{7}$$

$$\widehat{x}_{k|k} = \widehat{x}_{k|k-1} + \overline{L}_k\left(y_k - C_k\widehat{x}_{k|k-1}\right), \tag{8}$$

where the matrices $\overline{M}_k \in R^{r_k \times p}$ and $\overline{L}_k \in R^{n\times p}$ still have to be determined.

3.1. Time Update. Let $\widehat{x}_{k-1|k-1}$ and $\widehat{d}_{k-1|k-1}$ denote the optimal unbiased estimates of x_{k-1} and d_{k-1} given measurement sequence $\{y_0, y_1, \cdots, y_{k-1}\}$; then, the time update is

$$\widehat{x}_{k|k-1} = A_{k-1}\widehat{x}_{k-1|k-1} + G_{k-1}\widehat{d}_{k-1|k-1}. \tag{9}$$

The error in the estimate $\widehat{x}_{k|k-1}$ is given by

$$\widetilde{x}_{k|k-1} \triangleq x_k - \widehat{x}_{k|k-1} = A_{k-1}\widetilde{x}_{k-1|k-1} + G_{k-1}\widetilde{d}_{k-1} + w_{k-1}, \tag{10}$$

where $\widetilde{x}_{k|k} \triangleq x_k - \widehat{x}_{k|k}$ and $\widetilde{d}_k \triangleq d_k - \widehat{d}_{k|k}$. Consequently, the covariance matrix of $\widehat{x}_{k|k-1}$ is given by

$$P^x_{k|k-1} \triangleq E\left[\widetilde{x}_{k|k-1}\widetilde{x}^T_{k|k-1}\right] = \begin{bmatrix} A_{k-1} & G_{k-1}\end{bmatrix}\begin{bmatrix} P^x_{k-1|k-1} & P^{xd}_{k-1|k-1} \\ P^{dx}_{k-1|k-1} & P^d_{k-1|k-1}\end{bmatrix}\begin{bmatrix} A^T_{k-1} \\ G^T_{k-1}\end{bmatrix} + Q_{k-1}, \tag{11}$$

with $P^x_{k|k} \triangleq E[\widetilde{x}_{k|k}\widetilde{x}^T_{k|k}]$, $P^d_{k|k} \triangleq E[\widetilde{d}_k\widetilde{d}^T_k]$, $(P^{xd}_{k|k})^T = P^{dx}_{k|k} \triangleq E[\widetilde{d}_k\widetilde{x}^T_{k|k}]$.

3.2. Virtual Unknown Input Estimation. In this section, the estimation of the virtual unknown input $\overline{d}_k$ is considered.

3.2.1. Unbiased Virtual Unknown Input Estimation. Defining the innovation $\widetilde{y}_k \triangleq y_k - C_k\widehat{x}_{k|k-1}$, it follows from (5) that

$$\widetilde{y}_k = \overline{H}_k\overline{d}_k + e_k, \tag{12}$$

where e_k is given by

$$e_k = C_k\widetilde{x}_{k|k-1} + v_k. \tag{13}$$

Owing to $\widetilde{x}_{k|k-1}$ is unbiased, $E[e_k] = 0$ and $E[\widetilde{y}_k] = \overline{H}_kE[\overline{d}_k]$. So, we can obtain an unbiased estimate of the virtual unknown input $\overline{d}_k$ from $\widetilde{y}_k$.

Theorem 1. *Suppose $\widehat{x}_{k|k-1}$ is unbiased; then, (6) and (7) calculate the unbiased value of $\overline{d}_k$ if and only if $\overline{M}_k$ satisfies $\overline{M}_k\overline{H}_k = I_{r_k}$.*

Proof. This process is similar to the proof of Theorem 1 in [16], so it is omitted.

From Theorem 1, $\operatorname{rank}(\overline{H}_k) = r_k$ is a necessary and sufficient condition for an unbiased virtual unknown input estimator of form (7). The matrix $\overline{M}_k = (\overline{H}^T_k\overline{H}_k)^{-1}\overline{H}^T_k$ corresponding to the least-squares (LS) solution of (12) satisfies Theorem 1. But from the Gauss–Markov theorem, the LS solution is not necessarily minimum-variance as a result of

$$\widetilde{R}_k \triangleq E\left[e_ke^T_k\right] = C_kP^x_{k|k-1}C^T_k + R_k \neq cI, \tag{14}$$

where c is a positive real number. □

3.2.2. MVU Virtual Unknown Input Estimation. An MVU estimate of $\overline{d}_k$ is calculated by weighted LS (WLS) estimation.

Theorem 2. *Let $\widehat{x}_{k|k-1}$ be unbiased, and let $\widetilde{R}_k$ and $\overline{H}^T_k\widetilde{R}^{-1}_k\overline{H}_k$ be nonsingular; then, for*

$$\overline{M}^*_k = \left(\overline{H}^T_k\widetilde{R}^{-1}_k\overline{H}_k\right)^{-1}\overline{H}^T_k\widetilde{R}^{-1}_k, \tag{15}$$

(4) is the MVU estimator of $\overline{d}_k$. The variance of the optimal virtual unknown input estimate is

$$P^{*\overline{d}}_{k|k} = \left(\overline{H}^T_k\widetilde{R}^{-1}_k\overline{H}_k\right)^{-1}. \tag{16}$$

Proof. This process is similar to the proof of Theorem 2 in [16], so it is omitted.

We use $\widehat{\overline{d}}^*_{k|k}$ to express the optimal virtual unknown input estimate corresponding to $\overline{M}^*_k$ and let $\widetilde{\overline{d}}^*_k \triangleq \overline{d}_k - \widehat{\overline{d}}^*_{k|k}$. Then, $\widetilde{\overline{d}}^*_k$ is given by

$$\widetilde{\overline{d}}^*_k = \left(I - \overline{M}^*_k\overline{H}_k\right)\overline{d}_k - \overline{M}^*_ke_k = -\overline{M}^*_ke_k. \tag{17}$$

□

3.3. Measurement Update. In the last step, we use measurement y_k to update $\widehat{x}_{k|k-1}$. Using (8) and (12), we find that

$$\widetilde{x}_{k|k} = (I - \overline{L}_kC_k)\widetilde{x}_{k|k-1} - \overline{L}_k\overline{H}_k\overline{d}_k - \overline{L}_kv_k. \tag{18}$$

Consequently, (8) is unbiased for all $\overline{d}_k$ if and only if $\overline{L}_k$ contents

$$\overline{L}_k\overline{H}_k = 0. \tag{19}$$

Suppose $\overline{L}_k$ satisfy (19), from (18):

$$P^x_{k|k} = (I - \overline{L}_kC_k)P^x_{k|k-1}(I - \overline{L}_kC_k)^T + \overline{L}_kR_k\overline{L}^T_k. \tag{20}$$

So, we can calculate $\overline{L}_k$ by minimizing the trace of (20) under the unbiasedness constraint of (19).

Theorem 3. *$\overline{L}_k$ is given by*

$$\overline{L}_k^* = K_k^*\left(I - \overline{H}_k\overline{M}_k^*\right), \tag{21}$$

where $K_k^* = P_{k|k-1}^x C_k^T \widetilde{R}_k^{-1}$ minimizes the trace of (20) under the constraint of (19).

Proof. This process is similar to the proof of Theorem 3 in [16], so it is omitted.

We use $\widehat{x}_{k|k}^*$ to express the state estimate corresponding to $\overline{L}_k^*$. From (7) and (21),

$$\widehat{x}_{k|k}^* = \widehat{x}_{k|k-1} + K_k^*\left(I - \overline{H}_k\overline{M}_k^*\right)\left(y_k - C_k\widehat{x}_{k|k-1}\right) = \widehat{x}_{k|k-1} + K_k^*\left(y_k - C_k\widehat{x}_{k|k-1} - \overline{H}_k\widehat{\overline{d}}_{k|k}^*\right). \tag{22}$$

Then, we consider the expressions of $P_{k|k}^{*x} \triangleq E[\widetilde{x}_{k|k}^*\widetilde{x}_{k|k}^{*T}]$ and $P_{k|k}^{*x\overline{d}} \triangleq E[\widetilde{x}_{k|k}^*\widetilde{\overline{d}}_k^{*T}]$, where

$$\widetilde{x}_{k|k}^* \triangleq x_k - \widehat{x}_{k|k}^* = \left(I - \overline{L}_k^* C_k\right)\widetilde{x}_{k|k-1} - \overline{L}_k^* v_k. \tag{23}$$

From (20) and (21), we obtain

$$P_{k|k}^{*x} = P_{k|k-1}^x - K_k^*\left(\widetilde{R}_k - \overline{H}_k P_{k|k}^{*\overline{d}}\overline{H}_k^T\right)K_k^{*T}. \tag{24}$$

Using (23) and (17), it follows that

$$P_{k|k}^{*x\overline{d}} = -P_{k|k-1}^x C_k^T\overline{M}_k^{*T} = -K_k^*\overline{H}_k P_{k|k}^{*\overline{d}}. \tag{25}$$

Furthermore, by $\widehat{d}_{k|k} = T_k^+\widehat{\overline{d}}_{k|k}$, we can get

$$P_{k|k}^d = T_k^+ P_{k|k}^{*\overline{d}}\left(T_k^+\right)^T P_{k|k}^{x\,d} = \left(P_{k|k}^{dx}\right)^T = -\overline{K}_k\overline{H}_k P_{k|k}^{*\overline{d}}\left(T_k^+\right)^T. \tag{26}$$

□

3.4. Summary of NRTSF-DF Equations. In order to reflect NRTSF-DF clearly, summarize it as follows:

3.4.1. Time Update. Based on the unbiased estimates $\widehat{d}_{k-1|k-1}$ and $\widehat{x}_{k-1|k-1}$, the state estimates and corresponding variance matrix from the time instant $k-1$ to k are obtained:

$$\begin{aligned}\widehat{x}_{k|k-1} &= A_{k-1}\widehat{x}_{k-1|k-1} + G_{k-1}\widehat{d}_{k-1|k-1},\\ P_{k|k-1}^x &= \begin{bmatrix} A_{k-1} & G_{k-1}\end{bmatrix}\begin{bmatrix} P_{k-1|k-1}^x & P_{k-1|k-1}^{x\,d}\\ P_{k-1|k-1}^{dx} & P_{k-1|k-1}^d\end{bmatrix}\begin{bmatrix} A_{k-1}^T\\ G_{k-1}^T\end{bmatrix} + Q_{k-1}.\end{aligned} \tag{27}$$

3.4.2. Estimation of Virtual Unknown Input. Calculate the rank of H_k, make full rank decomposition of H_k, and calculate the virtual unknown input estimates $\widehat{\overline{d}}_{k|k}$ and corresponding variance matrix at time instant k:

$$\begin{aligned}\widetilde{R}_k &= C_k P_{k|k-1}^x C_k^T + R_k,\\ \overline{M}_k &= \left(\overline{H}_k^T\widetilde{R}_k^{-1}\overline{H}_k\right)^{-1}\overline{H}_k^T\widetilde{R}_k^{-1},\\ \widehat{\overline{d}}_{k|k} &= \overline{M}_k\left(y_k - C_k\widehat{x}_{k|k-1}\right),\\ P_{k|k}^{\overline{d}} &= \left(\overline{H}_k^T\widetilde{R}_k^{-1}\overline{H}_k\right)^{-1}.\end{aligned} \tag{28}$$

3.4.3. Measurement Update. Calculate the state estimate $\widehat{x}_{k|k}$ and corresponding variance matrix at time instant k:

$$\begin{aligned}K_k &= P_{k|k-1}^x C_k^T\widetilde{R}_k^{-1},\\ \overline{L}_k &= K_k\left(I - \overline{H}_k\overline{M}_k\right),\\ \widehat{x}_{k|k} &= \widehat{x}_{k|k-1} + \overline{L}_k\left(y_k - C_k\widehat{x}_{k|k-1}\right),\\ P_{k|k}^x &= P_{k|k-1}^x - K_k\left(\widetilde{R}_k - \overline{H}_k P_{k|k}^{\overline{d}}\overline{H}_k^T\right)K_k^T,\\ P_{k|k}^{x\overline{d}} &= \left(P_{k|k}^{\overline{d}x}\right)^T = -K_k\overline{H}_k P_{k|k}^{\overline{d}},\\ \widehat{d}_{k|k} &= T_k^+\widehat{\overline{d}}_{k|k},\\ P_{k|k}^d &= T_k^+ P_{k|k}^{\overline{d}}\left(T_k^+\right)^T,\\ P_{k|k}^{x\,d} &= \left(P_{k|k}^{dx}\right)^T = -K_k\overline{H}_k P_{k|k}^{\overline{d}}\left(T_k^+\right)^T.\end{aligned} \tag{29}$$

Also, note that if H_k is of full column rank, letting $\overline{H}_k = H_k$ and $T_k = I_m$, RTSF is obtained.

4. NRTSF

If $H_k = 0$, systems (1) and (2) are transformed into a linear discrete-time-varying system without direct feedthrough of unknown input to output. It can be expressed as

$$x_k = A_{k-1}x_{k-1} + G_{k-1}d_{k-1} + w_{k-1}, \tag{30}$$

$$y_k = C_k x_k + v_k. \tag{31}$$

The classical filter proposed by Gilljins and De Moor in [15] can solve the state estimation problem when $H_k = 0$, but the application conditions to use this filter are that the unknown input distribution matrix G_{k-1} in the system equation must meet $\operatorname{rank}(G_{k-1}) = m, k = 1, 2, \ldots$.

When the unknown input distribution matrix is not of full column rank, that is, $\operatorname{rank}(G_{k-1}) = r_k < m$, then the classical filter cannot be used. Similar to Section 3, we can also consider an NRTSF design method. The following is the NRTSF derivation process.

If $\operatorname{rank}(G_{k-1}) = r_k \le m$, perform full rank decomposition:

$$G_{k-1} = \overline{G}_{k-1}T_{k-1}, \tag{32}$$

where $\overline{G}_{k-1} \in R^{n\times r_k}, T_{k-1} \in R^{r_k\times m}$, and $\operatorname{rank}(\overline{G}_{k-1}) = \operatorname{rank}(T_{k-1}) = r_k$. The full rank decomposition steps are given in Appendix.

Defining the virtual unknown input by $\overline{d}_{k-1} = T_{k-1} d_{k-1}$, then $G_{k-1} d_{k-1} = \overline{G}_{k-1} \overline{d}_{k-1}$. Because the unknown input is estimated with one step delay, the estimation value of $\overline{d}_{k-1}$ is expressed as $\hat{\overline{d}}_{k-1|k}$ and the minimal norm estimation value of the unknown input d_{k-1} is

$$\hat{d}_{k-1|k} = T_{k-1}^{+} \hat{\overline{d}}_{k-1|k}, \tag{33}$$

where T_{k-1}^{+} is the Moore–Penrose inverse of T_{k-1}. Then, original system equation (30) is rewritten as

$$x_k = A_{k-1} x_{k-1} + \overline{G}_{k-1} \overline{d}_{k-1} + w_{k-1}, \tag{34}$$

where $\overline{d}_{k-1} \in R^{r_k}$ is the virtual unknown input vector.

Based on the system state equation (34) and output equation (31), we consider NRTSF of the form

$$\hat{x}_{k|k-1} = A_{k-1} \hat{x}_{k-1|k-1}, \tag{35}$$

$$\hat{\overline{d}}_{k-1|k} = \overline{M}_k \left(y_k - C_k \hat{x}_{k|k-1} \right), \tag{36}$$

$$\hat{x}_{k|k} = \hat{x}_{k|k-1} + \overline{L}_k \left(y_k - C_k \hat{x}_{k|k-1} \right), \tag{37}$$

where the matrices $\overline{M}_k \in R^{r_k \times p}$ and $\overline{L}_k \in R^{n \times p}$ still have to be determined. Compared with the previous section, the obvious difference is that the second step in NRTSF calculates the value of virtual unknown input $\overline{d}_{k-1|k}$, while the previous filter yields an estimate of virtual unknown input $\overline{d}_{k|k}$.

4.1. Time Update. Let $\hat{x}_{k-1|k-1}$ express the optimal unbiased estimates of x_{k-1} given measurement sequence $\{y_0, y_1, \ldots, y_{k-1}\}$; then, the time update is

$$\hat{x}_{k|k-1} = A_{k-1} \hat{x}_{k-1|k-1}. \tag{38}$$

Similarly, the covariance matrix of $\hat{x}_{k|k-1}$ is given by

$$P_{k|k-1}^{x} \triangleq A_{k-1} P_{k-1|k-1}^{x} A_{k-1}^{T} + Q_{k-1}, \tag{39}$$

with $P_{k|k}^{x} \triangleq E[\tilde{x}_{k|k} \tilde{x}_{k|k}^{T}]$, $\tilde{x}_{k|k} \triangleq x_k - \hat{x}_{k|k}$.

4.2. Virtual Unknown Input Estimation. The derivation idea in this section is the same as Section 3.2 except that the time index of unknown input is different.

4.2.1. Unbiased Virtual Unknown Input Estimation. Defining the innovation $\tilde{y}_k \triangleq y_k - C_k \hat{x}_{k|k-1}$, it follows from (31), (34), and (35) that

$$\tilde{y}_k = C_k \overline{G}_{k-1} \overline{d}_{k-1} + e_k, \tag{40}$$

where e_k is given by

$$e_k = C_k \left(A_{k-1} \tilde{x}_{k-1|k-1} + w_{k-1} \right) + v_k. \tag{41}$$

Due to the fact that $\hat{x}_{k|k-1}$ is unbiased, we can obtain an unbiased estimate of the virtual unknown input $\overline{d}_{k-1}$ from $\tilde{y}_k$.

Theorem 4. *Suppose $\hat{x}_{k-1|k-1}$ is unbiased; then, (35) and (36) calculate the unbiased value of $\overline{d}_{k-1}$ if and only if $\overline{M}_k$ satisfies $\overline{M}_k C_k \overline{G}_{k-1} = I_{r_k}$.*

Proof. This process is similar to the proof of Theorem 1, so it is omitted.

The matrix corresponding to the LS solution of (40) satisfies Theorem 4. But from the Gauss–Markov theorem, it is not necessarily minimum-variance as a result of

$$\begin{aligned} \tilde{R}_k &\triangleq E\left[e_k e_k^{T} \right] = C_k \left(A_{k-1} P_{k-1|k-1}^{x} A_{k-1}^{T} + Q_{k-1} \right) C_k^{T} + R_k \\ &= C_k P_{k|k-1}^{x} C_k^{T} + R_k \neq cI, \end{aligned} \tag{42}$$

where c is a positive real number. □

4.2.2. MVU Virtual Unknown Input Estimation. Through weighted LS estimation, we obtain an MVU estimate of $\overline{d}_{k-1}$.

Theorem 5. *Let $\hat{x}_{k-1|k-1}$ be unbiased and let $\tilde{R}_k$ and $F_k^{T} \tilde{R}_k^{-1} F_k$ be positive definite; then, for*

$$\overline{M}_k = \left(F_k^{T} \tilde{R}_k^{-1} F_k \right)^{-1} F_k^{T} \tilde{R}_k^{-1}, \tag{43}$$

where $F_k \triangleq C_k \overline{G}_{k-1}$, (33) is the MVU estimator of $\overline{d}_{k-1}$. The variance of the corresponding input estimate is

$$P_{k-1|k}^{\overline{d}} = \left(F_k^{T} \tilde{R}_k^{-1} F_k \right)^{-1}. \tag{44}$$

Proof. This process is similar to the proof of Theorem 2, so it is omitted. □

4.3. Measurement Update. First, the estimator must satisfy $E[\hat{x}_{k|k} - x_k] = 0$, which can be expressed as

$$E\left[\hat{x}_{k|k-1} + \overline{L}_k \left(C_k A_{k-1} x_{k-1} + C_k \overline{G}_{k-1} \overline{d}_{k-1} + C_k w_{k-1} + v_k - C_k \hat{x}_{k|k-1} \right) - A_{k-1} x_{k-1} - \overline{G}_{k-1} \overline{d}_{k-1} - w_{k-1} \right] = 0. \tag{45}$$

Consequently, (37) is unbiased for all possible $\overline{d}_{k-1}$ if and only if $\overline{L}_k$ satisfies

$$\overline{L}_k C_k \overline{G}_{k-1} - \overline{G}_{k-1} = 0. \tag{46}$$

Let $\overline{L}_k$ satisfy (46); then, $P_{k|k}^{x}$ is given by

$$\begin{aligned} P_{k|k}^{x} &= \left(I - \overline{L}_k C_k \right) \left(A_{k-1} P_{k-1|k-1}^{x} A_{k-1}^{T} + Q_{k-1} \right) \left(I - \overline{L}_k C_k \right)^{T} + \overline{L}_k R_k \overline{L}_k^{T} \\ &= \overline{L}_k \tilde{R}_k \overline{L}_k^{T} - P_{k|k-1}^{x} C_k^{T} \overline{L}_k^{T} - \overline{L}_k C_k P_{k|k-1}^{x} + P_{k|k-1}^{x}. \end{aligned} \tag{47}$$

So, we can calculate $\overline{L}_k$ by minimizing the trace of (47) under the unbiasedness constraint of (46).

Theorem 6. *$\overline{L}_k$ is given by*

$$\overline{L}_k = K_k + (I - K_k C_k)\overline{G}_{k-1}\overline{M}_k, \tag{48}$$

where $K_k = P^x_{k|k-1}C_k^T\widetilde{R}_k^{-1}$ minimizes the trace of (47) under the constraint of (46).

Proof. This process is similar to the proof of Theorem 3, so it is omitted.

Substituting (48) in (37) yields the equivalent state update:

$$\widehat{x}_{k|k} = \widehat{x}_{k|k-1} + \left[K_k + (I - K_k C_k)\overline{G}_{k-1}\overline{M}_k\right]\left(y_k - C_k\widehat{x}_{k|k-1}\right). \tag{49}$$

Form (47) and (48),

$$P^x_{k|k} = P^x_{k|k-1} - K_k\widetilde{R}_k K_k^T + (I - K_k C_k)\overline{G}_{k-1}P^{\overline{d}}_{k-1|k}\overline{G}_{k-1}^T(I - K_k C_k)^T. \tag{50}$$

□

4.4. Summary of NRTSF Equations

4.4.1. Time Update. Based on the unbiased estimates $\widehat{x}_{k-1|k-1}$, the state estimates and corresponding variance matrix from time instant $k-1$ to k are obtained:

$$\begin{aligned} \widehat{x}_{k|k-1} &= A_{k-1}\widehat{x}_{k-1|k-1}, \\ P^x_{k|k-1} &= A_{k-1}P^x_{k-1|k-1}A_{k-1}^T + Q_{k-1}. \end{aligned} \tag{51}$$

4.4.2. Estimation of Virtual Unknown Input. Calculate the rank of G_{k-1}, make full rank decomposition of G_{k-1}, and calculate the virtual unknown input estimates $\widehat{\overline{d}}_{k-1|k}$ and corresponding variance matrix at time instant k:

$$\begin{aligned} \widetilde{R}_k &= C_k P^x_{k|k-1}C_k^T + R_k, \\ F_k &= C_k\overline{G}_{k-1}, \\ \overline{M}_k &= \left(F_k^T\widetilde{R}_k^{-1}F_k\right)^{-1}F_k^T\widetilde{R}_k^{-1}, \\ \widehat{\overline{d}}_{k-1|k} &= \overline{M}_k\left(y_k - C_k\widehat{x}_{k|k-1}\right), \\ P^{\overline{d}}_{k-1|k} &= \left(F_k^T\widetilde{R}_k^{-1}F_k\right)^{-1}. \end{aligned} \tag{52}$$

4.4.3. Measurement Update. Calculate the state estimate $\widehat{x}_{k|k}$ and corresponding variance matrix at time instant k:

$$\begin{aligned} K_k &= P^x_{k|k-1}C_k^T\widetilde{R}_k^{-1}, \\ \overline{L}_k &= K_k + (I - K_k C_k)\overline{G}_{k-1}\overline{M}_k, \\ \widehat{x}_{k|k} &= \widehat{x}_{k|k-1} + \overline{L}_k\left(y_k - C_k\widehat{x}_{k|k-1}\right), \\ P^x_{k|k} &= P^x_{k|k-1} - K_k\widetilde{R}_k K_k^T + (I - K_k C_k)\overline{G}_{k-1}P^{\overline{d}}_{k-1|k}\overline{G}_{k-1}^T(I - K_k C_k)^T, \\ \widehat{d}_{k-1|k} &= T^+_{k-1}\widehat{\overline{d}}_{k-1|k}. \end{aligned} \tag{53}$$

5. Example

In this section, we consider the state and unknown input estimation problem when the system is interfered by d_k as well as zero-mean Gaussian white noise. Specifically, the estimation problem we consider were given in Du [23]. The parameters for the linear system are given by

$$\begin{aligned} A &= \begin{bmatrix} 0.5 & 2 & 0 & 0 & 0 \\ 0 & 0.2 & 1 & 0 & 1 \\ 0 & 0 & 0.3 & 0 & 1 \\ 0 & 0 & 0 & 0.7 & 1 \\ 0 & 0 & 0 & 0 & 0.1 \end{bmatrix}, \\ G &= \begin{bmatrix} 1 & 0 & 0 \\ 0 & 0 & 0 \\ 0 & 1 & 0 \\ 0 & 0 & 0 \\ 0 & 0 & 0.1 \end{bmatrix}, \\ C &= I_5, \\ H &= \begin{bmatrix} 0 & 0 & 1 \\ 0 & 0 & 0 \\ 0 & 1 & 0 \\ 0 & 0 & 0 \\ 0 & 0 & 0 \end{bmatrix}, \\ R &= 10^{-2} \times \begin{bmatrix} 1 & 0 & 0 & 0.5 & 0 \\ 0 & 1 & 0 & 0 & 0.3 \\ 0 & 0 & 1 & 0 & 0 \\ 0.5 & 0 & 0 & 1 & 0 \\ 0 & 0.3 & 0 & 0 & 1 \end{bmatrix}, \\ Q &= 10^{-4} \times \begin{bmatrix} 1 & 0 & 0 & 0 & 0 \\ 0 & 1 & 0.5 & 0 & 0 \\ 0 & 0.5 & 1 & 0 & 0 \\ 0 & 0 & 0 & 1 & 0 \\ 0 & 0 & 0 & 0 & 1 \end{bmatrix}. \end{aligned} \tag{54}$$

The unknown input $d_k = [d_{1k}d_{2k}d_{3k}]^T$ used in this example is given in Figure 1.

The results of using NRTSF-DF to estimate the unknown input are presented in Figure 2. From Figure 2, NERTSF-DF can estimate the unknown inputs d_{2k}, d_{3k} but has no effect on d_{1k}. The reason is that the direct feedthrough matrix H_k is not of full column rank and, therefore, there is no information about the unknown input d_{1k} in the measurement.

Since the unknown input only affects the first three elements of the system state, we only plot the true value and estimated value of the first, second, and third element of state vector x_k in Figure 3. And the estimation errors of x_{1k}, x_{2k}, and x_{3k} are shown in Figure 4. It can be seen from the figure that the state estimation value can track the true value.

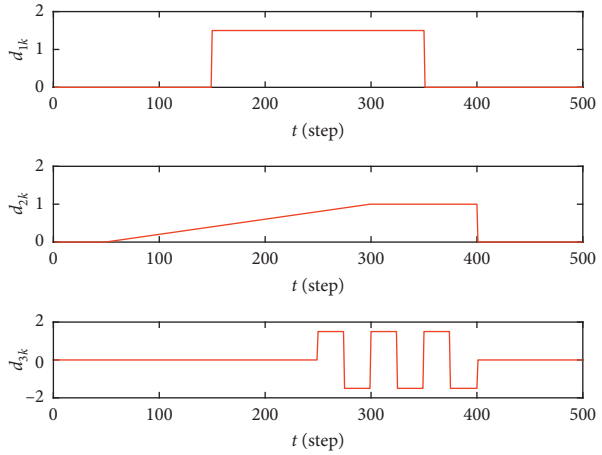

Figure 1: Actual values of the unknown input d_k.

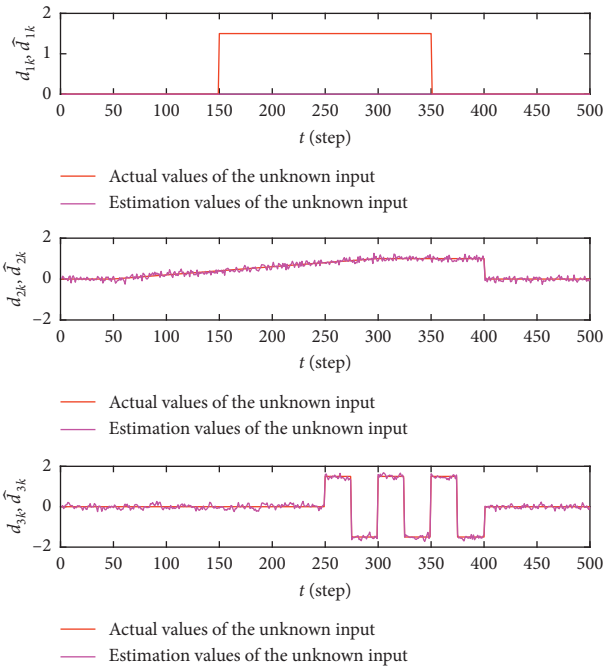

Figure 2: Estimation values of the unknown input d_k.

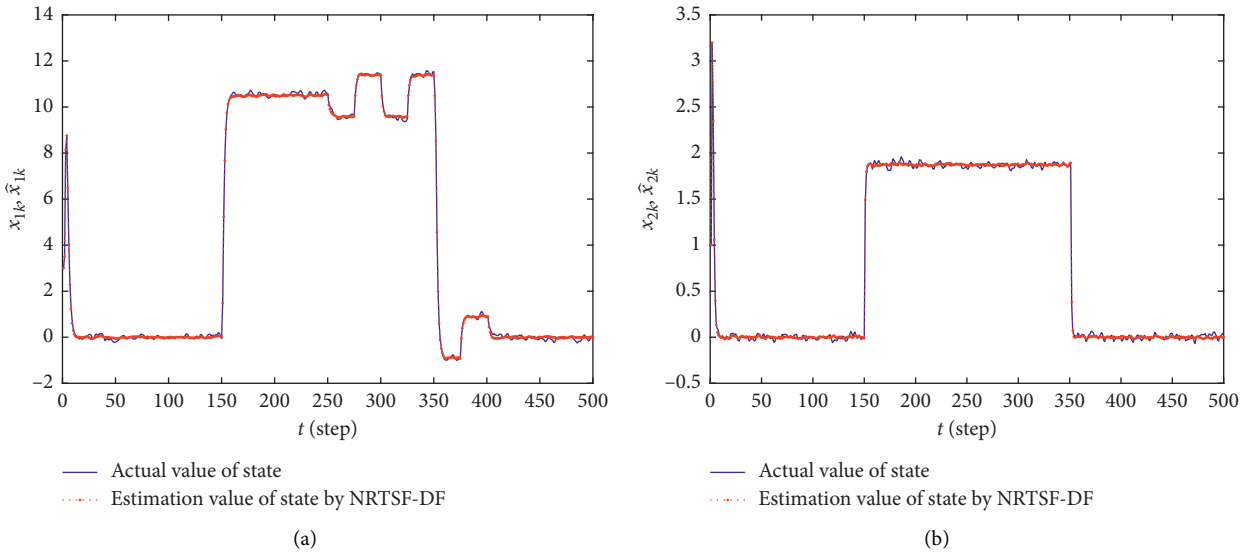

Figure 3: Continued.

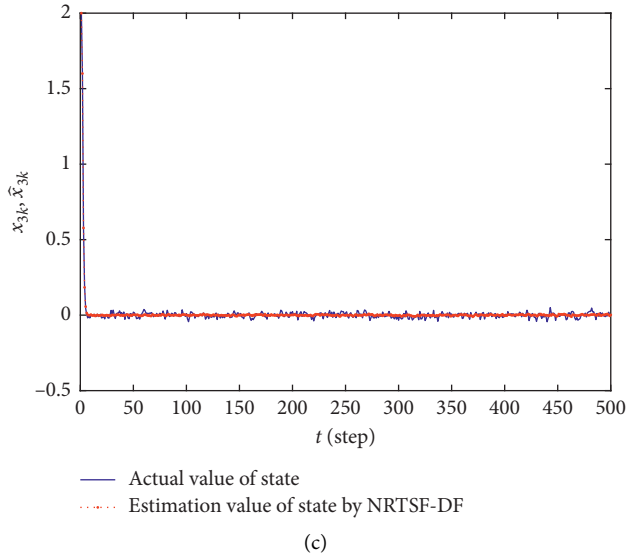

(c)

Figure 3: States and their estimations. (a) Estimation of state x_{1k}. (b) Estimation of state x_{2k}. (c) Estimation of state x_{3k}.

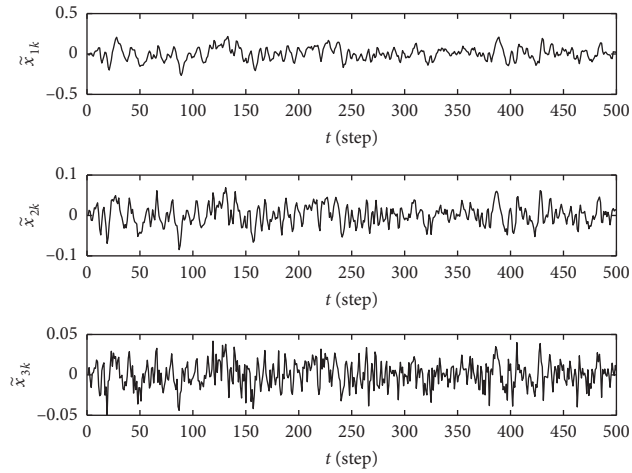

Figure 4: State estimation error.

For the linear system without direct feedthrough of unknown input to output, let $H = \begin{bmatrix} 0 & 0 & 0 \\ 0 & 0 & 0 \\ 0 & 0 & 0 \\ 0 & 0 & 0 \\ 0 & 0 & 0 \end{bmatrix}$ and $G = \begin{bmatrix} 1 & 0 & 0 \\ 0 & 0 & 0 \\ 0 & 1 & 0 \\ 0 & 0 & 0 \\ 0 & 0 & 0 \end{bmatrix}$; then, the system is transformed into a linear discrete system without direct feedthrough.

The results of using NRTSF to estimate the unknown input are shown in Figure 5. The NRTSF has no effect on d_{3k} because G_{k-1} is not of full column rank. And there is no information about the unknown input d_{3k} in the system state. Furthermore, there is no information about the d_{3k} in measurement.

Figures 6 and 7 show the true value, estimation value, and the estimation error of the first three elements of the state vector, respectively. From the figure, NRTSF is effective.

6. Conclusion

This paper discusses the problem of joint state and unknown input estimation for linear systems with an unknown input and proposes two novel filters, respectively, in accordance with the linear minimum-variance unbiased estimation criterion. For systems with direct feedthrough, a novel recursive three-step filter with direct feedthrough is proposed. This filter can solve the problem that the classical recursive three-step filter cannot be used when the unknown input distribution matrix is not of full column rank. For the situation that unknown input only affects system equation and the distribution matrix is not of full column rank, a novel

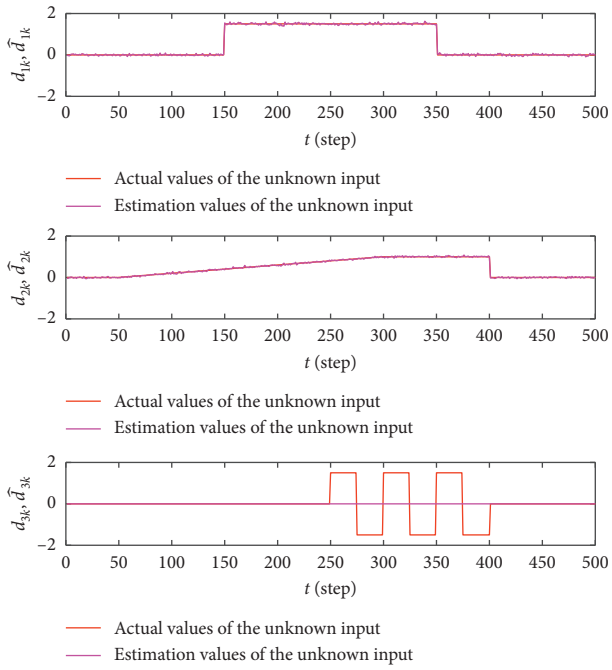

Figure 5: Estimation values of the unknown input d_k.

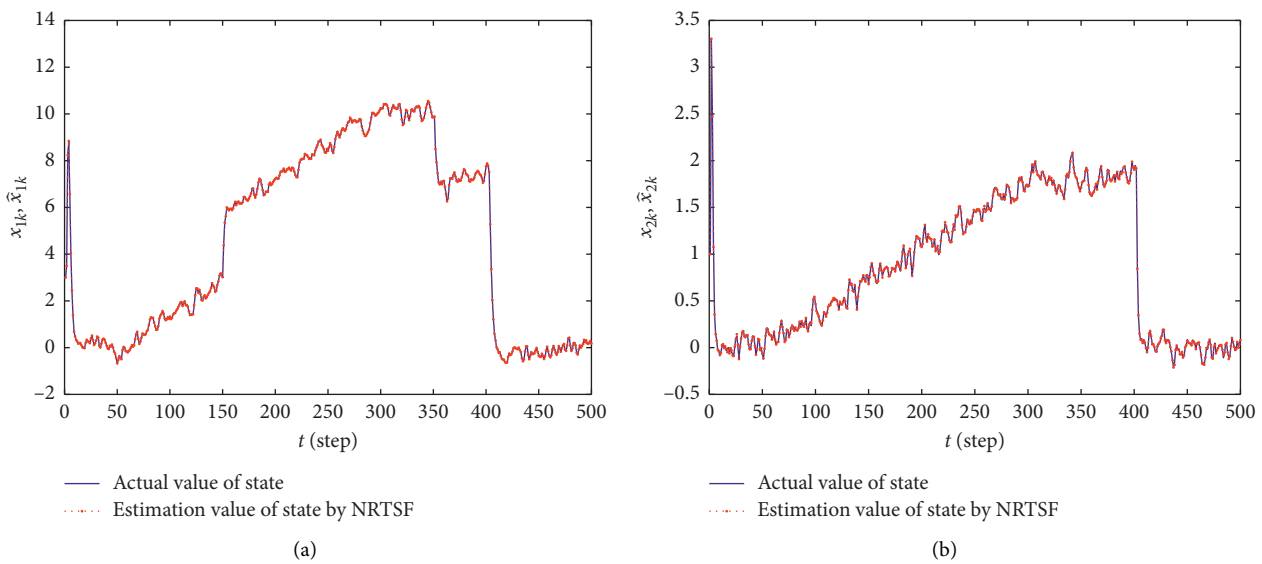

Figure 6: Continued.

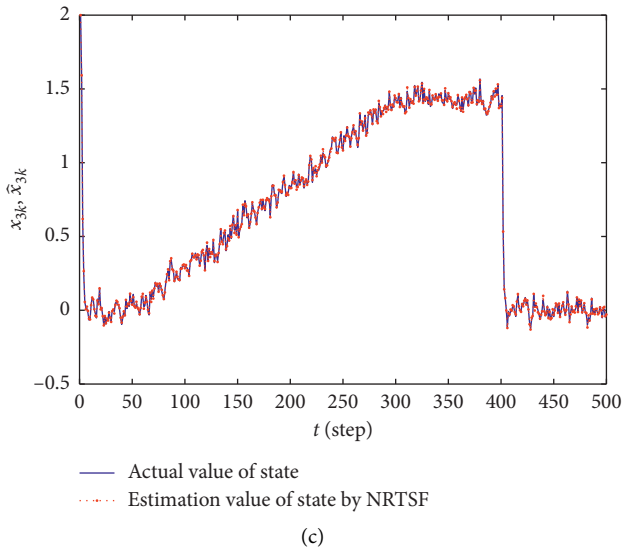

(c)

Figure 6: States and their estimations. (a) Estimation of state x_{1k}. (b) Estimation of state x_{2k}. (c) Estimation of state x_{3k}.

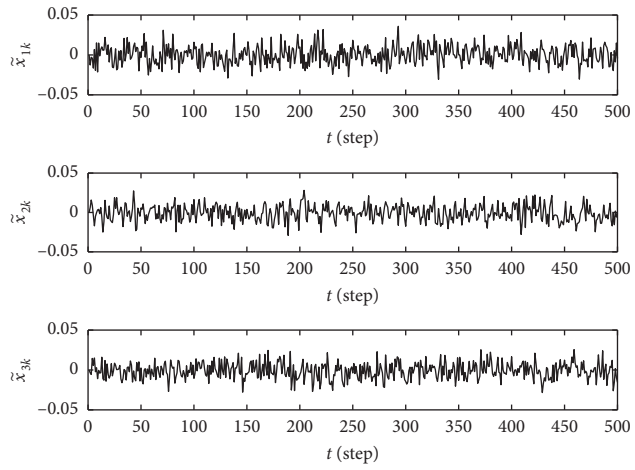

Figure 7: State estimation error.

recursive three-step filter is proposed. The simulation results show that both of the proposed filters can effectively estimate the unknown input and system state.

Appendix

There is a known matrix $H_k \in R^{p\times m}$. If $\text{rank}(H_k) = r_k < m$, then there is r_k order subformula in H_k, and the determinant of the subformula is nonzero. By swapping rows and columns of the matrix H_k, the subformula is located at the subblock $\tilde{H}_{11}$ of $\tilde{H}_k = \begin{bmatrix} \tilde{H}_{11} & \tilde{H}_{12} \\ \tilde{H}_{21} & \tilde{H}_{22} \end{bmatrix}$, while the rank of $\tilde{H}_k$ is equal to the rank of H_k. Since the r_k order subblock is nonsingular, the matrix $\tilde{H}_k$ can be expressed as

$$\tilde{H}_k = \begin{bmatrix} \tilde{H}_{11} \\ \tilde{H}_{21} \end{bmatrix} \begin{bmatrix} I & \tilde{H}_{11}^{-1}\tilde{H}_{12} \end{bmatrix}. \tag{A.1}$$

In other words, there are nonsingular matrices $D_k \in R^{p\times p}$ and $F_k \in R^{m\times m}$ satisfying

$$D_k H_k F_k = \begin{bmatrix} \tilde{H}_{11} \\ \tilde{H}_{21} \end{bmatrix} \begin{bmatrix} I & \tilde{H}_{11}^{-1}\tilde{H}_{12} \end{bmatrix}. \tag{A.2}$$

And then,

$$H_k = D_k^{-1} \begin{bmatrix} \tilde{H}_{11} \\ \tilde{H}_{21} \end{bmatrix} \begin{bmatrix} I & \tilde{H}_{11}^{-1}\tilde{H}_{12} \end{bmatrix} F_k^{-1} = \overline{H}_k T_k, \tag{A.3}$$

where $\overline{H}_k = D_k^{-1} \begin{bmatrix} \tilde{H}_{11} \\ \tilde{H}_{21} \end{bmatrix}$ and $T_k = \begin{bmatrix} I & \tilde{H}_{11}^{-1}\tilde{H}_{12} \end{bmatrix} F_k^{-1}$ are nonsingular matrices of rank r_k.

Data Availability

The data used to support the findings of this study are given in [23].

Conflicts of Interest

The authors declare that they have no conflicts of interest.

Acknowledgments

This research was supported by the National Natural Science Foundation of China (61703221) and the Shandong Provincial Natural Science Foundation Project (ZR2016FP10).

References

[1] R. E. Kalman, "A new approach to linear filtering and prediction problems," *Journal of Basic Engineering*, vol. 82, no. 1, pp. 35–45, 1960.

[2] P. K. Kitanidis, "Unbiased minimum-variance linear state estimation," *Automatica*, vol. 23, no. 6, pp. 775–778, 1987.

[3] Z. Gao, "On the centrality of disturbance rejection in automatic control," *ISA Transactions*, vol. 53, no. 4, pp. 850–857, 2014.

[4] L. Guo and S. Cao, "Anti-disturbance control theory for systems with multiple disturbances: a survey," *ISA Transactions*, vol. 53, no. 4, pp. 846–849, 2014.

[5] M. Darouach, M. Zasadzinski, and S. J. Xu, "Full-order observers for linear systems with unknown inputs," *Institute of Electrical and Electronics Engineers Transactions on Automatic Control*, vol. 39, no. 3, pp. 606–609, 1994.

[6] M. Hou and P. C. Muller, "Design of observers for linear systems with unknown inputs," *Institute of Electrical and Electronics Engineers Transactions on Automatic Control*, vol. 37, no. 6, pp. 871–875, 1992.

[7] P. Kudva, N. Viswanadham, and A. Ramakrishna, "Observers for linear systems with unknown inputs," *Institute of Electrical and Electronics Engineers Transactions on Automatic Control*, vol. 25, no. 1, pp. 113–115, 1980.

[8] M. Hou and R. J. Patton, "Input observability and input reconstruction," *Automatica*, vol. 34, no. 6, pp. 789–794, 1998.

[9] Y. Xiong and M. Saif, "Unknown disturbance inputs estimation based on a state functional observer design," *Automatica*, vol. 39, no. 8, pp. 1389–1398, 2003.

[10] B. Friedland, "Treatment of bias in recursive filtering," *Institute of Electrical and Electronics Engineers Transactions on Automatic Control*, vol. 14, no. 4, pp. 359–367, 1969.

[11] A. T. Alouani, T. R. Rice, and W. D. Blair, *A Two-Stage Filter for State Estimation in the Presence of Dynamical Stochastic Bias*, in *Proceedings of the 1992 American Control Conference*, pp. 1784–1788, Chicago, IL, USA, January 1992.

[12] M. Darouach and M. Zasadzinski, "Unbiased minimum variance estimation for systems with unknown exogenous inputs," *Automatica*, vol. 33, no. 4, pp. 717–719, 1997.

[13] M. Darouach, M. Zasadzinski, and M. Boutayeb, "Extension of minimum variance estimation for systems with unknown inputs," *Automatica*, vol. 39, no. 5, pp. 867–876, 2003.

[14] C. S. Hsieh, "Robust two-stage Kalman filters for systems with unknown inputs," *Institute of Electrical and Electronics Engineers Transactions on Automatic Control*, vol. 45, no. 12, pp. 2374–2378, 2000.

[15] S. Gillijns and B. De Moor, "Unbiased minimum-variance input and state estimation for linear discrete-time systems," *Automatica*, vol. 43, no. 1, pp. 111–116, 2007.

[16] S. Gillijns and B. De Moor, "Unbiased minimum-variance input and state estimation for linear discrete-time systems with direct feedthrough," *Automatica*, vol. 43, no. 5, pp. 934–937, 2007.

[17] Y. Cheng, H. Ye, Y. Wang, and D. Zhou, "Unbiased minimum-variance state estimation for linear systems with unknown input," *Automatica*, vol. 45, no. 2, pp. 485–491, 2009.

[18] C.-S. Hsieh, "Extension of unbiased minimum-variance input and state estimation for systems with unknown inputs," *Automatica*, vol. 45, no. 9, pp. 2149–2153, 2009.

[19] D. Varshney, M. Bhushan, and S. C. Patwardhan, "State and parameter estimation using extended Kitanidis Kalman filter," *Journal of Process Control*, vol. 76, pp. 98–111, 2019.

[20] M. Xiao, Y. Zhang, Z. Wang, and H. Fu, "An adaptive three-stage extended Kalman filter for nonlinear discrete-time system in presence of unknown inputs," *Isa Transactions*, vol. 75, pp. 101–117, 2018.

[21] W. Kai, F. Xiao, R. Jun et al., "State of charge (SOC) estimation of lithium-ion battery based on adaptive square root unscented kalman filter," *International Journal of Electrochemical Science*, vol. 15, no. 9, pp. 9499–9516, 2020.

[22] Z. Luo, H. Fang, and Y. Luo, "Constrained state estimation for nonlinear systems with unknown input," *Circuits, Systems, and Signal Processing*, vol. 32, no. 5, pp. 2199–2211, 2013.

[23] T. Du, *Research on Anti-disturbance Filter Theory and its Application in Polarization Integrated Navigation System*, Southeast University, Nanjing, China, 2016.

Hindawi
Mathematical Problems in Engineering
Volume 2020, Article ID 6654368, 11 pages
https://doi.org/10.1155/2020/6654368

Research Article

Underwater Terrain-Aided Navigation Relocation Method in the Arctic

Yanji Liu,[1] **Guichen Zhang**,[1] **and Chidong Che**[2]

[1]*Merchant Marine College, Shanghai Maritime University, Shanghai 201306, China*
[2]*State Key Laboratory of Ocean Engineering, Shanghai Jiao Tong University, Shanghai 200240, China*

Correspondence should be addressed to Yanji Liu; liuyanji@tongji.edu.cn

Received 31 October 2020; Revised 3 December 2020; Accepted 13 December 2020; Published 29 December 2020

Academic Editor: Kai Wang

To solve the localization failure problem of terrain-aided navigation (TAN) system of the autonomous underwater vehicle (AUV) caused by large area of underwater flat terrain in the Arctic, a navigation system with relocation part is constructed to enhance the robustness of localization. The system uses particle filter to estimate the AUV's position and reduce the nonlinear noise disturbance, and the prior motion information is added to avoid the mismatching caused by the similar altitude of low-resolution map. Based on the estimate data and the measured altitude data, the normalized innovation square (NIS) is used to evaluate the differentiation of terrain sequence, and the differentiation is used as a judgment of whether the AUV is in the switch location. A simulation experiment is carried out on the 500 m resolution underwater map of the Arctic. The results show that adding the prior motion information can restrain the divergence of the estimator; NIS can accurately reflect the sharp change of terrain sequence. After the relocation process, the AUV can still maintain the positioning accuracy within 2 km after running 50 km in the area including flat and rough terrain. This research solves the problem of localization errors in the Arctic flat terrain in the system level and provides a solution for the application of underwater navigation in the Arctic.

1. Introduction

The Arctic region has a vast water area and rich natural resources. However, the ice and snow covered on the surface of the water have hindered the application of GPS in the Arctic underwater navigation, reduced the large-scale navigation ability of underwater vehicles in Arctic waters, and increased the difficulty of underwater information collection [1, 2]. In addition, the limited energy carried by AUV limits the use of high-power navigation equipment. Although there are many research on the efficient utilization of batteries and controllers [3–6], low-power navigation mode is still needed for AUV continuous operating under a large area of Arctic ice. TAN uses the real-time altitude information to match the prior DEM (digital elevation map) and obtains the optimal calculated position through the optimization estimation method [7–9]. Since it is not necessary to deploy external auxiliary sensors to obtain global positioning reference posture, only a prior DEM and a low-power sensor which obtaining altitude are needed. With these advantages, TAN technology has been widely used [10–12].

TAN was first used in cruise missiles and has been widely used in underwater navigation [13, 14]. The early TAN system mainly used terrain contour matching (TERCOM) technology to obtain positioning information through altitude dataset matching. TERCOM technology is relatively mature, but it cannot effectively deal with process noise and observation noise [15, 16]. Among the three common regression filtering methods, Kalman filter [17, 18], point mass filter [19, 20], particle Filter (PF) [21, 22], Kalman filter requires the observation to be Gaussian distribution; it is not suitable for the application in non-Gaussian parameter situation. The point mass filter can solve the expression of

non-Gaussian observations, but it needs to calculate the whole posterior distribution space, which requires a large amount of calculation. Compared with point mass filter, the PF method has less computation and has a resampling mechanism to maintain the diversity of sampling and can deal with the ubiquitous nonlinear noise, which has been widely used [23–27]. Georgios [28] used the PF method to build the TAN system and carried out a long-range navigation accuracy test in the Southern Ocean. Based on the DEM with the resolution of 50 m, the positioning accuracy of TAN is within 200 m in multiple tests when the average moving distance of AUV is greater than 100 km, which can meet the needs of accurate positioning of underwater vehicles in a large-range operation.

The DEM of TAN and the underwater altitude detected by AUV both have noise disturbance, which will affect the positioning accuracy [29]. In extreme cases, when the noise disturbance is very large or when the terrain environment changes, it will lead to the failure of positioning. The commonly solutionis is to use the hypothesis-test method to calculate the confidence level of the state estimate HUGIN AUV uses the chi-square test method to estimate the confidence degree of the system and then makes a trade-off for the TAN estimation value [30].

At present, the resolution of the Arctic underwater DEM is only 500 m [31], and the low-resolution map has a large error with large noise, which affects the estimation of the location of AUV [32]. Salavasidis et al. [33] utilize the bilinear interpolation method to improve the resolution of the map, but it cannot eliminate the map noise. In addition, there are more flat terrain areas in the Arctic terrain, and the flat terrain with few features reduces the positioning ability of TAN, which leads to positioning failure. At present, there are many methods to improve the accuracy in a flat area; Aringnonsen and Hagen [34] utilize the pockmarks in the flat terrain as a sign to improve the positioning accuracy. Enns and Morrell [35] utilize the Viterbi algorithm to calculate the Bayesian dataset to obtain the most likely position of the present motion. Shandor and Stephen [36] adjusting the measurement variance to eliminate the over matching position and reducing the mismatching in the flat area. But more generally, in a large area of flat area, the deviation and matching value of altitude in all directions are similar.

When an AUV moves from a flat area to a rough terrain area, a robot kidnapping problem occurs. In the robot kidnapping problem, timing of triggering relocation is important [37]. In terrain aided navigation, it is necessary to accurately determine the switch location of flat terrain and rough terrain. Variance analysis can be used to distinguish the planeness of terrain, and the NIS method can produce more accurate results [38, 39]. Houts et al. [40] used the NIS window to estimate the confidence of PF filtering results and judge the change of terrain according to the confidence. The results show that the NIS window filtering method can effectively reduce the impact of noise disturbance and can accurately positioning the abnormal. By improving the weight distribution of PF and optimizing the likelihood function, the robustness of the system can be enhanced and the influence of flat terrain can be reduced slightly, but the positioning error caused by large flat terrain still cannot be solved [41, 42].

To eliminate positioning errors in the TAN system caused by the large area of flat terrain in the Arctic, this paper proposes a TAN positioning framework with the relocation system. The NIS is used to construct the confidence evaluation item to accurately judge the moment when AUV enters the rough area. Based on the accumulated navigation data and the sampled altitude data in the flat area, the relocation function is constructed, and the relocation process ensures the convergence of the TAN system when it leaves the flat area and ensures the accuracy of TAN positioning in a large scale. In addition, in order to solve the problem of low-resolution map causing low-terrain differentiation in a large area, a priori motion information enhancement method is applied to improve the calculation of weight to improve the accuracy of positioning estimation.

2. PF Position Estimation System

We use PF to estimate the AUV location; the essence is to use PF to correct the position on the basis of dead reckoning. This paper focuses on the positioning ability of TAN system in the horizontal plane. Therefore, the simplified two-dimensional AUV kinematic model is constructed as the basis of dead reckoning. In this paper, the sequential importance sampling and resampling (SISR) algorithm is selected as the filter of the TAN system to estimate the position of AUV.

2.1. AUV Kinematics. As shown in Figure 1, it is a 3-DOF kinematic coordinate system of AUV in the horizontal plane [43]. [v and w] are the velocity and angular velocity of AUV relative to the body coordinate, [x, y, and θ] is the pose of AUV relative to the global coordinate, and $|v/w|$ is the radius of rotation of the AUV around its turning center. The kinematic model is shown in equation (1), in which the lower subscript t represents the moment of motion estimation, and Δt is the step interval time.

$$\begin{pmatrix} x_{t+1} \\ y_{t+1} \\ \theta_{t+1} \end{pmatrix} = \begin{pmatrix} x_t \\ y_t \\ \theta_t \end{pmatrix} + \begin{pmatrix} -\frac{v}{w}\sin\theta + \frac{v}{w}\sin(\theta + w\Delta t) \\ \frac{v}{w}\cos\theta - \frac{v}{w}\sin(\theta + w\Delta t) \\ w\Delta t \end{pmatrix}. \quad (1)$$

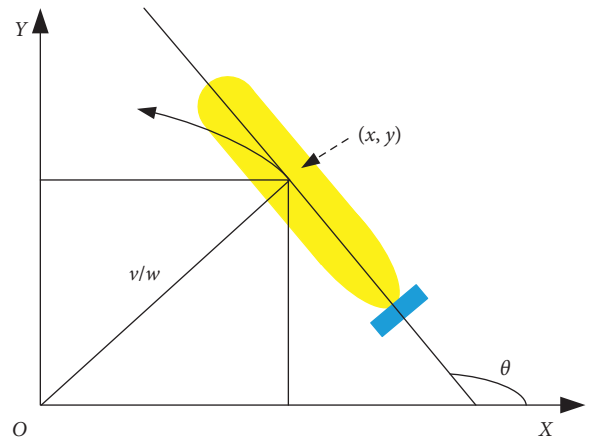

Figure 1: Three degrees of freedom of AUV kinematics.

The movement of AUV is mainly affected by two kinds of disturbance: one is the fluctuation of control input $[v, w]$ caused by the noise of airborne sensors such as inertial navigation and depth gauge; the other is caused by external factors such as ocean current and water density. Therefore, process noise can be divided into body noise and environmental noise, as equations (2) and (3) show, where $\sum_p$ is body noise covariance, $\sum_e$ is external noise covariance, the superscript $\wedge$ represents the state with noise, N represents the normal distribution, a_i, $(i = 1, 2, 3, 4)$ is constant coefficient, σ_x^2 is variance in x direction, and σ_y^2 is variance in y direction.

$$\sum_p = \begin{pmatrix} \hat{v} \\ \hat{w} \end{pmatrix} = \begin{pmatrix} v \\ w \end{pmatrix} + \begin{pmatrix} N\left(0, a_1 v^2 + a_2 w^2\right) \\ N\left(0, a_3 v^2 + a_4 w^2\right) \end{pmatrix}, \tag{2}$$

$$\sum_e = \begin{pmatrix} \hat{x} \\ \hat{y} \end{pmatrix} = \begin{pmatrix} x \\ y \end{pmatrix} + \begin{pmatrix} N\left(0, \sigma_x^2\right) \\ N\left(0, \sigma_y^2\right) \end{pmatrix}. \tag{3}$$

2.2. Prior Information Enhanced PF(PIEPF) Algorithm

2.2.1. SISR PF Algorithm. In this paper, the widely used SISR algorithm is used for positioning estimation [44]. There are many descriptions of SISR algorithm in the research literature. Here, the logic is briefly summarized. PF uses random distribution to approximate the probability density function of the system; by iterative calculation, the minimum variance estimation of the system state is obtained; PF can solve the state estimation problem of nonlinear system and is widely used. The SISR algorithm is shown in Table 1, where x is state variable, ω is particle weights, y is observation measurements, N are the number of particles, the upper subscript i is the particle index, and the lower subscript k is the time dimension.where $p(y_k|x_k^i)$ is the likelihood function of observations and can be expressed as

$$p\left(y_k|x_k^i\right) = \frac{1}{\sigma_y \sqrt{2\pi}} e^{-1/2\left(y_k^i - y_k/\sigma_y\right)^2}, \tag{4}$$

where σ_y is observation variance.

2.2.2. PIEPF. The low-resolution map results in similar terrain altitude in local area, and only using the observation value cannot effectively distinguish the difference of particles, which leads to the divergence of filtering. Combining the prior information of AUV motion and reasonably considering the influence of stable Arctic current, the particle weight including prior motion information is calculated as formula (4).

$$\omega_k^i = \omega_{k-1}^i p\left(y_k|x_k^i\right) p\left(x_k^i|x_{k-1}^i\right), \tag{5}$$

where $p(x_k^i \mid x_{k-1}^i)$ is the likelihood function of prior motion and can be expressed as

$$p\left(x_k^i|x_{k-1}^i\right) = \frac{1}{\sigma_x \sqrt{2\pi}} e^{-1/2\left(\mathrm{Dis}_k^i/\sigma_x\right)^2}, \tag{6}$$

where Dis_k^i is the Euclidean distance between each particle and the prior predicted position.

3. Relocation System

There are a large number of flat terrain areas without terrain features of the Arctic, which will lead to the divergence of TAN positioning. Although scholars have proposed a variety of methods to improve the positioning accuracy in the flat area, the improvement is limited, and it is not suitable for the Arctic with large flat terrain. In this paper, a TAN system with relocation item is designed. The system structure is shown in Figure 2. When the AUV moves from the flat area to the rough area and crosses the terrain junction point, the relocation flag is triggered.

In the process of relocation detection, the key item is to accurately determine the running area of AUV. However, the sensor and the prior DEM have large noise. Although the direct use of the measured altitude for comparative judgment is simple, it cannot eliminate the influence of noise, which is easy to cause misjudgment and positioning failure. NIS can evaluate the credibility of the measured values and reduce noise disturbance. When AUV operates in rough areas with rich terrain features or flat areas with less terrain

Table 1: Algorithm of SISR PF.

SISR PF
(1) $[\{x_k^i, \omega_k^i\}_{i=1}^N] = \text{SISR}[\{x_{k-1}^i, \omega_{k-1}^i\}_{i=1}^N, y_k, N]$
(2) FOR $i = 1: N$
(3) $x_k^i \sim p(x_k^i \mid x_{k-1}^i)$
(4) $\omega_k^i = \omega_{k-1}^i p(y_k \mid x_k^i)$
(5) END FOR
(6) $\text{S} = \text{SUM}[\{\omega_k^i\}_{i=1}^N]$
(7) FOR $i = 1: N$
(8) $\omega_k^i = \omega_k^i \text{S}^{-1}$
(9) END FOR
(10) $\{x_k^i, \omega_k^i\}_{i=1}^N = \text{RESAMPLE}[\{x_k^j, \omega_k^j\}_{j=1}^N]$

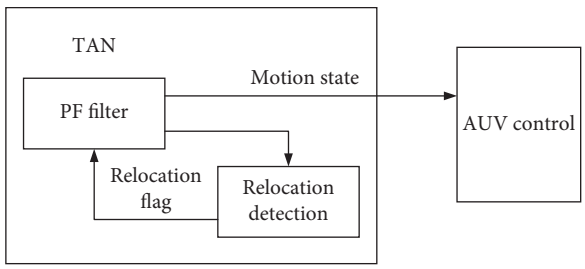

Figure 2: TAN system.

features, the measured values are close to the predicted values, and the NIS values are smaller. However, when the AUV enters the rough area from the flat area, the wrong estimated position will lead to a large difference between the measured value and the estimated value, resulting in a larger NIS value. In this paper, the NIS is used to construct a filtering window to estimate the confidence of observation; when NIS is greater than the threshold value, it indicates that the AUV enters the rough terrain from the flat terrain, which leads to the relocation process.

3.1. PF NIS. Innovation $\tilde{y}$ represents the difference between the measurements and the expected value as follows:

$$\tilde{y}_k = y_k - \mu_k, \tag{7}$$

where y is measurements, μ is expected value, low subscript k is the moment, and the expected value is the weighted average of altitude.

$$\mu_k = \sum_{m=1}^{M} \omega_k^m \hat{y}_k^m, \tag{8}$$

where $\hat{y}$ is the observations of particles and m is particle index.

Then, the variance of innovation S is

$$S_k = R_k + \sum_{m=1}^{M} \omega_k^m \left(\hat{y}_k^m - \mu_k\right)\left(\hat{y}_k^m - \mu_k\right)^T, \tag{9}$$

where R is observation variance.

The NIS can be expressed as

$$\text{NIS}_k = \tilde{y}_k^T S_k^{-1} \tilde{y}_k. \tag{10}$$

Different from variance, NIS is a dimensionless number, which represents the consistency between the distribution of new observations and the distribution of observations. The variance of NIS conforms to the chi-square distribution, so the reliability of the measurements can be judged. If the NIS value is relatively large, the measured value does not fall into a reasonable distribution range, which indicates that there is a big difference between the measurements and the predicted value. In order to further reduce the influence of abnormal measurements, the average value of NIS in a period of time is used as the evaluation basis,

$$\text{NIS}_k = \frac{1}{L} \sum_{i=K-L+1}^{K} \text{NIS}_i, \tag{11}$$

where L is time length.

3.2. Relocation Range. In order to illustrate the relocation ability of the TAN system, a simple sampling logic is used to realize the sampling after relocation. The method is to accumulate AUV running distance when the NIS value is credible. When the NIS value exceeds the threshold value, the accumulated distance is used as the basis of relocation range. Search for a similar sampling altitude within the relocation range to realize the sampling in the observation value. The logical is as follows:

Step 1: If the NIS value is less than the threshold, the AUV motion distance Dis is accumulated

Step 2: When the NIS value is abnormal, 1.5·Dis is set as the resampling radius and the present altitude value Hm_k is recorded

Step 3: Within the sampling range, num particles are uniformly distributed

Step 4: Calculating particles altitude Hs_k^i, when the difference between Hs_k^i and Hm_k is within the range of observation noise, the particle is preserved

After the above steps, resampling particles can be filtered out. After PF iteration, the particles in the wrong position will disperse rapidly, and the particles in the correct position can achieve good tracking.

4. Simulation

In this paper, simulation is used to verify the effectiveness of the proposed relocation logic. Based on the Arctic DEM of 500 m resolution, a local area close to Alaska in the United States is selected for the simulation study. The area contains rough terrain and flat terrain, which is convenient for comparative analysis.

4.1. Map Parameters. The map with longitude range (−180° and −168°) and latitude range (75° and 79°) is selected as the research area, as shown in Figure 3(a). In order to facilitate the analysis, the latitude and longitude map is transformed into the Cartesian coordinate system through scale conversion. The 3D terrain map is shown in Figure 3(b). The length, width, and height of the converted map are (800, 250, and −2.1) km, and the origin point of the map corresponds to longitude -180° and latitude 75°.

In this paper, the bilinear interpolation is used to refine the map altitude. The bilinear method is shown in the following equation:

$$f(x,y) = \frac{f(Q_{11})}{500^2}(x_2 - x)(y_2 - y) + \frac{f(Q_{21})}{500^2}(x - x_1)(y_2 - y) + \frac{f(Q_{12})}{500^2}(x_2 - x)(y - y_1) + \frac{f(Q_{22})}{500^2}(x - x_1)(y - y_1), \tag{12}$$

where $f(\cdot)$ is the altitude function, [x, y, and Q] is coordinate points, and the cross combination of [x_1 and x_2] and [y_1 and y_2] can form four corner coordinates [Q_{11}, Q_{12}, Q_{21}, and Q_{22}] around the point to be solved.

4.2. TAN Parameters. The parameter setting of the TAN system is shown in Table 2. In order to eliminate the disturbance of vertical motion, the AUV is set to run at a depth of 0 m, and in this situation, the observation noise is not a function of altitude but noise with a standard deviation of 5 m. The numerical value conforms to the characteristics of the acoustic altimeter. In order to fully explore the performance of the system, a current disturbance in Y direction of 0.1 m/s is added.

4.3. Results and Analyses. Figure 4 shows the positioning results of the TAN system in rough and flat terrain areas, respectively. The running time of each movement segment is set as 28 h, the running distance is 50 km, and the movement direction is 180°. It can be seen that although there is the current disturbance in Y direction, due to the rich terrain features, it has a good positioning results in the rough area. The estimated position calculated by TAN is very close to the reference path, and the average positioning error is within 1 km. In the flat terrain area, because of the lack of features, the TAN system cannot be accurately positioning, the movement path is random, and the positioning error is also divergent.

Figure 5 shows the comparison of path tracking error between PIEPF and ordinary PF. It can be seen that the overall tracking error of PIEPF is small and can effectively track the path. The PF method accurately tracks a certain distance and then diverges, which is caused by the similarity altitude of the low-resolution terrain. PIEPF method can track in the right direction with the aid of prior motion information.

Figure 6 shows the NIS values of TAN in different regions. It can be seen that the NIS values in the rough terrain area and flat terrain area are both within a 98% confidence interval. In the rough area, because of the accurate positioning, the observed altitude value is close to the predicted one, so the NIS value is small. In the flat terrain area, although it cannot be accurately located, because the altitude of the flat terrain area is close to the observation value, the difference is small, so the NIS value is small.

Figure 7 shows the positioning situation of AUV when moving from the flat area to rough area. When AUV is running in the flat area, due to lack of recognizable features, positioning fails, but the NIS value is kept within the credible range. When the AUV crosses the critical area and moves into the rough terrain area, there is a big deviation between the current measured altitude and the prior estimated one, which causes NIS anomaly. As can be seen from Figure 7(b), the NIS value increases rapidly and exceeds the trusted range.

Figure 8 shows the distribution of resampled particles and subsequent tracking and positioning. As shown in Figure 8(a), when the NIS value is abnormal, the cumulative distance of AUV is about 41 km, and the sampling radius is $1.5 \times 41 = 62$ km. Within the sampling radius of 62 km, 10,000 points are evenly sampled and 369 sampling points are finally accepted. Among them, 3 points are near the correct position and converge to the correct trajectory after PF iteration. Particles in other places diverge rapidly. Figure 8(b) shows the complete path, AUV loss in flat area, and when it reaches the rough area, it triggers relocation. After resampling, the AUV can return to the correct position.

5. Results

In this paper, we consider the characteristics of flat terrain and rough terrain in the Arctic region and use the NIS to trigger relocation, and the positioning failure caused by flat terrain is solved by relocation. The results show that the NIS value is sensitive to the area switching, which can accurately reflect the sharp change of terrain and can be used as a reliable judgment of the terrain area switching. In

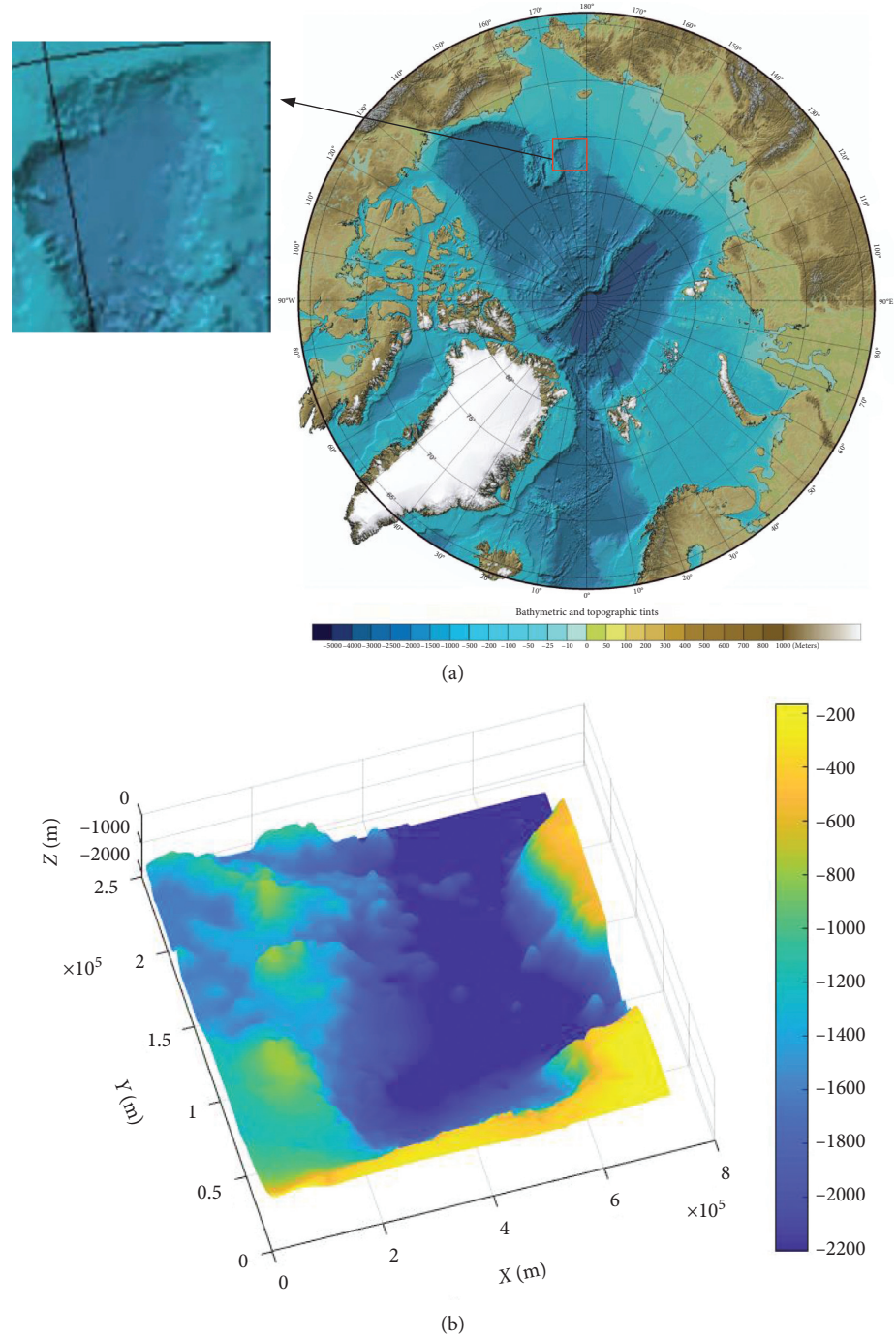

Figure 3: The terrain map of the research. (a) The selected area. (b) 3D DEM.

Table 2: Simulation parameters.

Parameters	Value
AUV velocity	0.5 m/s
Map resolution	500 m
Running depth	0 m
PF update frequency	1 Hz
Current disturbance (dx, dy)	(0,0.1 m/s)

Table 2: Continued.

Parameters	Value
Body noise (a_1, a_2, a_3, a_4)	$(0.1, 0.1, 0.001, 0.1)$
Process noise	6 m
Measurement noise	5 m
Particle numbers	1000
Initial attitude	(200 km, 100 km, 180°)(rough area), (500 km, 100 km, 180°)(flat area), and (290 km, 85 km, 180°)(flat-rough area)
NIS threshold THD_1	5.41 (98% confidence)
NIS time window L	20

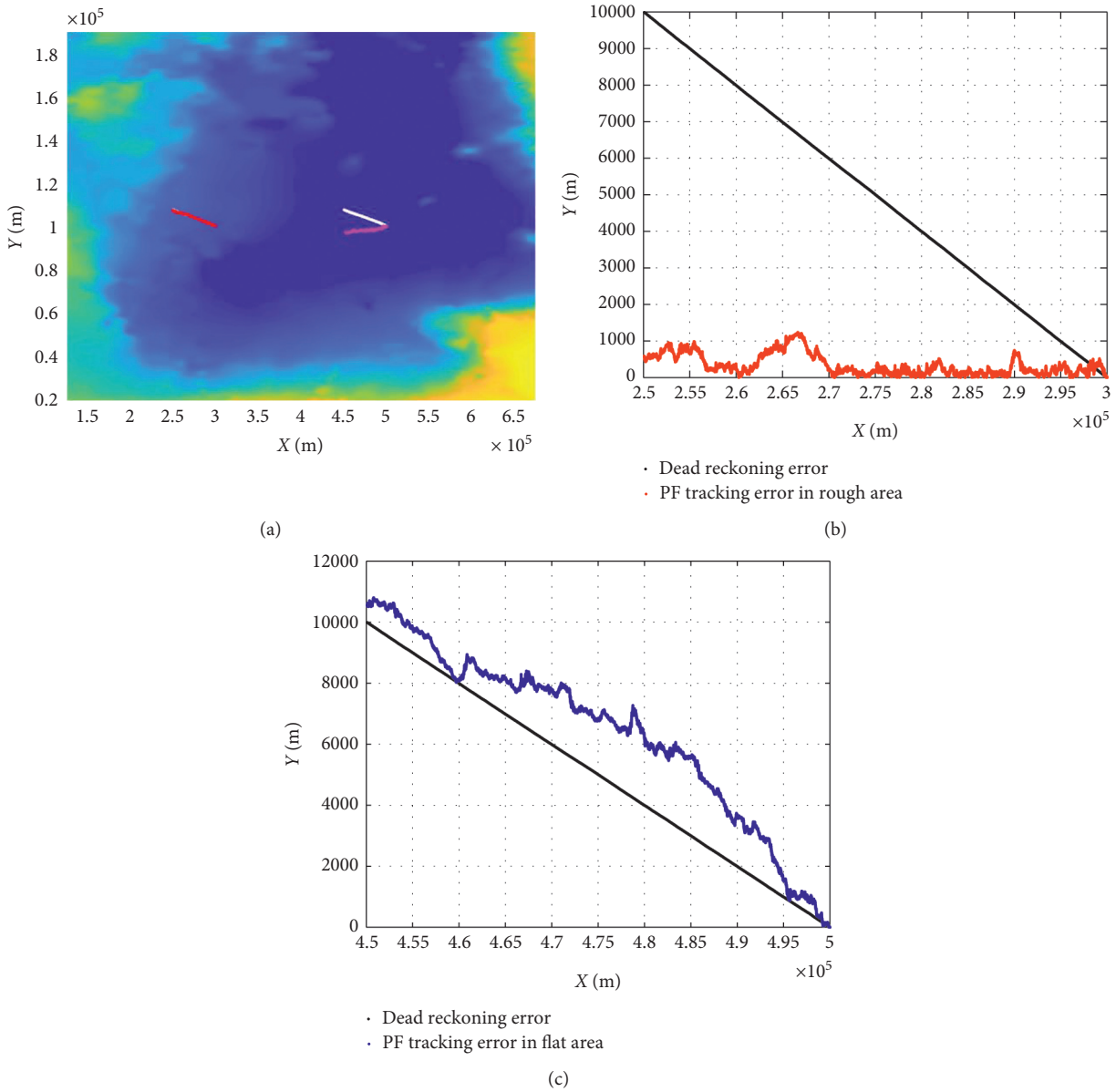

Figure 4: The localization results of TAN system in different terrain area. (a) TAN positioning path (the white path is the reference path, the red path is the positioning value in the rough area, and the pink path is the positioning value in the flat area). (b) Positioning error in rough area. (c) Positioning error in flat area.

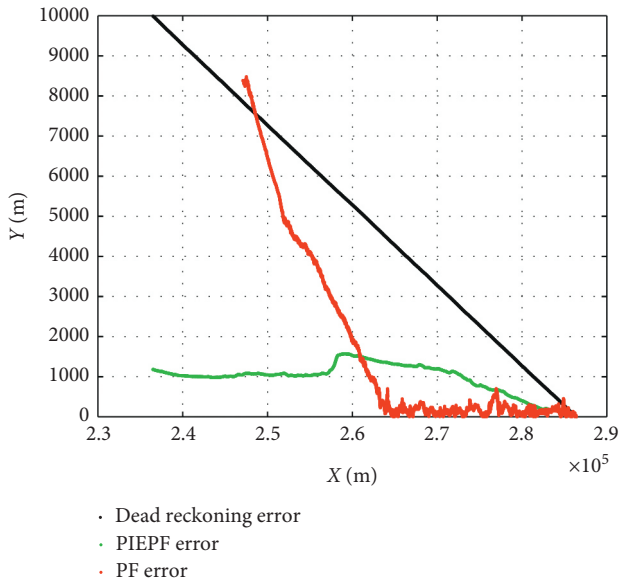

Figure 5: Tracking error of PIEPF and PF.

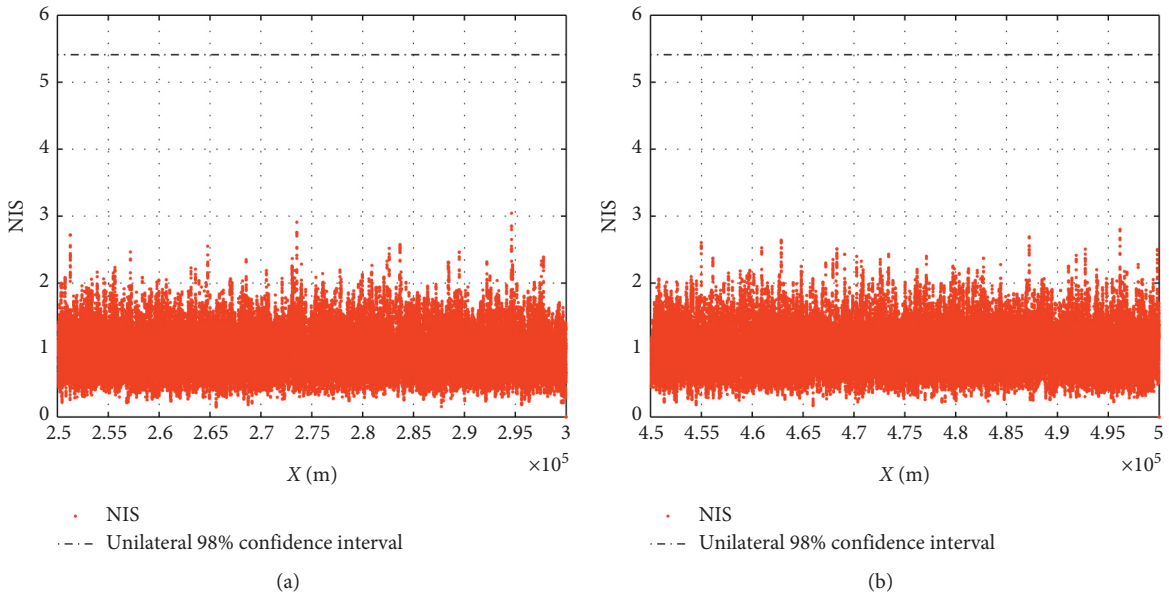

Figure 6: NIS values in different terrain area. (a) In rough area. (b) In flat area.

addition, on the basis of the PF framework, adding prior motion information can effectively avoid the divergence of filter, and the proposed method can be applied to underwater terrain aided navigation in the Arctic with a resolution of 500 m.

The following research will further explore the NIS value characteristics under the condition of large map interference, improve the resampling distribution function, and improve the performance of the TAN system.

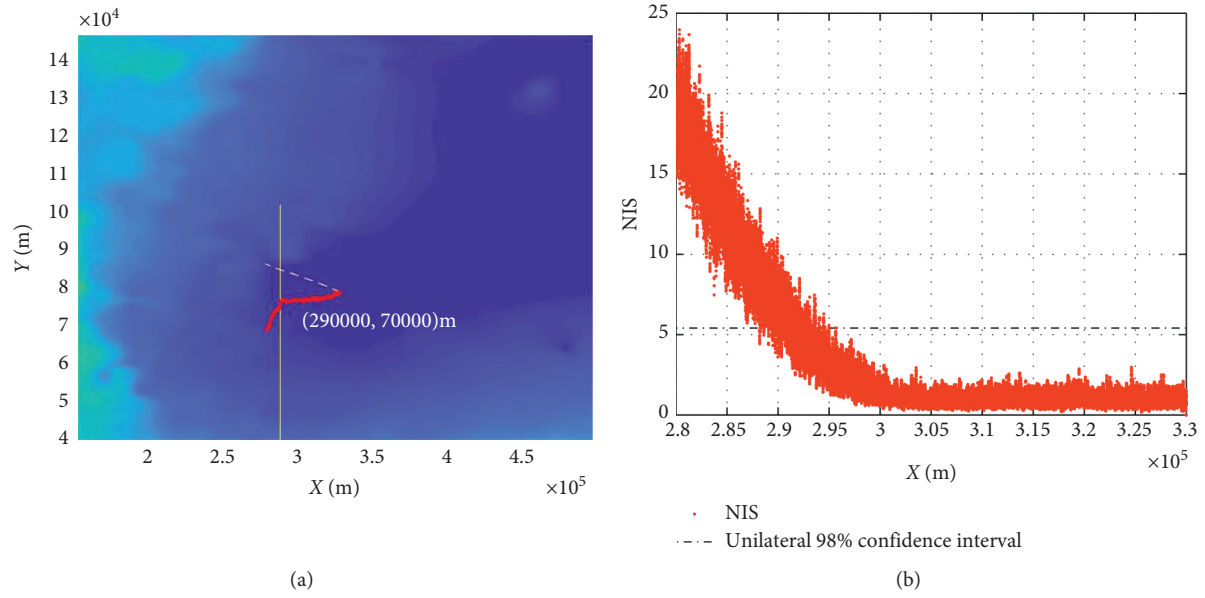

Figure 7: NIS outliers. (a) Movement path (the white dotted line represents the reference path, the red path is the actual positioning path, the intersection point of the yellow vertical line, and the red path is the critical position when entering the rough terrain). (b) NIS value.

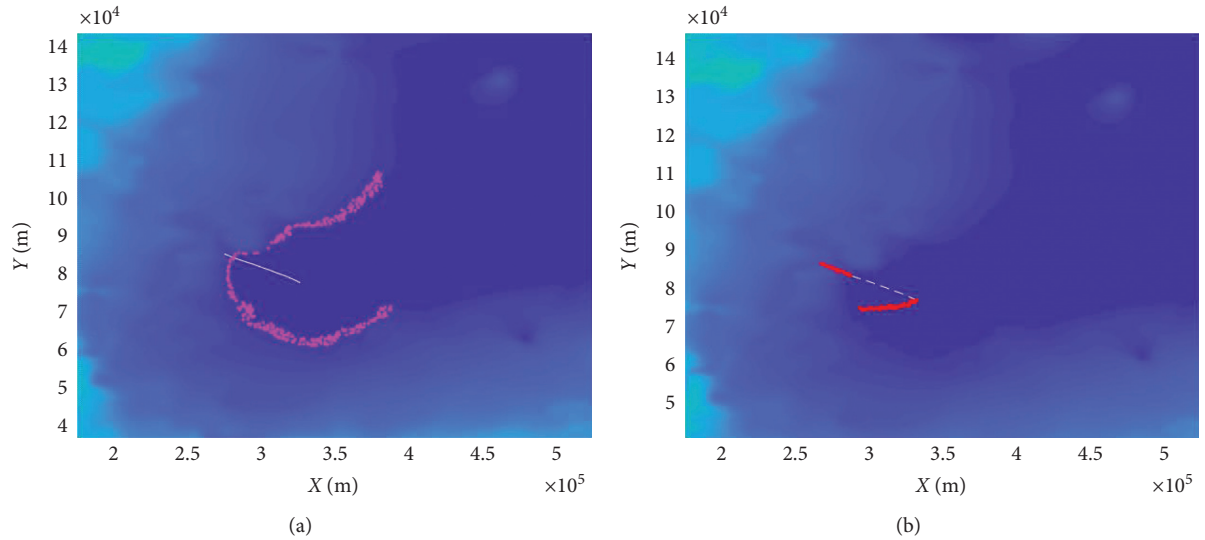

Figure 8: The tracking path of TAN system. (a) Resampling particles. (b) Tracking path.

Data Availability

The data used in this study are available from the corresponding author upon request.

Conflicts of Interest

The authors declare that they have no conflicts of interest.

Acknowledgments

This work was supported by the NSFC Projects of China under Grant no. 51779136 and Deep Blue Projects fund of Shanghai Jiao Tong University under Grant no. SL2020MS002.

References

[1] L. Ruotsalainen, V. Renaudin, and L. Pei, "Toward autonomous driving in Arctic areas," *IEEE Intelligent Transportation Systems Magazine*, vol. 12, no. 3, pp. 10–24, 2020.

[2] Q. Zhang, Z. Chen, Y. Cui et al., "A refined metric for multi-GNSS constellation availability assessment in polar regions," *Advances in Space Research*, vol. 66, no. 3, pp. 655–670, 2020.

[3] K. Wang, W. L. Wang, L. C. Wang et al., "An improved SOC control strategy for electric vehicle hybrid energy storage systems," *Energies*, vol. 13, no. 20, pp. 1–13, 2020.

[4] K. Wang, F. Xiao, J. B. Pang et al., "State of charge (SOC) estimation of Lithium-ion battery based on adaptive square root unscented kalman filter," *International Journal of Electrochemical Science*, vol. 15, no. 9, pp. 9499–9516, 2020.

[5] K. Wang, L. Li, Y. Lan, P. Dong, and G. Xia, "Application research of chaotic carrier frequency modulation technology in Two-Stage matrix converter," *Mathematical Problems in Engineering*, vol. 2019, Article ID 2614327, 8 pages, 2019.

[6] G. Xia, Y. Huang, F. Li et al., "A thermally flexible and multi-site tactile sensor for remote 3D dynamic sensing imaging," *Frontiers of Chemical Science and Engineering*, vol. 14, no. 6, pp. 1039–1051, 2020.

[7] M. Jose and M. Anibal, "Survey on advances on terrain based navigation for autonomous underwater vehicles," *Ocean Engineering*, vol. 139, pp. 250–264, 2017.

[8] Z. Song, H. Bian, and A. Zielinski, "Application of acoustic image processing in underwater terrain aided navigation," *Ocean Engineering*, vol. 121, pp. 279–290, 2016.

[9] D. Peng, T. Zhou, C. Xu, W. Zhang, and J. Shen, "Marginalized point mass filter with estimating tidal depth bias for underwater terrain-aided navigation," *Journal of Sensors*, vol. 2019, Article ID 7340130, 15 pages, 2019.

[10] E. J. Andrew and M. James, "Overview of terrain relative navigation approaches for precise lunar landing," in *Proceedings of the IEEE Aerospace Conference Proceedings*, Big Sky, MT, USA, March 2008.

[11] G. Salavasidis, A. Munafo, D. Fenucci et al., "Ultra-endurance AUVs: energy requirements and terrain-aided-navigation," *in Autonomous Underwater Vehicles: Design and Practice, The Institution of Engineering and Technology*, pp. 145–189, SciTech Publishing, Stevenage, UK, 2020.

[12] M. Christian, S. Bernard, B. Alexandre et al., "Terrain-aided navigation with an atomic gravimeter," in *Proceedings of the 2019 22th International Conference on Information Fusion (FUSION)*, Ottawa, Canada, July 2019.

[13] I. Nygren, "Robust and efficient terrain navigation of underwater vehicles," in *Proceedings of the IEEE/ION Position, Location and Navigation Symposium*, pp. 923–932, Monterey, CA, USA, May 2008.

[14] S. Carreno, P. Wilson, P. Ridao et al., "A survey on terrain based navigation for auvs," in *Proceedings of the IEEE OCEANS*, Seattle, WA, USA, September 2010.

[15] B. I. Korelitz and S. C Sommers, "Responses to drug therapy in ulcerative colitis. Evaluation by rectal biopsy and histopathological changes," *The American Journal of Gastroenterology*, vol. 64, no. 5, pp. 365–370, 1975.

[16] L. Zhao, N. Gao, B. Q. Nan et al., "A novel Terrain-aided Navigation algorithm combined with the TERCOM algorithm and particle filter," *IEEE Sensors Journal*, vol. 15, no. 2, pp. 1124–1131, 2015.

[17] L. Hostetler and R. Andreas, "Nonlinear Kalman Filtering techniques for terrain-aided navigation," *IEEE Transactions on Automatic Control*, vol. 28, no. 3, pp. 315–323, 1983.

[18] L. M. Downes, T. J. Steiner, and J. P. How, "Lunar terrain relative navigation using a convolutional neural network for visual crater detection," in *Proceedings of the 2020 American Control Conference*, pp. 4448–4453, Denver, CO, USA, July 2020.

[19] D. Meduna, *Terrain relative navigation for sensor-limited systems with application to underwater vehicles*, Stanford Univeristy, Stanford, CA, USA, 2011.

[20] Y.-g. Park and C. G. Park, "Two-Stage point mass filter on terrain referenced navigation for state augmentation," *Journal of Guidance, Control, and Dynamics*, vol. 43, no. 5, pp. 1003–1008, 2020.

[21] K. B. Anonsen and O. Hallingstad, "Terrain aided underwater navigation using point mass and particle filters," in *Proceedings of the IEEE/ION Position, Location, and Navigation Symposium*, Coronado, CA, USA, April 2006.

[22] A. Bachmann and S. B. Williams, "Terrain aided underwater navigation—a deeper insight into generic monte carlo localization," in *Proceedings of the Australasian Conference on Robotics and Automation*, Brisbane, Australia, 2003.

[23] J. Melo and A. Matos, "On the use of particle filters for terrain based navigation of sensor-limited AUVs," in *Proceedings of the MTS/IEEE Oceans'13 Conference*, Bergen, Norway, June 2013.

[24] R. P. Wang, Y. S. Chen, Y. Li et al., "High-precision initialization and acceleration of particle filter convergence to improve the accuracy and stability of terrain aided navigation," *ISA Transactions*, 2020, In press.

[25] C. Zhang, C. Guo, and D. Zhang, "Ship navigation via GPS/IMU/LOG integration using adaptive fission particle filter," *Ocean Engineering*, vol. 156, pp. 435–445, 2018.

[26] G. G. Rigatos, "Nonlinear kalman filters and particle filters for integrated navigation of unmanned aerial vehicles," *Robotics and Autonomous Systems*, vol. 60, no. 7, pp. 978–995, 2012.

[27] F. C. Teixeira, J. Quintas, and A. Pascoal, "AUV terrain-aided navigation using a Doppler velocity logger," *Annual Reviews in Control*, vol. 42, pp. 166–176, 2016.

[28] S. Georgios, M. Andrea, A. H. Catherine et al., "Terrain-aided navigation for long-endurance and deep-rated autonomous underwater vehicles," *Journal of Field Robotics*, vol. 36, no. 2, pp. 447–474, 2019.

[29] J. Lee, C. Sung, and S. Nam, "CRLB analysis for a robust TRN based on a combination of RNN and PF," *International Journal of Aeronautical and Space Sciences*, vol. 21, no. 1, pp. 265–276, 2020.

[30] B. A. Kjetil and K. H. Ove, "Recent developments in the HUGIN AUV terrain navigation system," in *Proceedings of the OCEANS'11 MTS/IEEE KONA*, Waikoloa, Hawaii, USA, September 2011.

[31] M. Jakobsson, L. Mayer, B. Coakley et al., "The international bathymetric chart of the arctic ocean (ibcao) version 3.0," *Geophysical Research Letters*, vol. 39, no. 12, pp. 1–6, 2012.

[32] D. Meduna, S. M. Rock, and R. McEwen, "Auv terrain relative navigation using coarse maps," in *Proceedings of the Unmanned Untethered Submersible Technology Conference*, Durham, NH, USA, August 2009.

[33] G. Salavasidis, A. Munafò, C. A. Harris, S. D. McPhail, E. Rogers, and A. B. Phillips, "Towards arctic AUV navigation," *IFAC-PapersOnLine*, vol. 51, no. 29, pp. 287–292, 2018.

[34] K. B. Aringnonsen and O. K. Hagen, "Terrain aided underwater navigation using pockmarks," in *Proceedings of the OCEANS 2009*, Biloxi, MS, USA, October 2009.

[35] R. Enns and D. Morrell, "Terrain-aided navigation using the viterbi algorithm," *Journal of Guidance, Control, and Dynamics*, vol. 18, no. 6, pp. 1444–1449, 1995.

[36] D. Shandor and R. Stephen, "Improving robustness of terrain-relative navigation for AUVs in regions with flat terrain," in *Proceedings of the IEEE/OES Autonomous Underwater Vehicles(AUV)*, Southampton, UK, September 2012.

[37] I. Bukhori and Z. H. Zool, "Detection of kidnapped robot problem in monte carlo localization based on the natural displacement of the robot," *International Jorunal of Advanced Robotic Systems*, vol. 14, no. 4, 2017.

[38] L. Cai, B. Boyacloglu, S. E. Webster et al., "Towards autotuning of kalman filters for underwater gliders based on consistency metrics," in *Proceedings of the OCEANS 2019*, Seattle, WA, USA, October 2019.

[39] A. J. Dean, J. W. Langelaan, and S. N. Brennan, "Improvements in terrain-based road vehicle localization by initializing an unscented kalman filter using particle filters," in *Proceedings of the 2010 American Control Conference*, pp. 700–707, Baltimore, MD, USA, July 2010.

[40] S. E. Houts, S. G. Dektor, and S. M. Rock, "A robust frame work for failure detection and recovery for terrain-relative navigation," in *Proceedings of the Unmanned Untethered Submersible Technology*, Portsmouth, NH, USA, September 2013.

[41] C. T. Francisico, Q. Joao, M. Pramod et al., "Robust particle filter formulations with application to terrain-aided navigation," *International Journal of Adaptive Control and Signal Processing*, vol. 31, pp. 608–651, 2017.

[42] D. Peng, T. Zhou, J. Folkesson, and C. Xu, "Robust particle filter based on Huber function for underwater terrain-aided navigation," *IET Radar, Sonar & Navigation*, vol. 13, no. 11, pp. 1867–1875, 2019.

[43] Y. J. Liu, G. C. Zhang, R. Lu et al., "Study on Particle Filter Based Terrain Aided Navigation under the Ultra-low Resolution Map of the Arctic," in *Proceedings of the 2020 39th Chinese Control Conference*, Shenyang, China, July 2020.

[44] C. T. Francisco, P. Antonio, and M. Pramod, "A novel particle filter formulation with application to terrain-aided navigation," *IFAC Proceedings Volumes*, vol. 45, no. 5, pp. 132–139, 2012.

Hindawi
Mathematical Problems in Engineering
Volume 2020, Article ID 6692547, 14 pages
https://doi.org/10.1155/2020/6692547

Research Article

Attitude Tracking of Rigid Spacecraft with Actuator Saturation and Fault Based on a Compound Control

Chunhua Cheng, Hang Yang, Qian Wang, Lin Li, Qiang Han, Huan Ouyang, Haiyang Ma, and Xinyi Lv

Qingdao Branch, Naval Aeronautic University, Qingdao 266041, China

Correspondence should be addressed to Chunhua Cheng; chch715@126.com

Received 29 October 2020; Revised 29 November 2020; Accepted 1 December 2020; Published 28 December 2020

Academic Editor: Jinyan Song

A compound control based on active disturbance rejection control (ADRC) scheme and slide mode control (SMC) is proposed to investigate the attitude tracking problem for a spacecraft with modeling uncertainties, external disturbances, actuator failures, and actuator saturations simultaneously. A positive term including control input is separated from the system, and then, the active disturbance rejection concept and the extended state observer (ESO) are applied to deal with the general uncertain item caused by uncertainties, external disturbances, actuator failures, and actuator saturations. The sliding mode surface is designed to transform the attitude tracking problem into attitude stabilization problem. In order to deal with the actuator saturations, a saturation degree coefficient and its corresponding adaptive law are introduced. Compared to other existing references, the proposed scheme does not need to know the structure or upper bound information of the inertial matrix uncertainties and external disturbances. Finally, the stability of the closed-loop system is analyzed by using input to state stability theory. Simulation results are given to verify the effectiveness of the proposed scheme. More importantly, the proposed technique can also be applied to the attitude stabilization of other aircraft, such as the attitude of unmanned aerial vehicle and helicopter in maritime rescue.

1. Introduction

With the development of space missions, the reliable control scheme is significantly important for the rigid spacecraft. As the part of spacecraft systems, attitude control plays an important role in spacecraft design and has been studied extensively under various scenarios [1–5]. The reliability of attitude control determines that the planned missions can be accomplished successfully or not. It is a significant challenge to obtain a steady attitude when there exist uncertainties, external disturbances, actuator failures, or saturations. However, lots of nonlinear control schemes are applied on attitude control in much literature. In [3, 4], an extended state observer sliding mode control (SMC) is proposed for spacecraft attitude control with inertia uncertainty and external disturbance. In [4, 5], the adaptive SMC is applied to attitude stabilization with control constraints. In the above adaptive SMC scheme, it is assumed that the inertia matrix and the external disturbance are bounded and satisfy certain conditions. In [6], two quasi-continuous higher-order sliding controllers are applied to spacecraft attitude-tracking. In [7], to alleviate chattering and ensure a smooth control for actuators by SMC, a second-order sliding mode controller based on anti-unwinding control method is proposed for the attitude stabilization of a rigid spacecraft. In [1], nonlinear H∞ robust controller is proposed for F-16 aircraft with mass and moment inertia uncertainties. To solve the associated Hamilton–Jacobi partial differential inequality, a special Lyapunov function with mass and moment inertia uncertainties is considered. A robust control law based on the mini-max approach and the inverse optimal approach is proposed for the attitude control with external disturbances [8]. In [9], the inverse optimal feedback control based on integrator backstepping is proposed for rigid spacecraft without considering the disturbances and uncertainties. The optimal adaptive controller is designed to achieve attitude tracking for rigid spacecraft [10]. To deal with the inertia matrix uncertainty and attenuate the

disturbance, both the adaptive control and the inverse optimal control approach are applied. However, the abovementioned controls are based on precise analytic structure of uncertainty to derive online updating algorithms for unknown but constant parameters in the system.

Actually, the inputs of spacecraft systems are usually limited, which are known as actuator saturation or input saturation. In practical systems, input saturation may lead to instability or unacceptable performance degradation for the spacecraft's attitude. To deal with the input saturation, lots of methods appeared [5, 11–15]. In [11], taking into account control input saturation, external disturbances, and parametric uncertainty, a variable structure control method is proposed for spacecraft attitude stabilization, which ensures the fast and accurate response. Thereafter, the continuous variable structure control approach is presented for attitude tracking [12]. In [13], two saturated finite-time attitude controllers based on the homogeneous method are proposed for rigid spacecraft subject to control input saturation, without considering the external disturbance and uncertainty. In [14], a saturated attitude control scheme composed of the quaternion part, the saturated angular velocity part, and the bounded antidisturbance part was proposed for spacecraft with bounded disturbances. In [15], two novel anti-unwinding attitude controllers based on the inverse optimal approach and unit quaternion are designed for spacecraft subject to uncertainty and external disturbance.

Note that the abovementioned references concentrate on the attitude control without actuator fault. In practice, besides the saturation, actuator failures also usually occur in spacecraft systems. As is known to all, control failures can lead to performance deterioration, instability, and even catastrophic accidents. Therefore, it is very important to design a controller with fault-tolerant capability to improve the spacecraft system reliability. In order to enhance the reliability of spacecraft systems, some scholars are focusing on fault-tolerant attitude control [16–19]. In [20], an adaptive fault-tolerant control method is proposed for the spacecraft subjected to two types of faults, without uncertainties and disturbances. In [16], an adaptive backstepping sliding mode control scheme is designed to achieve attitude tracking for flexible spacecraft with actuator failures, disturbances, and uncertainties. In [17], an adaptive fault-tolerant control based on the fuzzy logic system and sliding mode observers is presented for near-space vehicle without the bounds of the derivative of the faults. In [18], two integral-type sliding mode control schemes are used to compensate actuator faults for spacecraft with external disturbances.

However, as far as the authors know, few papers focus on the attitude control for the rigid spacecraft subjected to uncertainties, disturbances, failures, and actuator saturation simultaneously. In [2], a nonregression-based indirect robust approach is presented to achieve attitude tracking when accounting for uncertainties, disturbances, failures, and actuator saturation simultaneously. Although the uncertainty is done by its bound, it is assumed that the external disturbance and the inertia matrix are bounded and satisfy certain conditions. In [19], a variable structure control is developed for attitude stabilization of spacecraft with partial loss of actuator effectiveness fault and actuators saturation. Then, the authors proposed an adaptive sliding mode control for spacecraft subjected to partial loss of actuator effectiveness fault, and the control law is modified to ensure that the control signal never contains saturation [21]. The neural network is used to approximate uncertainties and online updating law to estimate the bound of actuator fault without any information of the fault. In [22], based on fuzzy logic and backstepping techniques, a robust adaptive control is proposed for spacecraft in the presence of uncertainties, disturbances, actuator failures, and input saturation. Actually, the spacecraft system with uncertainties, disturbances, actuator failures, and actuator saturation simultaneously is a more complicated uncertain nonlinear system, whose typical representative is a nonaffine nonlinear system. In [23–27], the active disturbance rejection technique presented in [28] is applied to the nonaffine nonlinear system. Therefore, in this paper, a compound control based on active disturbance rejection control (ADRC) scheme and slide mode control (SMC) is designed to achieve attitude tracking for the spacecraft system. To handle the saturation, the saturation coefficient is introduced and its adaptive law is designed. The main contribution of this paper compared to others is that the proposed scheme can achieve reliability against inertia matrix uncertainties, external disturbances, actuators faults, and saturation. Moreover, the actuator faults that the scheme can deal with by the proposed scheme include partial effectiveness loss fault, additive fault, and total fault. The proposed scheme does not depend on the precise analytic structure of inertia matrix and disturbances, nor depend on their bounds, which can also be applied in spacecraft systems with time-varying parameters.

This paper is organized as follows. The spacecraft attitude tracking problem and some preliminary results are described in Section 2. The compound control scheme is proposed to achieve the attitude tracking in Section 3. Several simulation results are presented in Section 4, and conclusions are drawn in Section 5.

2. Problem Formulation and Preliminaries

2.1. Attitude Dynamics. The mathematical models of the rigid spacecraft attitude dynamics are given by [2–4]

$$\mathbf{J}(t)\dot{\omega} = -\boldsymbol{\omega}^{\times}\mathbf{J}(t)\boldsymbol{\omega} + \mathbf{F}\mathbf{u} + \mathbf{d}(t), \tag{1}$$

$$\dot{q}_v = \frac{1}{2}\left(\mathbf{q}_v^{\times} + q_0\mathbf{I}_3\right)\boldsymbol{\omega}, \tag{2}$$

$$\dot{q}_0 = -\frac{1}{2}\mathbf{q}_v^{T}\boldsymbol{\omega}, \tag{3}$$

where $\mathbf{J}(t) \in \mathbf{R}^{3\times3}$ is the inertia matrix of the spacecraft determined by the mass distribution of the spacecraft, and obviously, it is symmetric positive definite. $\mathbf{u} \in \mathbf{R}^{3\times1}$ is the actual control torque generated by thrusters. $\mathbf{F} \in \mathbf{R}^{3\times1}$ is the thruster distribution matrix (for a given spacecraft, $\mathbf{F}$ is available and can be adjusted by changing the locations and directions of the thrusters [3]). $\mathbf{d}(t) \in \mathbf{R}^{3\times1}$ is the external

disturbance. $\mathbf{q} = [\mathbf{q}_v; q_0] \in \mathbf{R}^{4\times1}$ is the unit quaternion vector representing the spacecraft's attitude orientation, satisfying $\mathbf{q}_v^T\mathbf{q}_v + q_0^2 = 1$, where $\mathbf{q}_v = [q_1, q_2, q_3]^T$ and q_0 are the vector part and scalar components, respectively. $\mathbf{I}_3 \in \mathbf{R}^{3\times3}$ is the identity matrix, $\omega = [\omega_1, \omega_2, \omega_3]^T \in \mathbf{R}^3$ is the angular velocity of the spacecraft, and $\omega^\times$ is a skew symmetric matrix of ω and has the following form:

$$\boldsymbol{\omega}^\times = \begin{bmatrix} 0 & -\omega_3 & \omega_2 \\ \omega_3 & 0 & -\omega_1 \\ -\omega_2 & \omega_1 & 0 \end{bmatrix}. \tag{4}$$

Remark 1. $\mathbf{J}(t)$ may change or be uncertain over time due to fuel consumptions or onboard mission; therefore, $\mathbf{J}(t)$ should be viewed as uncertain item or unknown item so that it could not be used directly in control design. It is reasonable to assume the invertible $\mathbf{J}(t)$ in the form $\mathbf{J}(t) = \mathbf{J}_0 + \Delta\mathbf{J}(t)$, in which $\mathbf{J}_0$is the nominal inertia matrix and $\Delta\mathbf{J}(t)$ is the uncertainty. Compared to the above-mentioned references, both $\mathbf{J}_0$ and $\Delta\mathbf{J}(t)$ are unknown here, which is the most relaxed and simple condition.

Assumption 1. $\mathbf{q}$ and ω are available in feedback control design. In practical, angles and angular velocities can be measured with relative sensors.

Assumption 2. The external disturbances $\mathbf{d}(t) \in \mathbf{R}^{3\times1}$ are bounded.

The control objective is to make the aircraft track the desired attitude dynamics when the thrusters are constrained.

The torques generated by the constrained thrusters can be described as follows:

$$\begin{aligned} \mathbf{u} &= \operatorname{sat}(\mathbf{u}_0) = [\operatorname{sat}(u_{01}), \ldots, \operatorname{sat}(u_{03})]^T, \\ \operatorname{sat}(u_{0i}) &= \begin{cases} u_{0i}, & |u_{0i}| \le u_{i\max}, \\ u_{i\max}, & \text{otherwise}, \end{cases} \quad i = 1, \ldots, 3, \end{aligned} \tag{5}$$

where $\mathbf{u}_0$ is the thruster torque without limitation. The function $\operatorname{sat}(\cdot)$ is used to describe that the control torques generated by the thrusters are limited. $u_{i\max}$ indicates the maximum value of the control torque generated by the thruster.

According to [5, 29], the saturation function can be expressed as

$$\mathbf{u} = \operatorname{sat}(\mathbf{u}_0) = \varsigma(\mathbf{u}_0)\mathbf{u}_0, \tag{6}$$

with

$$\begin{aligned} \varsigma(\mathbf{u}_0) &= \operatorname{diag}[\varsigma_1(u_{01}), \ldots, \varsigma_n(u_{0n})], \\ \varsigma_i(u_{0i}) &= \begin{cases} \dfrac{u_{i\max}}{u_{0i}}\operatorname{sign}(u_{0i}), & |u_{0i}| > u_{i\max}, \\ 1, & \text{otherwise}. \end{cases} \quad i = 1, \ldots, n, \end{aligned} \tag{7}$$

Obviously, the coefficient $\varsigma_i(u_{0i}) \in (0, 1]$ denotes the saturation degree of u_{0i}.

Similar to [5], the desired attitude motion is supposed to be generated by

$$\dot{q}_{dv} = \frac{1}{2}(\mathbf{q}_{dv}^\times + q_{d0}\mathbf{I}_3)\boldsymbol{\omega}_d, \tag{8}$$

$$\dot{q}_{d0} = -\frac{1}{2}\mathbf{q}_{dv}^T\boldsymbol{\omega}_d, \tag{9}$$

where $\mathbf{q}_d = [\mathbf{q}_{dv}; q_{d0}] \in \mathbf{R}^{4\times1}$ is the desired unit quaternion vector of the spacecraft, satisfying $\mathbf{q}_{dv}^T\mathbf{q}_{dv} + q_{d0}^2 = 1$, where $\mathbf{q}_{dv} = [q_{d1}, q_{d2}, q_{d3}]^T$ and q_{d0} are the vector part and scalar component, respectively. $\omega_d = [\omega_{d1}, \omega_{d2}, \omega_{d3}]^T \in \mathbf{R}^{3\times1}$ is the desired angular velocity of the spacecraft. As in [3, 5], ω_d and $\dot{\omega}_d$ are assumed to be bounded.

The goal of the attitude tracking control is to design the controller so that the attitude in equations (1)–(3) tracks the desired attitude in equations (8)-(9), that is, to achieve $\mathbf{q} \longrightarrow \mathbf{q}_d$ and $\omega \longrightarrow \omega_d$. To analyse the attitude tracking problem, as in [3, 5], we define attitude orientation error $\mathbf{q}_e = [\mathbf{q}_{ev}; q_{e0}] \in \mathbf{R}^{4\times1}$ and angular velocity error $\omega_e = [\omega_{e1}, \omega_{e2}, \omega_{e3}]^T \in \mathbf{R}^{3\times1}$ as follows:

$$\mathbf{q}_{ev} = q_{d0}\mathbf{q}_v - \mathbf{q}_{dv}^\times\mathbf{q}_v - q_0\mathbf{q}_{dv}, \tag{10}$$

$$q_{e0} = \mathbf{q}_{dv}^T\mathbf{q}_v + q_0q_{d0}, \tag{11}$$

$$\boldsymbol{\omega}_e = \boldsymbol{\omega} - \mathbf{C}\boldsymbol{\omega}_d, \tag{12}$$

where $\mathbf{C} = (q_{e0}^2 - \mathbf{q}_{ev}^T\mathbf{q}_{ev})\mathbf{I}_3 + 2\mathbf{q}_{ev}\mathbf{q}_{ev}^T - 2q_{e0}\mathbf{q}_{ev}^\times$ is a rotation matrix, and note that $\|\mathbf{C}\| = 1$ and $\dot{C} = -\omega_e^\times\mathbf{C}$.

From equations (1)–(12), the attitude orientation error $\mathbf{q}_e$ and angular velocity error ω_e can be derived as follows:

$$\begin{aligned} \mathbf{J}(t)\dot{\omega}_e = &-\boldsymbol{\omega}^\times\mathbf{J}(t)\boldsymbol{\omega} + \mathbf{F}\varsigma(\mathbf{u}_0)\mathbf{u}_0 \\ &+ \mathbf{d}(t) + \mathbf{J}(t)(\boldsymbol{\omega}_e^\times\mathbf{C}\boldsymbol{\omega}_d - \mathbf{C}\dot{\omega}_d), \end{aligned} \tag{13}$$

$$\dot{q}_e = \frac{1}{2}\begin{bmatrix} \mathbf{q}_{ev}^\times + q_{e0}\mathbf{I}_3 \\ -\mathbf{q}_{ev}^T \end{bmatrix}\boldsymbol{\omega}_e. \tag{14}$$

It has been proved that through equations (10)–(12), the aim of $\mathbf{q} \longrightarrow \mathbf{q}_d$ and $\omega \longrightarrow \omega_d$ would be achieved by stabilizing systems (13)-(14) in [29].

In order to stabilize systems (13)-(14), as in [5, 6], the sliding surface can be selected as follows:

$$\mathbf{S} = \boldsymbol{\omega}_e + \mathbf{K}\mathbf{q}_{ev}, \tag{15}$$

where $\mathbf{K} = \operatorname{diag}[k_1, k_2, k_3]$ and $k_i > 0$ is a positive-designed constant.

Differentiating equation (15) and then multiplying by $\mathbf{J}(t)$, we can obtain the following:

$$\dot{S} = \mathbf{J}^{-1}\left[-\boldsymbol{\omega}^{\times}\mathbf{J}\boldsymbol{\omega} + \mathbf{F}\varsigma(\mathbf{u}_0)\mathbf{u}_0 + \mathbf{d}(t) + \mathbf{J}\left(\boldsymbol{\omega}_e^{\times}\mathbf{C}\boldsymbol{\omega}_d - \mathbf{C}\dot{\omega}_d\right) + \frac{1}{2}\mathbf{JK}\left(\mathbf{q}_{ev}^{\times} + q_{e0}\mathbf{I}_3\right)\boldsymbol{\omega}_e\right]. \tag{16}$$

In Section 3, the control $\mathbf{u}_0$ will be designed such that $\lim_{t\longrightarrow\infty}\mathbf{S} = 0$. According to Lemma 2.1 in [5], $\lim_{t\longrightarrow\infty}\mathbf{S} = 0$ can guarantee $\lim_{t\longrightarrow\infty}\omega_e = 0$ and $\lim_{t\longrightarrow\infty}\mathbf{q}_{ev} = 0$.

2.2. Input to State Stability

Lemma 1 (see [29]). *Consider the system* $\dot{x} = f(t, x, u)$*; there exists a* C^1 *function* $V: R_+ \times R^n \longrightarrow R_+$ *so that for all* $x \in R^n$ *and* $u \in R^m$*, it satisfies*

$$\gamma_1(|x|) \le V(t,x) \le \gamma_2(|x|),$$
$$|x| \ge \chi(|u|) \Longrightarrow \frac{\partial V}{\partial t} + \frac{\partial V}{\partial x} f(t,x,u) \le -\gamma_3(|x|), \tag{17}$$

where γ_1, γ_2*, and* χ*are class* κ_∞ *functions and* γ_3 *is a class* κ *function. Then, the system is input to state stable (ISS), and for all* t_0 *and* t *such that* $0 \le t_0 \le t$*, the following is satisfied:*

$$|x(t)| \le \beta\left(\left|x(t_0)\right|, t - t_0\right) + \gamma\left(\sup_{t_0 \le \tau \le t}|u(\tau)|\right), \tag{18}$$

where $\beta(\cdot)$ *is a class* κL *function and* $\gamma = \gamma_1^{-1}\gamma_2\rho$ *is a class* κ *function.*

3. Compound Control for Attitude Tracking

The first case considered here is the spacecraft with only three thrusters. Actually, there always exist two types of thruster faults in the practical spacecraft system. Therefore, partial effectiveness loss fault and additive fault are considered here. The second case considered is the spacecraft with more than three thrusters; however, some of it might experience losing power totally.

3.1. Spacecraft with Only Three Thrusters.

As the spacecraft has only three thrusters, $\mathbf{F}$ in equation (1) would be $\mathbf{I}_3$. When partial effectiveness loss fault and additive fault happen, the attitude dynamics should be described as follows:

$$\mathbf{J}(t)\dot{\omega} = -\boldsymbol{\omega}^{\times}\mathbf{J}(t)\boldsymbol{\omega} + \boldsymbol{\delta}(t)\mathbf{u} + \mathbf{A}(t) + \mathbf{d}(t), \tag{19}$$

where $\delta(t) = \mathrm{diag}[\delta_1, \delta_2, \delta_3]^T \in \mathbf{R}^{3\times3}$; $\delta_i \in (0, 1]$ denotes thruster effectiveness; and when $\delta_i = 1$ denotes that the thruster works normally, while $\delta_i \in (0, 1)$indicates that the thruster loses its effectiveness partially. $\mathbf{A}(t) = \mathrm{diag}[A_1(t), A_2(t), A_3(t)] \in \mathbf{R}^{3\times3}$ indicates the additive fault, and it is bounded.

Then, the sliding surface dynamics would be described by

$$\dot{S} = \mathbf{J}^{-1}\left[-\boldsymbol{\omega}^{\times}\mathbf{J}\boldsymbol{\omega} + \boldsymbol{\delta}(t)\mathbf{u} + \mathbf{A}(t) + \mathbf{d}(t) + \mathbf{J}\left(\boldsymbol{\omega}_e^{\times}\mathbf{C}\boldsymbol{\omega}_d - \mathbf{C}\dot{\omega}_d\right) + \frac{1}{2}\mathbf{JK}\left(\mathbf{q}_{ev}^{\times} + q_{e0}\mathbf{I}_3\right)\boldsymbol{\omega}_e\right]. \tag{20}$$

According to the active disturbance rejection concept in [23–26], equation (35) could be changed to the following:

$$\dot{S} = \mathbf{G} + \mathbf{B}_0\varsigma(\mathbf{u}_0)\mathbf{u}_0, \tag{21}$$

where $\mathbf{B}_0 \in \mathbf{R}^{3\times3}$ is a nonsingular matrix selected by the designer and $\mathbf{G}$ is the general uncertain item:

$$\mathbf{G} = \mathbf{J}^{-1}\left[-\boldsymbol{\omega}^{\times}\mathbf{J}\boldsymbol{\omega} + \boldsymbol{\delta}(t)\mathbf{u} + \mathbf{A}(t) + \mathbf{d}(t) + \mathbf{J}\left(\boldsymbol{\omega}_e^{\times}\mathbf{C}\boldsymbol{\omega}_d - \mathbf{C}\dot{\omega}_d\right) + \frac{1}{2}\mathbf{JK}\left(\mathbf{q}_{ev}^{\times} + q_{e0}\mathbf{I}_3\right)\boldsymbol{\omega}_e\right] - \mathbf{B}_0\varsigma(\mathbf{u}_0)\mathbf{u}_0. \tag{22}$$

It contains the unknown inertia matrix, external disturbance, and the uncertainties produced by thruster fault. To facilitate analysis, $\mathbf{B}_0$ is chosen as a diagonal matrix.

As in [4, 24–26], in order to deal with $\mathbf{G}$, the extended state observer (ESO) for equation (21) can be constructed as follows:

$$\begin{cases} \mathbf{E} = \mathbf{Z}_1 - \mathbf{S}, \\ \dot{Z}_1 = \mathbf{Z}_2 - \beta_1 g_{c1}(\mathbf{E}) + \mathbf{B}_0 \varsigma(\mathbf{u}_0)\mathbf{u}_0, \\ \dot{Z}_2 = -\beta_2 g_{c2}(\mathbf{E}), \end{cases}$$
$$g_{c1}(\mathbf{E}) = [E_1, E_2, E_3]^T, \tag{23}$$
$$g_{c2}(\mathbf{E}) = \begin{bmatrix} |E_1|^{\alpha_1}\operatorname{sign}(E_1) \\ |E_2|^{\alpha_1}\operatorname{sign}(E_2) \\ |E_3|^{\alpha_1}\operatorname{sign}(E_3) \end{bmatrix}, \quad 0 \le \alpha_1 \le 1,$$

where $\mathbf{E} = [E_1, E_2, E_3]^T \in \mathbf{R}^{3\times 1}$ is the estimation error of the ESO, $\mathbf{Z}_1 \in \mathbf{R}^{3\times 1}$ and $\mathbf{Z}_2 \in \mathbf{R}^{3\times 1}$ are the observer output, and $\beta_1 > 0$, $\beta_2 > 0$, and $1/4\beta_1^2 > \beta_2 > \|\dot{G}\|$are the observer gains. It has been proved in [4, 25] that for appropriate values of $\beta_1, \beta_2, g_{c1}(\cdot)$, and $g_{c2}(\cdot)$, the observer output $\mathbf{Z}_2$ approaches $\mathbf{G}$ and $\mathbf{Z}_1$ approaches $\mathbf{S}$.

With the uncertainties $\mathbf{G}$ estimated by the ESO, the sliding control law can be designed as

$$\mathbf{u} = \operatorname{sat}(\mathbf{u}_0),$$
$$\mathbf{u}_0 = -\mathbf{B}_0^{-1}[\boldsymbol{\tau}\mathbf{S} + \boldsymbol{\sigma}\operatorname{sig}(\mathbf{S})^r] - \mathbf{B}_0^{-1}\hat{\rho}\frac{\mathbf{S}}{\|\mathbf{S}\|}\left(\eta + \|\mathbf{Z}_2\|\right), \tag{24}$$

$$\dot{\hat{\rho}} = p_0\hat{\rho}^3\|\mathbf{S}\|\left(\eta + \|\mathbf{Z}_2\|\right), \quad \hat{\rho}(0) > 0, \tag{25}$$

with $\tau = \operatorname{diag}[\tau_1, \tau_2, \tau_3]$, $\tau_i > 0$, $\sigma = \operatorname{diag}[\sigma_1, \sigma_2, \sigma_3]$, $\sigma_i > 0$, and $\operatorname{sig}(\mathbf{S})^r = [|S_1|^r\operatorname{sign}(S_1), \ldots, |S_3|^r\operatorname{sign}(S_3)]^T$, $r \in (0, 1)$, where $p_0 > 0$ and $\eta > 0$ are positive constant parameters chosen by the designer. $\mathbf{Z}_2$ is the state of ESO equation (23), which can approach $\mathbf{G}$.

Theorem 1. *Consider a spacecraft system with partial effectiveness loss fault and additive fault; meanwhile, the thrusters are limited, which is stated in equation (19). If control scheme (24) is implemented, then the control objectives $\mathbf{q} \longrightarrow \mathbf{q}_d$ and $\omega \longrightarrow \omega_d$ would be achieved.*

Proof. Construct the Lyapunov function as follows:

$$V_s = \frac{1}{2}\mathbf{S}^T\mathbf{S} + \frac{1}{2p_0}\tilde{\rho}^T\tilde{\rho}, \tag{26}$$

where $\tilde{\rho} = \rho - \hat{\rho}^{-1}$ and $p_0 > 0$ is a designed constant. In view of equation (21), its time derivative can be given as follows:

$$\dot{V}_s = \mathbf{S}^T\dot{S} + \frac{1}{p_0}\tilde{\rho}^T\hat{\rho}^{-2}\dot{\hat{\rho}} = \mathbf{S}^T(\mathbf{G} + \mathbf{B}_0\varsigma(\mathbf{u}_0)\mathbf{u}_0) + \frac{1}{p_0}\tilde{\rho}^T\hat{\rho}^{-2}\dot{\hat{\rho}}. \tag{27}$$

Owing to both $\mathbf{B}_0$ and $\varsigma(\mathbf{u}_0)$ being diagonal matrices and combining with equation (24), equation (27) can be expressed as follows:

$$\begin{aligned} \dot{V}_s &= \mathbf{S}^T(\mathbf{G} + \varsigma(\mathbf{u}_0)\mathbf{B}_0\mathbf{u}_0) + \frac{1}{p_0}\tilde{\rho}^T\hat{\rho}^{-2}\dot{\hat{\rho}} \\ &= -\mathbf{S}^T(\varsigma(\mathbf{u}_0)\boldsymbol{\tau}\mathbf{S} + \varsigma(\mathbf{u}_0)\boldsymbol{\sigma}\operatorname{sign}(\mathbf{S})^r) \\ &\quad + \mathbf{S}^T\mathbf{G} - \mathbf{S}^T\varsigma(\mathbf{u}_0)\hat{\rho}\frac{\mathbf{S}}{\|\mathbf{S}\|}\left(\eta + \|\mathbf{Z}_2\|\right) + \frac{1}{p_0}\tilde{\rho}^T\hat{\rho}^{-2}\dot{\hat{\rho}} \\ &= -\sum_{i=1}^{3}\varsigma_i(u_{0i})\tau_i S_i^2 - \sum_{i=1}^{3}\varsigma_i(u_{0i})\sigma_i|S_i|^{r+1} \\ &\quad + \mathbf{S}^T\mathbf{G} - \frac{\hat{\rho}\left(\eta + \|\mathbf{Z}_2\|\right)}{\|\mathbf{S}\|}\sum_{i=1}^{3}\varsigma_i(u_{0i})S_i^2 + \frac{1}{p_0}\tilde{\rho}^T\hat{\rho}^{-2}\dot{\hat{\rho}}. \end{aligned} \tag{28}$$

As in [30], since$\varsigma_i(u_{0i}) \in (0, 1]$, then according to the density property of the real number, there would exist a constant ρ satisfying

$$0 < \rho \le \min_{1\le i\le 3}(\varsigma_i(u_{0i})) \le 1. \tag{29}$$

According to equation (29), it yields

$$\begin{aligned} \dot{V}_s \le &-\rho\left(\sum_{i=1}^{3}\tau_i S_i^2 + \sum_{i=1}^{3}\sigma_i|S_i|^{r+1}\right) \\ &+ \mathbf{S}^T\mathbf{G} - \frac{\hat{\rho}\left(\eta + \|\mathbf{Z}_2\|\right)}{\|\mathbf{S}\|}\sum_{i=1}^{3}\varsigma_i(u_{0i})S_i^2 + \frac{1}{p_0}\tilde{\rho}^T\hat{\rho}^{-2}\dot{\hat{\rho}}. \end{aligned} \tag{30}$$

According to equation (25), it is not difficult to note that $\hat{\rho}(0) > 0$ ensures that $\hat{\rho}$ is always larger than zero. Therefore, the following can be further obtained:

$$\begin{aligned} \dot{V}_s \le &-\rho\left(\sum_{i=1}^{3}\tau_i S_i^2 + \sum_{i=1}^{3}\sigma_i|S_i|^{r+1}\right) + \mathbf{S}^T\mathbf{G} \\ &- \rho\frac{\hat{\rho}\left(\eta + \|\mathbf{Z}_2\|\right)}{\|\mathbf{S}\|}\sum_{i=1}^{3}S_i^2 + \frac{1}{p_0}\tilde{\rho}^T\hat{\rho}^{-2}\dot{\hat{\rho}} \\ \le &-\rho\left(\sum_{i=1}^{3}\tau_i S_i^2 + \sum_{i=1}^{3}\sigma_i|S_i|^{r+1}\right) + \mathbf{S}^T\mathbf{G} - \rho\hat{\rho}\left(\eta + \|\mathbf{Z}_2\|\right)\|\mathbf{S}\| \\ &+ \frac{1}{p_0}\tilde{\rho}^T\hat{\rho}^{-2}\dot{\hat{\rho}}. \end{aligned} \tag{31}$$

According to equation (25) and $\rho = \tilde{\rho} + \hat{\rho}^{-1}$in equation (31), it yields

$$\begin{aligned}\dot{V}_s &\le -\rho\left(\sum_{i=1}^{3}\tau_i S_i^2 + \sum_{i=1}^{3}\sigma_i|S_i|^{r+1}\right) + \mathbf{S}^T\mathbf{G} - \left(\widetilde{\rho} + t\widehat{\rho}^{-1}\right)\widehat{\rho}\left(\eta + \|\mathbf{Z}_2\|\right)\|\mathbf{S}\| + \frac{1}{p_0}\widetilde{\rho}^T\widehat{\rho}^{-2}p_0\widehat{\rho}^3\|\mathbf{S}\|\left(\eta + \|\mathbf{Z}_2\|\right)\\ &\le -\rho\left(\sum_{i=1}^{3}\tau_i S_i^2 + \sum_{i=1}^{3}\sigma_i|S_i|^{r+1}\right) + \mathbf{S}^T\mathbf{G} - \eta\|\mathbf{S}\| - \|\mathbf{Z}_2\|\|\mathbf{S}\| \le -\rho\left(\sum_{i=1}^{3}\tau_i S_i^2 + \sum_{i=1}^{3}\sigma_i|S_i|^{r+1}\right)\\ &\quad - \eta\|\mathbf{S}\| + \|\mathbf{S}\|\left(\|\mathbf{G}\| - \|\mathbf{Z}_2\|\right) \le -\rho\left(\sum_{i=1}^{3}\tau_i S_i^2 + \sum_{i=1}^{3}\sigma_i|S_i|^{r+1}\right) - \eta\|\mathbf{S}\| + \|\mathbf{S}\|\|G - \mathbf{Z}_2\|\\ &\le -\rho\sum_{i=1}^{3}\sigma_i|S_i|^{r+1} - \eta\|\mathbf{S}\| - \rho\min_i\tau_i\|\mathbf{S}\|^2 + \|\mathbf{S}\|\|\mathbf{G} - \mathbf{Z}_2\|.\end{aligned} \tag{32}$$

Then, $\|\mathbf{G} - \mathbf{Z}_2\|$ can be viewed as the disturbance input of the closed loop system consisting of equations (20), (23), (24), and (25). When $\|\mathbf{S}\| \ge \chi(\|\mathbf{G} - \mathbf{Z}_2\|)$, with $\chi(\|\mathbf{G} - \mathbf{Z}_2\|) = 1/\rho\min_i\tau_i\|\mathbf{G} - \mathbf{Z}_2\|$, equation (32) is smaller than zero. Therefore, the closed loop system is ISS. Based on Lemma 1, it is easy to conclude that the estimation error $\|\mathbf{G} - \mathbf{Z}_2\|$ by ESO will affect that whether the dynamic of the sliding mode converges to the sliding surface $\mathbf{S} = 0$. According to the principle of ESO, it is shown that $\mathbf{Z}_2$ can only converge into a residual set of $\mathbf{G}$, which means that $\|\mathbf{G} - \mathbf{Z}_2\|$ will converge into a small residual set of zero. That is to say, the dynamic of the sliding mode will be restricted to the neighborhood of the sliding surface. Fortunately, this neighborhood can be reduced to any small size by selecting the ESO parameters $\beta_1, \beta_2, g_{c1}(\cdot)$, and $g_{c2}(\cdot)$ and the controller parameters τ, σ, and η. Furthermore, τ and σ determine the speed of convergence and the final error. According to equation (24), the bigger the parameters τ and σ are, the faster the speed converging to zero and the smaller the approach error is. □

Remark 2. Obviously, $\chi(\|\mathbf{G} - \mathbf{Z}_2\|) = 1/\rho\min_i\tau_i\|\mathbf{G} - \mathbf{Z}_2\|$ is a class κ_∞ function, so Lyapunov function (26) satisfies Lemma 1; that is to say, the closed loop system is ISS.

Remark 3. In order to ensure the stability for the dynamic of the sliding mode and the ability to approach the selected sliding surface, $\widehat{\rho}(0)$ and τ_i should satisfy $\widehat{\rho}(0)\tau_i > 1$. The reason is that $\dot{V}_s \le -\rho\min_i\tau_i\|\mathbf{S}\|^2 + \|\mathbf{S}\|^2 + \|\mathbf{G} - \mathbf{Z}_2\|^2/4$, and ρ is designed as an incremental function.

Remark 4. ^{B_0} determines the effectiveness of the active disturbance rejection. Although ^{B_0} can be selected as an arbitrary diagonal matrix, the closer ^{B_0} is to the real value, the better the effect of the active disturbance rejection.

Remark 5. As $\mathbf{S}$ crosses the zero, the controller in equation (24) will be discontinuous, which will result in chattering. Therefore, the bounded layer should be introduced to eliminate the chattering. As in [5], equation (24) can be modified as follows:

$$\mathbf{u}_0 = -\mathbf{B}_0^{-1}\left[\boldsymbol{\tau}\mathbf{S} + \boldsymbol{\sigma}\mathrm{sig}(\mathbf{S})^r\right] - \mathbf{B}_0^{-1}\widehat{\rho}\frac{\mathbf{S}}{\|\mathbf{S}\| + \varepsilon}\left(\eta + \|\mathbf{Z}_2\|\right), \tag{33}$$

where $\varepsilon > 0$ is the bounded layer, and it should be selected to be small enough.

3.2. Spacecraft with More than Three Thrusters. When the spacecraft has more than three thrusters, some of which might suffer from total fault, then the attitude dynamics would be described as follows [2]:

$$\mathbf{J}(t)\dot{\omega} = -\boldsymbol{\omega}^{\times}\mathbf{J}(t)\boldsymbol{\omega} + \mathbf{F}\Gamma\mathbf{u} + \mathbf{d}(t), \tag{34}$$

where $\Gamma = \mathrm{diag}[\Gamma_1, \ldots, \Gamma_n] \in \mathbf{R}^{n\times n}$ denotes the work status of the thrusters. $\Gamma_i = 0$ means that the thruster has either totally failed or been shut down purposely.

Correspondingly, sliding surface dynamics (16) would be described by

$$\begin{aligned}\dot{S} = \mathbf{J}^{-1}\big[&-\boldsymbol{\omega}^{\times}\mathbf{J}\boldsymbol{\omega} + \mathbf{F}\Gamma\mathbf{u} + \mathbf{d}(t) + \mathbf{J}\left(\boldsymbol{\omega}_e^{\times}\mathbf{C}\boldsymbol{\omega}_d - \mathbf{C}\dot{\omega}_d\right)\\ &+ \frac{1}{2}\mathbf{J}\mathbf{K}\left(\mathbf{q}_{ev}^{\times} + q_{e0}\mathbf{I}_3\right)\boldsymbol{\omega}_e\big].\end{aligned} \tag{35}$$

Firstly, we can choose $\mathbf{B}_0$ as $\mathbf{B}_0 = \begin{bmatrix}1&0&0&0&\ldots&0\\0&1&0&0&\ldots&0\\0&0&1&0&\ldots&0\end{bmatrix}_{3\times n}$.

According to the active disturbance rejection concept in [23–26], equation (35) could be changed to the following:

$$\dot{S} = \mathbf{G} + \mathbf{B}_0\varsigma(\mathbf{u}_0)\mathbf{u}_0, \tag{36}$$

where $\mathbf{G}$ is the total uncertain item, which can be written as follows:

$$\begin{aligned}\mathbf{G} = \mathbf{J}^{-1}\big[&-\boldsymbol{\omega}^{\times}\mathbf{J}\boldsymbol{\omega} + \mathbf{F}\Gamma\mathbf{u} + \mathbf{d}(t) + \mathbf{J}\left(\boldsymbol{\omega}_e^{\times}\mathbf{C}\boldsymbol{\omega}_d - \mathbf{C}\dot{\omega}_d\right)\\ &+ \frac{1}{2}\mathbf{J}\mathbf{K}\left(\mathbf{q}_{ev}^{\times} + q_{e0}\mathbf{I}_3\right)\boldsymbol{\omega}_e\big] - \mathbf{B}_0\varsigma(\mathbf{u}_0)\mathbf{u}_0.\end{aligned} \tag{37}$$

It contains the unknown inertia matrix, external disturbance, and uncertainties produced by thrusters fault.

And then, it is interesting to find that the sliding dynamics can be stabilized with a slight modification to the above controller, as follows:

$$\mathbf{u} = \mathbf{sat}(\mathbf{u}_0),$$
$$\mathbf{u}_0 = -\mathbf{B}_0^T[\boldsymbol{\tau}\mathbf{S} + \boldsymbol{\sigma}\mathrm{sig}(\mathbf{S})^r] - \mathbf{B}_0^T\widehat{\rho}\frac{\mathbf{S}}{\|\mathbf{S}\|}\left(\eta + \|\mathbf{Z}_2\|\right), \tag{38}$$

$$\dot{\widehat{\rho}} = p_0\widehat{\rho}^3\|\mathbf{S}\|\left(\eta + \|\mathbf{Z}_2\|\right), \quad \widehat{\rho}(0) > 0, \tag{39}$$

where all the control parameters are defined as before. The stability of the closed loop system can be analyzed by using the same Lyapunov function. Combining controller (38) and adaptive law (39), the derivative of the Lyapunov function can be given as follows:

$$\begin{aligned}\dot{V}_s = {} & \mathbf{S}^T\mathbf{G} - \mathbf{S}^T\mathbf{B}_0\varsigma(\mathbf{u}_0)\mathbf{B}_0^T[\boldsymbol{\tau}\mathbf{S} + \boldsymbol{\sigma}\mathrm{sig}(\mathbf{S})^r] \\ & - \mathbf{S}^T\mathbf{B}_0\varsigma(\mathbf{u}_0)\mathbf{B}_0^T\widehat{\rho}\frac{\mathbf{S}}{\|\mathbf{S}\|}\left(\eta + \|\mathbf{Z}_2\|\right) \\ & + \frac{1}{p_0}\widetilde{\rho}^T\widehat{\rho}^{-2}p_0\widehat{\rho}^3\|\mathbf{S}\|\left(\eta + \|\mathbf{Z}_2\|\right).\end{aligned} \tag{40}$$

Note that the multiplication of a vector and a diagonal matrix in equation (40) satisfies the following:

$$\mathbf{S}^T\mathbf{B}_0\varsigma(\mathbf{u}_0) = \overline{\varsigma}\mathrm{diag}\left(\mathbf{S}^T\mathbf{B}_0\right) \text{ with } \overline{\varsigma} = [\varsigma_1, \ldots, \varsigma_n]. \tag{41}$$

Then, it is not difficult to calculate the right side of equation (40) and it can be expressed as

$$\dot{V}_s = -\sum_{i=1}^{3}\varsigma_i(u_{0i})\tau_i S_i^2 - \sum_{i=1}^{3}\varsigma_i(u_{0i})\sigma_i|S_i|^{r+1} + \mathbf{S}^T\mathbf{G} - \frac{\widehat{\rho}\left(\eta + \|\mathbf{Z}_2\|\right)}{\|\mathbf{S}\|}\sum_{i=1}^{3}\varsigma_i(u_{0i})S_i^2 + \widetilde{\rho}^T\widehat{\rho}\|\mathbf{S}\|\left(\eta + \|\mathbf{Z}_2\|\right). \tag{42}$$

According to equation (39), $\widehat{\rho}$ is a positive parameter. Combining equation (29), we can obtain the following:

$$\begin{aligned}\dot{V}_s \le {} & -\rho\sum_{i=1}^{3}\tau_i S_i^2 - \rho\sum_{i=1}^{3}\sigma_i|S_i|^{r+1} + \mathbf{S}^T\mathbf{G} - \frac{\widehat{\rho}\left(\eta + \|\mathbf{Z}_2\|\right)}{\|\mathbf{S}\|}\rho\sum_{i=1}^{3}S_i^2 + \widetilde{\rho}^T\widehat{\rho}\|\mathbf{S}\|\left(\eta + \|\mathbf{Z}_2\|\right) \le -\rho\sum_{i=1}^{3}\tau_i S_i^2 - \rho\sum_{i=1}^{3}\sigma_i|S_i|^{r+1} + \mathbf{S}^T\mathbf{G} \\ & - \frac{\widehat{\rho}\left(\eta + \|\mathbf{Z}_2\|\right)}{\|\mathbf{S}\|}\left(\widetilde{\rho} + t\widehat{\rho}^{-1}\right)\sum_{i=1}^{3}S_i^2 + \widetilde{\rho}^T\widehat{\rho}\|\mathbf{S}\|\left(\eta + \|\mathbf{Z}_2\|\right) \le -\rho\sum_{i=1}^{3}\tau_i S_i^2 - \rho\sum_{i=1}^{3}\sigma_i|S_i|^{r+1} + \|\mathbf{S}\|\left(\|\mathbf{G}\| - \|\mathbf{Z}_2\|\right).\end{aligned} \tag{43}$$

Consider $\|\mathbf{G} - \mathbf{Z}_2\|$ as the disturbance input of the closed loop system consisting of equations (35), (23), (38), and (39). When $\|\mathbf{S}\| \ge \chi(\|\mathbf{G} - \mathbf{Z}_2\|)$, with $\chi(\|\mathbf{G} - \mathbf{Z}_2\|) = 1/\rho\min_i\tau_i\|\mathbf{G} - \mathbf{Z}_2\|$, equation (43) is less than zero. Therefore, the entire closed-loop system is ISS for $\|\mathbf{G} - \mathbf{Z}_2\|$, and the following theorem can be established.

Theorem 2. *Consider a spacecraft system; meanwhile, the thrusters are limited, which is stated in equation (34). If control scheme (38) is implemented, then the control objectives* $\mathbf{q} \longrightarrow \mathbf{q}_d$ *and* $\omega \longrightarrow \omega_d$ *would be achieved.*

Remark 6. Similar to Remark 5, in order to eliminate the chattering, equation (38) can be modified as follows:

$$\mathbf{u}_0 = -\mathbf{B}_0^T[\boldsymbol{\tau}\mathbf{S} + \boldsymbol{\sigma}\mathrm{sig}(\mathbf{S})^r] - \mathbf{B}_0^T\widehat{\rho}\frac{\mathbf{S}}{\|\mathbf{S}\| + \varepsilon}\left(\eta + \|\mathbf{Z}_2\|\right), \tag{44}$$

where $\varepsilon > 0$ is the bounded layer and it should be selected to be small enough.

4. Simulation Results

To verify the effect of the scheme proposed above, several simulations on a spacecraft under various conditions are conducted. The limit of thrusters is selected as $u_{i\max} \le 5\,\mathrm{N}\cdot\mathrm{m}$. The initial values for the spacecraft are selected as $\mathbf{q}(0) = [0.3, -0.2, -0.3, 0.8832]^T$ and $\omega(0) = [0, 0, 0]^T$ rad/s . The initial values for the desired unit quaternion is set to $\mathbf{q}_d(0) = [0, 0, 0, 1]^T$. The unknown nominal inertial matrix and its uncertainties are chosen as

$$\mathbf{J}_0 = \begin{bmatrix} 20 & 1.2 & 0.9 \\ 1.2 & 17 & 0.4 \\ 0.9 & 1.4 & 15 \end{bmatrix}\mathrm{kg}\cdot\mathrm{m}^2, \tag{45}$$

$$\Delta\mathbf{J} = \mathrm{diag}[\sin(0.1t), 2\sin(0.2t), 3\sin(0.3t)]\,\mathrm{kg}\cdot\mathrm{m}^2,$$

and the disturbances are selected as $\mathbf{d}(t) = \begin{bmatrix} 0.1\sin(0.1t) \\ 0.2\sin(0.2t) \\ 0.3\sin(0.3t) \end{bmatrix}\mathrm{N}\cdot\mathrm{m}$.

The ESO parameters are designed as $\beta_1 = 70, \beta_2 = 30$ and $\alpha_1 = 0.25$. And, the initial states of ESO are set to $\mathbf{Z}_1(0) = \mathbf{Z}_2(0) = [0\ 0\ 0]^T$. The parameters of the control law in equations (24), (25), (38), and (39) are selected as $\mathbf{K} = 2\mathbf{I}_3$, $\tau = 50\mathbf{I}_3$, $\sigma = 0.01\mathbf{I}_3$, $r = 0.3$, $p_0 = 1$, $\eta = 20$, and $\varepsilon = 0.1$. The initial value for adaptive law is set to $\widehat{\rho}(0) = 0.1$.

In order to verify the performance of ESO, the desired angular velocity is set to a sinusoidal signal, such as $\omega_d(t) = [0.5\sin(\pi t/100), 0.5\sin(2\pi t/100), 0.5\sin(3\pi t/100)]$ rad/s.

4.1. Simulation for Spacecraft with Only Three Thrusters. In this section, it is assumed that thrusters have partial effectiveness loss fault and additive fault, such as $\delta_i(t) = 0.8 + 0.1\sin(t)$ and $A_i(t) = 10 + 10\sin(t)$.

Simulation results are given to show the performance of control law (24). Figure 1 demonstrates the attitude quaternion tracking error. The attitude quaternion tracking error curve indicates that the proposed control law achieves the desired attitude tracking in 5 s. The spacecraft has achieved the desired angular velocity in 5 s from the angular tracking error curve exhibited in Figure 2. From Figures 1 and 2, the validity of the conclusion of Theorem 1 can be verified such that control law (24) can make the spacecraft converge to the desired attitude and angular velocity in spite of the saturation, uncertainties, and disturbances.

From the sliding surface depicted in Figure 3, it could be drawn that the dynamic of sliding mode converge into the neighborhood of the sliding surface $\mathbf{S} = 0$ very quickly. According to equation (15), as $\mathbf{S}$ is equal to 0, $\omega_e = -\mathbf{K}\mathbf{q}_{ev}$, which is exactly reflected in Figures 1 and 2. The control torques produced by three thrusters are illustrated in Figure 4. They are limited by $u_{i\max} = 5N \cdot \mathrm{m}$. The adaptive law depicted in Figure 5 shows that although the parameter $\widehat{\rho}$ cannot converge to a certain constant, its change is very slow. However, the dynamic of the sliding mode just only converges into the neighborhood of the sliding surface $\mathbf{S} = 0$ and not converges to $\mathbf{S} = 0$. The performance of ESO is illustrated in Figure 6, which verifies that the total influence produced by the absolutely unknown inertial matrix, external disturbance, and actuator fault can be well estimated via ESO.

4.2. Simulation for Spacecraft with More than Three Thrusters. In this section, three thrusters with fading fault and the other three with totally failed fault are assumed, which is depicted as follows [2]:

$$\Gamma = \mathrm{diag}[0.5, 0.7, 0.7, 0, 0, 0] \in \mathbf{R}^{n\times n}. \tag{46}$$

Assume that the six thrusters are distributed as

$$\mathbf{F} = \begin{bmatrix} 1 & 0 & 0 & 0.2 & 0.1 & 0.3 \\ 0 & 1 & 0 & 0.6 & 0.5 & 0.3 \\ 0 & 0 & 1 & 0 & 0.2 & 0.4 \end{bmatrix}. \tag{47}$$

For the simulation purposes, the system's initial states, inertial matrix and its uncertainties, disturbances, and other parameters are all the same as above.

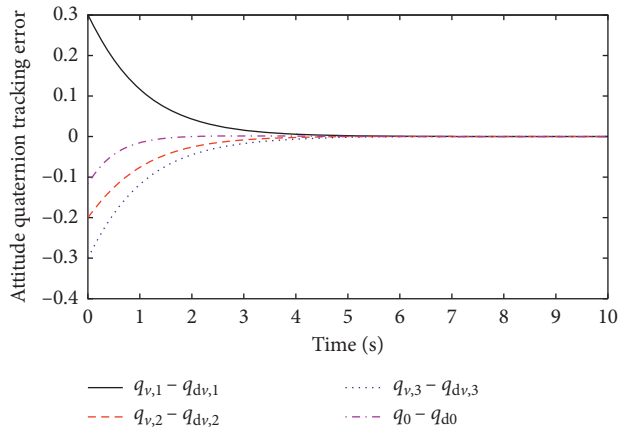

Figure 1: Attitude quaternion tracking error.

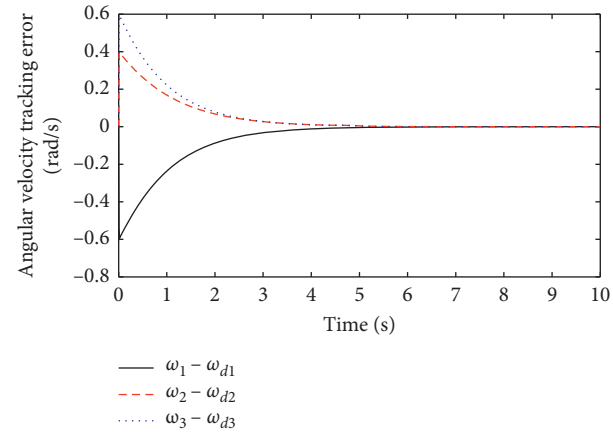

Figure 2: Angular velocity tracking error.

Figure 7 demonstrates the attitude quaternion tracking error. The attitude quaternion tracking error curve indicates that the proposed control law achieves the desired attitude tracking in 5 s. The spacecraft has achieved the desired angular velocity in 5 s from the angular tracking error curve exhibited in Figure 8. From Figures 7 and 8, the validity of the conclusion of Theorem 2 could be verified such that control law (38) can make the spacecraft converge to the desired attitude and angular velocity in spite of the saturation, uncertainties, and disturbances.

From the sliding surface depicted in Figure 9, it could be drawn that the dynamic of sliding mode converge into the neighborhood of the sliding surface $\mathbf{S} = 0$ very quickly. According to equation (15), as $\mathbf{S}$ is equal to 0, $\omega_e = -\mathbf{K}\mathbf{q}_{ev}$, which is exactly reflected in Figures 7 and 8. The control torques produced by six thrusters are illustrated in Figure 10. They are limited by $u_{i\max} = 5\,\mathrm{N} \cdot \mathrm{m}$. From Figure 10, it is obviously deduced that three thrusters show totally failed fault which is consistent with equation (46).

Define $\mathbf{T} = \mathbf{F}\Gamma\varsigma(\mathbf{u})\mathbf{u}$; then, the control torques for spacecraft are illustrated in Figure 11. It can be seen that the applied moment for spacecraft does not exceed the upper limit. The adaptive law depicted in Figure 12 shows that although the parameter $\widehat{\rho}$ cannot converge to a certain

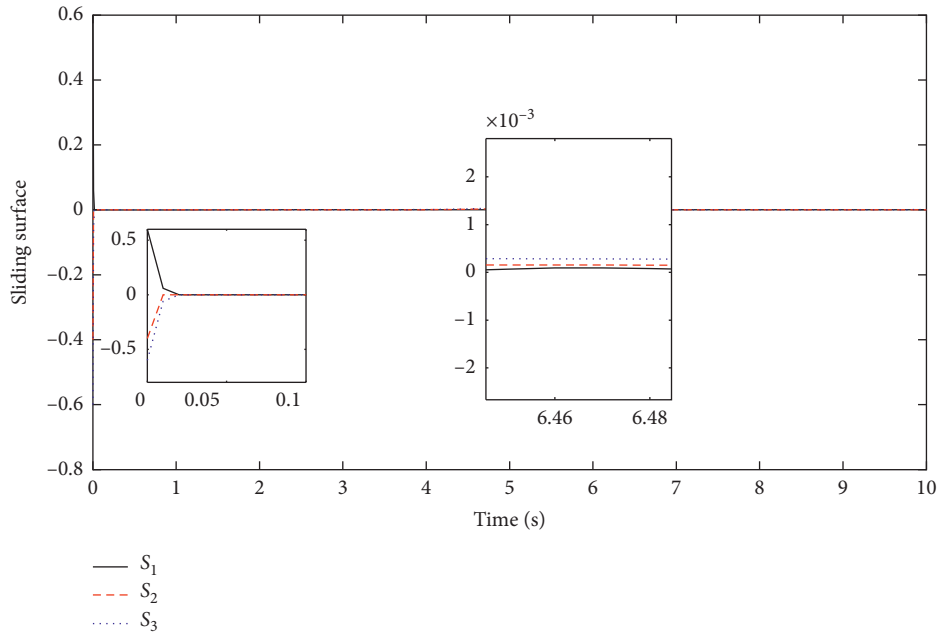

Figure 3: Sliding surface.

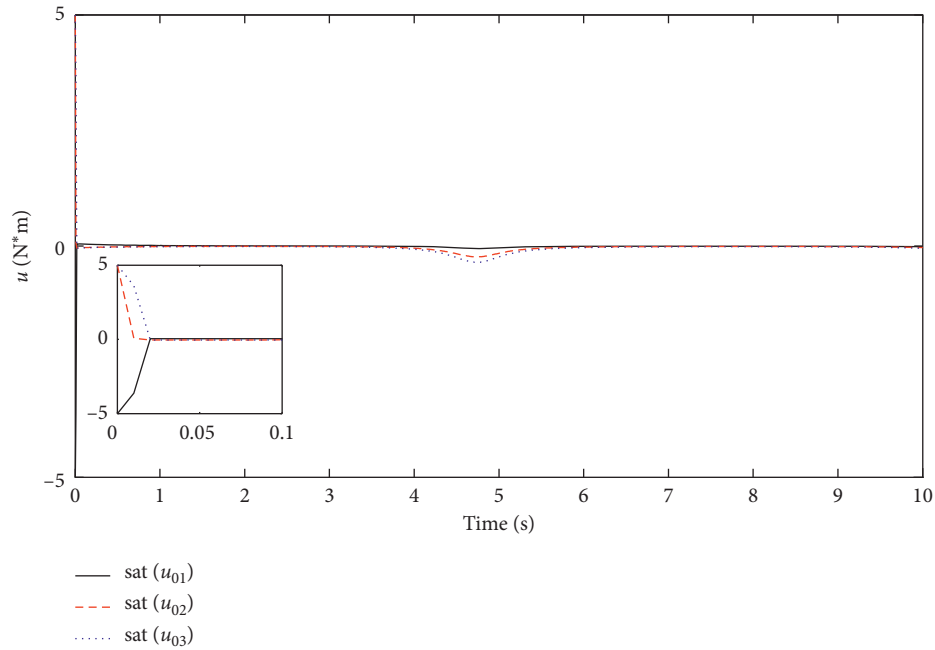

Figure 4: Control input.

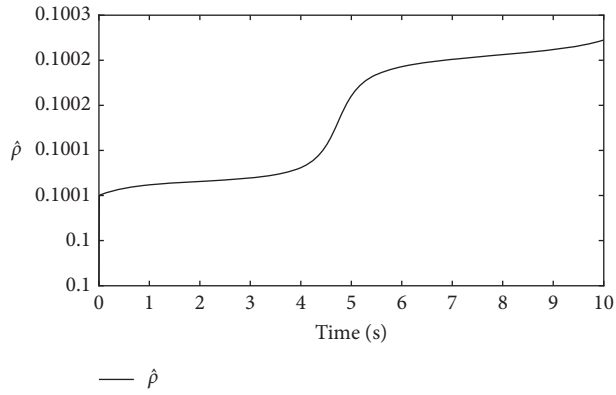

Figure 5: Adaptive law of the parameter $\widehat{\rho}$.

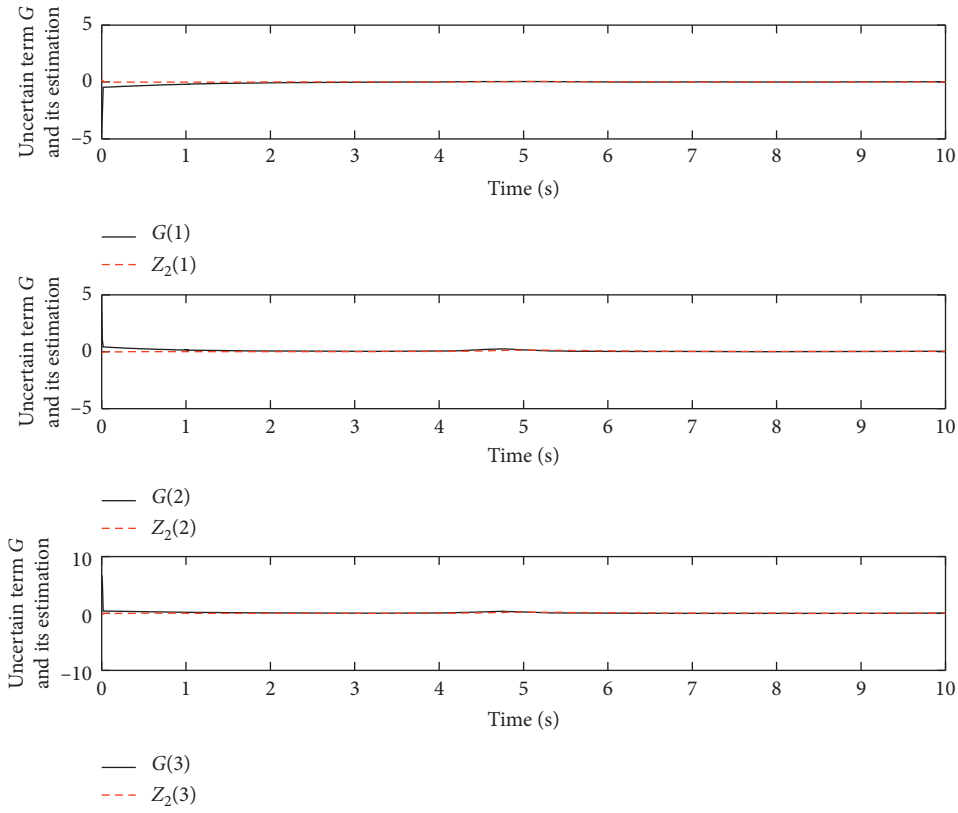

Figure 6: Estimation of general uncertainties by ESO.

constant, its change is very slow. However, the dynamic of sliding mode just only converges into the neighborhood of the sliding surface $\mathbf{S} = 0$ and not converges to $\mathbf{S} = 0$. The performance of ESO is illustrated in Figure 13, which verifies that the total influence produced by the absolutely unknown inertial matrix, external disturbance, and actuator fault can be well estimated via ESO.

Based on Figures 1–13, it can be concluded that the proposed scheme has achieved a good performance on attitude tracking by using ADRC and SMC.

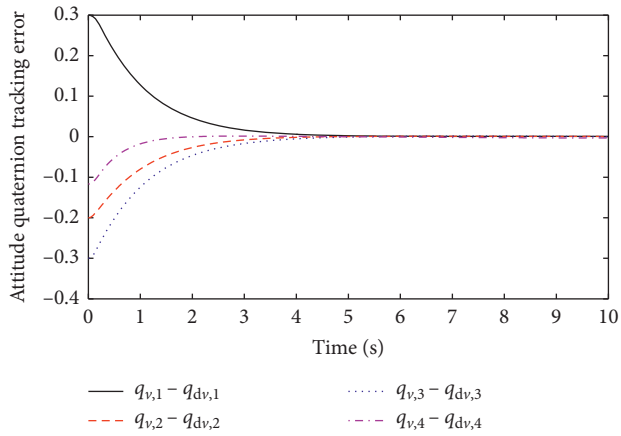

Figure 7: Attitude quaternion tracking error.

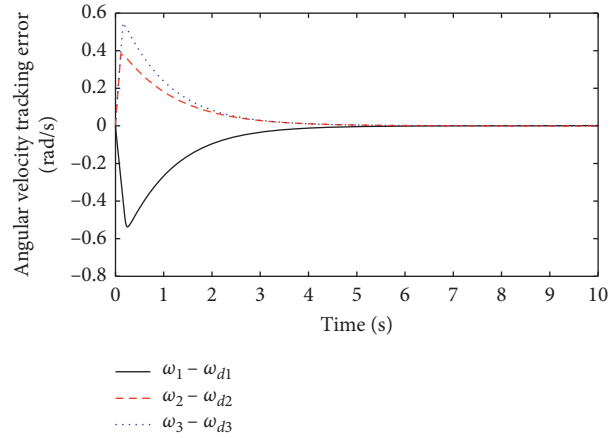

Figure 8: Angular velocity tracking error.

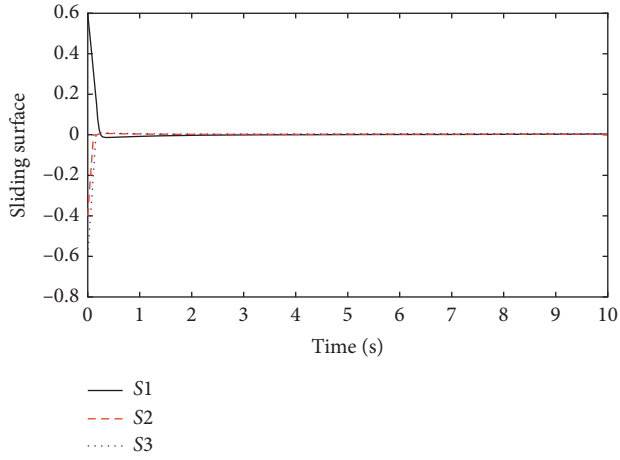

Figure 9: Sliding surface.

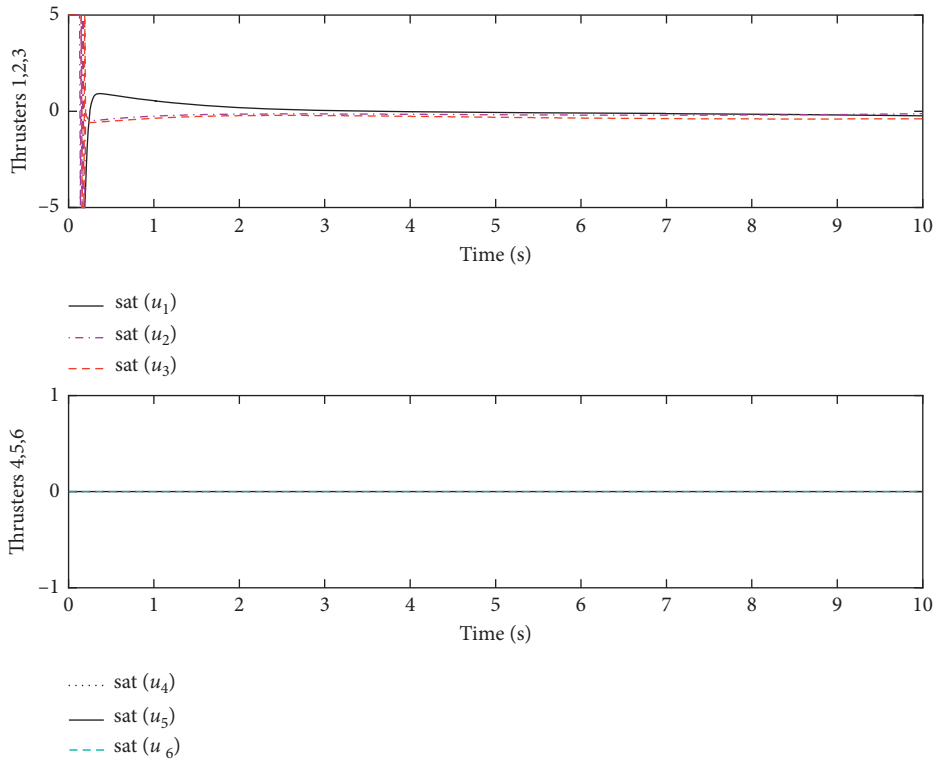

Figure 10: Control input produced by six thrusters.

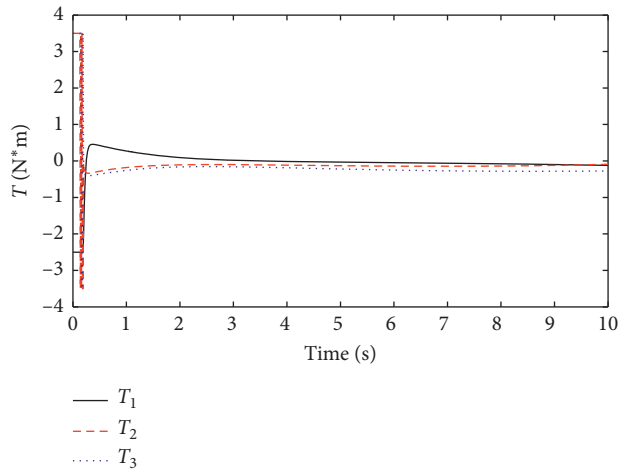

Figure 11: Control inputs acting on aircraft.

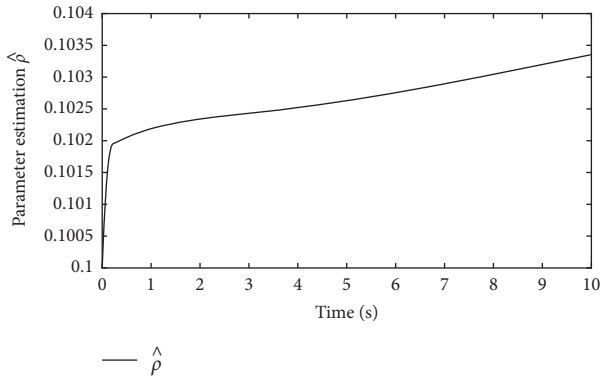

Figure 12: Adaptive law of the parameter $\hat{\rho}$.

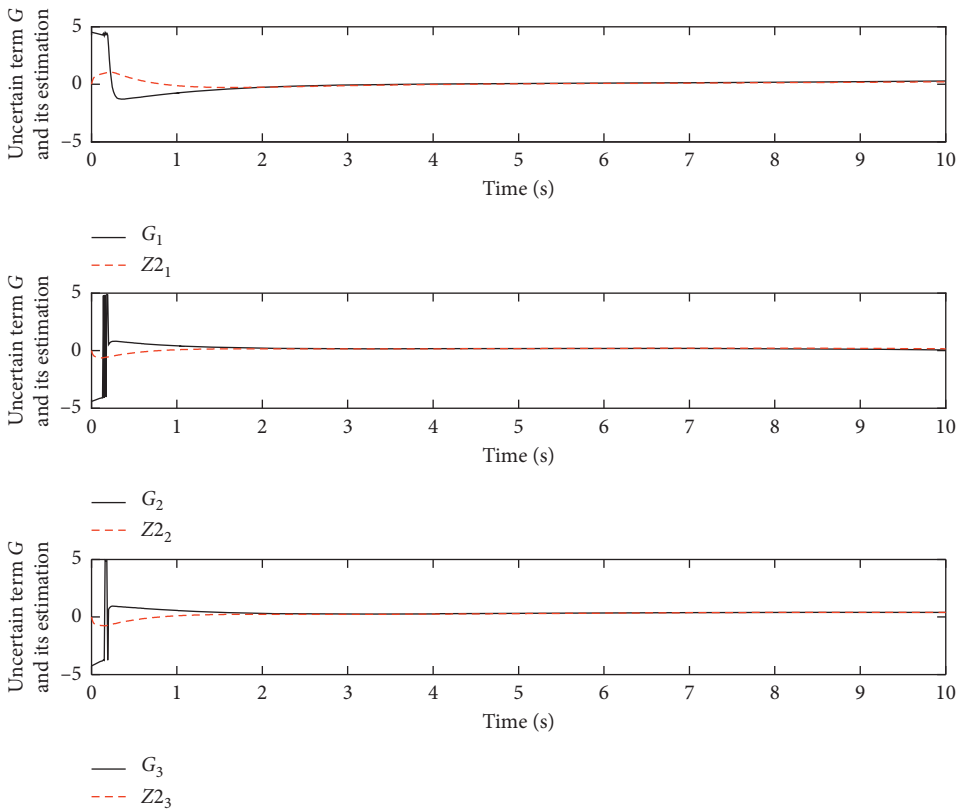

Figure 13: Estimation of general uncertainties by ESO.

5. Conclusions

In this paper, the attitude tracking problem for a spacecraft with uncertainties, external disturbances, actuator failures, and saturations is considered. The developed scheme for attitude tracking does not need to know the structure or upper bound information of the inertial matrix uncertainties and external disturbances. Based on ADR concept, the total uncertainties are attenuated by ESO, and the parameter adaptive method is used to deal with the thruster saturation problem; meanwhile, the sliding mode control law ensures the attitude tracking effect. Moreover, the proposed method can be well accommodated for the spacecraft with part of thrusters with total fault and saturation. Several simulation results have proved the effect of the proposed method.

Data Availability

The data used to support the findings of this study are included within the article.

Conflicts of Interest

The authors declare that they have no conflicts of interest.

Acknowledgments

This work was supported in part by the Natural Science Foundation of Shandong Province, China (Grant no. Zr2019mf065).

References

[1] C.-C. Kung, "Nonlinear Hꝏ robust control applied to F-16 aircraft with mass uncertainty using control surface inverse algorithm," *Journal of the Franklin Institute*, vol. 345, no. 8, pp. 851–876, 2008.

[2] W. Cai, X. H. Liao, and Y. D. Song, "Indirect robust adaptive fault-tolerant control for attitude tracking of spacecraft," *Journal of Guidance, Control, and Dynamics*, vol. 31, no. 5, pp. 1456–1463, 2008.

[3] Z. Zhu, Y. Xia, M. Fu, and S. Wang, "Attitude tracking of rigid spacecraft based on extended state observer," in *Proceedings of the 2010 3rd International Symposium on Systems and Control in Aeronautics and Astronautics*, pp. 621–626, IEEE, Harbin, China, June 2010.

[4] Y. Xia, Z. Zhu, M. Fu, and S. Wang, "Attitude tracking of rigid spacecraft with bounded disturbances," *IEEE Transactions on Industrial Electronics*, vol. 58, no. 2, pp. 647–659, 2011.

[5] Z. Zhu, Y. Xia, and M. Fu, "Adaptive sliding mode control for attitude stabilization with actuator saturation," *IEEE Transactions on Industrial Electronics*, vol. 58, no. 10, pp. 4898–4907, 2011.

[6] C. Pukdeboon, A. S. I. Zinober, and M.-W. L. Thein, "Quasi-continuous higher order sliding-mode controllers for spacecraft-attitude-tracking maneuvers," *IEEE Transactions on Industrial Electronics*, vol. 57, no. 4, pp. 1436–1444, 2010.

[7] P. M. Tiwari, S. Janardhanan, and M. un-Nabi, "Spacecraft anti-unwinding attitude control using second-order sliding mode," *Asian Journal of Control*, vol. 20, no. 1, pp. 455–468, 2017.

[8] Y. Park, "Robust and optimal attitude stabilization of spacecraft with external disturbances," *Aerospace Science and Technology*, vol. 9, no. 3, pp. 253–259, 2005.

[9] M. Krstic and P. Tsiotras, "Inverse optimal stabilization of a rigid spacecraft," *IEEE Transactions on Automatic Control*, vol. 44, no. 5, pp. 1042–1049, 1999.

[10] W. Luo, Y.-C. Chu, and K.-V. Ling, "Inverse optimal adaptive control for attitude tracking of spacecraft," *IEEE Transactions on Automatic Control*, vol. 50, no. 11, pp. 1639–1654, 2005.

[11] J. D. Boskovic, S.-M. Li, and R. K. Mehra, "Robust adaptive variable structure control of spacecraft under control input saturation," *Journal of Guidance, Control, and Dynamics*, vol. 24, no. 1, pp. 14–22, 2001.

[12] J. D. Boskovic, S.-M. Li, and R. K. Mehra, "Robust tracking control design for spacecraft under control input saturation," *Journal of Guidance, Control, and Dynamics*, vol. 27, no. 4, pp. 627–633, 2004.

[13] A.-M. Zou, A. H. J. de Ruiter, and K. D. Kumar, "Finite-time attitude tracking control for rigid spacecraft with control input constraints," *IET Control Theory & Applications*, vol. 11, no. 7, pp. 931–940, 2017.

[14] H. Jinchang and Z. Honghua, "A simple saturated control framework for spacecraft with bounded disturbances," *International Journal of Robust and Nonlinear Control*, vol. 26, no. 3, pp. 367–384, 2015.

[15] H. Long, F. Liu, J. Zhao, X. Xia, and C. Zhu, "Anti-unwinding constrained attitude control for flexible spacecraft with actuator saturation," *Proceedings of the Institution of Mechanical Engineers, Part G: Journal of Aerospace Engineering*, vol. 230, no. 1, pp. 90–104, 2015.

[16] Y. Jiang, Q. Hu, and G. Ma, "Adaptive backstepping fault-tolerant control for flexible spacecraft with unknown bounded disturbances and actuator failures," *ISA Transactions*, vol. 49, no. 1, pp. 57–69, 2010.

[17] Q. Shen, B. Jiang, and V. Cocquempot, "Fuzzy logic system-based adaptive fault-tolerant control for near-space vehicle attitude dynamics with actuator faults," *IEEE Transactions on Fuzzy Systems*, vol. 21, no. 2, pp. 289–300, 2013.

[18] Q. Shen, D. Wang, S. Zhu, and E. K. Poh, "Integral-type sliding mode fault-tolerant control for attitude stabilization of spacecraft," *IEEE Transactions on Control Systems Technology*, vol. 23, no. 3, pp. 1131–1138, 2015.

[19] Q. Hu, B. Xiao, and M. I. Friswell, "Robust fault-tolerant control for spacecraft attitude stabilisation subject to input saturation," *IET Control Theory & Applications*, vol. 5, no. 2, pp. 271–282, 2011.

[20] Y. Han, J. D. Biggs, and N. Cui, "Adaptive fault-tolerant control of spacecraft attitude dynamics with actuator failures," *Journal of Guidance, Control, and Dynamics*, vol. 38, no. 10, pp. 2033–2042, 2015.

[21] B. Xiao, Q. Hu, and Y. Zhang, "Adaptive sliding mode fault tolerant attitude tracking control for flexible spacecraft under actuator saturation," *IEEE Transactions on Control Systems Technology*, vol. 20, no. 6, pp. 1605–1612, 2012.

[22] A.-M. Zou and K. D. Kumar, "Adaptive fuzzy fault-tolerant attitude control of spacecraft," *Control Engineering Practice*, vol. 19, no. 1, pp. 10–21, 2011.

[23] C. Cheng, Y. Di, J. Xu, and T. Yuan, "Advanced backstepping control based on ADR for non-affine non-strict feedback nonlinear systems," *Automatika*, vol. 59, no. 2, pp. 220–230, 2018.

[24] C. H. Cheng, Y. HU, and J. WU, "Auto disturbance controller of non-affine nonlinear pure feedback systems," *Acta Automatica Sinica*, vol. 40, no. 7, pp. 1528–1536, 2014.

[25] C. Chunhua, H. Yunan, and W. Jinhua, "Auto disturbance rejection controller for non-affine nonlinear systems with adaptive observers," *Control Theory & Applications*, vol. 31, no. 2, pp. 148–158, 2014.

[26] C. Chun-hua, W. Jin-hua, Y. Hu, and L. Jing, "Adaptive control of non-affine nonlinear 320 system with saturation constraint," *Control Theory & Applications*, vol. 31, no. 8, pp. 1000–1008, 2014.

[27] K. Wang, F. Xiao, J. Pang, J. Ren, C. Duan, and L. Li, "State of charge (SOC) estimation of lithium-ion battery based on adaptive square root unscented kalman filter," *International Journal of Electrochemical Science*, vol. 15, no. 9, pp. 9499–9516, 2020.

[28] J. Han, *Active Disturbance Rejection Control Technique-The Technique for Estimating and Compensating the Uncertainties*, National Defense Industry Press, Beijing, China, 2008.

[29] M. Krstic, I. Kanellakopoulos, and V. Petar, *Nonlinear and Adaptive Control Design*, Wiley, New York, NY, USA, 1995.

[30] Q. Hu, "Robust adaptive sliding mode attitude maneuvering and vibration damping of three-axis-stabilized flexible spacecraft with actuator saturation limits," *Nonlinear Dynamics*, vol. 55, no. 4, pp. 301–321, 2008.

Hindawi
Mathematical Problems in Engineering
Volume 2020, Article ID 6698688, 15 pages
https://doi.org/10.1155/2020/6698688

Research Article

Segmented Power Supply Preset Control Method of High-Speed Rail Contactless Traction Power Supply System considering Regenerative Braking Energy Recovery

Ruoqiong Li,[1] **Junjie Wang**,[1] **Xuan Zhao**,[1] **and Xin Li**[2]

[1]*School of Automation & Electrical Engineering, Lanzhou Jiaotong University, Gansu 730070, China*
[2]*School of New Energy & Power Engineering, Lanzhou Jiaotong University, Gansu 730070, China*

Correspondence should be addressed to Ruoqiong Li; liruoqiong26@163.com and Junjie Wang; 15139152002@163.com

Received 16 October 2020; Revised 23 November 2020; Accepted 8 December 2020; Published 21 December 2020

Academic Editor: Licheng Wang

For high-speed rail with high energy consumption, the recovery and utilization of regenerative braking energy is essential to improve the energy consumption of high-speed rail. As a technical link, the energy bidirectional feed inductively coupled power transfer (ICPT) system can realize the regenerative braking energy recovery of the contactless traction power supply system. Furthermore, considering that the braking energy of the high-speed rail is the largest when entering the station during the whole line operation, the braking section of the station is mainly considered. This paper proposes a preset control method for segmented power supply of the energy bidirectional feed ICPT system considering regenerative braking energy recovery. By establishing the steady-state mathematical model of the bidirectional ICPT system, the influence of the internal phase-shift angles φ_1 and φ_2 and the external phase-shift angle γ on the operating state of the system is analyzed. To realize system synchronization under the operation of EMUs, a train braking model is established through force analysis, and a power preset controller is designed to realize the synchronous control of the power flow of the bilateral system. According to the braking process of the train entering the station, the switching control method of the segment coil under the different conditions of the single train entering the station and the multitrain entering the station is proposed to ensure the reliability and flexibility of the train power supply. The simulation results of the 350 kW ICPT system simulation model show that the system can operate stably when the power transmission simulation is switched, and the transmission efficiency can reach 89%, which proves the feasibility of the control method. Energy-saving estimates show that a single train can recover about 200–300 kWh of electric energy during single braking. The comparison with the measured data verifies the accuracy of the modeling in this paper.

1. Introduction

Electrified rail transit system is an important load of the power system. According to statistics, by the end of 2018, China's high-speed railway operation mileage has reached 29000 km, and the total power consumption of the railway in 2018 is up to 71.1 billion kWh, of which high-speed railway consumes about 40% [1].

Energy-saving operation is the key and difficult point for the further development of rail transit at present. It is of great significance to research renewable energy storage in the field of high-speed railway, heavy-duty railway, long ramp line, or railway terminal station. As a braking system, regenerative braking is an effective energy-saving operation measure. It can reduce the speed by reversing the operation of the motor. Regenerative braking technology uses the motor of the train as the generator to convert mechanical energy into electrical energy and return it to the power grid. Moreover, according to the analysis of measured data, the proportion of regenerative energy consumption increases with the increase of braking initial speed [1]. For high-speed railway, the recycling of regenerative braking energy is important to improve the energy consumption of high-speed railway [2].

In the aspect of high-speed railway traction power supply, at present, the electric locomotive is mainly driven

by the catenary, and the excessive meeting of trains will impact the catenary and onboard electric equipment. In addition to the impact of extreme weather, the problems of pantograph wear, spark, and corrosion are also serious. The contactless power supply adopts the medium-voltage DC power supply system, which overcomes the problems of the traditional single-phase AC contact power supply method such as bow-to-network coupling, negative sequence, excessive phase separation, contact line galloping, and complex regenerative braking energy storage and utilization schemes. According to the principle of electromagnetic induction, ICPT technology supplies the electric energy to the locomotive in a contactless way through the inductive coupling between coils. Furthermore, the characteristics of the ICPT system, such as short distance, high power, and high efficiency, determine its good development prospects in the field of rail transit [3]. When the train is at rest, Professor Pugi Luca of Italy proposed the innovative application of radio energy transmission technology in the railway "Parking" function (power collection under static state) [4]. South Korea has designed an MW level train contactless real-time current collection system experimental line, and its system efficiency can reach 82.7% [5]. Professor Seung Beop Lee's team improved the existing ferrite energy transmission module while meeting the system electromagnetic field strength, magnetic saturation, and induced voltage, optimized the design framework of railway wireless charging system, saved construction cost [6], and further improved the construction feasibility of railway contactless traction power supply system.

For contact traction power supply system regenerative braking energy recovery, there are three common solutions: energy consumption, feedback, and recovery. The energy-consuming structure is simple and easy to realize, but this solution is not energy-saving. The feedback type is mainly divided into direct feedback to the power grid and other trains using the same bridge arm. Although the cost is saved, the impact on the power grid is large, and the harmonic problem is serious. Professor Pugi Luca studied the basis of the existing train model of energy feedback of contact traction system. Aiming at two trains performing their tasks in the opposite direction on the same line, considering feeders and different types of reversible and irreversible substations, a simple and efficient model was obtained [7]. Besides, a control strategy with feedforward control is introduced into the energy storage system to suppress bus voltage fluctuations. By introducing a nonlinear interference observer (NDO), the shortcomings of traditional feedforward control methods that require remote measurement are solved [8]. In the recovery scheme, the energy storage device is used to realize energy storage and dispatching, and peak and valley reduction can be realized, which is a feasible scheme [9–14]. For the recycling scheme, some scholars put forward an energy storage scheme and control strategy of traction power supply system based on railway power regulator, which solves the problem of negative sequence and harmonic current compensation after the energy storage device is connected to the traction power supply system [15]. Also, a coordinated control strategy is proposed by combining the supercapacitor with the railway regulator to solve the problem of runaway discharge of the supercapacitor [16]. In the aspect of the battery management system, some scholars proposed an adaptive square root Unscented Kalman Filter algorithm based on the second-order Thevenin equivalent circuit model, which improves the accuracy of battery state estimation [17]. The intervention of the energy storage system increases the utilization space of the regenerative braking energy of the train. In the multitrain operation system considering the ground energy storage system, the research on the energy-saving operation of the train has a deeper field and significance. In addition, the hybrid energy storage system has been widely used because of its high efficiency. Professor Wang Kai's team proposed an improved state of charge (SOC) control energy allocation strategy for the hybrid energy storage system of electric vehicles (EV), which improves energy utilization and reduces the battery aging effect [18].

Research on regenerative braking energy recovery of contactless traction power supply system is very rare. Besides, the traditional ICPT system can only achieve a one-way flow of energy and complete one-way traction power supply and cannot provide a feedback channel for regenerative braking energy. Therefore, the ICPT system with energy bidirectional feed is the key to solve the problem of contactless traction power supply regenerative braking energy recovery. Its bidirectional energy feedback characteristic is first proposed to be used in the practical application environment of V2G [19], which can solve the danger brought by plug-in charging and achieve the best energy scheduling. Based on the application background of rail transit, the forward transmission mode of bidirectional ICPT system can realize traction power supply, and the reverse transmission mode provides a recovery channel for regenerative braking energy. While the traditional disadvantages of contact traction power supply system are solved, it is convenient to realize the feedback, recovery, and utilization of regenerative braking energy, which provides strong technical support for the early realization of transportation energy Internet.

At present, the common bidirectional ICPT system control methods need real-time communication to ensure the synchronization of the bidirectional system, which brings great economic and technical problems. In this regard, Professor Udaya K. Madawala proposed a method to adjust the power flow direction by detecting the active and reactive power in the resonance network without real-time communication and only using a controller at the secondary side, but the current distortion rate is very high [20]. Chen Kainan's team at Tsinghua University has made a comprehensive study on the bidirectional ICPT system. In [21], the efficiency optimization control strategy of the bidirectional ICPT system with multiple degrees of freedom is first proposed. However, it still needs real-time communication to achieve synchronization. In [22], a method based on disturbance and observation is proposed to realize the synchronization of bilateral control signals. Reference [23] can realize phase synchronization and maximum efficiency point tracking independent of real-time wireless

communication. However, the above control strategies still need weak wireless communication to identify the mutual inductance value. Combined with the actual situation of high-speed rail operation, the communication cost is very high, which is not suitable for the field of rail transit. In terms of modeling of induction power transmission system, Professor Pugi Luca's team innovatively proposed that the system model should be equivalent to the lumped mechanical model, and then the conventional modal analysis method used to study the mechanical vibration system was used to optimize it [24], which provided a new idea for the modeling of bidirectional ICPT system.

In addition, the high-speed rail runs fast, the traction power is high, and the power supply process is dynamic, so the design of the power supply coil should ensure the stability and efficiency of the system. There are two types of power supply coil structure in the ICPT system: long rail type and segmented type. The structure of the long rail coil is simple, but there are some problems, such as low utilization rate, large coil impedance, and electromagnetic compatibility. The single unit capacity of the segmented coil is small, which can realize time-sharing segmented power supply and has higher reliability. Therefore, in practical application, the segmented coil is more ideal [25–27]. At present, the ICPT system subsection power supply is mainly based on one-way power flow to load position detection and coil subsection control research. For the sake of my knowledge, the energy bidirectional feed ICPT system has not yet shown a typical subsection power supply scheme.

Given the above problems, this paper divides the regenerative braking process of the train according to the characteristic curve, according to the energy flow relationship of the braking process, through the onboard controller responsible for the adjustment of the power flow size and direction of the converter on the side of the train and the ground controller responsible for the power control, provides the switching logic to the ground coil switching, and obtains a sectionalized power supply line suitable for the regenerative braking energy recovery of the high-speed railway cycle power preset switching control method. Firstly, the energy bidirectional feed ICPT system with a segmented power supply is introduced, and its steady-state mathematical model is established. The relationship between the transmission power and the phase-shift angle of the converter is analyzed. Secondly, the three-stage braking model of the train is established by force analysis. According to the braking model, the power flow control method is introduced, and the sectional coil control method for a single train and multitrain operation is proposed, respectively. Finally, through the establishment of a simulation model in MATLAB/Simulink, the feasibility of the control method is verified, and the energy-saving is estimated.

2. Notation

The notation system is composed of three parts: symbols, parameters, and decision variables. The main purpose of the system is to help query symbols in equations. The interpretation of symbols may be repeated in some places in this paper to achieve better understanding.

Symbols

ICPT: Inductively coupled power transfer
EMU: Electric multiple units.

Parameters

ω: The angular frequency of converter
M: The coil mutual inductance
$\dot{u}_1$: Fourier expansion of primary converter output voltage
$\dot{u}_2$: Fourier expansion of secondary converter output voltage
U_1: The fundamental component in the output voltage of the primary converter
U_2: The fundamental component in the output voltage of the secondary converter
I_2: The phasor of current in secondary resonance coil
I_2: The output current
γ: The phase-shifted phase angle between two-side converter drive signals
φ_1: The internal shifted phase angle between primary converter drive signals
φ_2: The internal shifted phase angle between secondary converter drive signals
P_1: The input active power
Q_1: The input reactive power
P_2: The output active power
Q_2: The output reactive power
θ_P: The power phase angle
P_{in}: The input power considering loss
P_{out}: The output power considering loss
η_{all}: The overall efficiency of bidirectional ICPT system
G: The train gravity
N: The rail supporting force
F_q: The train traction
W_0: The basic resistance
W_f: The additional resistance
W_s: The additional tunnel resistance
W_r: The additional curve resistance
W_i: The additional ramp resistance
W_z: The regenerative braking force
v_1: The speed at point 1 by linear interpolation
v_2: The speed at point 2 by linear interpolation
F_1: The traction at point 1 by linear interpolation
F_2: The traction at point 2 by linear interpolation
f_q: The traction per unit weight
m: The total train mass
g: The gravitational acceleration
W_1: The regenerative braking force at point 1 by linear interpolation
W_2: The regenerative braking force at point 2 by linear interpolation
w_z: The regenerative braking force per unit weight
w_0: The unit basic resistance
v: The real-time train speed
i: The slope of the ramp
w_i: The unit ramp additional resistance

R: The curve radius
w_r: The unit curve additional resistance
L_s: The length of the train inside the tunnel
w_s: The additional resistance per unit tunnel
c: The unit resultant force
a: The train acceleration
μ: The high-speed rail slewing weight factor
v_0: The initial speed of regenerative braking
v_s: The speed in each stage of regenerative braking
s_n: The distance of each stage of regenerative braking
t_0: The initial time of regenerative braking
t_n: The time of each stage of regenerative braking
η: The comprehensive transmission efficiency of contact traction system
P_z: The regenerative braking power
C_s: The train resultant force
P_s: The traction power
P_{ref}: The reference power calculated by power model
P_0: The measured power
$|P_{\text{out}}|$: The absolute value of the output power
Q: The total energy can be recovered during regenerative braking
P_n: The power of each stage of regenerative braking.

Decision variables

A: The empirical constant
η_G: The transmission efficiency of gearbox
η_M: The transmission efficiency of traction motor
η_I: The transmission efficiency of inverter
η_C: The transmission efficiency of rectifier
η_T: The transmission efficiency of automotive transformer.

3. Energy Bidirectional Feed ICPT System

3.1. System Structure. The segmented power supply structure of the bidirectional ICPT system is shown in Figure 1. The system is composed of onboard part and ground part. When the system is in traction mode, the ground part first obtains 35 kV direct current from the 110 kV AC network side through the AC/DC link, then obtains the standard 2800 V direct current for the bidirectional ICPT system through the PET link, and finally passes through the magnetic coupling coil transmits energy to the vehicle-mounted part. The vehicle-mounted part obtains 2800 V direct current and then supplies energy to the electric motor through the DC/AC link to realize train traction. When the system is in the regenerative braking mode, the onboard part of the motor reverses to become a generator, through the AC/DC link to obtain the standard 2800 V direct current for the bidirectional ICPT system, and then the regenerative braking energy is fed back to the ground part through the magnetic coupling coil. The ground part selectively feeds back the regenerative braking energy to the DC bus through the PET link or recovers the regenerative braking energy through energy storage devices such as supercapacitors and batteries. The segmented coil structure is adopted to meet the demand for long-distance power supply of high-speed railway and improve the transmission efficiency.

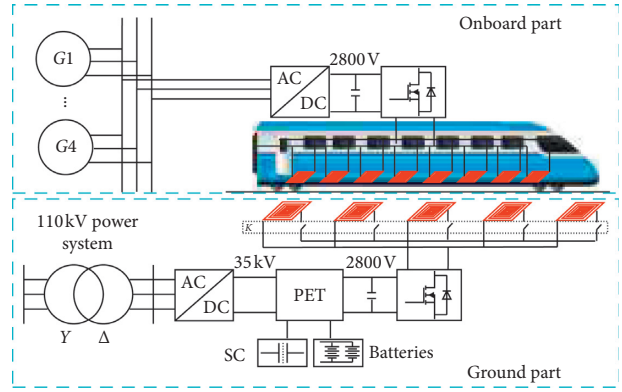

Figure 1: Schematic diagram of the bidirectional ICPT system segmented power supply structure.

3.2. Mathematical Model of Bidirectional ICPT System. As shown in Figure 2, compared to a unidirectional ICPT system, there are H-bridge converters composed of MOSFETs (or IGBTs) and diodes in antiparallel on both sides of the bidirectional ICPT system to implement the on-demand conversion process of electrical energy. In the compensation network part, this paper adopts a dual LCC type composite resonance compensation structure, which is more robust than the typical LC series compensation structure. Compared with the LCL compensation structure, the system power of the LCC structure is higher under the same parameters. Therefore, the LCC structure is more suitable for dynamic bidirectional wireless power supply [28]. In Figure 2, $Lp1$ and $Ls1$ are the coil self-inductance, C_{p1}, C_{p2}, and L_{p2} are the primary side resonance compensation capacitors and inductances, respectively, C_{s1}, C_{s2}, and L_{s2} are the secondary side resonance compensation capacitors and inductances, and R_p and R_s the equivalent resistances of primary and secondary resonant circuits, respectively. u_1 and u_2 are the output voltages of the original secondary converter, i_1 and i_2 are the currents in the primary and secondary resonance network, and U_1 and U_2 are the DC grid voltage and the train's equivalent DC power supply voltage, respectively.

Control methods for power flow can be divided into two categories. In the first type, the H-bridge converter on one side works in the inverting state and the controllable switching devices in the H-bridge converter on the other side are all turned off, and the diode is used to work in the rectified state [29], but the work efficiency of this control strategy is greatly affected by load changes.

Phase-shift control is currently a relatively mature control method that can be used in dynamic bidirectional wireless energy transmission systems. When phase-shift control is used, Figure 3 shows the relationship between the control signals (S_{11}, S_{12}, S_{21}, and S_{23}) and system variables when the system is operating in resonance. It can be seen from Figure 3 that φ_1 and φ_2 are the internal phase-shift angles of the control signals of the primary and secondary converters and γ is the external shift phase angles between the control signals of the primary and secondary converters, and the upper and lower bridge leg switches on and off complementarily with a duty

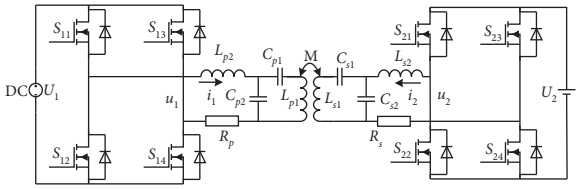

Figure 2: Topology structure of bidirectional ICPT system.

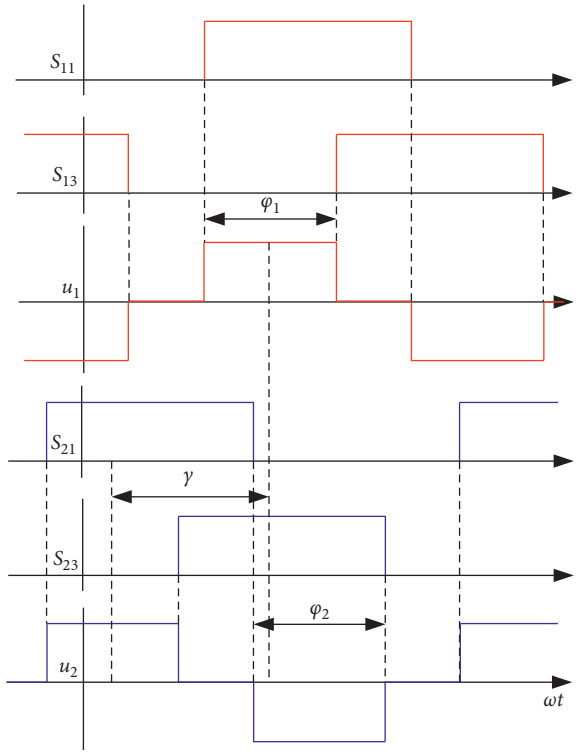

Figure 3: Drive signal and output voltage of the converter.

cycle of 0.5 in constant frequency. Besides, in the bidirectional ICPT system, the dead time between drive signals is small and has a little effect on the power transmission characteristics, so it is ignored in the following analysis.

The transmission power of the bidirectional ICPT system is mainly related to the primary and secondary voltages and the fundamental component of the current. Due to the resonant operating characteristics, the higher harmonics contribute little to power transmission. To simplify the analysis, the fundamental harmonic approximation method can be used [30]. The simplified model of the fundamental wave of the bidirectional ICPT system is shown in Figure 4 [28].

It can be seen from the above figure that the output voltages u_1 and u_2 of the primary and secondary full bridges are replaced by their fundamental components $\dot{u}_1$ and $\dot{u}_2$, which can be obtained by Fourier series expansion:

$$\begin{cases} \dot{u}_1 = \dfrac{2\sqrt{2}}{\pi} U_1 \sin\dfrac{\varphi_1}{2} \angle 0, \\ \dot{u}_2 = \dfrac{2\sqrt{2}}{\pi} U_2 \sin\dfrac{\varphi_2}{2} \angle -\gamma. \end{cases} \tag{1}$$

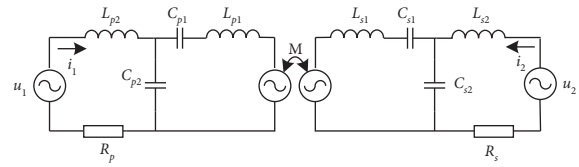

Figure 4: Fundamental simplified model of the bidirectional ICPT systems.

Since the bidirectional ICPT system can be used as a good filter for the first harmonic at the resonance frequency, based on the basic harmonic analysis method, when the bidirectional ICPT system is in resonance, u_1 and u_2 can be expressed as

$$\begin{cases} \dot{U}_1 = R_p \dot{I}_1 + j\omega M \dot{I}_2, \\ \dot{U}_1 = R_s \dot{I}_2 + j\omega M \dot{I}_1. \end{cases} \tag{2}$$

By substituting (2) into (1), the fundamental component of i_2 can be derived as

$$\dot{I}_2 = \frac{2\sqrt{2} R_p U_2 \sin(\varphi_2/2)\cos\gamma}{\pi\left[R_p R_s + (\omega M)^2\right]} + \frac{2\sqrt{2} j\left(R_p U_2 \sin(\varphi_2/2)\sin\gamma - \omega M U_1 \sin(\varphi_1/2)\right)}{\pi\left[R_p R_s + (\omega M)^2\right]}. \tag{3}$$

To achieve high-efficiency operation of the bidirectional ICPT system, the value of the out-shifted phase angle γ is set to $\pi/2$ when the power is transferred in the forward direction, and the value of the out-shifted phase angle γ is set to when the power is transferred in the reverse direction $3\pi/2$ [28]. Therefore, in order to achieve the synchronous control of the bilateral preset controller and achieve the expected phase synchronization state, the working state with γ equal to $\pi/2$ or $3\pi/2$ is set as the control index of the preset controller.

By analyzing the output current I_2, it can be obtained that the power is affected by the phase-shift angle. From (3), the relationship between the output current I_2 and the internally shifted phase angles φ_1 and φ_2 and the externally shifted phase angle γ is

$$I_2 = \frac{4\sqrt{2}\omega M U_1 \sin(\varphi_1/2)\sin(\varphi_2/2)\sin\gamma}{\pi^2\left[R_s R_p + (\omega M)^2\right]} - \frac{4\sqrt{2} R_p U_2 \sin^2(\varphi_2/2)}{\pi^2\left[R_s R_p + (\omega M)^2\right]}. \tag{4}$$

As shown in Figure 5, the maximum value of I_2 is obtained when γ is equal to $\pi/2$ (the minimum value is obtained when γ is equal to $3\pi/2$); that is, when the phase-shift angle is $\pi/2$ or $3\pi/2$, the forward or reverse transmission power is maximum and the transmission efficiency is optimal, which verifies the accuracy of the modeling in this paper.

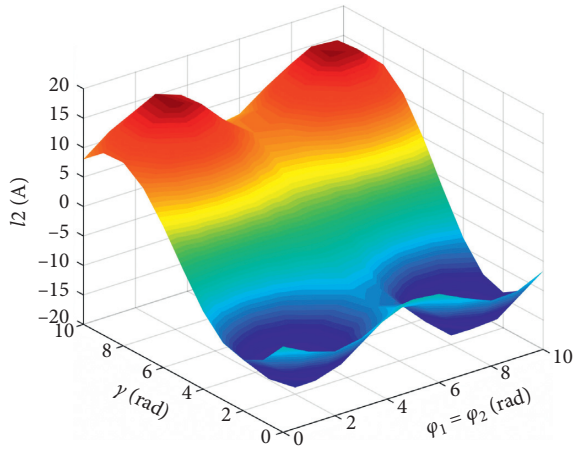

Figure 5: Relationship between I_2 and γ.

Because the braking model proposed in this paper corresponds to the real-time power model of the train, the actual control object is the flow and flow direction of active power and reactive power. Therefore, according to equations (2) and (3), the active power and reactive power output by the system can be expressed as

$$\begin{cases} P_1 = \dfrac{4\sqrt{2}\,R_s U_1^2 \sin^2(\varphi_2/2)}{\pi^2\left[R_s R_p + (\omega M)^2\right]} \\ \quad + \dfrac{4\sqrt{2}\,\omega M U_1 U_2 \sin(\varphi_1/2)\sin(\varphi_2/2)\sin\gamma}{\pi^2\left[R_s R_p + (\omega M)^2\right]}, \\ Q_1 = \dfrac{4\sqrt{2}\,j\omega M U_1 U_2 \sin(\varphi_1/2)\sin(\varphi_2/2)\cos\gamma}{\pi^2\left[R_s R_p + (\omega M)^2\right]} \\ \quad + \dfrac{4\sqrt{2}\,j R_s U_1^2 \sin^2(\varphi_2/2)}{\pi^2\left[R_s R_p + (\omega M)^2\right]}, \end{cases} \tag{5}$$

$$\begin{cases} P_2 = \dfrac{4\sqrt{2}\,R_p U_2^2 \sin^2(\varphi_2/2)}{\pi^2\left[R_s R_p + (\omega M)^2\right]} \\ \quad - \dfrac{4\sqrt{2}\,\omega M U_1 U_2 \sin(\varphi_1/2)\sin(\varphi_2/2)\sin\gamma}{\pi^2\left[R_s R_p + (\omega M)^2\right]}, \\ Q_2 = \dfrac{4\sqrt{2}\,j R_s U_1^2 \sin^2(\varphi_2/2)}{\pi^2\left[R_s R_p + (\omega M)^2\right]} \\ \quad - \dfrac{4\sqrt{2}\,j\omega M U_1 U_2 \sin(\varphi_1/2)\sin(\varphi_2/2)\cos\gamma}{\pi^2\left[R_s R_p + (\omega M)^2\right]}. \end{cases}$$

The power phase angle is defined here to make the external phase-shift angle γ between converters consistent with the flow direction of output power [20].

$$\theta_P = \arccos\left(\frac{P_2}{\sqrt{P_2^2 + Q_2^2}}\right). \tag{6}$$

When the system is fully tuned, the reactive power can be ensured to be zero by adjusting the power phase angle θ_P to 0 or π. Therefore, when θ_P is 0 or π, it corresponds to the maximum value of the forward and reverse transmissions of the system. Combining the above analysis, it can be concluded that θ_P of 0 or π corresponds to γ of $\pi/2$ or $3\pi/2$.

According to [29], the input and output power of the primary and secondary sides of the bidirectional ICPT system should be expressed as (if the switching loss is considered)

$$\begin{cases} P_{\text{in}} = P_1 + P_{\text{loss\_}p}, \\ P_{\text{out}} = |P_2| - P_{\text{loss\_}s}. \end{cases} \tag{7}$$

To simplify the analysis, the switching loss is ignored. Thus, the overall work efficiency of the system can be expressed as follows:

$$\eta_{\text{all}} = \frac{P_{\text{out}}}{P_{\text{in}}} = \frac{|P_2|}{P_1}. \tag{8}$$

Based on the above mathematical analysis of the bidirectional ICPT system, the control method more suitable for the application background of this paper is to control the output side (i.e., train side) to work at 0 or π power angle θ_P, so as to ensure the high efficiency of the system while eliminating the communication channel to achieve bilateral phase synchronization.

4. EMU Brake Model

4.1. EMU Parameters. This article uses CR400BF EMU as an example for calculation. The specific parameters are shown in Table 1 [31]. It has the advantages of the good overall performance of the car body, high safety, and reliability and is currently the world's highest speed EMU operating.

Under normal circumstances, EMUs use a combination of regenerative braking and electropneumatic braking. To verify the proposed control strategy, this paper assumes a pure regenerative braking method to analyze the braking process of the train at the station.

4.2. Force Analysis of EMU. This paper uses a single-particle train model for analysis, as shown in Figure 6.

Except for gravity G and rail support force N, there are mainly traction force F_q, basic resistance W_0, additional resistance W_f (including additional tunnel resistance W_s, curve additional resistance W_r, and ramp additional resistance W_i), and braking force W_z in the direction of train movement.

Table 1: CR400BF EMU parameters.

EMU parameters	Parameter value
Train mass	501t
Train formation	4M4T
Train length	200 m
Top speed	400 km/h
Maximum braking distance	6500 m
Motor power	650 kW
Installed power	10400 kW
Capacity	576

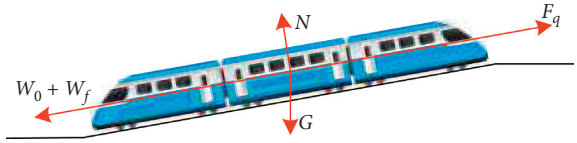

Figure 6: Single-particle train model.

The traction force F_q of the train is determined by the traction characteristic curve of the train, which is generally obtained by the manufacturer or the traction experiment. The traction force-speed characteristic curve of CR400BF is shown in Figure 7 [31].

This paper uses linear interpolation to calculate the value. Assuming that two points (v_1, F_1) and (v_2, F_2) on the traction characteristic curve are known and the point (v_q, F_q) is a point between v_1 and v_2, then the calculation equation of point traction is as follows:

$$F_q = F_1 + \frac{(F_2 - F_1) \times (v_q - v_1)}{v_2 - v_1}. \tag{9}$$

Thus, the traction unit weight is as follows:

$$f_q = \frac{F_q}{Mg}. \tag{10}$$

The calculation method of the train braking force W_z differs depending on the braking method. When regenerative braking is used, the value can be calculated by linear interpolation based on the regenerative braking characteristic curve. The regenerative braking characteristic curve of CR400BF is shown in Figure 8 [31].

As above, assuming that two points (v_1, W_1) and (v_2, W_2) on the traction characteristic curve are known and the point (v_z, W_z) is a point between v_1 and v_2, the equation for calculating this point is as follows:

$$W_z = W_1 + \frac{(W_2 - W_1) \times (v_z - v_1)}{v_2 - v_1}. \tag{11}$$

Therefore, the regenerative braking force per unit weight is

$$w_z = \frac{W_Z}{mg}. \tag{12}$$

In addition, the resistance when the train is running needs to be considered. The resistance can be divided into two types: basic resistance W_0 and additional resistance W_f.

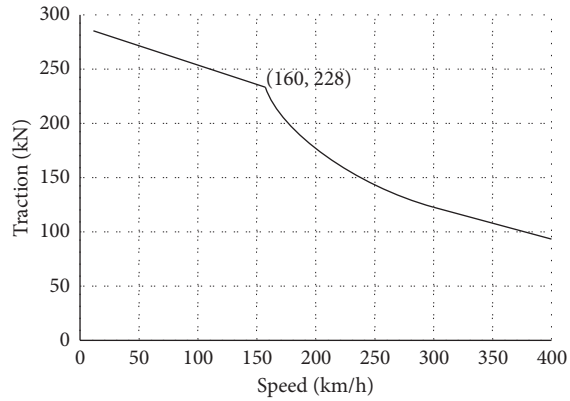

Figure 7: CR400BF traction characteristic curve.

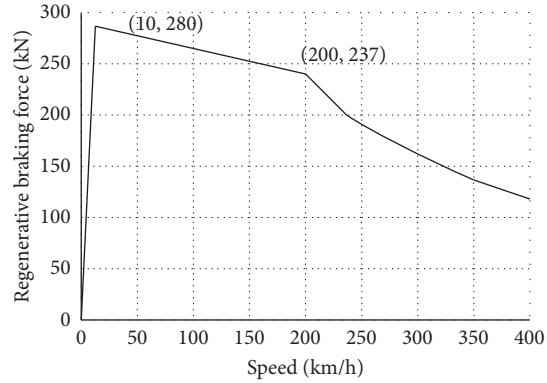

Figure 8: CR400BF regenerative braking characteristic curve.

The basic resistance mainly comes from the frictional resistance of the axle bearing, the rolling friction between the wheelset and the rail, the sliding friction between the wheelset and the rail, the resistance caused by the wheel-rail impact vibration, and the air resistance. The above reference factors are too complicated for analysis, so the basic resistance equation is generally derived from experience. The basic resistance equation of CR400BF is

$$w_0 = 3.99 + 0.0127v + 0.001092v^2. \tag{13}$$

The additional resistance is mainly affected by the slope of the line, the radius of the curve, and the tunnel. It is based on experience, and the calculation equations of each model are not much different. The equations are as follows:

$$\begin{aligned} w_i &= \frac{1000W_i}{mg} \approx i, \\ w_r &= \frac{A}{R}, \\ w_s &= 0.00013L_s. \end{aligned} \tag{14}$$

Therefore, the resulting unit force c of the train is

$$c = f_q - w_i - w_r - w_s - w_0 - w_z. \tag{15}$$

4.3. Segment Analysis of Braking Process. Referring to the method of establishing ATP safety braking curve in IEEE1474.1 [32], this paper combines the onboard ATP reaction stage and traction cancellation reaction stage in the traditional five-stage braking process, retains the train inertia stage, combines the braking establishment stage and braking stage, and finally simplifies it into three-stage braking process, that is, equipment response and traction removal stage, train coasting stage, and braking establishment to parking stage.

Stage 1. Equipment response delay and traction removal stage: the ICPT system keeps the energy flow forward, and the bilateral preparations suspend the system and remove power.

Stage 2. During the train idle stage, the ICPT system is suspended.

Stage 3. From the brake establishment to the stop stage, the ICPT system starts to transmit energy in the reverse direction, and the two sides start to control the system with reference to the preset brake model.

According to the typical parameter [32] in IEEE1474.1, the reference time of each stage can be obtained. The resultant force and the working condition of the ICPT system are shown in Table 2.

For the purpose of better analyzing the specific establishment process of the three-stage brake model, the following flowchart analysis is made, as shown in Figure 9. As shown in the figure, firstly, before the braking model starts to work, the initial parameters of the train are sampled and the motion characteristic parameters are extracted, such as initial speed v_0, ramp i, curve radius R, and tunnel length L_s, and then enter into the calculation of the resultant force and real-time speed of the braking model in the first stage. When the time is greater than the set value of the first stage time, the process is judged to enter the second stage of calculation. Similar to the first stage, the resultant force and real-time speed of the second stage are calculated according to the final calculation results of the first stage. When the time is greater than the set value of the second stage time, the process is judged to enter the third stage of operation. In the final braking stage, the judgment process is finished and the three-stage braking model is output when the real-time speed is less than or equal to 0.

Based on the above analysis, a three-stage braking model is established. Its main purposes are to provide a reliable reference speed and resultant force for the power model, to provide a PWM generator with an out-of-phase angle γ that controls the direction of power flow, and to provide switching logic for coil switching control.

First of all, to obtain the *v-s* braking curve at each stage, the relationship between the unit resultant force and the acceleration needs to be found first. When considering the EMU rotation weight coefficient (experience value 0.08), the relationship is

$$a = \frac{gc}{1000(1+\mu)} = \frac{0.00981}{(1+\mu)}c \tag{16}$$

Therefore, the speed of each stage can be expressed as

$$v_s = \frac{v_0}{3.6} - at = \frac{v_0}{3.6} - \frac{0.00981}{(1+\mu)}ct. \tag{17}$$

The distance of each stage can be expressed as

$$s_n = \int_{t_0}^{t_n} v\mathrm{d}t. \tag{18}$$

It can be known from the above analysis that the brake model can obtain the real-time speed v_s of the train only by specifying the initial braking speed v_0 of the train and the braking distance s_n at each stage.

5. Control Strategy

Preset control mainly includes an onboard controller and ground controller, as shown in Figure 10. Among them, the onboard controller is mainly responsible for adjusting the power flow size and direction of the onboard side ICPT system, and the braking model provides the core reference for the control strategy. Besides power control, the ground controller also needs to provide the switching logic of the grounding coil.

5.1. Power Model. Since the contact train transmission system includes multiple electric energy conversion processes, the equation for the comprehensive transmission efficiency η of the contact traction system is

$$\eta = \eta_G \cdot \eta_M \cdot \eta_I \cdot \eta_C \cdot \eta_T. \tag{19}$$

According to the measured data, the overall transmission efficiency of the contact traction system η is generally 0.85.

From this, the regenerative braking power of the train can be obtained as

$$P_z = \frac{1000C_s v_s}{3.6}\eta. \tag{20}$$

In addition, the traction power is

$$P_s = \frac{1000C_s v_s}{3.6\eta}. \tag{21}$$

5.2. Power Flow Control Method. The braking model works according to the given initial braking speed v_0 and the expected braking distance s. The calculated real-time speed v_s is passed to the power model to obtain the reference power P_{ref}. After comparing it with the measured power P_0, the error signal is transmitted to the PI. The control module generates an internally shifted phase angle φ for adjusting the amount of transmitted power and realizes the amount of power adjustment by the PWM generator. Besides, the braking model compares the preset reference value of power phase angle $\theta_{P\mathrm{ref}}$ with that of real-time power phase angle θ_P and transmits the error to PI controller to obtain the value of external phase angle γ, which is transmitted to PWM generator to realize the power direction adjustment. The control block diagram is shown in Figure 11.

Table 2: Operating conditions of the ICPT system corresponding to the combined forces at each stage.

	Unit force	ICPT system working condition	Time (s)
Stage 1	$c = f_q - w_i - w_r - w_s - w_0$	Forward transmission	1~4
Stage 2	$c = -w_i - w_r - w_s - w_0$	Pause transmission	0.5~1
Stage 3	$c = -w_i - w_r - w_s - w_0 - w_z$	Reverse transmission	Uncertain

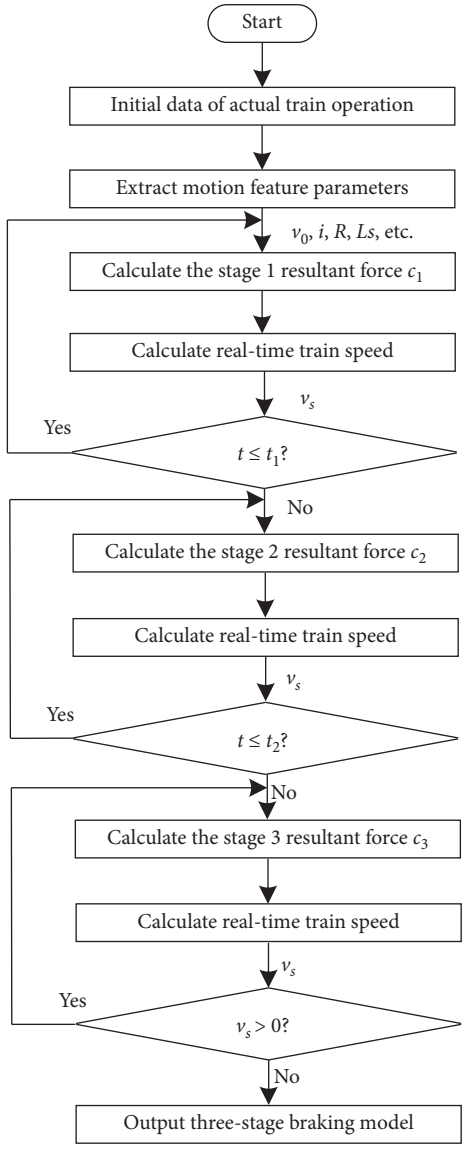

Figure 9: Flowchart of brake model construction.

It can be seen from the above that the internal phase-shift angles φ_1 and φ_2 of both sides determine the transmission power at the same time. The real-time reference power calculated according to the power model is compared with the measured power calculated from the measured voltage and current, and the error is transmitted to the PI control module to obtain the real-time internal shift phase angles φ_1 and φ_2. The phase-shift angle γ is directly given by the braking model. The bilateral PWM generator can control the converter according to the phase-shift angle inside and out, so as to control the direction of power flow and the amount of power.

5.3. Coil Switching Control Method. The switching process of segmented coils can be divided into two parts: transient and steady state. Because the onboard coils of the high-speed rail are evenly distributed, they can be regarded as a whole, so the simplified switching process can be ignored. If the train coil is considered as a whole, the switching process of the ground coil can be analyzed based on the length of the train body and the braking distance. Therefore, this paper does not analyze the transient process, only the steady-state process.

Secondly, according to preliminary estimates, during the three-stage braking process of the high-speed rail pit stop, regenerative braking energy mainly exists in the third stage, and the braking distance in the third stage accounts for the highest proportion, about 70% of the entire braking process 80%. At this time, the overall switching of the ground coil cannot guarantee the power requirements of the rail transit and the stability of the output voltage. Therefore, this paper uses the first two stages to switch the ground coil as a whole based on the preset braking distance, and the final stage divides the preset braking distance into four segments for control.

Table 3 lists the segment coil switch logic.

The schematic diagram of the ground coil switching at each stage is shown in Figure 12. This segmented switching coil method can ensure the voltage of the ground coil during the switching process on the premise of meeting the power requirements of rail transit, thereby improving the effectiveness.

The above analysis is based on the switching control method of the train-mounted and ground coils when the single-track single train brakes. However, in the actual operation of the station, there are still multiple trains entering and leaving the station simultaneously. Therefore, in order to improve the effectiveness of the preset switching control of the segmented coils and to meet the coordinated scheduling of regenerative braking energy between the medium-voltage DC bus and the energy storage device under multitrain operating conditions, further work has been done here. This paper analyzes the operating conditions of two trains with double tracks; with the purpose of collaborative regenerative energy scheduling and improving the feasibility of the preset control proposed, the preset switching control logic of multitrain segment coils is obtained.

In this section, the working conditions of A and B trains in and out of the station are divided into three scenes for analysis. The specific analysis results are shown in Table 4.

In the valley filling charging scene, both trains are in regenerative braking conditions and the regenerative braking power is less than the set value of the trough transformer bottom charging power. The ground coils of the

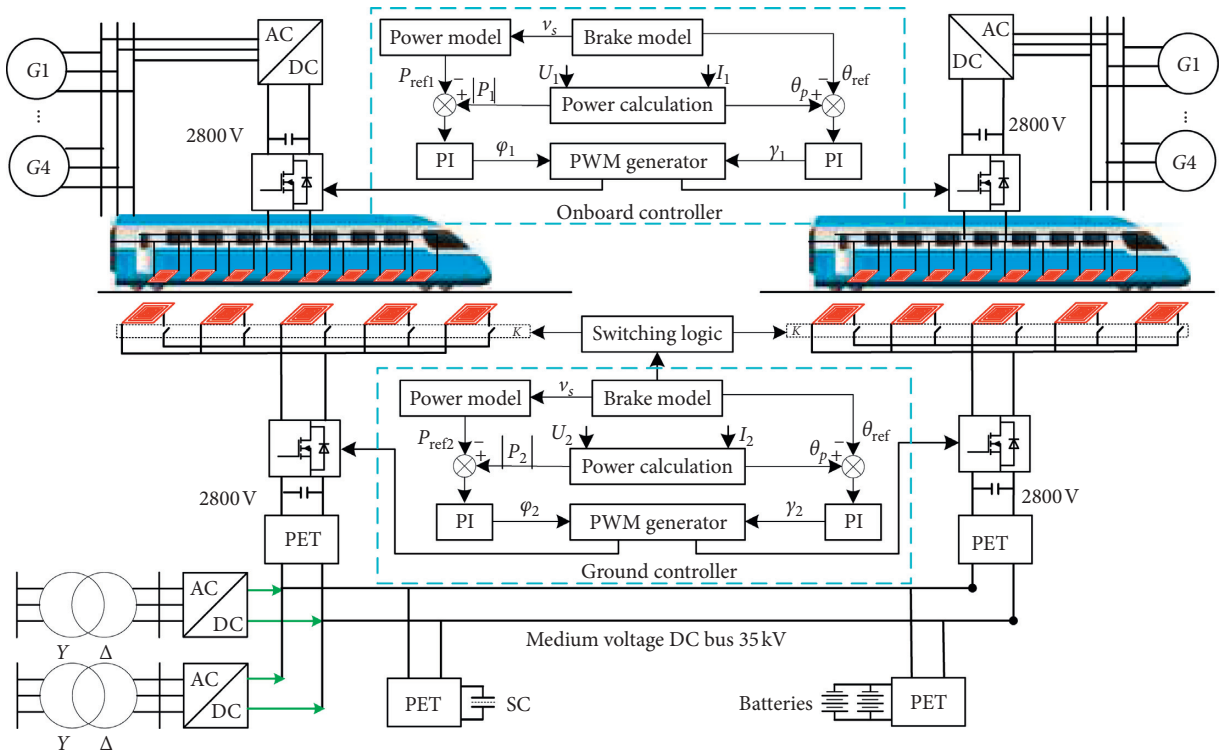

Figure 10: System overall control schematic diagram.

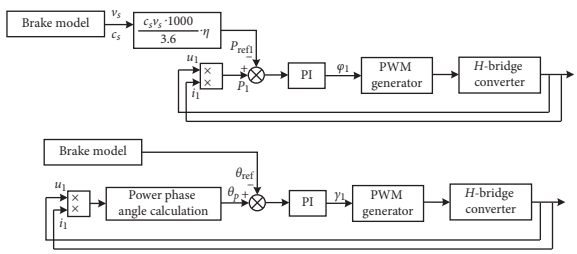

Figure 11: Power flow control block diagram.

A and B train's tracks are switched according to the preset switching control strategy of the coil proposed above. The DC bus and the energy storage device simultaneously recover the train regenerative braking energy.

In the peaking discharge scene, both trains are in regenerative braking conditions and the regenerative braking power is greater than the peak-shaving power setting value of the traction transformer. The ground coil of A's track is switched according to the proposed coil preset switching control strategy. The ground coil of B's track is closed. B enters the station by air braking or resistance braking. The DC bus is disconnected, and the energy storage device recovers the regenerative braking energy of the train until the capacity reaches the set value and charging stops.

In the power divert scene, A is in regenerative braking mode and B is in traction mode. The ground coil of A's track is switched according to the proposed coil preset switching control strategy. The energy storage device is suspended, the regenerative braking energy is fed back to the DC bus, and the regenerative braking power of A is diverted to B through the DC bus to fill the power required for starting.

6. Simulation Results

To verify the feasibility of the bidirectional ICPT system control method and the accuracy of the train braking model, as shown in Figures 13 and 14, a bidirectional ICPT system simulation model and a train braking simulation model were established in MATLAB/Simulink, respectively. See Table 5 for brake model simulation parameters.

For the coil design part, refer to the EMU parameters in Table 1. The train formation of CR400BF EMU is 4M4T, each motor train is equipped with four electric motors with a rated power of 650 kW, and the total installed power is 10.4 MW. Considering that the transmission power of the single-coil ICPT system is about 350 kW (when the rated working voltage is 2800 v), each motor train is equipped with 8 magnetic induction coupling coils, and every two coils are connected in parallel to supply power to a motor to ensure the entire train operation.

Therefore, this paper uses a 350 kW bidirectional ICPT system simulation prototype for verification. The system simulation parameters are shown in Table 6.

The simulation results are as follows.

Figure 15(a) is the train braking curve obtained by simulation according to the three preset times and initial braking speed in Table 5, and then the power curve shown in Figure 15(b) is obtained by simulation based on this. In the first stage, the train keeps traction, and the power decreases gradually with the increase of speed. In the second stage, the reference power of the train is 0; in the third stage, the train

Table 3: Segmented coil switching logic.

Stages	Ground coil status
Stage 1	The ground coil is turned on as a whole according to the preset distance of stage 1
Stage 2	The ground coil is turned off as a whole based on the preset distance of stage 2
Stage 3	The preset distance of stage 3 is divided into four small sections, and the ground coils are turned on or turned off as a whole based on the distance of each small section

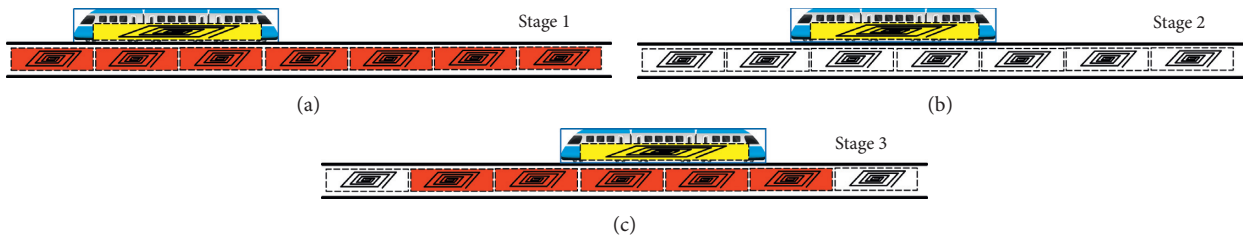

Figure 12: Ground coil switching diagram.

Table 4: The analysis of multitrain scenes.

Type of scene	Trains status	Ground coil status	Bus side status	Energy storage device
Valley filling charging	A and B are in regenerative braking	Both train tracks switch normally	Energy recovery	Charge
Peaking discharge	A and B are in regenerative braking	A track switches normally; B track turns off the coil	Disconnect	Charge
Power divert	A is in regenerative braking and B is in traction working condition	Both train tracks switch normally	Energy supply	Stop

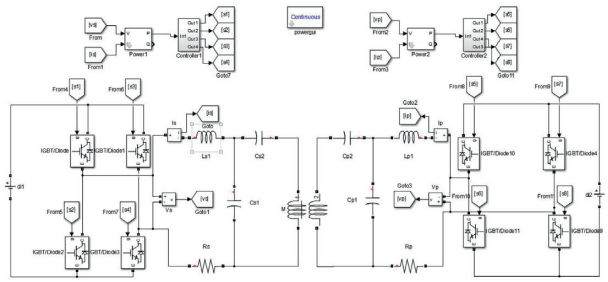

Figure 13: Simulation diagram of bidirectional ICPT system.

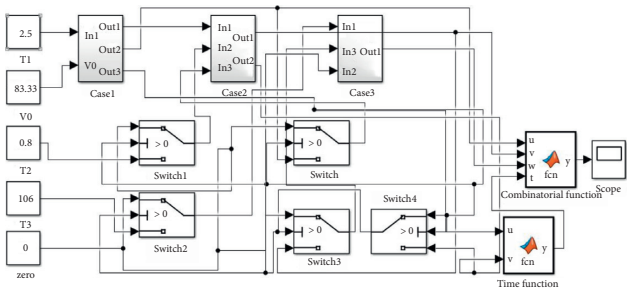

Figure 14: Simulation diagram of train brake model.

starts to brake, and the system power decreases with the decrease of the speed, which is consistent with the ICPT system working condition of each stage analyzed above, which proves the accuracy of the train braking model.

Table 5: Braking model simulation parameters.

Parameters	Value
v_0/m/s	83.33
t_n (t_1/t_2/)/s	2.5/0.8/106

Figure 16 is a waveform diagram of the primary and secondary currents i_1 and i_2 and the primary and secondary voltages u_1 and u_2 when the ICPT system power is 350 kW. It can be seen from the waveforms of i_1 and i_2 that the waveforms of i_1 and i_2 are both sine waves, indicating that the system is in resonance. When the system transmits the power in the forward direction, the primary current is larger than the secondary current, which is caused by system loss.

For the purpose of verifying the effectiveness of the control strategy proposed in this paper, a simulation process of switching the power transmission direction is added to the simulation system. It can be seen from Figure 17 that when the power transmission direction is switched at 0.01 s, the voltage of the primary and secondary side changes little and is relatively stable. There are certain fluctuations in the primary and secondary side current, but the fluctuation time is very short (< 1 ms), and the peak value of the fluctuation is about 1.05 times of the current when it is stable, which has little effect on the system. Figure 18 is the transmission power waveform diagram of the system after the system switches the power transmission direction at 0.0.1 s. It can be

Table 6: Bidirectional ICPT system simulation parameters.

Parameters	Value
U_1 (V)	2800
C_{p1} (nF)	146.5
C_{p2} (nF)	146.5
L_{p1} (μH)	48.4
L_{p2} (μH)	24.3
R_p (Ω)	1.5
M (μH)	16
U_2 (V)	2800
C_{s1} (nF)	146.5
C_{s2} (nF)	146.5
L_{s1} (μH)	48.4
L_{s2} (μH)	24.3
R_s (Ω)	1.5
f (kHz)	85

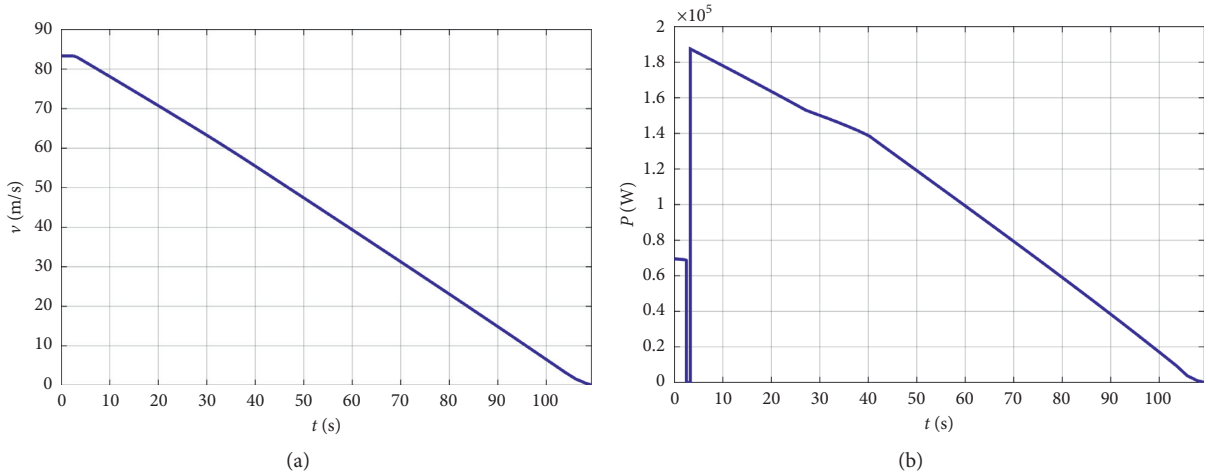

Figure 15: (a) Train brake curve. (b) System power curve.

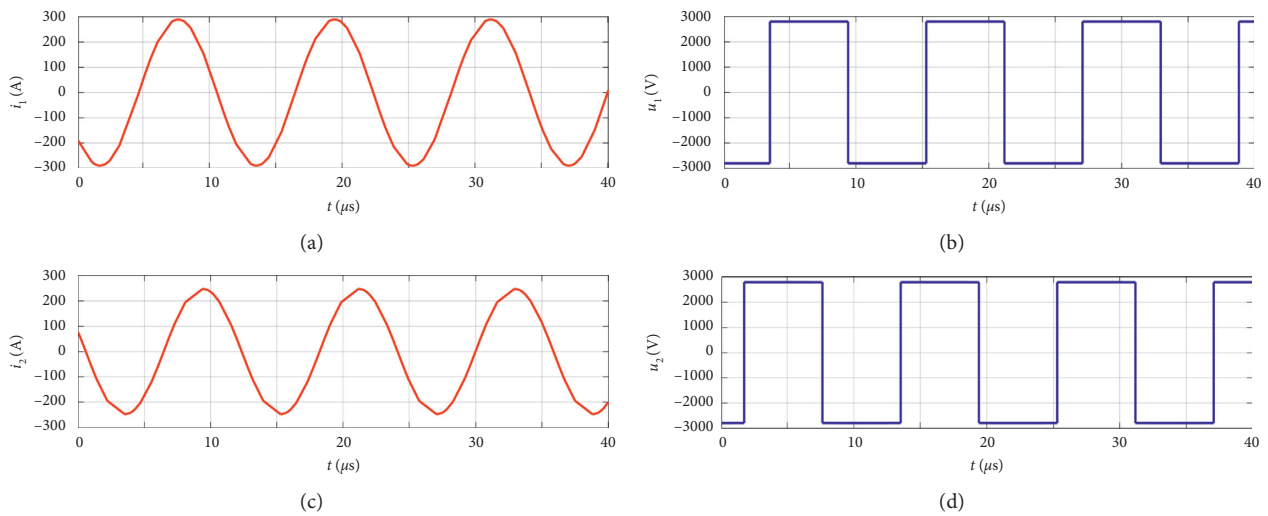

Figure 16: (a) Primary side current waveform at 350 kW power. (b) Primary side voltage waveform at 350 kW power. (c) Secondary side current waveform at 350 kW power. (d) Secondary side voltage waveform at 350 kW.

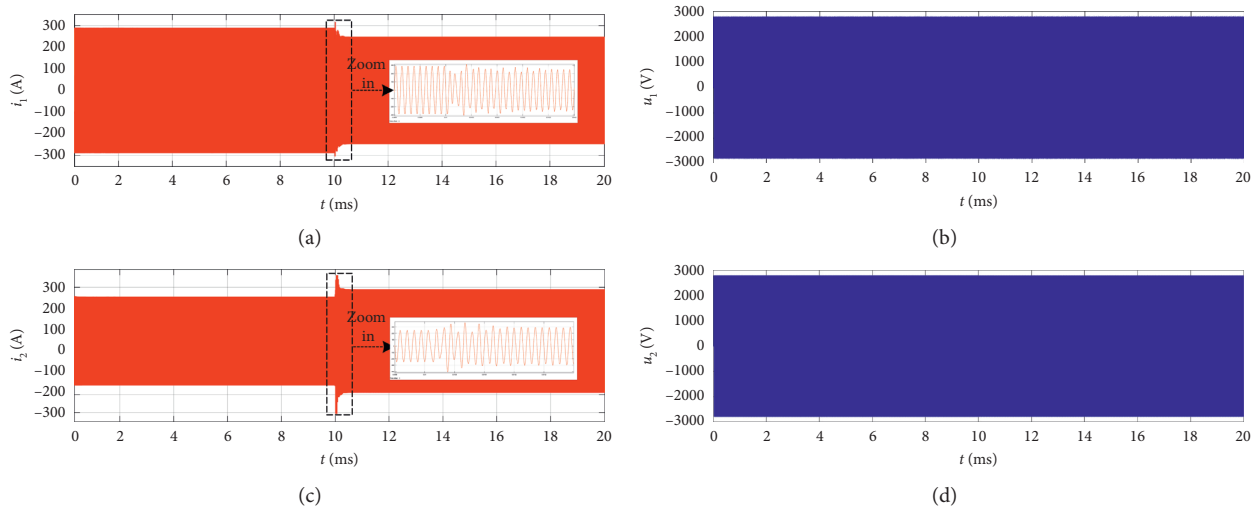

Figure 17: (a) Primary side current waveform when switching the power transmission direction at 0.01 s. (b) Primary side voltage waveform when switching the power supply direction at 0.01 s. (c) Secondary side current waveform when switching the power transmission direction at 0.01 s. (d) Secondary side voltage waveform when switching the power transmission direction at 0.01 s.

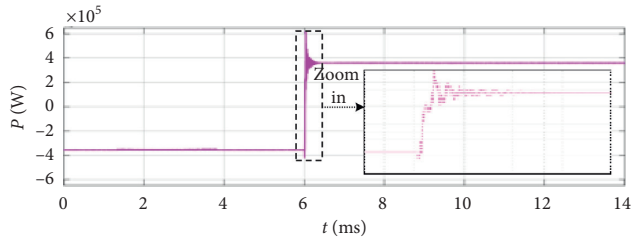

Figure 18: The waveform of system power when switching the power transmission direction at 0.01 s.

seen from the figure that the power fluctuation time is also very short (< 1 ms), and the peak power fluctuation is about 600 kW. Figure 19 shows the simulation system transmission efficiency, which can reach about 89%.

7. Energy-Saving Estimate

Taking common operating conditions as an example, 80% of the number of members is taken, and the per capita mass is 70 kg. After calculation, the total mass of the train is 533.2 t.

Under the preset control strategy proposed in this paper, it can be seen through simulation that the simulation efficiency of the bidirectional ICPT system can reach 89%. Based on the process of braking model calculation, combined with the operating efficiency of the ICPT system, it can be estimated that it can be recycled. The energy Q is

$$Q = \int_{t_0}^{t_n} P_n \eta \mathrm{d}t. \tag{22}$$

In this section, energy-saving estimates are made when the initial braking speed of the train is 250 km/h, 300 km/h, and 350 km/h. The regenerative braking energy that can be recovered during the entire braking process is shown in Table 7.

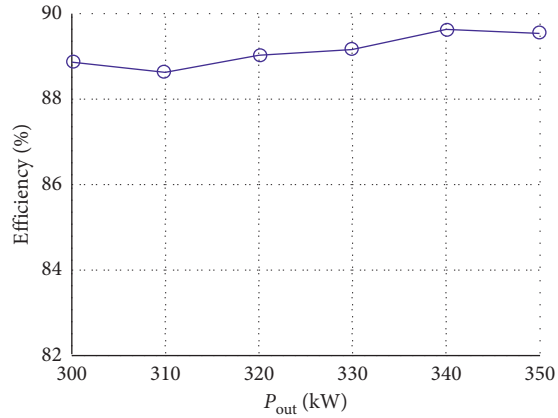

Figure 19: Simulation efficiency results for bidirectional ICPT system.

Table 7: Corresponding power recovery at the initial train speed.

Initial velocity (km/h)	Total mass (t)	Electric energy (kW·h)
350	533.2	366.47
300	533.2	269.8
250	533.2	187.53

According to the measured data of regenerative braking energy in the actual operation of high-speed rail, literature 1 defines four types of typical processes based on two indicators: the duration of the regenerative braking process and the amplitude of the regenerative braking power [1]. In the process with the longest duration and the highest power, the braking lasted for 200 s, and the total regenerative braking energy was 323.77 kWh. It can be seen from the above table that, based on the high-speed rail noncontact traction power supply system proposed in this paper, each single train lasts for about 110 s from braking to stopping, and the total regenerative braking energy is about 200–300 kWh. The measured data corresponds to this, which proves the modeling accuracy of this paper.

8. Conclusion

This paper proposes a preset bidirectional ICPT system segmented power supply preset control method that takes into account regenerative braking energy recovery. The steady-state model of the bidirectional ICPT system is analyzed, and the mathematical model of the train brake is established through the force analysis. The power preset control method and the segmented coil switching control method are proposed by using the above models. A 350 kW bidirectional ICPT system simulation prototype and a train braking simulation model were established in MATLAB/Simulink. The results show that the ICPT system can operate stably when the power transmission direction is switched, and the system efficiency reaches 89%, which verifies the feasibility of the proposed control method. In addition, the calculation results of the braking simulation model are consistent with the expected working conditions of each stage of the ICPT system, which proves the accuracy of the train braking model. Finally, an energy-saving estimate at multiple speed levels is carried out. The simulation results show that the estimated regenerative braking energy is consistent with the measured data, which proves the correctness of the braking model proposed in this paper.

Data Availability

The data used to support the findings of this study are available from the corresponding author upon request.

Conflicts of Interest

The authors declare that they have no conflicts of interest.

Acknowledgments

This work was supported by the National Natural Science Foundation of China (Project no. 51767015), the Gansu Provincial Natural Science Foundation of China (Gansu Provincial Science and Technology Plan, Project no. 18JR3RA117), and Lanzhou Jiaotong University-Tianjin University Joint Innovation Fund Project (Project no. 2019051).

References

[1] H. Hu and J. Chen, "Research on regenerative braking energy storage and utilization technology of high-speed railway," *CSEE*, vol. 40, pp. 246–256, 2020.

[2] M. Khodaparastan, A. A. Mohamed, and W. Brandauer, "Recuperation of regenerative braking energy in electric rail transit systems," *IEEE Transactions on Intelligent Transportation Systems*, vol. 20, no. 8, pp. 2831–2847, 2019.

[3] L. Shi, Z. Yin, L. Jiang, and Y. Li, "Advances in inductively coupled power transfer technology for rail transit," *CES Transactions on Electrical Machines and Systems*, vol. 1, no. 4, pp. 383–396, 2017.

[4] L. Pugi, A. Reatti, and F. Corti, "Application of wireless power transfer to railway parking functionality: preliminary design considerations with series-series and LCC topologies," *Journal of Advanced Transportation*, vol. 2018, p. 14, Article ID 8103140.

[5] J. H. Kim, B.-S. Lee, J.-H. Lee et al., "Development of 1-MW inductive power transfer system for a high-speed train," *IEEE Transactions on Industrial Electronics*, vol. 62, no. 10, pp. 6242–6250, 2015.

[6] S. B. Lee, S. Ahn, and I. G. Jang, "Simulation-Based feasibility study on the wireless charging railway system with a ferriteless primary module," *IEEE Transactions on Vehicular Technology*, vol. 66, no. 2, pp. 1004–1010, 2017.

[7] L. Pugi, F. Grasso, and G. Rossi, "Energy simulation of tramway systems, simplified and efficient models," 2018.

[8] R. Li, X. Zhao, J. Wang, and X. Li, "Research on energy distribution of regenerative braking in station for contactless traction power supply system based on bidirectional energy interaction ICPT system," *IEEE Access*, vol. 8, pp. 203930–203944, 2020.

[9] S. Lin, D. Huang, and A. Wang, "Research on the regeneration braking energy feedback system of urban rail transit," *IEEE Access*, vol. 99, pp. 1–7, 2019.

[10] S. Wei, J. Wang, and H. Wang, "The braking mode simulation and analysis for high-speed railway," 2011.

[11] M. Khodaparastan, A. Mohamed, and W. Brandauer, "Recuperation of regenerative braking energy in electric rail transit systems," *IEEE Access*, vol. 1, pp. 1–17, 2019.

[12] Y. Lu, Y. Zhao, and X. Zhao, "Status analysis of regenerative braking energy utilization equipments in urban rail transit," 2017.

[13] S. Li, S. Wu, S. Xiang, Y. Zhang, J. M. Guerrero, and J. C. Vasquez, "Research on synchronverter-based regenerative braking energy feedback system of urban rail transit," *Energies*, vol. 13, no. 17, p. 4418, 2020.

[14] Y. Deng, Y. Li, and H. Chen, "Study on energy absorption scheme of rail transit," in *Proceedings of the 2018 IEEE 3rd Advanced Information Technology, Electronic and Automation Control Conference*, pp. 1430–1433, Chongqing, China, October 2018.

[15] W. Wei, H. Hu, K. Wang, and J. Chen, "Energy storage scheme and control strategies of high-speed railway based on railway power conditioner," *Transactions on China Electrotechnical Society*, vol. 34, pp. 1290–1299, 2019.

[16] Q. Ma, X. Guo, P. Luo, and Z. Zhang, "Coordinated control strategy design of new type railway power regulator based on super capacitor energy storage," *Transactions on China Electrotechnical Society*, vol. 34, pp. 765–776, 2019.

[17] K. Wang, X. Feng, J. Ren et al., "State of charge (SOC) estimation of lithium-ion battery based on adaptive square root

unscented kalman filter," *International Journal of Electrochemical Science*, vol. 15, no. 9, pp. 9499–9516, 2020.

[18] K. Wang, W. Wang, L. Wang, and L. Li, "An improved soc control strategy for electric vehicle hybrid energy storage systems," *Energies*, vol. 13, no. 20, p. 5297, 2020.

[19] U. K. Madawala and D. J. Thrimawithana, "A bidirectional inductive power interface for electric vehicles in V2G systems," *IEEE Transactions on Industrial Electronics*, vol. 58, no. 10, pp. 4789–4796, 2011.

[20] Y. Tang, Y. Chen, U. K. Madawala, D. J. Thrimawithana, and H. Ma, "A new controller for bidirectional wireless power transfer systems," *IEEE Transactions on Power Electronics*, vol. 33, no. 10, pp. 9076–9087, 2018.

[21] F. Liu, K. Chen, Y. Jiang, and Z. Zhao, "Research on the overall efficiency optimization of the bidirectional wireless power transfer system," *Transactions on China Electrotechnical Society*, vol. 34, pp. 891–901, 2019.

[22] F. Liu, K. Chen, Y. Jiang, and Z. Zhao, "Phase synchronization of control signals based on perturbation and observation for bidirectional wireless power transfer system," 2018.

[23] T. Tan, K. Chen, Y. Jiang, L. Yuan, and Z. Zhao, "A bidirectional wireless power transfer system control strategy independent of real-time wireless communication," *IEEE Transactions on Industry Applications*, vol. 56, no. 2, pp. 1587–1598, 2020.

[24] L. Pugi, A. Reatti, and F. Corti, "Application of modal analysis methods to the design of wireless power transfer systems," *Meccanica*, vol. 54, pp. 321–331, 2019.

[25] M. Fan, L. Shi, Z. Yin, and L. Jiang, "Research on control strategy of segmented power supply for mobile inductive power transfer system," *Transactions on China Electrotechnical Society*, vol. 38, pp. 2112–2120+2226, 2018.

[26] H. Seung, K. Jae, and L. Jun, "Development of a 60 kHz, 180 kW, over 85% efficiency inductive power transfer system for a tram," *Energies*, vol. 9, p. 1075, 2016.

[27] X. Zhang, J. Wang, Q. Yang, B. Wei, and S. Wang, "The power coupling mechanism and switching control for dynamic wireless power supply system of electric vehicle," *Transactions on China Electrotechnical Society*, vol. 34, pp. 3093–3101, 2019.

[28] X. Zhang, T. Cai, S. Duan et al., "A control strategy for efficiency optimization and wide ZVS operation range in bidirectional inductive power transfer system," *IEEE Transactions on Industrial Electronics*, vol. 66, no. 8, pp. 5958–5969, 2019.

[29] J.-Y. Lee, B.-M. Han, and M. Neath, "A bidirectional wireless power transfer EV charger using self-resonant PWM," *IEEE Transactions on Power Electronics*, vol. 30, no. 4, pp. 1784–1787, 2015.

[30] B. X. Nguyen, D. M. Vilathgamuwa, G. H. B. Foo et al., "An efficiency optimization scheme for bidirectional inductive power transfer systems," *IEEE Transactions on Power Electronics*, vol. 30, no. 11, pp. 6310–6319, 2015.

[31] C. Meng, *Operation Diagram Based Traction Calculation for Multiple Trains*, Beijing Jiaotong University, Beijing, China, 2019.

[32] Rail Transit Vehicle Interface Standards Committee of the IEEE Vehicular Technology Society, *IEEE Guide for the Calculation of Braking Distances for Rail Transit Vehicles*, The United States of America: the Institute of Electrical and Electronics Engineers, Inc., Beijing, China, 2009.

Hindawi
Mathematical Problems in Engineering
Volume 2020, Article ID 6655031, 13 pages
https://doi.org/10.1155/2020/6655031

Research Article

Energy Management Strategy for High-Altitude Solar Aircraft Based on Multiple Flight Phases

Mou Sun,[1] **Chuan Shan**,[1] **Kang-wen Sun**,[2,3] **and Yu-hong Jia**[1]

[1]*School of Aeronautic Science and Engineering, Beihang University, Beijing 100191, China*
[2]*Institute of Unmanned System, Beihang University, Beijing 100191, China*
[3]*Yunnan Innovation Institute, Beihang University, Kunming 650233, China*

Correspondence should be addressed to Kang-wen Sun; sunkw100@buaa.edu.cn

Received 11 October 2020; Revised 10 November 2020; Accepted 27 November 2020; Published 9 December 2020

Academic Editor: Kai Wang

Making use of solar energy to fly is an up-and-coming technology in the human aviation field since solar energy is renewable and inexhaustible, and more and more attention and efforts have been directed to the development of high-altitude solar aircraft (HSA). Due to the technical constraints of the rechargeable battery, the HSA must carry sufficient batteries to meet the flight power consumption at night, which seriously limits the flight endurance of HSA. To solve this contradiction, the paper has proposed a new energy management strategy (EMS) of multiple flight phases for HSA based on the gravitational energy storage and mission altitude, which aims to achieve the goal of long-endurance flight for HSA. The integrated model of this new EMS includes the aerodynamic model, the kinematic model, the solar irradiation model, the battery model, and the energy management model. Compared with the current EMS of level flight, the flight path of HSA in the new EMS has been divided into five phases: the lower altitude level flight at night, the maximum power ascending for mission altitude, the level flight at mission altitude, the maximum power ascending for higher altitude, and the longest gliding endurance. At last, the calculation of the new EMS for Zephyr 7 is studied by MATLAB/Simulink, and the calculation results indicate that about 22.9% of energy surplus can be stored in battery with the new EMS for Zephyr 7 compared with the current EMS, which is equal to reducing the rechargeable battery weight from 16.0 kg to 12.3 kg. Besides, the results of simulation in the four seasons also show that the new EMS is a very promising way to achieve the long-endurance goal for high-altitude HSA when the flight conditions satisfy some constraints like the deficiency of solar flux and the limit of battery mass.

1. Introduction

Nowadays, environmental pollution and energy crisis are the tough challenges that the world and humanity are facing [1]. Due to the rapid development of solar cell technology, solar energy can gradually play a leader role in exploring the field of renewable and clean energy [1–3]. Therefore, making use of solar energy to fly is a research hotspot, which has attracted a lot of research groups all around the world during the past few years [4–10].

Since the solar energy is renewable and inexhaustible, it has the potential to redefine and increase the flight endurance of aircraft. In the last ten years, many countries and research teams have made great efforts to develop the high-altitude solar aircraft (HSA) [2, 6–12] for the reason that the HSA have the ability to stay over a wide area at high altitude for long endurance; they can function as geostationary satellites, but they are much economical [13, 14]. They are ideally suited to be widely employed in many applications such as natural monitoring, border patrol, planetary exploration, communications relay, remote sensing, field investigations, network services, and electronic warfare [14]. Over the past years, there are two series of high-altitude long-endurance (HALE) solar-powered aircraft programs which aim to achieve the goal of the HALE flight: Zephyr and ERAST [7, 15, 16]. However, due to the technical limitations of rechargeable battery and structure, none of these aircraft has achieved the HALE flight in real sense. As a

result of those pioneering and advanced research studies and experiments, scholars and researchers have gradually realized that the key factor restricting the long-endurance flight of HSA is the problem of how to meet the power consumption at night with the constraints on the weight of the battery [2, 14, 16]. Under the current technique level, the weight of rechargeable battery occupies about 45% of the total mass of aircraft [3, 11]. Meanwhile, the HSA technologies like solar cell conversion efficiency and battery specific capacity are unable to improve rapidly. Therefore, the regenerative power technology such as energy management strategy (EMS) is the key to achieving long-endurance flight for HSA.

In recent decades, some studies have focused on the regenerative power technologies about drones and their applications. The studies [17, 18] show that the efficiency and the attitude angles of the solar cell directly affect the energy production power for the applications of solar drone platform. Especially, Scheiman et al. have built an Unmanned Aerial Vehicle (UAV) with a variety of solar cell technologies in the wing. In order to extend flight endurance, the solar cells mainly include thin flexible GaAs, high efficiency Si, and triple junction InGaP/GaAs/Ge. As a result, the UAV power management system is experimentally verified to perform well. The studies [19, 20] conducted thorough analytical research on rechargeable battery based on energy system of drone. These works are significant in the selection of battery and the estimation of the battery capacity for HSA. The studies [21–26] researched energy system and EMS for HSA and airships, and some important conclusions have been obtained. Some of these designed energy systems which had been experimentally tested and verified have made significant and pioneering contributions to the development for solar drone EMS. In addition, many scholars and researchers have studied and improved the EMS in other fields to increase the power efficiency of energy system, which include the hybrid vehicle, the air conditioning, and the light electric bus [27–31]. However, none of these research papers have studied the EMS for HSA in real sense based on multiple fight phases. As is known, the HSA need to have a multiple-phase flight process in engineering applications, which generally includes executing mission in higher altitude, cruising in lower altitude, and flight paths for gravity energy storage. In the higher altitude level flight during the daytime, the HSA can perform mission like regional residency and circle hover, as well as charging the battery smoothly with the electricity generated by the solar cells. In the lower altitude at night, the HSA can achieve the goal of long endurance with lower power consumption. Meanwhile, those two different level flight altitudes are also beneficial to realize the gravity energy storage strategy. Therefore, the above-mentioned multiple flight stages should be designed in the EMS for long-endurance HSA, and to the best of our knowledge, almost none of these energy systems is introduced and involved in the published literature.

This article is inspired by these considerations and a study [32] that proposes the EMS based on the idea that the surplus solar energy can be stored in gravitational potential during the daytime. The contributions of this study can be summarized as follows:

(1) The new EMS model based on multiple flight phases for HSA is proposed, which is more suitable for the day and night cycle flight in engineering applications.

(2) The design of mission altitude for level flight in the multiple flight phases indicates and provides the possibility that HSA perform missions such as the regional residence, the straight back, and the circle hover, and the HSA can function as geostationary satellites.

(3) In order to calculate the new EMS for HSA, an integrated MATLAB/Simulink calculation program including the aerodynamic model, the kinematic model, the solar flux model, the battery model, and the EMS model is established.

(4) Due to the particularity of energy system, the research results also show that a suitable EMS can be more beneficial to long endurance for HSA on condition of lower solar irradiation and shorter daytime.

2. Models and Methods

A typical HSA energy system [21, 22] mainly includes solar cell, voltage converter with maximum power point tracking (MPPT) function, energy management system, and rechargeable battery with management system, as shown in Figure 1. In the daytime, the electricity generated by solar cells on the wings can directly supply the power through the energy management system. Meanwhile, the excess solar energy will charge the battery. At night, the HSA power is all provided by the rechargeable battery. As a result, the HSA could fly uninterruptedly at day and night for long-endurance goal.

Based on this energy system of HSA, the models and methods used in the paper will be introduced and established as follows.

2.1. Aircraft Kinematic and Aerodynamic Models. As shown in Figure 2, the study defines the $O_gX_gY_gZ_g$ as the earth-fixed frame, and the aircraft body-fixed frame is $O_bX_bY_bZ_b$, where O_gX_g, O_gY_g, and O_gZ_g represent the north, the west, and the straight directions through the ground. O_bX_b is located in a symmetric position parallel to the fuselage axis and points forward, O_bY_b points perpendicularly to the right of the plane of symmetry, and O_bZ_b obeys the right hand axis rule and is perpendicular to O_bX_b, O_bY_b.

In this paper, the study of the new EMS mainly focuses on the energy supply and consumption characteristics of the energy system for HSA. Thus, the three-dimensional dynamic equations of HSA can be simplified as follows [33]:

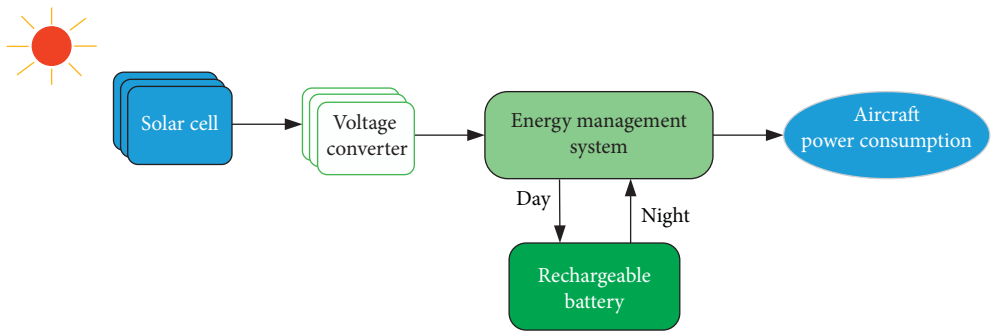

Figure 1: Schematic picture of energy system for high-altitude solar aircraft.

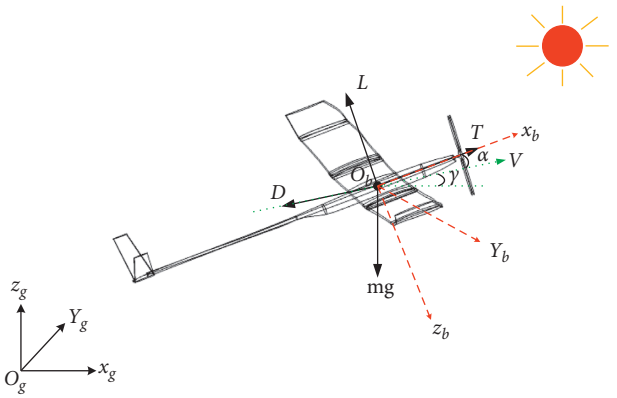

Figure 2: Schematic diagram of three-dimensional forces acting on solar-powered aircraft.

$$\begin{cases} \dfrac{dv}{dt} = \dfrac{T\cos\alpha}{m} - \dfrac{D}{m} - g\cdot\sin\gamma, \\ \dfrac{d\gamma}{dt} = \dfrac{T\sin\alpha}{mv} + \dfrac{L}{mv}\cos\psi - \dfrac{g}{v}\cos\gamma, \\ \dfrac{d\varphi}{dt} = \dfrac{L}{mv\cos\gamma}\sin\psi, \\ \dfrac{dx}{dt} = v\cos\gamma\cos\varphi, \\ \dfrac{dy}{dt} = v\cos\gamma\sin\varphi, \\ \dfrac{dh}{dt} = v\sin\gamma, \end{cases} \tag{1}$$

where x, y, and h are the HSA north, east, and altitude positions in the earth-fixed frame, v is the HSA speed, ψ is the roll angle of the HSA, φ is the yaw angle, γ is the flight path angle, m is the total mass of HSA, and g is the gravity acceleration. T, L, and D mean the thrust force, aerodynamic lift, and drag forces of the HSA.

As shown in Figure 2, the angle of attack α is the angle between velocity vector direction and O_bX_b axis direction, and the pitching angle θ is the sum of α and γ.

Generally speaking, the aerodynamic forces L and D of the HSA can be expressed in the following formula:

$$\begin{cases} L = \dfrac{1}{2}\rho v^2\cdot S_W C_L, \\ D = \dfrac{1}{2}\rho v^2\cdot S_W C_D, \end{cases} \tag{2}$$

where S_W is the wing area, C_D and C_L are the drag and lift coefficients, and ρ is the air density.

2.2. Solar Irradiation Model. As is known, the solar radiation intensity is related to many factors, including the date, latitude, and longitude. The paper summarizes a lot of literature [2, 3, 22, 32–34] about the calculation of solar flux, and the solar power per square meter in the earth-fixed frame can be calculated by the following formula:

$$\begin{cases} P_S = I_{SC}\cdot\tau\cdot\sin(H_S), \\ I_{SC} = I_0\cdot\left(\dfrac{1+\varepsilon\cdot\cos(2\pi(n-4)/365)}{1-\varepsilon^2}\right)^2, \\ \sin(H_S) = \sin\phi\sin\delta + \cos\phi\cos\delta\cos(\pi - \pi\cdot t/12), \\ \delta = \dfrac{23.45\pi}{180}\sin\left(360\dfrac{284+n}{365}\right), \end{cases} \tag{3}$$

where P_S is the solar power in per square meter, I_0 is the solar irradiance constant that has a value of 1367 W/m^2, τ is the transmittance factors, H_S is the solar elevation angle as shown in Figure 3, ε is the eccentricity ratio of earth, n is the day number of the year, ϕ is the location latitude, t is the true local solar time, and δ is the solar declination angle.

Equation (3) shows a more concise and complete calculation about the P_S in the earth-fixed frame. In particular, the transmittance factor τ is affected by atmospheric

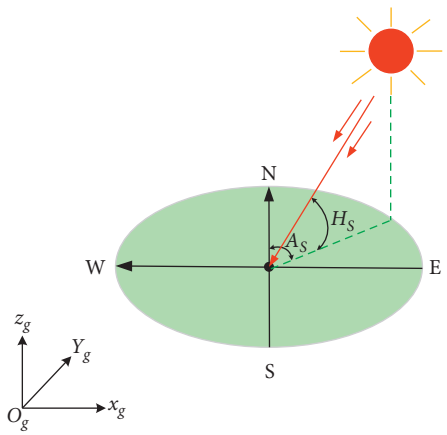

Figure 3: Schematic diagram of the sun azimuth and the elevation angle.

transparency and so on. That includes the modifying factors, the atmospheric pressure of different altitudes, and the air mass ratio which are described in literature [21]. The parameter t is related to the standard time and the longitude of the location. Those parameters in integrated equation (3) can be introduced and calculated by the formulas in the literature above, which are not be described in detail here.

With the HSA transforming the flight altitude and attitude during the daytime, the solar energy on the wings surface generated by solar cells will always change in time. Therefore, a relatively accurate solar flux model about the attitude and altitude of the HSA needs to be set up to calculate solar energy collection. Based on the display in Figure 2 and the calculation of P_S in the earth-fixed frame from (3), the solar flux model for HSA can be obtained by the coordinate conversion principle between the body-fixed frame $O_bX_bY_bZ_b$ and the earth-fixed frame $O_gX_gY_gZ_g$.

Firstly, the P_S in each direction calculation I_{Xg}, I_{Yg}, and I_{Zg} (positive and negative represent directions) can be expressed by the following formula:

$$\begin{cases} I_{Xg} = P_S \cdot \cos H_S \cdot \cos A_S, \\ I_{Yg} = P_S \cdot \cos H_S \cdot \sin A_S, \\ I_{Zg} = P_S \cdot \sin H_S, \end{cases} \tag{4}$$

where A_S is the sun azimuth angle, as shown in Figure 3.

Secondly, based on the coordinate conversion principle, the solar radiation intensities I_{Xb}, I_{Yb}, and I_{Zb} received in the body-fixed frame can be calculated by the following formula:

$$\begin{bmatrix} I_{Xb} \\ I_{Yb} \\ I_{Zb} \end{bmatrix} = \begin{bmatrix} \cos\theta\cos\varphi & \cos\theta\sin\varphi & -\sin\theta \\ \sin\psi\sin\theta\cos\varphi - \cos\psi\sin\varphi & \sin\psi\sin\theta\sin\varphi + \cos\psi\cos\varphi & \cos\theta\sin\psi \\ \cos\varphi\sin\theta\cos\psi + \sin\varphi\sin\psi & \cos\psi\sin\theta\sin\varphi - \sin\psi\cos\varphi & \cos\theta\cos\psi \end{bmatrix} \begin{bmatrix} I_{Xg} \\ I_{Yg} \\ -I_{Zg} \end{bmatrix}. \tag{5}$$

To sum up, the solar energy collection model for HSA can be established into a MATLAB function file for further model integration. This solar flux intensity calculation model of HSA on the wings is related to the longitude, latitude, altitude, date, moment, pitch angle, yaw angle, and roll angle.

2.3. Energy Management Strategy. As shown in Figure 1, the function of energy management system is to control the energy flow for HSA, which mainly includes the battery management system and the switching system of power supply mode. During the daytime, the maximum electrical energy generated by solar cells and voltage converter is divided into two parts: one part directly supplies electricity to the propulsion motors and on-board equipment, and the other part will recharge the battery with excess energy. At night, the power supply mode of the energy management system is that the battery powers the propulsion system and the equipments on board. The efficiency values of each component of the energy system are listed in Table 1.

Generally speaking, the MPPT function will be embedded in the solar voltage converter. Therefore, the η_{mppt} is the efficiency of converting solar energy into electricity in this study. Besides, it will not distinguish between battery charging and discharging efficiency in general research field. In order to simplify the calculation, this paper assumes that the battery charge and discharge efficiency are equal to 0.98 and the propulsion system efficiency is reasonably given as 0.7 although the efficiencies of motors and airscrew will vary with altitude and Reynolds number. Thus, the thrust T of the propulsion system can be obtained by the following formula:

$$T = \eta_{\text{ma}} \cdot \frac{P_{\text{prop}}}{v}, \tag{6}$$

where P_{prop} is the propulsion system power.

2.3.1. Current Energy Management Strategy Based on Level Flight. The purpose of EMS for HSA is to realize long-endurance flight with the limit of battery mass at night. For most of the reported HSA energy systems, the EMS can be expressed as flying with minimum power consumption with the constraints of lift and weight balance, thrust and drag balance, and energy supply and demand balance, as shown in Figure 4.

Generally, the surplus energy will charge the battery by the current EMS if the output solar power P_{mppt} of the voltage converter is larger than the power P_{prop} (as on-board equipment power can be ignored for the P_{prop}). Meanwhile, the insufficient required power will be supplemented by the

Table 1: The efficiency of each component in the energy management system.

Components	Symbol	Value	Units
Solar cell	η_{sc}	0.2	–
Voltage converter	η_{mppt}	0.95	–
Battery	η_b	0.98	–
Battery manager	η_{bm}	0.99	–
Motors and airscrew	η_{ma}	0.7	–

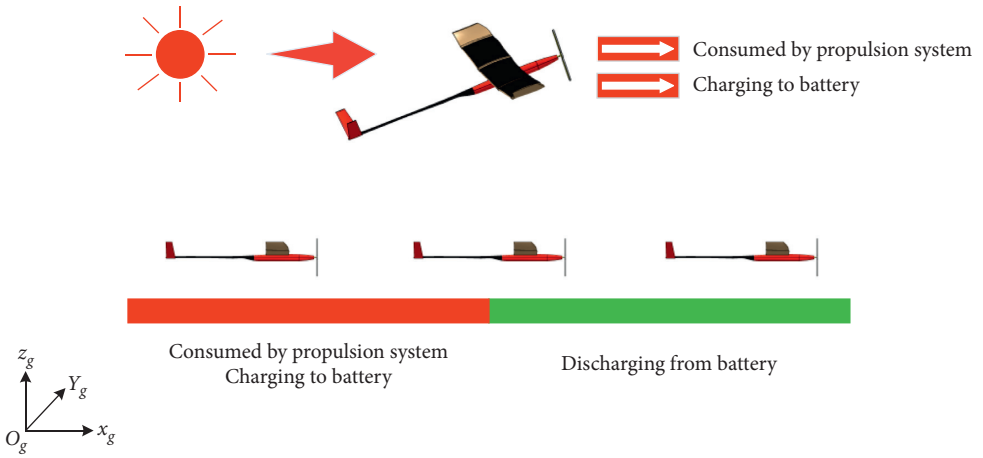

Figure 4: Schematic diagram of the current energy management strategy based on level flight.

battery when the P_{mppt} is less than the P_{prop}. The output power P_{mppt} of the voltage converter is calculated as follows:

$$P_{mppt} = \begin{bmatrix} I_{Xb} \\ I_{Yb} \\ I_{Zb} \end{bmatrix} \cdot S_{SC} \cdot \eta_{mppt}, \tag{7}$$

where S_{SC} is the solar cells area in the wing. For the HSA level flight,

$$\begin{cases} \gamma = 0, \\ D = T \cdot \cos\alpha, \\ L = mg - T \cdot \sin\alpha. \end{cases} \tag{8}$$

The power consumption of the aircraft in level flight can be obtained as shown in the following formula:

$$\begin{aligned} \eta_{ma} \cdot P_{prop} = P_{level} = T \cdot v = \frac{D \cdot v}{\cos\alpha} \\ = \frac{C_D}{C_L^{(3/2)}} \left(\frac{mg - T \cdot \sin\alpha}{\cos\alpha} \right) \sqrt{\frac{2(mg - T \cdot \sin\alpha)}{\rho \cdot S_W}}. \end{aligned} \tag{9}$$

The angle of attack α control command for the HSA flight path can be expressed as

$$\begin{aligned} \alpha_{level}^{*} &= \min_{\alpha_{min} < \alpha < \alpha_{max}} \left(P_{prop} \right) \\ &= \min_{\alpha_{min} < \alpha < \alpha_{max}} \left\{ \frac{C_D}{C_L^{(3/2)}} \left(\frac{mg - T \cdot \sin\alpha}{\cos\alpha} \right) \sqrt{\frac{2(mg - T \cdot \sin\alpha)}{\rho \cdot S_W}} \right\}. \end{aligned} \tag{10}$$

Therefore, the current EMS of HSA can be expressed as follows:

$$\dot{E} = \begin{cases} q_{max}, & \left(P_{mppt} - P_{prop}\right)\eta_b\eta_{bm} \geq q_{max}, \\ \left(P_{mppt} - P_{prop}\right)\eta_b\eta_{bm}, & 0 \leq \left(P_{mppt} - P_{prop}\right)\eta_b\eta_{bm} < q_{max}, \\ \dfrac{\left(P_{mppt} - P_{prop}\right)}{\left(\eta_b\eta_{bm}\right)}, & \left(P_{mppt} - P_{prop}\right)\eta_b\eta_{bm} < 0, \\ \dfrac{-P_{prop}}{\left(\eta_b\eta_{bm}\right)}, & P_{mppt} = 0, \\ 0, & Q_B \leq Q_{B\_min} \text{ or } Q_B \geq Q_{B\_max}, \end{cases} \tag{11}$$

where $\dot{E}$ is the battery charge and discharge power (positive means charging; negative means discharging), q_{max} is the battery maximum charging power, and Q_B is the electricity energy in battery.

2.3.2. Energy Management Strategy Based on Multiple Flight Phases. As shown in (11), the current EMS of HSA is relatively simple because more attention has been paid to the engineering applications, and the HSA can achieve long-endurance flight only by carrying more batteries. However, the more batteries will increase the power consumption during the level flight. Thus, the current EMS which simply relies on battery to store energy is not an effective way of

using solar energy, and the research of new EMS based on multiple flight phases including the lower cruising altitude and higher mission altitude for HSA will be particularly important.

The flight path of EMS based on multiple flight phases proposed in this paper is mainly divided into five stages, as shown in Figure 5. The design of mission altitude h_2 is beneficial to the engineering applications, and this is also conducive to charging the battery smoothly. Besides, it can be seen that the HSA can also execute a flight mission in a stable process in the mission altitude h_2 with the lower wind speed. On the other hand, the HSA can cruise in lower power consumption due to the lower altitude h_1 at night. At the same time, some missions like surveillance can be implemented at this altitude. Therefore, the above-proposed long-endurance flight path is significant for HSA in engineering applications, and the details of the phases are as follows.

(1) Phase 1: Lower Power Level Flight at Night. The stage of flight starts at time t_4 at the night before when the HSA reaches the altitude h_1, and finishes at time t_0 when the output solar power P_{mppt} of the voltage converter is larger than the required power P_{prop} in h_1 altitude. During this stage, the HSA is only supplied by battery for cruising. The required power for level flight of the HSA can be gained by (9). The proposed EMS at this stage can be represented by the following formula:

$$\dot{E} = \begin{cases} \dfrac{-P_{\text{prop}}}{(\eta_b \eta_{\text{bm}})}, & Q_B > Q_{B\_\min}, \\ 0, & Q_B \le Q_{B\_\min}. \end{cases} \tag{12}$$

(2) Phase 2: Maximum Power Ascending for Higher Altitude. The phase of flight begins at time t_0 when the solar energy on the wings generated by solar cells at flight altitude h_1 is enough to sustain the climbing flight, and the stage finishes at time t_1 when the HSA reach the mission altitude h_2. During the whole phase, all the electrical energy generated by solar cells is applied for ascending. Thus, the proposed EMS of HSA satisfies

$$\begin{cases} \dot{E} = 0, \\ P_{\text{mppt}} = P_{\text{prop}} = \dfrac{T \cdot v}{\eta_{\text{ma}}}. \end{cases} \tag{13}$$

(3) Phase 3: Higher Altitude Charging Battery. This stage of flight starts at time t_1 when HSA get to the mission altitude h_2 for level flight, and ends at time t_2 when the solar energy charges the battery to the $Q_{B\_\max}$. In this stage, HSA only charge the battery at the mission altitude h_2, where some missions can be performed. The power supply mode is as follows: one part of the electricity generated by the solar cells is used to sustain the flight of the HSA, while the rest of the solar energy will charge the battery. At this stage, the proposed EMS of HSA is represented by the following formula:

$$\dot{E} = \begin{cases} q_{\max}, & \left(P_{\text{mppt}} - P_{\text{prop}}\right)\eta_b \eta_{\text{bm}} \ge q_{\max}, \\ \left(P_{\text{mppt}} - P_{\text{prop}}\right)\eta_b \eta_{\text{bm}}, & 0 < \left(P_{\text{mppt}} - P_{\text{prop}}\right)\eta_b \eta_{\text{bm}} < q_{\max}, \\ 0, & Q_B \ge Q_{B\_\max}. \end{cases} \tag{14}$$

(4) Phase 4: Maximum Power Ascending for More Gravitational Potential Energy. This stage of flight begins at time t_2, with no task execution at mission altitude h_2, and finishes at time t_3 if the solar flux is zero. This stage consists of two processes: maximum power climbing when the P_{mppt} of voltage converter is more than the P_{prop}, and powered gravity gliding when the P_{mppt} could not satisfy the power consumption at its altitude. In this maximum power ascending phase, the HSA can make full use of the excess solar energy to gain the maximum altitude. The mode of power supply in this phase is as follows: all the solar energy is applied for powering the HSA for ascending and the battery is neither charged nor discharged. Therefore, the proposed EMS of HSA satisfies

$$\begin{cases} \dot{E} = 0, \\ P_{\text{mppt}} = P_{\text{prop}} = \dfrac{T \cdot v}{\eta_{\text{ma}}}, \\ Q_B = Q_{B\_\max}. \end{cases} \tag{15}$$

(5) Phase 5: Longest Endurance Gliding. This phase of flight starts at time t_3 when there is no solar energy production by the solar cell and finishes at time t_4 when the HSA glides to the lower altitude h_1. During the entire phase, there is no solar energy to provide the HSA propulsion system and the thrust is zero. Besides, the battery will not supply any energy to the flight of HSA as the way to use gravity energy reserving. During the phase, the proposed EMS of HSA satisfies

$$\begin{cases} \dot{E} = 0, \\ Q_B = Q_{B\_\max}, \\ T = 0. \end{cases} \tag{16}$$

To sum up, (12)–(16) constitute the EMS of HSA based on multiple flight phases.

2.4. Problem Implementation Frame and Solving Process. As shown in Figure 5 above, in phase 1, the HSA flight altitude is the altitude h_1, and the P_{mppt} is basically close the zero, which is much smaller than P_{prop} until t_0 time. During phase 2, the HSA climbs quickly between the altitude h_1 and altitude h_2, and the output power P_{mppt} of the voltage converter is greater than the required power P_{prop}. In phase 3, the HSA only charges the battery at the mission altitude h_2 by the surplus from the P_{mppt} to the P_{prop}. During phase 4, the output power P_{mppt} is used to power the aircraft for

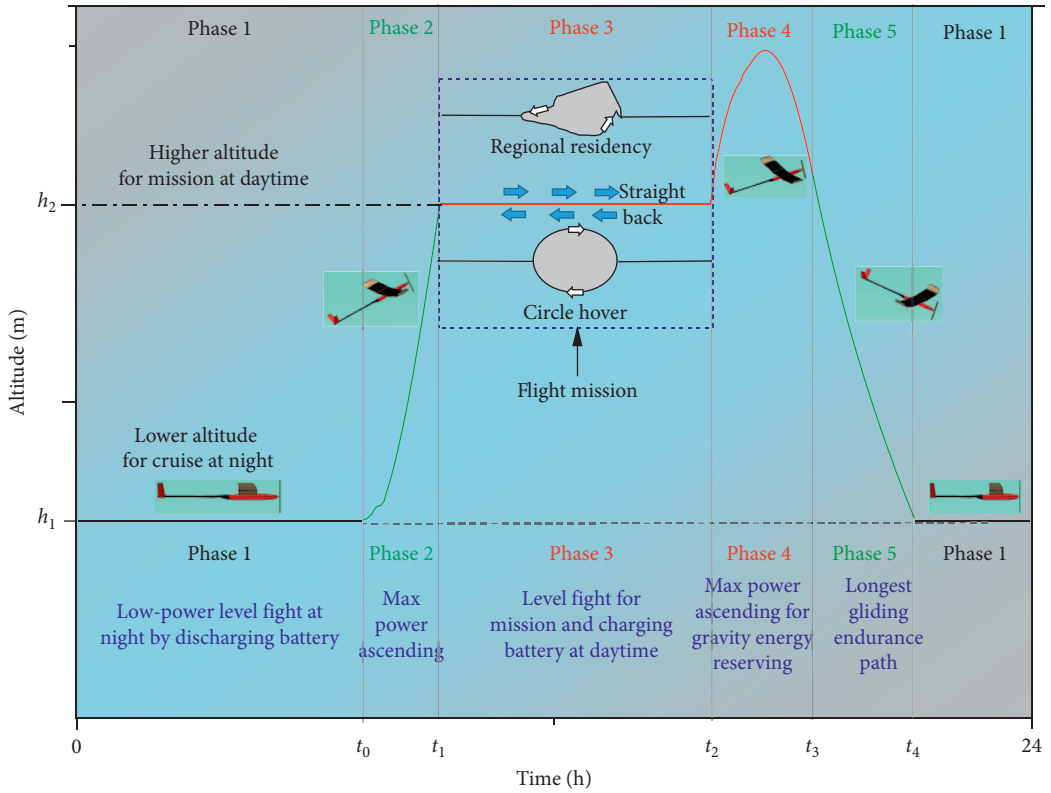

Figure 5: Schematic diagram of flight path of energy management strategy based on multiple flight phases.

ascending, which is equal to the propulsion system consumption P_{prop}. At the last phase, the HSA glides to the cruising altitude h_1 under the condition that the P_{mppt} and P_{prop} are zero. Therefore, the three variables flight altitude h, propulsion power P_{prop}, and solar power P_{mppt} can be used to determine which flight phase the aircraft is in. The efficiency of each component in energy management system must be also added in judging the phase. As a result, the HSA can adopt the appropriate proposed EMS at different phases. Table 2 shows the logical relationship to determine each flight phase according to h, P_{prop}, and P_{mppt}.

In phase 4, the logical relationship about flight altitude h is set as $h > h_2$, which may be seen to be unreasonable as the HSA may be at altitude $h_1 < h < h_2$ before the sunset at weak irradiation. However, the study carefully conducts many flight path simulations based on our previous research [35], and it can be concluded that the flight altitude h at t_3 time is greater than h_2, the same as the other research conclusions [5]. Meanwhile, the study will also take flight time $t > t_{noon}$ (the local standard time at noon) as the logical relationship in the proposed EMS model for following up further simulation. Therefore, the logical relationship in Table 2 can be reasonably used to build the new EMS model.

Based on the above introduction, a simulation application model of HSA about the proposed EMS calculation has been built as shown in Figure 6, where the aircraft kinematic and aerodynamic models are established based on (1) and (2). The solar irradiation model can be calculated according to (3)–(5).

In summary, the integrated model as shown in Figure 6 can calculate the new EMS in MATLAB/Simulink for HSA based on multiple flight phases, and it cloud be also used for the current EMS calculation with some modifications. The solving process is mainly the parameters initialization and calculation results analysis.

3. Simulation and Discussion

3.1. Simulation Parameters Setting. To illustrate the idea and advantage of the proposed EMS above, the results of numerical simulations on the current EMS and the new EMS have been calculated for comparison in this section, respectively. Firstly, the common atmospheric environment of the flight area has been analyzed for parameters settings, and the flight location of the HSA is set to Sanya, China (109°E, 18.3°N). Meanwhile, the initial configuration parameters of HSA are listed in Table 3; they are gained from Zephyr 7 because it has a detailed and comprehensive introduction in all the literature [3, 6, 11, 15] of HSA.

During the simulation process, the flight start time of Zephyr 7 is at 00 : 00 in June 20. The conditions parameters are shown in Table 4.

3.2. Results and Discussion. As the initialization of the setting parameters above shows, the calculation results between the current EMS and the proposed EMS of the HSA have been obtained by the MATLAB/Simulink. The comparisons of altitude h, quantity of electricity in battery Q_B, battery charge

Table 2: Logical relationship to determine each flight phase.

Variables	Phase 1	Phase 2	Phase 3	Phase 4	Phase 5
h	$h = h_1$	$h_1 < h < h_2$	$h = h_2$	$h > h_2$	$h > h_1$
P_{mppt}&P_{prop}	$P_{mppt} < P_{prop}$	$P_{mppt} = P_{prop}$	$P_{mppt} > P_{prop}$	$P_{mppt} = P_{prop}$	$P_{mppt} = P_{prop} = 0$

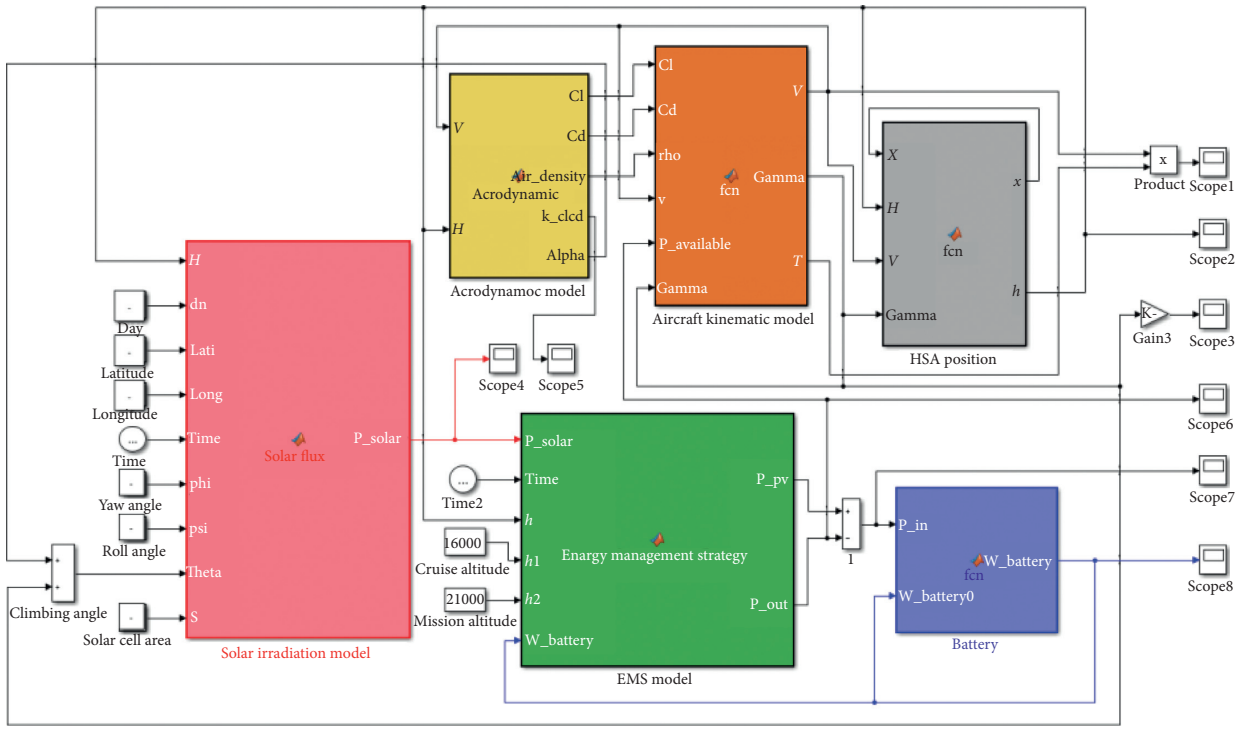

Figure 6: Simulation model of proposed energy management strategy for solar-powered aircraft based on multiple flight stages.

Table 3: The initial configuration parameters for model.

Parameters	Values	Units	Descriptions
m	50	kg	Mass of aircraft
Q_{B_max}	6	kWh	Total power capacity of battery
$Q_{B\_0:\ 00}$	3.5	kWh	The initial electric quantity of battery
b	22.5	m	Span length
S_W	25.3	m^2	Wing area
S_{SC}	16.2	m^2	Area of solar cells

Table 4: The simulation conditions parameters.

Parameters	Values	Units	Descriptions
h_1	16	km	Cruising altitude
h_2	21	km	Mission altitude
d_n	174	–	day number
Lati	18.3	°	Latitude of location
Long	109	°	Longitude of location

and discharge power $\dot{E}$, HSA speed v, pitching angel θ, and propulsion power P_{prop} are shown in Figures 7–11, respectively. Meanwhile, the red dotted line in each figure represents the available solar power P_{mppt} in the wings of the HSA, which also starts at 00 : 00 in June 20. Generally, the green line represents the parameter in the proposed EMS based on multiple flight phases, and the black line means the parameter in the current EMS of level flight.

Figure 7 shows that the highest altitude of the HSA can reach about 30 km at time 14 : 46 based on the proposed EMS, which indicates that HSA makes full use of the solar energy to acquire higher altitude. As a result, the HSA can fly by gravitational potential energy at about 18 : 30–22 : 00 as shown in Figure 9.

Figure 8 and 9 show that the battery discharge time of the proposed EMS is 3.50 hours later than the current EMS. As a result, compared to the current EMS, about 22.9% of energy surplus can be stored in battery with the proposed EMS during the long-endurance flight, which is conducive to the

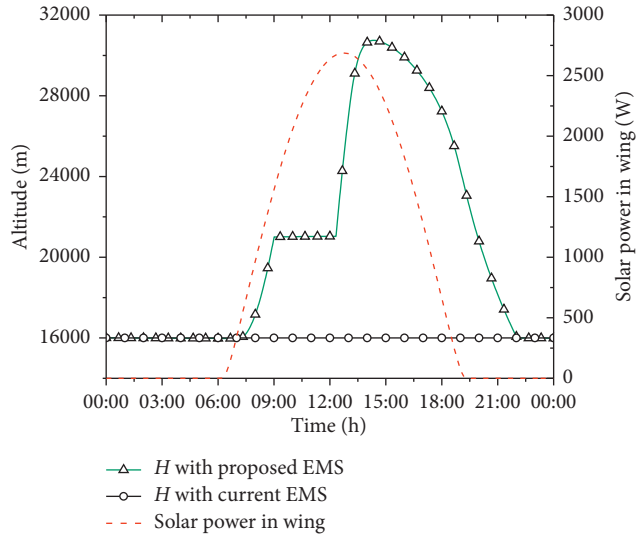

Figure 7: The comparison of altitude in the two energy management strategies.

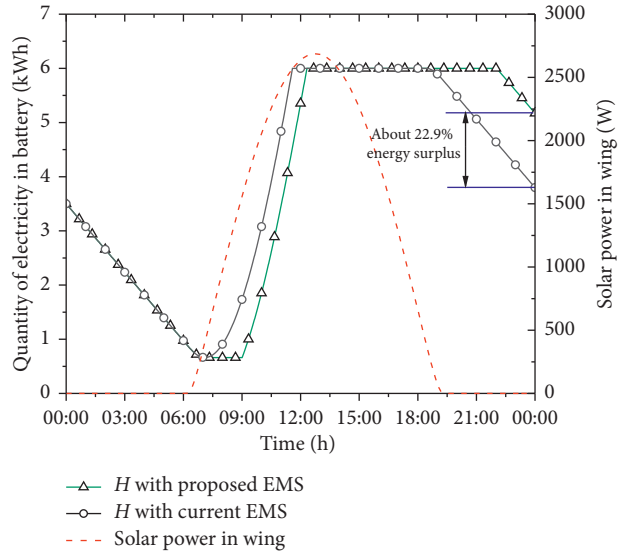

Figure 8: The comparison of quantity of electricity in battery in the two energy management strategies.

long-endurance flight of the HSA, especially the power consumption at night.

Figure 10 shows that the speed and pitching angle have the same trend as the flight altitude as shown in Figure 7, and the speed and pitching angle are constant in the current EMS and are changing in the proposed EMS. In addition, the changing of speed and propulsion power at sunrise and sunset in Figures 10 and 11 also indicate that the simulation results are reasonable with the proposed EMS based on multiple flight phases. Moreover, it is very attractive to analyze the changes like battery power and solar power at these special moments, which are helpful to understand the problem and validate the model.

In addition, a simulation example has been completed in different seasons (Spring Mar. 20, Summer Jun. 20, Autumn Sep. 20, and Winter Dec. 20) in Sanya. The simulation results are shown in Figures 12 and 13, and Figure 12 shows the variety of altitude and solar power in wings based on the proposed EMS in the four seasons. It can be concluded that the maximum flight altitude and the time of filling the battery will be strongly associated with the level of solar irradiation, especially in winter. Furthermore, Figure 13 displays the electric quantity of the batteries between the new EMS and the current EMS in the four seasons, and it clearly indicates that the current EMS cannot meet day and night flight for HSA in winter as the final electric quantity in battery is less than $Q_{B\_0:\,00} = 3.5$ kWh. What is more, the final electric quantity of the batteries with the proposed EMS in the four seasons is always larger than the $Q_{B\_0:\,00}$ with the current EMS. Therefore, the proposed EMS based on multiple flight phases is a very promising way to achieve the

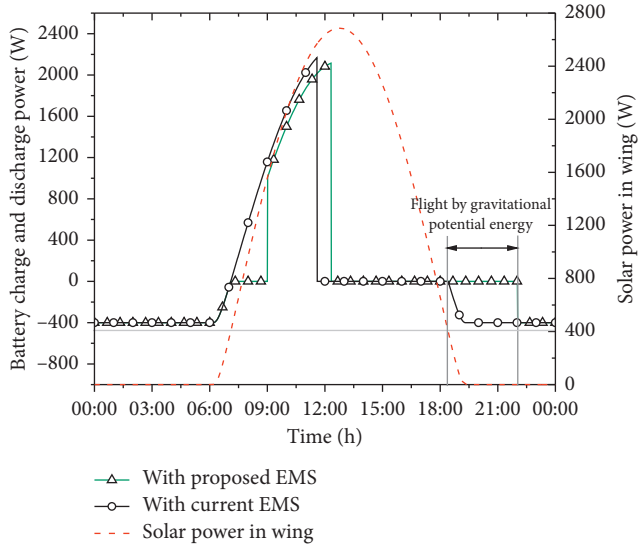

Figure 9: The comparison of battery charge and discharge power in the two energy management strategies.

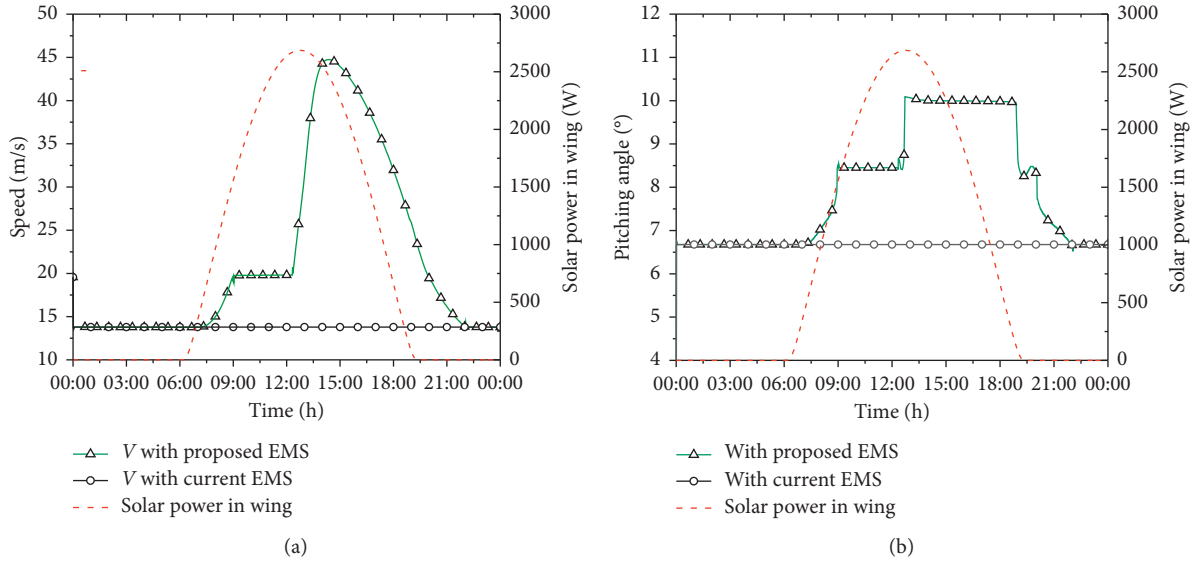

Figure 10: The comparison of speed and pitching angle in the two energy management strategies: (a) speed; (b) pitching angel.

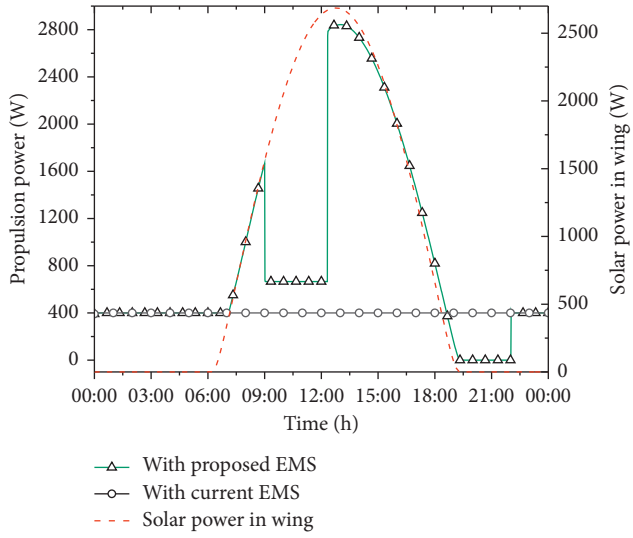

Figure 11: The comparison of propulsion power in the two energy management strategies.

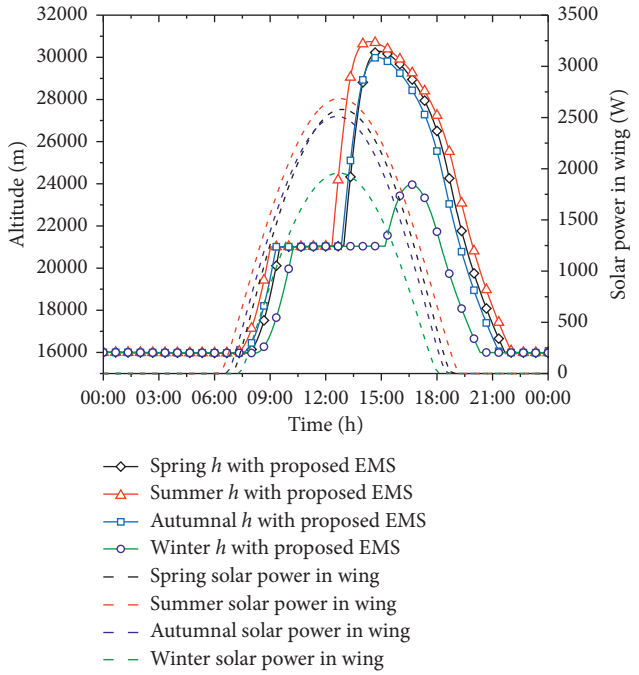

Figure 12: The variety of altitude and solar power in wing based on the proposed energy management strategy in the four seasons.

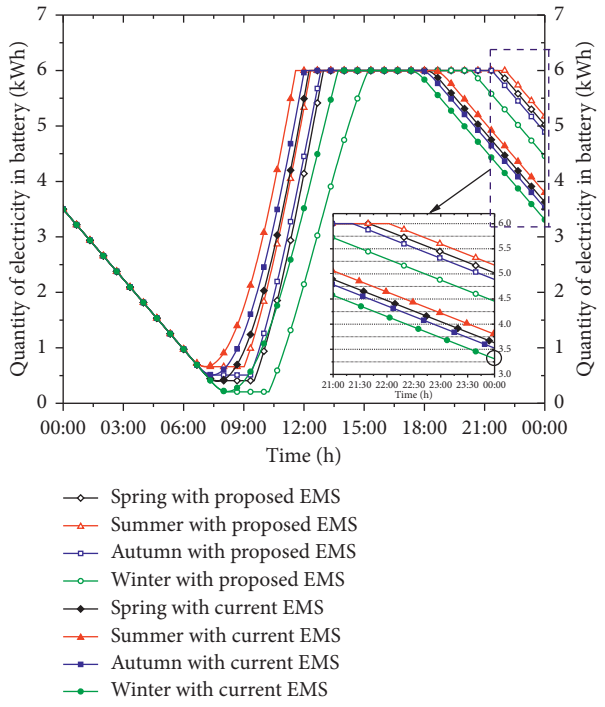

Figure 13: The comparison of electric quantity in battery in the four seasons based on the two energy management strategies.

long-endurance goal on condition of lower solar irradiation and shorter daytime for HSA.

4. Conclusions

In this paper, a new EMS based on multiple flight phases including the mission altitude has been proposed to enhance the fight endurance for HSA. Compared to the current relatively simple EMS, the fight path of the proposed EMS has five phases, namely, the lower altitude level flight at night, the maximum power ascending for mission altitude, the level flight at mission altitude, the maximum power ascending for higher altitude, and the longest gliding endurance. Phase 2, phase 4, and phase 5 could make good fitness and use of the gravity energy reserving strategy, and phase 3 shows and provides the possibility that HSA perform missions such as the regional residence, the straight back, and the circle hover just by more power consumption under the sufficient irradiation condition during the daytime. Besides, phase 3 can also give a smooth charging process relative to other research, which is more conducive to engineering applications.

The results of numerical simulations for Zephyr 7 on different season days have shown that the energy surplus with the new EMS is always more than the current EMS, since a fair amount of solar energy has been stored by the gravity energy reserving strategy based on this multiple flight phases. From the simulation results, the discharge time of Zephyr 7 battery can be delayed for about 3.50 hours with the proposed EMS on summer season days, and about 22.9% of energy surplus can be stored during the night, which is equal to reducing the battery weight from 16.0 kg to 12.3 kg. In addition, the simulation results on winter season days clearly indicate that Zephyr 7 can fly across the day and night, but the current EMS cannot. Therefore, the new proposed EMS is a very promising way to achieve the long-endurance goal for HSA when the flight conditions satisfy some constraints such as the deficiency of solar flux and the limit of battery mass.

It is also necessary to note that the study is a new two-dimensional multiple-flight-phase EMS for HSA based on our previous research of 3D trajectory optimization, and the specific typical missions were not added to the simulation calculations because the purpose of this study is the new EMS and its calculations. Thus, some improved research will be studied and analyzed in the future.

Data Availability

The data used to support the findings of this study are included within the article.

Conflicts of Interest

The authors declare no conflicts of interest.

Authors' Contributions

M. S. and K. S. were responsible for conceptualization. M. S. contributed to methodology as well as writing, reviewing, and editing the manuscript. C. S. was responsible for software and data curation. M. S., Y. J., and C. S. participated in validation. K. S. helped with formal analysis, resources, visualization, and funding acquisition. Y. J. carried out investigation, supervision, and project administration in

addition to writing the original draft of the manuscript. All authors have read and agreed to the published version of the manuscript.

Acknowledgments

This work was supported by the National Natural Science Foundation of China under Grant no. 51775021; the Key Laboratory of Aircraft Advanced Design Technology (Beihang University), Ministry of Industry; and the Fundamental Research Funds for the Central Universities under Grant no. YWF-18-BH-Y-165, the fifth youth top talent support program of Beihang University.

References

[1] O. R. Alvi, "Development of solar-powered aircraft for multipurpose application," in *Proceedings of 2010 AIAA SDM Student Symposium, 51st AIAA/ASME/ASCE/AHS/ASC Structures*, Orlando, FL, USA, April 2010.

[2] A. Noth, "Design of solar powered airplanes for continuous flight," Ph.D. thesis, Swiss Federal Institute of Technology Zurich, Zurich, Switzerland, 2008.

[3] X. Gao, "Research on high-altitude long-endurance flight based on energy storage by gravitational potential and energy extraction from wind shear," Ph.D. thesis, National University of Defense Technology, Changsha, China, 2014.

[4] "Zephyr pioneering the stratosphere," http://www.airbus.com.

[5] K. Sun, M. Zhu, L. Wang, and H. Liu, "Analysis of the hybird powered system for high-altitude unmanned aircraft," *Advances in Materials Science and Engineering*, vol. 2015, Article ID 380709, 9 pages, 2015.

[6] U. Papa, S. Ponte, and G. Core, "Conceptual design of a small hybird unmanned aircraft system," *Journal of Advanced Transportation*, vol. 2017, Article ID 9834247, 10 pages, 2017.

[7] T. Noll, J. Brown, M. Perez-Davis, S. Ishmael, G. Tiffany, and M. Gaier, *Investigation of the Helios Protype Aircraft Mishap*, Mishap Reprot, Hamptom, VA, USA, 2004.

[8] X.-Z. Gao, Z.-X. Hou, Z. Guo, R.-F. Fan, and X.-Q. Chen, "The equivalence of gravitational potential and rechargeable battery for high-altitude long-endurance solar-powered aircraft on energy storage," *Energy Conversion and Management*, vol. 76, pp. 986–995, 2013.

[9] Y. Huang, J. Chen, H. Wang, and G. Su, "A method of 3D path planning for solar-powered UAV with fixed target and solar tracking," *Aerospace Science and Technology*, vol. 92, pp. 831–838, 2019.

[10] Y. Zuo, P. Chen, L. Fu, Z. Gao, and G. Chen, "Advanced aerostructural optimization techniques for aircraft design," *Mathematical Problems in Engineering*, vol. 2015, Article ID 753042, 12 pages, 2015.

[11] X. Zhu, *Generalized Energy Based Conceptual Design Method of Solar-Powered Airplane*, Ph.D. thesis, National University of Defense Technology, Changsha, China, November 2014.

[12] R. Hannes, "Fly around the world with a solar powered airplane," in *The 26th Congress of International Council of the Aeronautical Sciences*, p. 8954p. 8954, Anchorage, Alaska, USA, 14-19 Semptember 2008.

[13] J. Gonzalo, D. López, D. Domínguez, A. García, and A. Escapa, "On the capabilities and limitations of high altitude pseudo-satellites," *Progress in Aerospace Sciences*, vol. 98, pp. 37–56, 2018.

[14] E. Cestino, "Design of solar high altitude long endurance aircraft for multi payload & operations," *Aerospace Science and Technology*, vol. 10, no. 6, pp. 541–550, 2006.

[15] Z. Z. Annabel, *A High Altitude Long Endurance Unmanned Air Vehicle*, Master Thesis, University of Surrey, Guildford, UK, 2009.

[16] Nasa Dryden Flight Research Center, "Helios solar/fuel cell aircraft crashes," *Fuel Cells Bulletin*, vol. 8, p. 6, 2003.

[17] S. Herrería-Alonso, A. Suárez-González, M. Rodríguez-Pérez, R. F. Rodríguez-Rubio, and C. López-García, "A solar altitude angle model for efficient solar energy predictions," *Sensors*, vol. 20, no. 5, p. 1391, 2020.

[18] D. Scheiman, R. Holeisel, D. Edwards et al., "Enhanced endurance of a unmanned aerial vehicles using high efficiency Si and III-V solar cells," in *Proceedings of the 2017 IEEE 44th Photovoltaic Specialist Conference*, pp. 3514–3519, Washington, DC, USA, June 2017.

[19] V. Dwivedi, P. Kumar, A. K. Ghosh, and G. Kamath, "Selection of size of battery for solar powered aircraft," in *Proceedings of the 11th IFAC Conference on Control Applications in Marine Systems, Robotics, and Vehicles*, pp. 424–430, Opatija, Croatia, September 2018.

[20] X.-Z. Gao, Z.-X. Hou, Z. Guo, and X.-Q. Chen, "Reviews of methods to extract and store energy for solar-powered aircraft," *Renewable and Sustainable Energy Reviews*, vol. 44, pp. 96–108, 2015.

[21] J. Liao, Y. Jiang, J. Li et al., "An improved energy management strategy of hybrid photovoltaic/battery/fuel cell system for stratospheric airship," *Acta Astronautica*, vol. 152, pp. 727–739, 2018.

[22] C. Shan, M. Lv, K. Sun, and J. Gao, "Analysis of energy system configuration and energy balance for stratospheric airship based on position energy storage strategy," *Aerospace Science and Technology*, vol. 101, Article ID 105844, 2020.

[23] J.-K. Shiau and D.-M. Ma, "Development of an experimental solar-powered unmanned aerial vehicle," *Journal of the Chinese Institute of Engineers*, vol. 38, no. 6, pp. 701–713, 2015.

[24] S. Schopferer, C. Liersch, M. Brizon, and S. Froese, "Evaluating the energy balance of high altitude platforms at early design stages," in *Proceedings of the International Conference on Unmanned Aircraft Systems*, pp. 170–177, Arlington, VA USA, June 2016.

[25] B. G. Gang, H. Kim, and S. Kwon, "Ground simulation of a hybrid power strategy using fuel cells and solar cells for high-endurance unmanned aerial vehicles," *Energy*, vol. 141, pp. 1547–1554, 2017.

[26] S. C. Arum, D. Grace, P. D. Mitchell, M. D. Zakaria, and N. Morozs, "Energy management of solar-powered aircraft-based high altitude platform for wireless communications," *Electronics*, vol. 9, no. 1, p. 179, 2020.

[27] Y. Zhang, Y. Liu, and Y. Liu, "An hybrid dynamical modeling and control approach for energy saving of central air conditioning," *Mathematical Problems in Engineering*, vol. 5, pp. 1–12, Article ID 6389438, 2018.

[28] K. Wang, W. Wang, L. Wang, and L. Li, "An improved SOC control strategy for electric vehicle hybrid energy storage systems," *Energies*, vol. 13, no. 20, p. 5297, 2020.

[29] G. Pulido, G. Perales, J. Campaña, G. Gómez, and E. Velázquez, "Energy considerations for tracking in DC to DC power converters," *Mathematical Problems in Engineering*, vol. 2019, Article ID 1098243, 9 pages, 2019.

[30] K. Wang, X. Feng, J. Pang, J. Ren, C. Duan, and L. Li, "State of charge (SOC) estimation of lithium-ion battery based on adaptive square root unscented kalman filter," *International*

Journal of Electrochemical Science, vol. 15, no. 9, pp. 9499–9516, 2020.

[31] J. Yan, H. Wang, S. Zhong, Y. Lan, and K. Huang, "Control strategy for the energy optimization of hybrid regenerative braking energy utilization system used in electric locomotive," *Mathematical Problems in Engineering*, vol. 2018, Article ID 2510487, 13 pages, 2018.

[32] X.-Z. Gao, Z.-X. Hou, Z. Guo, J.-X. Liu, and X.-Q. Chen, "Energy management strategy for solar-powered high-altitude long-endurance aircraft," *Energy Conversion and Management*, vol. 70, pp. 20–30, 2013.

[33] G. Sachs, J. Lenz, and F. Holzapfel, "Unlimited endurance performance of solar UAVs with minimal or zero electric energy storage," in *Proceedings of the AIAA Guidance, Navigation, and Control Conference*, Chicago, IL, USA, August 2009.

[34] J. Wu, H. Wang, Y. Huang, M. Zhang, and Z. Su, "Solar-powered aircraft endurance map," *Journal of Guidance Control and Dynamics*, vol. 42, pp. 687–694, 2018.

[35] M. Sun, X. Ji, K. Sun, and M. Zhu, "Flight strategy optimization for high-altitude solar-powered aircraft based on gravity energy reserving and mission altitude," *Applied Sciences*, vol. 10, no. 7, p. 2243, 2020.

Hindawi
Mathematical Problems in Engineering
Volume 2020, Article ID 8880661, 10 pages
https://doi.org/10.1155/2020/8880661

Research Article

An Early Warning Method of Distribution System Fault Risk Based on Data Mining

Yeying Mao,[1] Zhengyu Huang,[1] Changsen Feng,[2] Hui Chen,[1] Qiming Yang,[1] and Junchang Ma[1]

[1]*State Grid Suzhou Power Supply Company, Suzhou 215004, China*
[2]*College of Information Engineering, Zhejiang University of Technology, Hangzhou 310023, China*

Correspondence should be addressed to Changsen Feng; fcs@zjut.edu.cn

Received 9 September 2020; Revised 20 September 2020; Accepted 20 November 2020; Published 7 December 2020

Academic Editor: Kai Wang

Accurate warning information of potential fault risk in the distribution network is essential to the economic operation as well as the rational allocation of maintenance resources. In this paper, we propose a fault risk warning method for a distribution system based on an improved RelieF-Softmax algorithm. Firstly, four categories including 24 fault features of the distribution system are determined through data investigation and preprocessing. Considering the frequency of distribution system faults, and then their consequences, the risk classification method of the distribution system is presented. Secondly, the K-maxmin clustering algorithm is introduced to improve the random sampling process, and then an improved RelieF feature extraction method is proposed to determine the optimal feature subset with the strongest correlation and minimum redundancy. Finally, the loss function of Softmax is improved to cope with the influence of sample imbalance on the prediction accuracy. The optimal feature subset and Softmax classifier are applied to forewarn the fault risk in the distribution system. The 191-feeder power distribution system in south China is employed to demonstrate the effectiveness of the proposed method.

1. Introduction

As the last step in the power industry, the distribution system is closely and directly connected to end-users [1, 2]. The stable operation of the distribution system is crucial to the reliable power supply for users [3–5]. However, the distribution system has a complex network structure and various equipment components and even worse, the external factors that cause distribution system faults are highly random. Since the causal relationship is nonlinear, the conventional fault prediction method based on the electrical mechanism is challenging to function. Therefore, exploring the potential risks in the distribution system operation process and furtherly taking corresponding measures have become a severe challenge to power supply companies [6, 7].

The concept of distribution system fault risk is put forward in [8], and the fault probability index system and fault consequence index system are established, respectively, from two dimensions of possibility and severity. In [9], time series, gray theory, and statistical analysis are applied to deeply analyse the distribution system's fault repair data and extract fault characteristics. However, the above methods focus on the definition of failure risk and the establishment of an index system, and the correlation analysis of failure outage factors and the establishment of the fault early warning model are less studied.

Data mining has recently been widely applied in the field of power systems due to its excellent computing performance and adaptability [10–13]. The fuzzy classification algorithm is developed in [14] to identify the fault cause. In [15], the correlation mining method between load characteristics and air temperature index is proposed based on the linkage analysis theory. Association rule mining is implemented in [16] to conduct fault cause analysis, which can effectively identify critical variables that have a substantial impact on fault. In [17], a novel framework of distribution system fault detection is presented to cope with the power system complexity and double-way power flows, and the

support vector data description method is adopted due to the limited available fault data. In [18], the fault line selection problem is transformed into a classification problem, including data preparation, training, classification, and evaluation.

For the feature dimension reduction, the characteristics and main algorithms of filtering, encapsulation, and embedded dimension reduction methods are summarized in [19, 20], and the robustness, prediction accuracy, and interpretability of different algorithms are compared. Literature [21] proposed a feature extraction method suitable for high-dimensional data. This method can extract feature vectors strongly related to classification but has poor performance in removing redundancy. In [22], principal component analysis is utilized to extract the main components from high-dimensional features through matrix transformation and eliminate the weak value information. Literature [23] conducts correlation recognition and redundancy removal for feature vectors based on correlation analysis theory.

Many researchers [24, 25] have explored the classification method and applied it to distribution system fault prediction [26–28]. Literature [29] presented a fault risk warning method of the distribution system based on improved support vector machine algorithm. Literature [30] focuses on meteorological factors and presents a distribution system fault classification prediction method combining AdaBoost and decision tree. Literature [31, 32] introduces the overall structure of a distribution operation analysis system and expands the application of the massive fault data to the fault risk level prediction and weak spot identification. However, the distribution system fault is an accidental event, and the proportion of fault data samples is far less than that of normal operation data sample; that is, the distribution system fault prediction is a typical unbalanced sample problem. Therefore, it is necessary to improve the model to adapt to the classification prediction of minority categories of samples.

Given the aforementioned consideration, a fault warning method based on improved RelieF-Softmax algorithm for the distribution system is proposed. Firstly, data acquisition and data preprocessing are carried out to determine the initial associated feature set of distribution system faults, and a fault risk classification method of the distribution system is proposed. Secondly, because of the RelieF algorithm's deficiency in the initial sampling and redundancy removal, an improved RelieF feature extraction method combined with the correlation coefficient method is proposed to screen out the fault optimal feature vector with the strongest correlation and minimum redundancy. Finally, a fault risk level prediction model of distribution system based on improved Softmax classifier is established to enhance unbalanced sample prediction accuracy. Taking 191 feeder lines in south China as examples, the analysis results demonstrate the effectiveness of the fault risk warning method proposed in this paper, which can provide crucial guiding significance to the operation practice.

The remainder of this paper is given as follows. Section 2 describes the preprocessing of distribution system data. The improved RelieF algorithm is presented in Section 3, and a fault risk warning method of the distribution system based on improved Softmax loss function is proposed in Section 4. The numerical results of the presented method are detailed in Section 5. The final section of the paper gives conclusions based on this study.

2. Preprocessing of Distribution System Data

2.1. Data Collection. By investigating the widely used information management systems related to the distribution system of State Grid Corporation Company of China, six systems, including the distribution production management system, distribution automation system, electricity information collection system, geographical information system, 95598 customer service system, and marketing business management system, are selected to collect the operation data, equipment data, and historical fault information of the distribution system. The data classification and data sources are detailed in Table 1.

2.2. Data Preprocessing. Preprocessing the initial data is necessary to improve the prediction accuracy, generally including data cleaning, data transformation, data integration, and outlier diagnosis.

Data cleaning is to process the vacant and repeated values in the initial data to ensure the data set's integrity, consistency, and rationality. The empty values in the data samples can be eliminated or replaced by the mean or the median. The repeated value recognition rules could be set based on the logical relationship between the data samples. For example, if the feeder name and the power failure time of two samples are the same, it is considered that there may exist a repeated sample and one of them should be eliminated. Other rules can be presented according to the specific problems and decision-maker preferences.

Data transformation, mainly including standardized processing, data grading, and quantization, makes it easier to perform data analysis. The max-min method, z-score method, or decimal scaling method can be used for standardized data processing. For data such as rainfall, thunderstorm, and wind, continuous numerical values should be discretized and classified to highlight data differences.

Data integration is to integrate, summarize, and correlate data from multiple sources. Due to the diversity of data sources, it is necessary to cross-verify the data. For example, according to the historical faults data, the planned power failure part can be eliminated according to the power loss information of the user side, that is, the power failure only caused by the faults. Afterwards, this part's power failure information can be verified and compared with the power failure information recorded in the faults work order.

The outlier diagnosis effectively identifies and eliminates the wrong inputs and meaningless values that may appear in the initial data. Outliers may lead to a decrease in the accuracy of prediction results. Therefore, statistical methods, clustering, or graph-based methods should be applied to search and delete outliers.

Finally, the initial feature set could be obtained after a series of data preprocessing, as shown in Table 2.

Table 1: Related data of distribution system fault warning.

Category	Data sources	Specific information
Fault data	95598 customer service system, marketing business management system and distribution automation system	Power outage time, power outage frequency, name of feeder, substation of power outage feeder, number of affected households, feeder construction mode, power supply area classification
Meteorological information	China meteorological network	Rainfall, minimum temperature, maximum temperature, average temperature, humidity, wind speed, wind level, visibility, cloud cover, snowfall, thunderstorm day
Operation data	Electricity information collection system	Distribution transformer capacity, real-time load
Parameter data	Geographical information system and distribution production management system	The total length of the feeder, the length of the overhead section, the length of the cable, the operation time, and the substation

Table 2: Initial fault feature set of distribution system.

Category	Variable	Feature
Fault data	f_1	Fault risk level
	f_2	Monthly fault frequency
	f_3	Number of households affected by power failure
Meteorological information	f_4	Monthly cumulative rainfall
	f_5	Monthly mean temperature
	f_6	Monthly highest temperature
	f_7	Monthly extreme weather days
	f_8	Monthly mean humidity
	f_9	Monthly extreme humidity days
	f_{10}	Monthly gale days
	f_{11}	Monthly thunderstorm days
	f_{12}	Monthly snowy days
Operation data	f_{13}	Maximum monthly load
	f_{14}	Average monthly load
	f_{15}	Month classification
Parameter data	f_{16}	The geographical location classification
	f_{17}	Feeder construction mode
	f_{18}	Power supply area classification
	f_{19}	Length of overhead feeder section
	f_{20}	Length of cable feeder segment
	f_{21}	Total length of the feeder
	f_{22}	Number of feeder segment switches
	f_{23}	Number of feeder transformers
	f_{24}	Feeder operation time

2.3. Fault Risk Classification. Distribution system fault risk consists of the frequency of failure and the consequences of failure. Given the assessment indexes of power grid companies, the failure rate (the frequency of failure) of 100 km and the number of households affected by power failure (the influenced scope of fault) are selected as the basis for the classification of distribution system fault risk. Among them, the former is an important index used by power supply companies to assess each branch company's annual operation level, which reflects the fault frequency of distribution network feeders per unit length. The latter is similarly a standard index to measure the reliability of the power supply of distribution system, reflecting the scope of the influence of power failure.

Equation (1) is utilized to obtain the failure rate of the feeder per 100 km per month.

$$S_i = \frac{\sum_{j=1}^{n_f} f_{ij}}{L_i}, \tag{1}$$

where S_i represents the monthly failure rate per 100 km of the feeder i, f_{ij} denotes the state of the j_{th} power failure of the feeder i, and L_i is the length of the feeder i.

Equation (2) gives the mathematical definition of the number of households affected by the monthly power failure.

$$C_i = \sum_{j=1}^{n_f} \sum_{k \epsilon F_{ij}} n_{ij,k} t_{ij,k}, \tag{2}$$

where C_i is the number of households affected by the monthly power failure of the feeder i, n_f is the total number

of power failure accidents in that month, and F_{ij} is the set of transformers affected in the j_{th} power failure of the feeder i. $n_{ij,k}$ and $t_{ij,k}$ represent the number of households and power failure time of the k_{th} affected transformer in the j_{th} power failure of the feeder i, respectively.

Because of the calculated feeder failure rate per month of 100 km and the number of households affected by power failure, the power failure risk level of the distribution system can be divided into general, emergency, and severe. Referring to a city in south China in 2018, the annual failure rate is 2.502 times/ 100 km·year, and the number of households affected by the distribution system failure is 102,500 households. The fault risk classification is shown in Table 3. It should be pointed out that the threshold value of each level can be adjusted according to the actual situation of the local distribution system, and the higher risk level of any two indexes is taken as the result in the calculation.

3. Fault Feature Extraction of Distribution System Based on Improved RelieF Algorithm

The dimension and quality of input vectors directly affect the accuracy of classification prediction results. Too many input vectors may lead to model overfitting and operation efficiency reduction, and input collinearity will reduce the model's stability. Therefore, it is necessary to extract the optimal fault feature subset and screen the strongest correlation and the least redundant vectors, to improve the efficiency and accuracy of fault risk prediction.

3.1. RelieF Algorithm. RelieF algorithm is a typical filtering feature selection method to extract feature vectors with a significant distinguishing degree for target classification. In the RelieF algorithm, weight is assigned to each feature based on the distance measurement, so as to evaluate the ability of feature vectors to distinguish target categories.

The specific definition is as follows: for sample set D, randomly select sample s and find k nearest neighbors in the same kind of s, which are defined as H and k nonnearest neighbors, which are defined as M. In this paper, Euclidean metric is employed to measure the distance between samples. The calculation formula of the characteristic difference between samples is described as follows:

$$\text{diff}(a, X, Y) = \begin{cases} \dfrac{X(a) - Y(a)}{\max(a) - \min(a)} & \text{a is continuous,} \\ 0 \quad \text{a is discrete } X(a) \neq Y(a), \\ 1 \quad \text{a is discrete } X(a) = Y(a), \end{cases} \tag{3}$$

where diff (a, X, Y) represents the difference between sample X and sample Y on feature a.

The weight updating formula is defined as follows:

$$W_a = W_a - \sum_{i=1}^{k} \frac{\text{diff}(a, H_i, s)}{tk} + \sum_{M \notin \text{class}(s)} \frac{\left[(N(M)/(1 - N(\text{class}(s)))) \sum_{i=1}^{k} \text{diff}(a, M_i, s) \right]}{tk}, \tag{4}$$

where W_a denotes the weight value of feature a, k is the number of the nearest neighbor sample, t is the number of sampling, H_i and M_i represent the i_{th} nearest neighbor and non-nearest neighbor of the sample s, respectively, and class( ) is the ratio function of the sample number to the total sample number.

3.2. Improved RelieF Algorithm. Although the RelieF algorithm has no restrictions on data types and relatively high operating efficiency, it still has the following disadvantages:

(1) Considering that the initial random sampling is put back sampling, the selected sample may be too limited due to repeated sampling. Since the repeated sample does not provide new information for the classification and is an invalid input, the model results' accuracy may be affected.

(2) The algorithm has a weak ability to distinguish the redundant features, which leads to a considerable noise of the input features.

Given the consideration mentioned above, the RelieF algorithm is improved from two aspects. On the premise that the algorithm flow remains unchanged, the clustering algorithm is introduced to cluster the initial data, and a hierarchical sampling algorithm based on clustering is proposed. Due to the deficiency of redundancy elimination in the RelieF algorithm, the feature extraction method combining RelieF and the correlation coefficient method is presented to identify and eliminate redundant features effectively.

3.2.1. Hierarchical Sampling Based on K-Maxmin Clustering Algorithm. The K-maxmin distance method selects data point as far as possible as the clustering center based on Euclidean distance, so as to effectively avoid the situation that the initial clustering center may be too close when compared to the k-means method. The K-maxmin algorithm is with high efficiency and is unnecessary to determine the initial clustering number. Due to the page limit, the K-maxmin clustering algorithm process can refer to the literature [33], which will not be described here.

The K-maxmin clustering algorithm is introduced to cluster the initial feature set, and then stratified sampling is applied in line with the category proportion. The total sampling number M is distributed to all categories proportionally, and the number of sampling points of each category can be determined by the proportion of the category to the total sample. In this way, the low probability of local sampling in random sampling can be effectively avoided. Besides, each sampling is strictly limited to

Table 3: Classification of fault risk level in distribution system

Risk level	Status	Failure rate of 100 km	Households affected by power failure
1	General	=0	0
2	Emergency	(0, 0.208]	[0, 270]
3	Severe	≥0.208	≥270

nonrepeated sampling, which ensures that each sampling is assigned with new weight for the feature vectors, so as to significantly improve the classification effect of random sample points on the classification results.

3.2.2. Correlation Coefficient Method. Pearson coefficient is an indicator of the degree of linear correlation between variables, widely used in statistics. Its value is between (−1, 1). If it is positive, it means a positive correlation between two variables, or otherwise, it means a negative correlation. The higher the absolute value is, the higher the correlation will be. Pearson correlation coefficient calculation formula is described as follows.

$$\rho_{XY} = \frac{\mathrm{Cov}(X, Y)}{\sigma_X \sigma_Y}, \tag{5}$$

where Cov (X, Y) is the covariance of sample X and sample Y, and σ_X and σ_Y are the variances of sample X and sample Y, respectively.

The correlation coefficient matrix can be obtained by calculating the correlation coefficient between each input vector. It is generally believed that the correlation is strong if the correlation coefficient is higher than 0.7, and the corresponding feature vector pair will be put into the redundant set. Suppose that the features extracted by RelieF algorithm show redundant features, the input vectors with a small weight value of redundant feature pairs will be eliminated, and only one feature vector is retained.

3.3. Optimal Feature Extraction Method Based on the Improved RelieF Algorithm. The flow chart of the feature extraction method based on improved RelieF algorithm is depicted in Figure 1. Firstly, the initial data set is clustered by K-maxmin algorithm to realize stratified sampling and nonrepeated sampling. Secondly, the improved RelieF algorithm is applied to identify the feature vectors that can significantly distinguish the target classification. Finally, the correlation coefficient method is conducted to reduce the optimal feature subset's dimension, and the redundant feature vectors are furtherly eliminated to obtain the optimal feature subset.

4. Fault Risk Warning Method of Distribution System Based on Improved Softmax Loss Function

4.1. Improved Softmax. Softmax classification [34] is an extension of binary classification logistic regression to solve multiple classification problems. Its algorithm is based on Softmax regression, and the category with the highest output probability is the prediction category.

For input data with m dimensions $\{(x_1, y_1), (x_2, y_2), ..., (x_m, y_m)\}$, where x_i is the input vector, y_i is the corresponding category vector, and there are K categories; namely, y_i belongs to $\{1, 2, ..., K\}$. Softmax regression is used to estimate the probability that the input data belongs to each category. For any input vector, its prediction function can be expressed as

$$h_\theta(x) = P(y_i = j|x, \theta) = \frac{1}{\left(1 + e^{-\theta^T x}\right)},$$

$$h_\theta(x_i) = \begin{bmatrix} P(y_i = 1|x_i, \theta) \\ P(y_i = 2|x_i, \theta) \\ \vdots \quad \vdots \quad \vdots \\ P(y_i = K|x_i, \theta) \end{bmatrix} = \sum_{j=1}^{K} e^{\theta_j^{\mathrm{T}} x_i} \begin{bmatrix} e^{\theta_1^{\mathrm{T}} x_i} \\ e^{\theta_2^{\mathrm{T}} x_i} \\ \vdots \\ e^{\theta_K^{\mathrm{T}} x_i} \end{bmatrix}, \tag{6}$$

where $P(\ )$ represents the probability of occurrence within parentheses. $\theta = [\theta_1, \theta_2, ..., \theta_K]$ is the weight vector of $n \times K$, and n is the number of sample features. $\sum_{j=1}^{K} e^{\theta_j^{\mathrm{T}} x_i}$ is a normalized parameter that guarantees the sum of the probabilities to be 1.

The Softmax loss function is based on the logarithmic cross entropy theory, which can be expressed as

$$J(\theta) = -\frac{1}{m}\left\{\sum_{i=1}^{m}\sum_{j=1}^{K}\left[\mathrm{Ind}(y_i = j)\log\left(\frac{e^{\theta_j^{\mathrm{T}} x_i}}{\sum_{j=1}^{K} e^{\theta_j^{\mathrm{T}} x_i}}\right)\right]\right\}, \tag{7}$$

where Ind ($y_i = j$) is 0-1 indicating function, if true in parentheses, the value is 1, otherwise 0.

Combined with equations 6 and 7, the classification prediction problem can be transformed to solve the prediction function parameter, with equation (7) being minimized, so as to obtain the probability of different categories of the sample. The physical meaning of the loss function defined in equation (7) is to make the proportion of the correct classification samples as large as possible. Still, this function assumes no difference between the categories in the proper classification under the condition of sample data equilibrium. However, in the problem of fault early warning for the distribution system, the loss of high risk is mistaken for the low risk could be much bigger than the reverse. In other words, the correct classification of high risk is more important than the correct classification of low risk, and the low risk data account for a large proportion in the studied samples. Therefore, the loss function of equation (7) is improved to adapt to the proposed strategy in this paper.

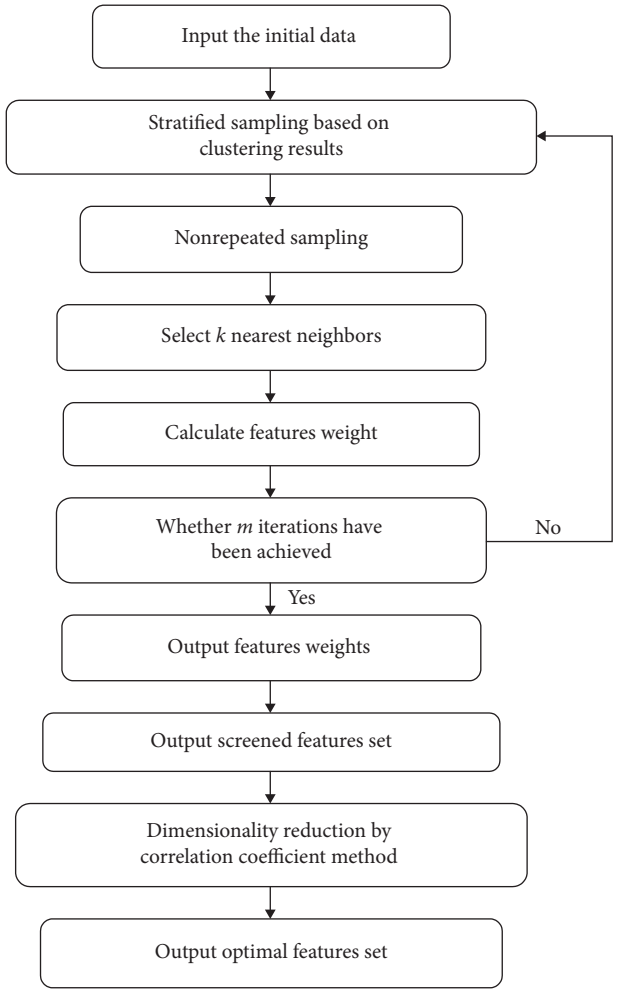

Figure 1: Flowchart of feature extraction method based on improved RelieF algorithm.

$$J(\theta) = -\frac{1}{m}\left\{\sum_{i=1}^{m}\sum_{j=1}^{K}\left[\alpha_j \mathrm{Ind}(y_i = j)\log\left(\frac{e^{\theta_j^{\mathrm{T}} x_i}}{\sum_{j=1}^{K} e^{\theta_j^{\mathrm{T}} x_i}}\right)\right]\right\} + \lambda\sum_{t=1}^{n}\sum_{j=1}^{K}\theta_{lj}^2, \tag{8}$$

where the first item is to measure the classification error, α_j is the category weight to adjust the sample imbalance degree and increase the weight of minority class being mistaken for other categories. The second item is the regularization function, where λ is the regularization parameter and called $L2$ norm. Regularization function can make it easy to obtain the optimal global solution while avoiding the training model's overfitting and improving the model's generalization ability.

The gradient descent method is a common optimization method to solve the maximum or minimum value of a function. Hence, it is employed to train the Softmax classifier. The partial derivative of equation (8) can be expressed as

$$\frac{\partial}{\partial\theta_j}J(\theta) = -\frac{1}{m}\left\{\sum_{i=1}^{m}\alpha_j x_i\left[\mathrm{Ind}(y_i = j) - h_\theta(x_i)\right]\right\} + \frac{2}{\lambda}\theta_j. \tag{9}$$

According to equation (10), update theta with each iteration:

$$\theta_j := \theta_j - \delta\frac{\partial}{\partial\theta_j}J(\theta), \tag{10}$$

where δ is the iteration step.

4.2. Fault Risk Warning Method of Distribution System. The data-driven fault warning method can be divided into three stages: data acquisition and preprocessing, feature extraction, and risk level prediction. The research idea and risk warning process of this paper are illustrated in Figure 2.

Data acquisition and preprocessing. Collect fault data, operation data, parameter data, and meteorological information and perform data cleaning, integration, and outliers diagnose as required. Determine the fault risk classification based on the failure rate of 100 km and the number of households affected by power failure. Consequently, the initial sample set can be obtained, where each row represents a sample, each column denotes a feature, and the last column represents the fault risk level.

Feature extraction. Feature extraction includes two aspects: remove weak correlation and redundancy. The improved RelieF algorithm and correlation coefficient method are presented to obtain the optimal feature subset with the strongest correlation and minimum redundancy.

Risk level prediction. The improved Softmax is proposed to train the training set and learn the mapping relationship between the fault influencing factors and the fault risk level of the distribution system. Based on this learning model, the fault risk level of test samples can be reasonably predicted.

5. Case Study

A total of 191 feeders and their data from January 2018 to December 2018 in a southern city are collected as training samples to predict the monthly feeder fault risk level from January 2019 to June 2019.

5.1. Data Preprocessing. The failure data, operation data, ledger data, and meteorological data of 191 feeders collected from January 2018 to December 2018 are processed by the method in Section 2. Taking each feeder as a unit, 24 fault features of 4 categories are obtained, as shown in Table 2. Among them, f_1 fault risk level can be determined comprehensively in line with f_2 and f_3. After preprocessing, the initial data set is obtained with 2292 samples, including 2154 samples of class I, 95 samples of class II, and 43 samples of class III.

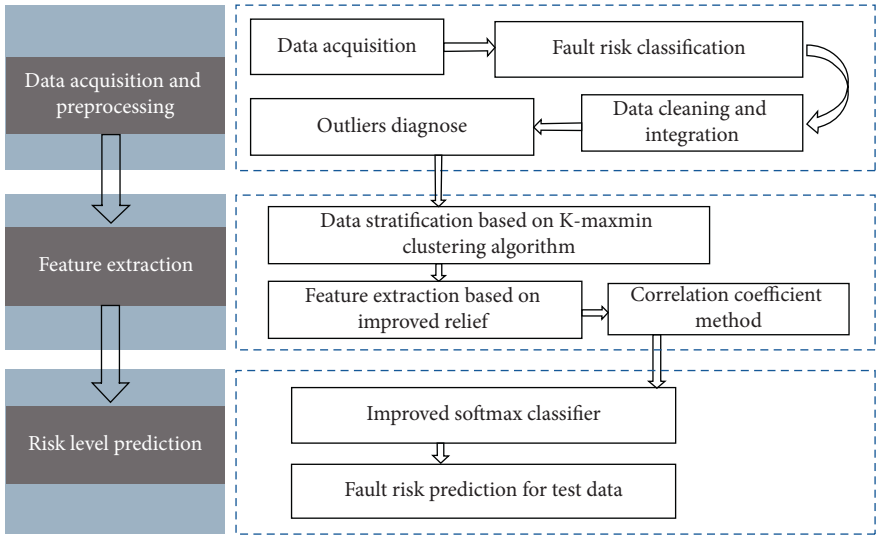

Figure 2: Flowchart of fault risk warning method for distribution system.

5.2. Analysis of Feature Extraction Results. The number of categories obtained based on K-maxmin clustering algorithm is 5, and the sampling proportion of each cluster can be determined according to the ratio of the sample number of each cluster in the total sample. Afterwards, the improved RelieF algorithm is applied to extract key fault feature, in which the number of sampling is 30, the nearest neighbor number is 8, and the number of iterations is 20. The calculation result of the feature weight is depicted in Figure 3. The dotted line in Figure 3 is the average value of weight 0.127, which is also the threshold value of feature weight screening. As can be seen from Figure 4, 10 feature weights are lower than the threshold, so the weak correlation features that are eliminated are $\{f_{23}, f_{20}, f_8, f_{22}, f_{24}, f_4, f_{12}, f_{19}, f_{18}, f_{17}\}$. According to the Pearson correlation coefficient method as mentioned earlier, there are three strongly correlated vector pairs (f_5, f_6), (f_7, f_9), and (f_7, f_{11}), and therefore f_{11}, f_9 and f_6 are eliminated, and the optimal feature set obtained is $\{f_7, f_{10}, f_{15}, f_5, f_{21}, f_{13}, f_{14}, f_{16}\}$, as shown in Table 4.

The result of feature extraction in Table 4 reflects that the features directly related to the fault are retained. Among them, the maximum monthly load, the average monthly load, the month classification, and the geographical location of the feeder correspond to the load characteristics, geographical characteristics, and time characteristics of the fault, respectively, and they have a relatively obvious and direct correlation with the feeder fault. In terms of meteorological data and ledger data, the monthly extreme weather days, monthly gale days, and the total length of feeder are retained, and some redundant indexes are effectively eliminated. According to the distribution system's actual operation in different areas, the optimal feature set obtained may also be different.

It is necessary to conduct sensitivity analysis. The sampling number and the nearest neighbor number are adjusted to 80 and 10, respectively. The calculation results show little difference from Table 4, indicating that the improved RelieF algorithm is relatively stable, and there is no

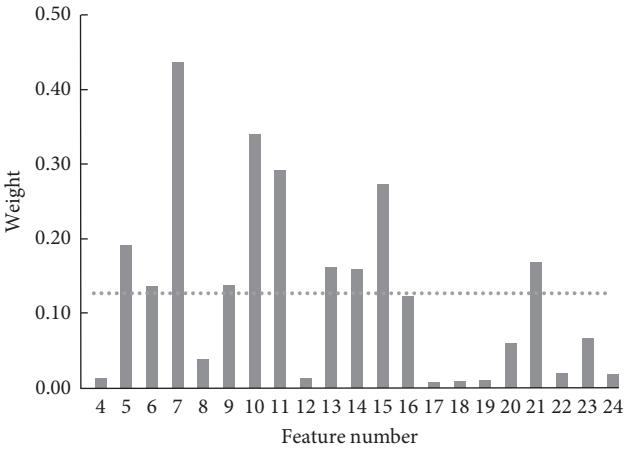

Figure 3: Feature weights.

1088	8	2	99.09%
1	39	0	97.5%
0	0	8	100.00%
99.91%	82.98%	80.00%	99.04%

Figure 4: Obfuscation matrix of predicted model.

Table 4: Optimal features subset.

Variable	Weight	Feature
f_7	0.43588	Monthly extreme weather days
f_{10}	0.33952	Monthly gale days
f_{15}	0.27240	Month classification
f_5	0.19035	Monthly mean temperature
f_{21}	0.16770	Total length of feeder
f_{13}	0.16135	Maximum monthly load
f_{14}	0.15948	Average monthly load
f_{16}	0.12939	The geographical location classification

need to increase the number of iterations to improve the performance.

5.3. Early Warning of Distribution System Fault Risk. Eight optimal features are extracted to train the Softmax classifier, and the monthly failure risk levels of 191 feeders from January to June 2019 are predicted. In order to measure the processing ability of the model to unbalanced samples, the definitions of commonly used accuracy and recall rate are slightly adjusted in this paper, and the classification accuracy T_{pr} and recall rate T_{re} for minority classes are proposed. H_a, A_r and confusion matrix are also introduced as evaluation indexes of the model.

The classification accuracy T_{pr} and recall rate T_{re} can be defined as follows:

$$T_{\text{pr}} = \frac{T_2 + T_3}{F_2 + F_3 + T_2 + T_3},$$
$$T_{\text{re}} = \frac{T_2 + T_3}{F_1 + T_2 + T_3}, \tag{11}$$

where T_2 and T_3 are the numbers of correct classification in the target categories II and III, respectively, and F_1, F_2 and F_3 are the numbers of mistaken classification in the target category in the three categories, respectively.

H_a is the weighted harmonic value of precision rate and recall rate, which can evaluate the overall performance of the model, and its results are more focused on the classification performance of minority category.

$$H_a = \frac{\left(1 + \beta^2\right) T_{\text{re}} T_{\text{pr}}}{\beta^2 T_{\text{re}} + T_{\text{pr}}}, \tag{12}$$

where β is the weight coefficient, is positive, and represents the relative relationship between model recall and precision. In this paper, the value is set to 1.

A_r is the proportion of correctly classified samples to all samples, which can measure the model's overall classification performance and can be expressed as

$$A_r = \frac{T_1 + T_2 + T_3}{T_1 + T_2 + T_3 + F_1 + F_2 + F_3}. \tag{13}$$

As to the Softmax classifier initialization, the weight attenuation parameter is 0.002, and the corresponding value of α for each category is inversely proportional to the ratio of category sample size, which is set as 1, 20, and 50, respectively. The gradient descent learning rate is set as 0.1, and the number of iterations is 500.

5.3.1. Prediction Results. The model prediction results are shown in Figure 4. Each row represents the actual category, and each column denotes the prediction category. The diagonal elements represent the number of samples correctly classified, and the off-diagonal elements represent the number of samples incorrectly classified. The last horizontal row and last vertical column represent the classification accuracy and recall rate of various categories. The last element represents the overall prediction accuracy rate of the model.

Figure 4 shows that the recall rate of all levels of 1146 test samples is 99.09%, 97.5%, and 100.00%, respectively, the accuracy rate is 99.91%, 82.98%, and 80.00%, and the overall classification accuracy rate is 99.04%. The classification accuracy of the first category is relatively high, which is because the number of samples in the first category is large, which corresponds to the samples without faults or with less impact, and the learning performance is good. The classification accuracy of category III is low, mainly because the total number of such samples is small, and any misclassification will greatly impact the results.

In the case of unbalanced samples, the model's recall rate is reasonable, and the recall rate of categories II and III with serious risk level is similar to that of category I, which indicates that the model can effectively identify high risk faults of the distribution system. It can be concluded from the confusion matrix that the misclassification in the prediction model mainly focuses on category I into II or III, indicating that the model focuses more on the recall rate of categories II and III with high risk, which is due to the higher cost of misclassification of the high risk categories.

5.3.2. Comparison of Different Prediction Methods. Four indexes including T_{re}, T_{pr}, H_a and A_r are utilized to compare the prediction results of the training set and test set of the improved RelieF-Softmax (denoted as A), improved Softmax (denoted as B without feature extraction), and improved RelieF (denoted as C without improvement in Softmax loss function). The predicting results are shown in Table 5.

It can be found from Table 5 that Case A, based on the improved RelieF-Softmax algorithm, performs well in both the training set and the test set, and its performance is better compared to Case B and Case C, indicating that the improved model has better generalization ability. Besides, it can be seen that feature extraction can improve classification performance to a certain extent by comparing Case A and Case B. Further, by comparing the training set and the test set of Case B, it can be concluded that the training classification effect of the model is significantly better than that of the test set, which is because too much redundant input vector will make the model passively learn too much information, and the complex model will lead to the reduction of generalization performance.

By comparing Case A and Case C, it can be found that the recall rate of Case A is considerably higher than that of

Table 5: Predicting results of different cases.

Algorithm	T_{re}	T_{pr}	H_a	A_r
A (training set)	0.9855	0.8242	0.8977	0.9865
A (test set)	0.9792	0.8246	0.8952	0.9904
B (training set)	0.9565	0.7765	0.8571	0.9817
B (test set)	0.9375	0.6716	0.7826	0.9791
C (training set)	0.8986	0.7654	0.8267	0.9799
C (test set)	0.8750	0.7636	0.8155	0.9869

Case C, indicating that the former can effectively identify high risk categories with better classification performance. For the distribution system fault prediction problem, there are various influencing factors and complex correlations. The distribution system fault data itself belongs to a minority of samples, so it is necessary to adopt the improved RelieF-Softmax algorithm to improve the model's adaptability and prediction efficiency.

6. Conclusions

In this paper, a fault risk warning method of distribution system based on improved RelieF-Softmax algorithm is proposed, and the following conclusions can be drawn.

Compared with the single dimension reduction method, the feature extraction method based on the improved RelieF algorithm can effectively overcome the deficiency, which is the fact that the traditional RelieF algorithm cannot remove the redundancy, reduce the dimension of features, and therefore improve the classification performance. The failure data in a year are analysed based on data mining technology, and the fault risk level of the distribution system is predicted. The model can effectively identify minority category samples and avoid misclassification of high risk samples that lead to severe consequences. The proposed method can provide a scientific basis for maintenance and repair resource configuration for the distribution system.

This paper aims to put forward the thinking of the fault risk early warning method for the distribution system. Due to the differences in regional information level, distribution system operational means, and the distribution system data acquisition method, the regional features should be considered in the concrete analysis. In the future, the relevant data of distribution system in an all-round way should be extracted as thoroughly as possible, and the distribution system falt features need to be identified through association mining and other efficient means, such as deep learning, and the accuracy and efficiency of the fault early warning can be enhanced further.

Data Availability

The data can be accessed from the distribution system of State Grid Corporation Company (http://www.js.sgcc.com.cn/sz/).

Conflicts of Interest

The authors declare no conflicts of interest.

Acknowledgments

This research was funded by State Grid Suzhou Power Supply Company. This work was supported by the World Class Urban Distribution Network Demonstration Project of Suzhou Historic District.

References

[1] L. Wang, R. Yan, F. Bai, T. K. Saha, and K. Wang, "A distributed inter-phase coordination algorithm for voltage control with unbalanced PV integration in LV systems," *IEEE Transactions on Sustainable Energy*, p. 1, 2020.

[2] L. Wang, R. Yan, and T. K. Saha, "Voltage regulation challenges with unbalanced PV integration in low voltage distribution systems and the corresponding solution," *Applied Energy*, vol. 256, 2019.

[3] T. Morstyn, A. Teytelboym, and M. D. McCulloch, "Designing decentralized markets for distribution system flexibility," *IEEE Transactions on Power Systems*, vol. 34, no. 3, pp. 2128–2139, 2018.

[4] B. Sultana, M. W. Mustafa, U. Sultana, and A. R. Bhatti, "Review on reliability improvement and power loss reduction in distribution system via network reconfiguration," *Renewable and Sustainable Energy Reviews*, vol. 66, pp. 297–310, 2016.

[5] Y. Xu, C. C. Liu, K. P. Schneider, F. K. Tuffner, and D. T. Ton, "Microgrids for service restoration to critical load in a resilient distribution system," *IEEE Transactions on Smart Grid*, vol. 9, no. 1, pp. 426–437, 2018.

[6] A. Arif, Z. Wang, J. Wang, and C. Chen, "Power distribution system outage management with co-optimization of repairs, reconfiguration, and DG dispatch," *IEEE Transactions on Smart Grid*, vol. 9, no. 5, pp. 4109–4118, 2018.

[7] Z. Lin, D. Duan, Q. Yang et al., "Data-driven fault localization in distribution systems with distributed energy resources," *Energies*, vol. 13, no. 1, p. 275, 2020.

[8] S. Y. Ge, Z. H. Zhu, H. Liu et al., "Comprehensive evaluation method for distribution network fault risk," in *Proceedings of the 4th Annual General Conference of The European Political Science Association (CSU-EPSA)*, vol. 26, no. 7, pp. 40–45, June 2014, in Chinese.

[9] Y. M. Zeng, *Analysis and Application of Electric Rush Repair Data*, Xiamen University, Xiamen, China, 2018, in Chinese.

[10] A. S. Zamzam, X. Fu, and N. D. Sidiropoulos, "Data-driven learning-based optimization for distribution system state estimation," *IEEE Transactions on Power Systems*, vol. 34, no. 6, pp. 4796–4805, 2019.

[11] Y. Zhou, Y. Huang, J. Pang, and K. Wang, "Remaining useful life prediction for supercapacitor based on long short-term memory neural network," *Journal of Power Sources*, vol. 11, no. 4, pp. 2687–2697, 2020.

[12] Y. Zhou, Y. Wang, K. Wang et al., "Hybrid genetic algorithm method for efficient and robust evaluation of remaining useful life of supercapacitors," *Applied Energy*, vol. 260, 2020.

[13] H. Jiang, Y. Zhang, E. Muljadi, J. J. Zhang, and D. W. Gao, "A short-term and high-resolution distribution system load forecasting approach using support vector regression with hybrid parameters optimization," *IEEE Transactions on Smart Grid*, vol. 9, no. 4, pp. 3341–3350, 2018.

[14] L. Xu, M.-Y. Chow, and L. S. Taylor, "Power distribution Fault Cause identification with imbalanced data using the data mining-based fuzzy classification E-Algorithm," *IEEE*

Transactions on Power Systems, vol. 22, no. 1, pp. 164–171, 2007.

[15] R. Ma, X. Zhou, Z. Peng et al., "Data mining on correlation feature of load characteristics statistical indexes considering temperature," in *Proceedings of the International Conference on Computer Science and Environmental Engineering (CSEE)*, vol. 35, no. 1, pp. 43–51, Florence, Italy, May 2015.

[16] M. Doostan and B. H. Chowdhury, "Power distribution system fault cause analysis by using association rule mining," *Electric Power Systems Research*, vol. 152, pp. 140–147, 2017.

[17] Z. Lin, D. Duan, Q. Yang et al., "One-class classifier based fault detection in distribution systems with distributed energy resources,," in *2018 IEEE Global Conference on Signal and Information Processing (GlobalSIP 2018)*, IEEE, Anaheim, CA, USA, November 2018.

[18] Z. Shao and L. Wang, "Fault line selection method for distribution system based on big data and feature classification," in *2017 China International Electrical and Energy Conference (CIEEC)*, October 2017.

[19] Z. Q. Li, J. Q. Du, B. Nie et al., "Summary of feature selection methods," *Computer Engineering and Applications*, vol. 55, no. 24, pp. 10–19, 2019.

[20] Z. Zeng, H. Zhang, R. Zhang, and Y. Zhang, "A mixed feature selection method considering interaction," *Mathematical Problems in Engineering*, vol. 2015, Article ID 989067, , 2015.

[21] L. X. Zhang, *Study on Feature Selection and Ensemble Learning Based on Feature Selection for High-Dimensional Datasets*, Tsinghua University, Beijing, China, 2014, in Chinese.

[22] D. Jain and V. Singh, "An efficient hybrid feature selection model for dimensionality reduction," *Procedia Computer Science*, vol. 132, pp. 333–341, 2018.

[23] D. R. Hardoon, S. Szedmak, and J. Shawe-Taylor, "Canonical correlation analysis: an overview with application to learning methods," *Neural Computation*, vol. 16, no. 12, pp. 2639–2664, 2004.

[24] S. S. Gururajapathy, H. Mokhlis, H. A. B. Illias, and L. J. Awalin, "Support vector classification and regression for fault location in distribution system using voltage sag profile," *IEEJ Transactions on Electrical and Electronic Engineering*, vol. 12, no. 4, pp. 519–526, 2017.

[25] G.-T. Xia, C. Li, K. Wang, and L.-W. Li, "Structural design and electrochemical performance of PANI/CNTs and MnO2/CNTs supercapacitor," *Science of Advanced Materials*, vol. 11, no. 8, pp. 1079–1086, 2019.

[26] K. Wang, L. Li, Y. Lan, P. Dong, and G. Xia, "Application research of chaotic carrier frequency modulation technology in two-stage matrix converter," *Mathematical Problems in Engineering*, vol. 2019, Article ID 2614327, , 2019.

[27] O. W. Chuan, N. F. Ab Aziz, Z. M. Yasin, N. A. Salim, and N. A. Wahab, "Fault classification in smart distribution network using support vector machine," *Indonesian Journal of Electrical Engineering and Computer Science*, vol. 18, no. 3, pp. 1148–1155, 2020.

[28] K. Wang, L. Li, W. Xue et al., "Electrodeposition synthesis of PANI/MnO2/graphene composite materials and its electrochemical performance," *International Journal of Electrochemical Science*, vol. 12, no. 9, pp. 8306–8314, 2017.

[29] K. Y. Liu, X. Z. Wu, C. Shi, and D. Jia, "Fault risk early warning of distribution network based on data mining," *Electric Power Automation Equipment*, vol. 38, no. 5, pp. 148–153, 2018.

[30] W. Zhang, W. X. Sheng, K. Y. Liu, and S. Du, "A Prediction method of fault risk level for distribution network considering correlation of weather factors," *Power System Technology*, vol. 42, no. 8, pp. 2391–2398, 2018.

[31] W. Zhang, W. Sheng, S. Du et al., "Architecture and technology implementation of massive data based distribution network operation analysis system," *Automation of Electric Power Systems*, vol. 44, no. 3, pp. 147–155, 2020.

[32] M. Pignati, L. Zanni, P. Romano, R. Cherkaoui, and M. Paolone, "Fault detection and faulted line identification in active distribution networks using synchrophasors-based real-time state estimation," *IEEE Transactions on Power Delivery*, vol. 32, no. 1, pp. 381–392, 2017.

[33] Y. Zhang and L. Chen, "Research on feature extraction method based on clustering and PCA fusion," *Computer Engineering and Applications*, vol. 46, no. 11, pp. 148–150, 2010.

[34] Y. Lecun, Y. Bengio, and G. Hinton, "Deep learning," *Nature*, vol. 521, no. 7553, pp. 436–444, 2015.

Hindawi
Mathematical Problems in Engineering
Volume 2020, Article ID 8884228, 16 pages
https://doi.org/10.1155/2020/8884228

Review Article

Alternative to Oil and Gas: Review of Economic Benefits and Potential of Wind Power in Pakistan

Xinting Hu,[1] Muhammad Imran,[2,3] Mengyun Wu,[2] Hee Cheol Moon,[4] and Xiaochen Liu[1,5]

[1]*School of Management, Jiangsu University, Zhenjiang 212013, Jiangsu, China*
[2]*School of Finance & Economics, Jiangsu University, Zhenjiang 212013, Jiangsu, China*
[3]*Department of Management Sciences, FATA University, Dara Adamkhel, KPK, Pakistan*
[4]*Department of International Trade, Chungnam National University, Daejeon 34134, Republic of Korea*
[5]*School of International Trade & Economy, Changzhou Vocational Institute of Textile and Garments, Changzhou, China*

Correspondence should be addressed to Muhammad Imran; imran@ujs.edu.cn and Hee Cheol Moon; hcmoon@cnu.ac.kr

Received 26 August 2020; Revised 31 October 2020; Accepted 4 November 2020; Published 29 November 2020

Academic Editor: Licheng Wang

Pakistan is one of those countries that are heavily dependent on hydrocarbon fuel for energy production. This results in severe CO_2 emissions that lead to climate change. Although renewable energy resources such as wind are available in abundance, they have not been fully utilized and so energy crises in Pakistan increase every year. This study focuses on using wind energy as an alternative to thermal power sources as the main source of power generation in Pakistan. This research also helps in designing a project management tool to prioritize sources of power generation, including both renewables and nonrenewables, while also considering projects' technical, environmental, social and economic criteria. An Analytical Hierarchy Process has been used to analyze the four main criteria and 12 subcriteria. The analysis revealed that wind energy is the best source among all options for power generation source, followed by solar. Oil, gas, and coal, the other three alternatives, were well below in a comparative analysis. Gas achieves overall better performance if only economic criteria are considered, but due to shortfalls in availability and diminishing reserves, this source is also not feasible. Relying on wind power as the only energy source will not be technically possible, but it can become a leading energy source inside Pakistan. This will reduce the burden on thermal energy sources and make the country more energy-secure, rather than relying heavily on imported oil and gas, as it currently does. Wind power generation capacity in Pakistan is increasing, so that the cumulative capacity is around 2118 MW installed and commissioned by the end of 2018.

1. Introduction

Energy plays an important role in shaping a country's economy. In identifying different sources of energy, environmental impact, fuel source, and social impact are very much under consideration. Huge investments have been made in research and development of renewable energy worldwide, not only to counter environmental degradation but to create energy-secure countries [1].

After the oil embargo by Middle Eastern producers against the West in the midseventies, it was realized that other sources of energy must be identified for energy security. Traditional sources of energy are diminishing and will completely die out by the end of this century. The rapidly increasing prices of oil and gas due to instability in the Middle East pose a great risk to any economy [2–6]. Issues around pollution and environmental degradation, whose main causes are greenhouse gases arising from long-term continuous, excessive use of oil, gas, and coal for power generation, have turned world opinion against the use of fossil fuels. The international community is directing policies and strategies towards energy conversion and finding alternative energy sources [7].

Denmark and Italy have reported a high level of wind energy penetration and generated 30% of their electricity via

wind. Germany has reported a 22.9% renewable electric generation [8] (Renewable Energy Policy Network for the 21st Century). Germany showed much promise in solar energy decades ago, and it reached a landmark when half the country's daytime demand was met by solar power in 2012 [4, 9, 10]. Renewable energy (RE) is spreading across the globe and is becoming increasingly affordable. Developing countries are more interested in improving their RE share compared to developed countries, resulting in shifts of markets and investment to the developing world [8].

1.1. The Case of Pakistan. Pakistan has long been dependent on the use of fossil fuels for the generation of electricity. But the world has changed its priorities in power generation and it is time for Pakistan to find a more sustainable, environmentally friendly, and affordable source of energy for electricity generation as an alternative to fossil fuels. It has three key concerns: reserve exhaustion, environmental degradation, and energy security [11, 12]. For two decades, Pakistan has been suffering from a severe energy crisis. Power production mainly depends on fossil fuels and there is low production from wind and solar resources. Hence, there is a need to utilize abundantly available wind energy [12–15].

Pakistan's major energy supplies come from oil, coal, gas, hydro, biomass, and nuclear. This makes it a net importer of energy [11]. Sixty percent of its foreign reserves are used for imports of fossil fuels [16]. The power sector alone consumed 40.4% of total oil used in the country on one recent measure [17].

1.2. Fossil Fuel Consumption. In consumption, natural gas was highest at 49.5%, followed by oil at 30.8%. Of clean energy sources, hydro was a mere 12.5%, which declined from 13.6% from 2011/12.

During 2011/12, a total of 95,365 GWH of electricity was generated, of which 64.3% was thermal, 29.9% hydro, and 5.8% nuclear and imported [17]. Thus, the bulk of power generation coming from thermal power can be diverted towards industrial usage and reduce the fuel import bill, as shown in Figure 1 above. The bulk of gas (27.8%) and oil (40.7%) was used to generate electricity (Figures 2 and 3).

1.3. Problem Statement. The diminishing of fossil fuels inside Pakistan and the stress on existing resources calls for gradual transition towards RE sources [11, 15, 18]. Pakistan has been fortunate in having vast renewable resources, and exploitation of these resources for energy generation is required [7, 14, 19]. Pakistan's energy crisis is not in fact a huge one if we compare it with ongoing developmental work globally.

For the past two decades, hydro power, which was the leading source of power generation in Pakistan, has become problematic. Efforts in this sector slowed down greatly due to political differences [20]. According to the Integrated Energy Plan (IEP) 2009–2022, Pakistan needs to increase its power generation capacity by up to 50,000 MW by 2022. To achieve this, a 12% share has to be from alternative energy.

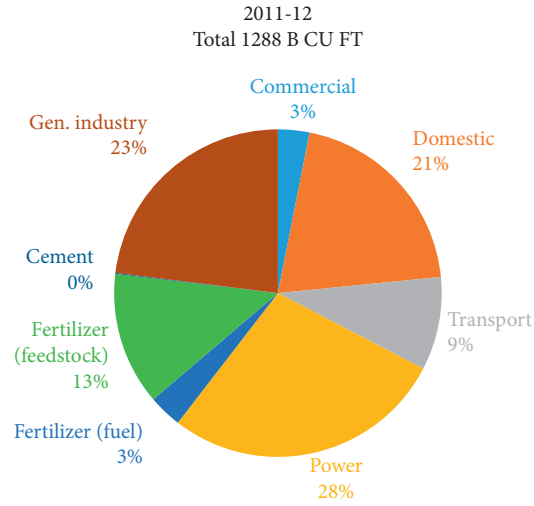

Figure 1: Natural gas consumption in Pakistan by sector (source: Pakistan energy book).

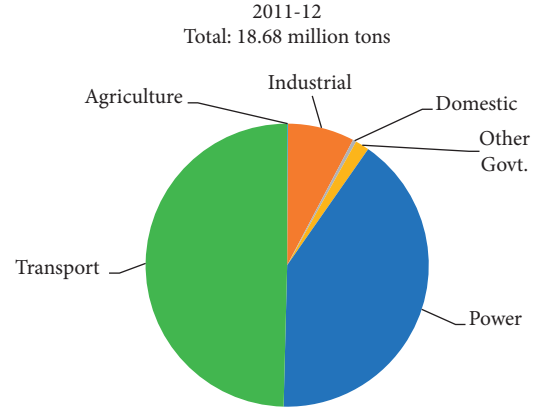

Figure 2: Petroleum consumption in Pakistan by sector (source: Pakistan energy book).

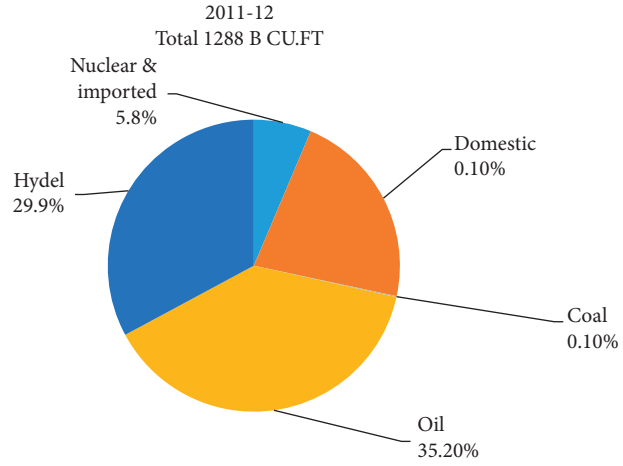

Figure 3: Electricity generation 2011-12 by source in Pakistan (source: Pakistan energy book).

The plan is to install 17,400 MW of alternative clean energy, and 17,392 MW of hydro power installation is also required [21].

Pakistan also relies on fossil fuel, which is also main source of CO_2 emissions in the country. In order to reduce dependency on fossil fuels, this study is an effort to investigate the potential of wind power as an alternative to oil and gas.

1.4. Objectives of the Study. Wind power, the cheapest source of energy among alternatives, is considered the best substitute for oil and gas [4, 14, 15, 20, 22–24]. Pakistan can also find solutions to reduce its reliance on importing oil and utilize natural gas for other purposes instead of using it for generating energy, which can be produced by other alternatives, especially by wind. Exploiting fully a single Gharo Keti Bandar Wind Corridor can resolve current and future energy requirements of the country for many years to come.

The main objective of this study, using the Analytic Hierarchy Process (AHP), is to answer the following questions in empirical terms while considering both qualitative and quantitative data of technical, economic, social, and environmental features of power plants:

What alternative source of power generation is preferable in Pakistan?

How much better is a wind source than non-RE sources?

Can Pakistan completely rely on wind energy as one of the leading sources of power generation?

This study will also help in implementing wind energy projects to meet their goals and in making decisions on power projects with a focus on wind power projects while also considering the environmental and social benefits that arise.

2. Literature Review

Fossil fuels have long been a primary source of power generation around the world. Pakistan has been struggling with power shortage for some considerable time. Previous governmental policies to counter power shortages were mainly focused on fossil fuel-based power production. These power plants require oil and gas as their generating fuels. Pakistan does not hold large oil reservoirs, and to meet its demand, it has to rely on imported oil; depletion of gas reservoirs has begun to show its effects.

According to research, the peak fossil fuel use (except for coal) will occur before 2030. The worst-case scenario is that it will occur in 2028: "As peaking is approached, liquid fuel prices and price volatility will increase dramatically and without timely mitigation, the economic, social, and political costs will be unprecedented" [1]. Except for coal, fossil fuel use is expected to diminish by the end of 2042 [5]. To deal with this, the world is trying to build different modes of energy saving technologies and to find different sources of energy [7].

Multi Criteria Decision Making (MCDM) has been used extensively in energy-related problems. It helps governments and organizations plan and make policies in the energy sector by offering an avenue for differing and varied objectives [23, 25, 26]. It has a unique capacity to work on multidimension goals and criteria and can include qualitative as well as quantitative data. A multidimensional criterion permits stakeholders to evaluate and analyze alternatives across numerous dimensions, unlike standard cost benefit analysis, which is one-dimensional. Factors can range from technical, financial, social, and environmental to fuzzy dimensions [4, 27]. In most decision making, judgments are not crisp and are usually made on intuition and very little expert judgments are involved. It also provides a way to include qualitative data for analysis.

The most commonly used MCDM techniques are Analytic Hierarchy Process, Analytic Network Process, Weighted Sum Method, Weighted Product Method, Preference Ranking Organization Method for Enrichment Evaluation (PROMETHEE II), Elimination and Choice Expressing Reality (ELECTRE), Macbeth, The Technique for Order Preference by Similarity to Ideal Solutions (TOPSIS), and Goal Programming [4, 22, 28, 29]. Pohekar and Ramachandran [26] analysed 90 papers and found out that AHP is the most admired MCDM tool. This is followed by PROMETHEE II and ELECTRE. AHP was developed by Thomas Satty in the 1970s. It has been extensively used in energy planning. This is due to its ability to convert a complex goal structure into a simple hierarchy [26]. The method has been used in energy decision making, resource selection, site selection and impacts on living standards, etc. Ahmad and Tahar [28] and Amer and Daim [20] used it for selection of RE sources and for selection among RE sources inside Pakistan. Stein [4] used AHP to rank both renewable and nonrenewable energy technologies. Kahraman et al. [23] used fuzzy AHP for selection of the most appropriate renewable source. Chatzimouratidis and Pilavachi [29]; Lee et al. [24]; and Akash et al. [30] used AHP with 'Benefits, Opportunities, Costs, and Risks' (BOCR) for selection among wind farms and for comparison between various sorts of renewable and nonrenewable power stations.

2.1. Related Work in Pakistan. A literature review reveals that not much work has been done to find the benefit or loss associated with analyzing all four criteria (technical, economic, social, and environmental) of power plants in Pakistan. Pakistan is one of those countries that are heavily dependent on hydrocarbon fuel for energy production, which results in severe climate change [31, 32]. Researchers discussed only the environmental benefits of wind farm projects in Pakistan. Sahira and Qureshi [33] assessed the potential inside the country and the barriers and limitations of RE sources. Mirzaa et al. [34] reported the efforts made for development of wind power in Pakistan and the prospects of improving electricity connectivity through RE sources in remote areas. Bhutto et al. [7] discussed the prospect of past, present, and future of wind energy in Pakistan along with the hurdles encountered in its development. Amer, M. and

Daim et al. [20] used AHP to rank only RE sources using European and US data. It was the first effort to rank RE sources in Pakistan but excluded fossil fuel power plants. Prioritizing energy sources, which include both renewable and fossil fuel power plants, and using local data as far as possible are required. This will give a good insight into determining the best energy sources for power production in Pakistan.

Pakistan needs to widen its energy mix to meet its energy demand, given the immense power potential in RE sources. Hydro has long been used as the primary source, whereas solar and wind are prospective energy sources [35]. Pakistan has a vast coastline in the south and places in the northern region which provide excellent wind power potential [32, 34].

There has been a lack of research work in the renewable energy sector in Pakistan to find in empirical terms the benefits of environmental and social aspects of power plants, together with technical and economic aspects, in order to rank different types of energy sources. AHP as a MCDM tool has been used previously but not very effectively because data have been European- and US-based only. For the different criteria and subcriteria, data are unavailable except in a few instances. Using data effectively to rank different technologies is required. AHP helps in prioritizing energy sources and also reveals in empirical terms if wind power is or is not suitable for power generation, compared to other sources. It provides a clear overview of the answers we seek. Wind flows across the planet from higher concentration regions towards areas of lower concentrations. The higher the atmospheric pressure gradient, the higher the wind speed is. A higher speed means greater power can be converted into useful energy. Wind energy has long been used for mechanical means to grind grain or pump water and sail ships across the ocean. With the progress of time and innovation, mechanical power generated through wind energy has been converted into electrical power to light houses [20, 34, 36].

2.2. Scope of Wind Energy in Pakistan. The Government of Pakistan (GoP) has established two institutes to support the development, guidance, and research work in the RE sector. The Alternative Energy Development Board (AEDB) was established in 2003 as a central body to make possible the growth of RE, to provide support and to develop plans related to RE. The Pakistan Council of Renewable Energy Technologies (PCRET) was established in 2001 to carry out research and development, provide training, and promote RE [20, 37].

Various studies show that wind energy has a great potential in Pakistan and needs to be exploited [33, 34]. A general opinion is that wind energy is the best available option amongst renewable sources in Pakistan [7, 19, 20, 38].

The Government of Pakistan's Integrated Policy 2009–2022 declares the Gharo Keti Bandar wind corridor in Sindh as a permanent wind corridor, thereby removing any prospect of financial interests annulling the land lease by Government of Sindh [21]. The Gharo Keti Bandaar Wind corridor alone has a potential of 60,000 MW [37].

Currently, two wind power projects, a 50 MW Fauji Fertilizer Company Energy Limited (FFCEL) and a 56 MW Zorlu Enerji, have been completed and are contributing electricity to the national grid.

In Figure 4, the shaded regions clearly show large areas suitable for wind energy Exploration. A total of 132 GW wind power can be installed in these windy areas. Almost 9% of Pakistan's total area has Class 3 or above windy area [37, 39]. Current sites allocated for Wind Power Projects in Pakistan are in Jhimber, Keti Bnadar, and Gharro, all in Sindh. Table 1 provides a full list of projects.

2.3. Wind Tariff Determined by NEPRA (National Electric Power and Regulatory Authority). The Renewable Energy policy announced by Government of Pakistan in 2006 gives tremendous incentives to investors to purchase all their energy from the wind farm at their doorstep. A new and distinctive concept of wind risk has been incorporated to overcome the fears of investors about the reliability and accuracy of wind data [21, 34]. This concept has been added to ensure wind farm developers are unaffected by circumstances which are outside their control, such as wind speed and density, whereas they are responsible for factors like availability of wind farms, efficiency of wind turbines, etc. [20]. The other provisions are grid access at the door step, economic inducements like tax rebate and asset depreciation, etc. 18% return on even-handedness, ROE in dollar terms, and repatriation of capital for overseas investors [34].

NEPRA determined the upfront tariff of wind power plant as follows:

Total tariff = O and M + insurance + return on equity + Principal repayment of debt + Interest, where O and M = 1.6040 Rs/kwh

Insurance = 0.7833 Rs/kwh

Return on equity = 4.6902 Rs/kwh.

The net annual capacity factor for plants was determined at 31% of the total capacity; excess energy produced shown as below.

The tariff is only applicable to the first 500 MW power after 2013, and the company opting for this tariff must achieve financial closure by the end of 2014 (see Table 2).

The concept of wind risk which was part of Renewable Energy Policy 2006 has been taken away from the upfront tariff. But the successful achievements of Zorlu Enerji and FFCEL wind farm projects make the wind risk concept quite unnecessary.

2.3.1. Upfront Tariff for Solar Photo Voltaic (Solar PV Cells Are Usually Made up of Silicon Cells that Convert Solar Energy to Electricity). The upfront tariff of solar determined by NEPRA reveals that the per MW cost of solar PV is US$1.9007 Million. This cost of solar energy is much compared to the overnight cost of Solar PV in Annual Energy Outlook, 2011 published by EIA. The cost stands at US$4.697 Million [4].

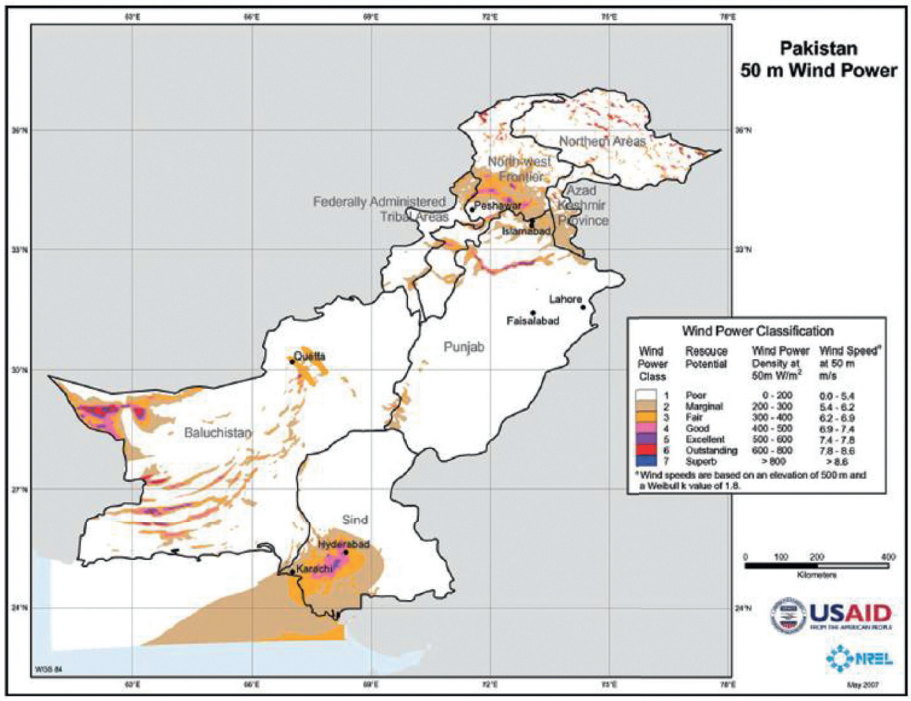

Figure 4: Wind power classification map at 50 m height (source: National renewable energy laboratory (NREL)).

Table 1: Land allocation with generation capacity for wind power projects in Pakistan (source: alternative energy development board).

S. No.	Company	Project capacity (MW)	Location of land
1	Tenaga Generasi Ltd	50	Kuttikun
2	Foundation Wind Energy-II Pvt Ltd. (Green Power Pvt Ltd)	50	Kuttikun
3	Hydro China Dawood Power Ltd.	50	Bhambore
4	Master Wind Energy Ltd.	50	Jhimper
5	Zephyr Power Ltd.	50	Bhambore
6	Foundation Wind Energy-I Ltd. (Beacon Energy Ltd)	50	Kuttikun
7	Sachal Energy Development Pvt Ltd.	50	Jhimper
8	Fauji Fertilizer Company Energy Ltd.	50	Jhimper
9	Yunus Energy (Pvt) Ltd.	50	Jhimper
10	Metro Power co.(Pvt) Ltd.	50	Jhimper
11	Gul Ahmed Energy Ltd.	50	Jhimper
12	Zorlu Enerji Pakistan Ltd.	56.4	Jhimper
13	Wind eagle-1 Ltd.	50	Jhimper
14	Wind eagle-2 Ltd.	50	Jhimper
15	Sapphire Wind Power Company (Pvt) Ltd.	50	Jhimper
16	Three Gorges First Wind Farm Pakistan Pvt. ltd (CWE)	50	Jhimper

Table 2: Capacity factor considered for determination of wind power projects upfront levelized tariff.

Net annual capacity factor	% of prevailing tariff
Above 31% to 32%	75
Above 32% to 33%	50
Above 33% to 34%	25
Above 34% to 35%	20
Above 35%	10

The upfront tariff was calculated for southern and northern regions due to variance in the solar irradiation:

$$\text{Total Tarrif} = \text{O\&M} + \text{Insurance} + \text{Return on Equity} + \text{Debt Servicing}, \quad (1)$$

where for the Southern Region, O&M = 1.7391 Rs/kwh, Insurance = 1.1594 Rs/kwh, Return on Equity = 5.8583 Rs/kwh, and Debt Servicing = 12.3570 Rs/kwh for first ten years.

Hence, the final upfront tariff for the first 10 years of service is up to 21.1138 Rs/kwh and for the remaining 15 years is 8.7568 Rs/kwh. The levelized cost in US dollars is 16.3063 cents for 25 years.

For the Northern Region, O&M = 1.8137 Rs/kwh, Insurance = 1.2091 Rs/kwh, Return on Equity = 6.1097 Rs/kwh, and Debt Servicing = 12.8872 Rs/kwh for first 10 years.

The net final upfront tariff for first 10 years becomes 20.9712 Rs/kwh and for the remaining 15 years is 8.6976 Rs/kwh. The levelized cost in US dollars for all 25 years becomes 17.0060/kwh cents.

If the net annual plant capacity factor increases from the cited capacity factors of 16.78% and 17.50% for northern and southern regions, respectively, the tariff will be calculated according to Table 3.

2.4. Structural Hierarchy. Structuring the hierarchy between criteria and alternatives is the first step towards achieving the objective in AHP. The hierarchy contains four criteria and 12 subcriteria, as shown in Figure 5.

Table 3: Capacity factor considered for determination of solar PV levelized upfront tariff (source: national electric power regulatory authority).

Net annual plant capacity factors	% of the prevalent tariff
Above 16.78%/17.50% to 17.78%/18.50%	75
Above 17.78%/18.50% to 18.78%/19.50%	50
Above 18.78%/19.50% to 18.78%/20.50%	25
Above 19.78%/20.50% to 18.78%/21.50%	20
Above 20.78%/21.50%	10

3. Technical Criteria

3.1. Efficiency. Efficiency refers to how much practical energy we can obtain from a resource. High efficiency of an energy source means it is economically feasible [11, 40]. Efficiency of an energy source is the ratio between the corresponding Btu content of a kWh of electricity (which is 3,412 Btu) by the heat rate, which is expressed in BTU/kwh [41]. The efficiency of renewables cannot be calculated using the same formula, since they do not require heat to produce electricity [4]. Consequently, the EIA does not have values for hydro, solar, and wind. According to Betz's Law (Betz's Law evaluates the maximum power that can be exploited from wind), theoretically wind turbines can only harness 59.3% of wind power, but practically their efficiency is around 34% [4].

3.2. Capacity Factor. Capacity Factor determines how much electricity a power plant will actually produce under real conditions. Most renewables lag behind conventional energy sources when it comes to capacity factors due to seasonal non-availability of energy sources. Thermal power plants have a capacity factor above 80% and nuclear and geothermal factors at above 90%. The capacity factor for solar is the lowest [41]. The capacity factor determined by NEPRA for upfront tariff determination for wind and solar is 31% and 17.5% (Table 4).

3.3. Environment Criteria

3.3.1. Land Requirement. Electricity generation requires use of land to extract fuel and for installation of power plants; the required land usage can vary from site to site and the power source. This is one of the most important factors in determining the economic value of a power plant [23, 42]. A plant can affect the quality of life, especially when constructed near cities. It can cause rupture in day-to-day activities and the land could have been used for other purposes. In the case of a wind farm, depending upon topography and source availability, a mere 1–10% of the entire area of a wind farm is used by the wind turbine, sub-station, living areas, and connection roads, and the remaining land is available to be used for farming, grazing, etc., unlike land use by other energy sources [43]. A summary is given in Table 5.

3.3.2. External Costs. External costs have been taken from ExternE Project (ExternE is the well-known acronym for "External Costs of Energy" and a synonym for a series of projects starting from the early 1990s till 2005; it is an approach for calculating environmental external costs [44]). It ranks all the chief energy technologies in terms of their external costs. These are the hidden costs associated with each technology which affect human health, potentially cause injury, and lead to harm flora and fauna. The data show that wind with an external cost of 0.19 cent/kwh is the lowest cost, whereas coal and oil are among the highest [4, 44].

3.3.3. Loss of Life Expectancy. The other decisive factor is Loss of Life Expectancy (LLE). This shows the level of loss of human life ensuing in every phase of the entire period of the power plant (Table 6).

4. Methodology

When it comes to evaluating multiple options with conflicting criteria, the multicriteria decision making method is used. This has been used many times for energy problems over the years. It works on several dimensions, allowing the decision to be made across diverse options, including individual opinions.

4.1. Analytical Hierarchy Process. AHP has been used extensively for decision making solutions, ranging from site selection to prioritizing energy sources in corporate and government sectors [24, 45]. It remains the most widely used and highly regarded approach for decision makers and group decision makers. AHP works by decomposing a multifaceted problem into simple questions and then, further down, into alternative courses of action whose solutions when combined can lead us to answer the original complex problem [4, 46]. It works by using fuzzy logic rather than permanent and precise ideas. The decisions that we generally make are not absolute but are made up of rational thinking defined only in fuzzy terms. In an effective AHP model, a problem is broken down into a hierarchy, followed by prioritizing the criteria and finally synthesizing the results [24, 47]. A problem which is the objective of the decision making is at the top of the hierarchy and is decomposed into general criteria, then further broken down into secondary criteria, also called subcriteria, and then into tertiary criteria or sub-subcriteria. The information is then synthesized to decide the relative importance of each alternative. AHP allows both qualitative as well as quantitative data to be analysed.

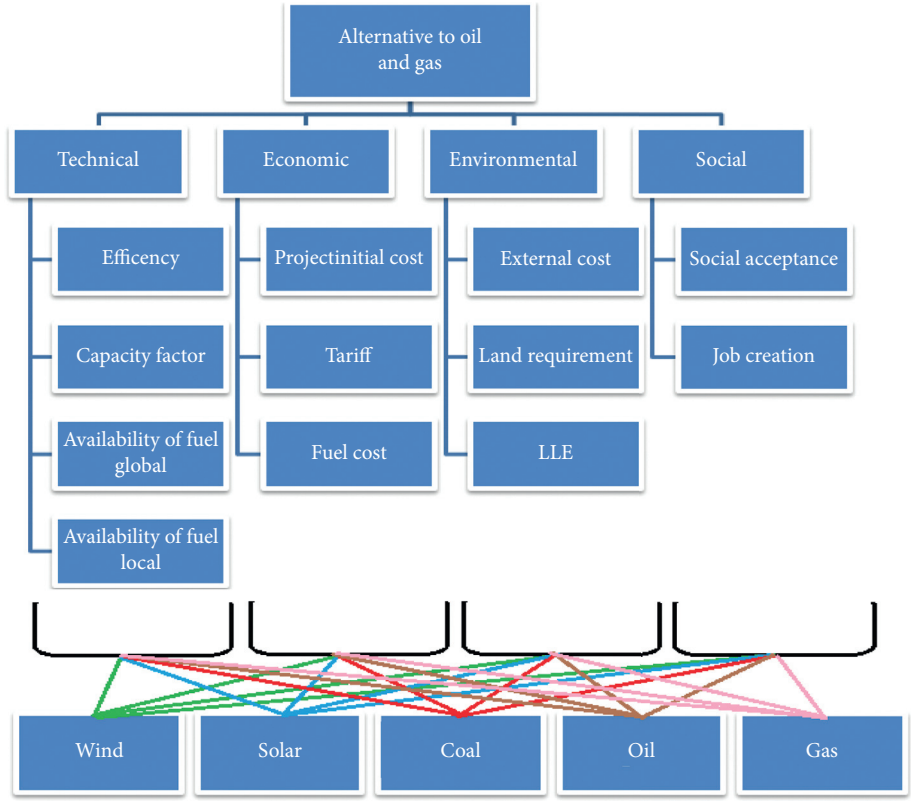

Figure 5: Hierarchy structure (source: author's work).

Table 4: Technical criteria data.

Type of power plant	Efficiency[a]	Availability of fuel (global)	Availability of fuel (local)[c]	Capacity factor
Wind	35	500	500	31[d]
Solar	15	500	500	17.5[d]
Coal	45	107[b]	200	85[e]
Oil	44	31[b]	14	87[f]
Gas	39	33[b]	17	87[e]

Source: [a]Euro Electric; [b][5]; [c]Assumed from data available in Pakistan Energy Year Book, 2012; [d]Capacity Factor determined for NEPRA upfront tariff; [e]Annual Energy Outlook, 2013; [f][4].

Table 5: Land required by technologies for power generation (source: [20, 22]).

Technology	Land requirement (km^2/1000 MW)
Solar PV	35
Wind	100
Hydro	750
Biomass	5000
Coal	2.5
Oil	2.5
Gas	2.5
Nuclear	2.5

Structuring the problem is the first phase of the process. This involves recognizing alternatives and defining criteria into a hierarchy. What criterion contributes to which alternative is recognized. After structuring the problem, the criteria are prioritized as the comparative preference of alternatives with criteria.

To determine the criteria weight, pair-wise comparison of one criterion over another is defined. The pair-wise comparison is set in terms of how much A is more or less significant than B. It can be done using a rough estimate or may be by using a historical data, etc. The historical data can clearly give us comparison data, e.g., if, on an equal measure of fuel, the mileage of a car A is 15 km and that of car B is 30 km, then car B is clearly twice as efficient as car A. In the cases of no historical data, a rough estimate can be made by experts in that particular field or those who are in decision-level positions.

As given below in Table 7, Satty proposed a 9-point comparison scale, where 1 is equally preferred and 9 is extremely preferred [4, 45]. If alternative A is less important than alternative B, than we enter a reciprocal value like 1/5, 1/7, etc. When evaluated, the data are further entered into a square matrix "depending upon the number of comparisons" representing all possible comparisons.

Table 6: External cost and Loss of life of different sources of technologies.

Technology	External cost (EU cent/kwh)[a]	External cost (US cent/kwh)[b]	LLE (days)[c]
Solar	0.60	0.834	0.1[d]
Wind	0.19	0.2641	0.1[d]
Hydro	0.54	0.7506	2.3
Biomass	2.01	2.7939	3.5
Coal	5.71	7.9369	8.4
Oil	5.70	7.923	4.5
Gas	1.85	2.5715	0.8
Nuclear	0.39	0.5421	0.8

Source: [a]ExternE; [b]Euros converted into US dollars (1 Euro = US $1.39, as of March 2014); [c][4]; [d]Negligible (i.e., <1.0), hence an estimate of 0.1 was used.

Table 7: Scale of relative importance according to [45].

Intensity of importance	Definition
1	Equal importance
2	Weak
3	Moderate importance
4	Moderate plus
5	Strong importance
6	Strong plus
7	Very strong or demonstrated importance
8	Very, very strong
9	Extreme importance

4.2. Evaluation Criteria. A number of objectives supplied the limit of the design of the research. Sources of energy which are being used at a high level, including both RE and non-RE sources, were considered. Therefore, wind, solar, coal, oil, and gas were selected to serve the purpose of alternatives which can also reduce CO_2 emissions. In order to evaluate each source of energy alternative on the basis of criteria and subcriteria, four of the most important criteria, Financial, Technical, Environmental and Social, were included. These include all the necessary characteristics for determining the overall significance of a power plant. The criteria and subcriteria have been taken into account in the research. They have been used to analyze coal, oil, and gas, with wind and solar energy as an alternative source of power generation. Twelve subcriteria were identified.

The study was based upon renewable technology and nonrenewable technology. 'Renewable' includes wind and solar; nonrenewable incorporates coal, oil, and gas.

4.3. Data Collection. The data have been collected from international and national organizations. The wind energy-related data have been collected from NEPRA and AEDB sources. The data have also been collected from Fauji Fertilizer Company Energy Limited, a subsidiary company of Fauji Fertilizer Company Ltd. This is the first wind power project in the Pakistan. The data have been collected directly from the site office of the project and also from the official source (Website of FFCEL (http://www.ffcel.com.pk) and AEDB (http://www.aedb.org)) as shown in Table 8.

4.4. Expert Choice. Expert Choice is software based upon AHP to help make decisions by adopting a structural approach and prioritizing. Expert Choice has been widely used in the Government sector, industry, and academia to bring together skill, perception, and detailed information. It helps in structuring decisions into smaller levels, assesses the significance of competing dimensions, and further breaks these down into sublevels and defines alternative choices. The process involves not only historic data but also logic and intuition. Expert Choice also allows for an effortless approach to conducting sensitivity analysis by just changing the weights of criteria in order to measure the effect of diverse information for analysis in cases of different outcomes.

4.5. Expert Opinion. To answer the question "Can Pakistan completely rely on wind energy as one of the leading sources of power generation?" experts from the wind sector were chosen to give their opinion. Six experts from FFCEL, Nordex Pakistan Private Limited, and AEDB were asked this question. The question was asked of the Assistant Director Wind (AEDB), the Senior Executive Engineer (FFCEL), the Senior Engineer (FFCEL), the Service Field Operation Manager (Nordex), and two Services Engineers (Nordex).

5. Empirical Results

The data have been analysed using the software Expert Choice; which works on the principle of AHP used for MCDM. The model incorporates of four tiers, encompassing criteria, subcriteria, alternatives, and goals. The software accepts both qualitative and quantitative data. The criteria and sub criteria were defined and their relative importance to each other was compared. All the criteria (Economic, Technical, Environmental, and Social) have been considered as of equal importance; the sub criteria were Capacity Factor, Efficiency, Fuel Availability (Local), Fuel Availability (Global), Project Initial Cost, Tariff, Fuel Cost, Land Requirement, LLE, External Cost, Social Acceptance, and Job Creation, all given equal weighting, as shown in Figure 6. The inconsistency ratio for criteria weighting was 0.00, which showed that all the judgments were perfectly consistent.

The data were entered directly into the data grid, as shown in Figure 6. The subcriteria data were entered by proportion of the total weight of the criteria. The data which were adverse were entered by taking the reciprocal of the

Table 8: Sources of data for AHP.

Criteria	Subcriteria	Source
Technical	Capacity factor	EIA, Annual Energy Outlook 2013 Oil [4] Coal, Wind, Solar-NEPRA
	Efficiency	Euro Electric http://www.euroelectric.org
	Availability of Fuel (Local)	Assumed from data available in PEYB, 2012
	Availability of Fuel (Global)	[5]
Economic	Project Initial cost	Oil and Gas-Annual Energy Outlook 2011 Wind, Solar coal-NEPRA http://www.nepra.org.pk
	Tariff	Oil and Gas-An overview of electricity sector in Pakistan 2011, Islamabad Chamber of Commerce and Industries Wind, Solar Coal [48] http://www.nepra.org.pk
	Fuel cost	[4]
Environmental	External cost	http://www.ExternE.info
	Land requirement	[22]
	LLE	[4]
Social	Job creation	[20, 22, 29]
	Social acceptance	European wind energy association http://www.ewea.orh

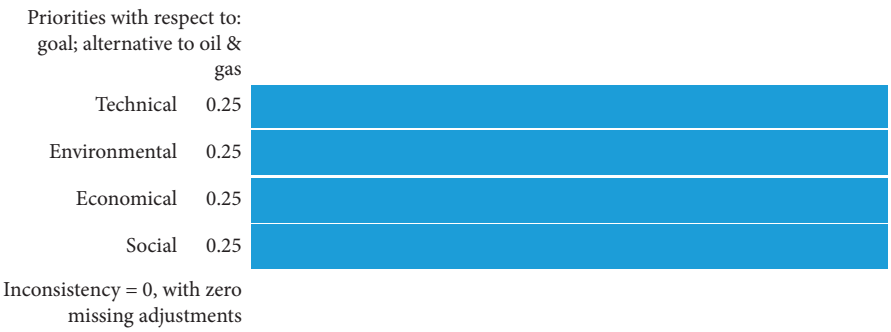

Figure 6: Priority graph.

actual value and then taking the percent of every alternative against the total. The overall synthesis of the data with respect to goal, alternative to Oil and Gas, is shown in Figure 7, which shows wind as 0.302 of the total proportion, followed by solar as 0.259 and then by gas, coal, and oil with 0.174, 0.135, and 0.130, respectively.

The results (Figure 7) showed that wind power is the best available resource inside the country, followed by solar. There is a substantial gap between the two renewable and fossil fuel sources.

Wind and solar show that they are excellent sources on all the criteria. The results illustrate that wind and solar offer, by and large, the best benefits across various aspects. They perform well above fossil fuels technically, environmentally and socially. Economically their initial cost is much higher than fossil fuel-based power plants, but in the long run, they outperform them in this criterion as well. Gas also shows equal significance in the economic criteria, but lags behind in the other three criteria against renewable, as shown in Figure 8.

Gas is the most preferred energy source by a short margin, if only the economic criterion is considered, as shown in Figures 9 and 10. The overall result clearly encourages investors to invest in both these green energy sectors, especially wind. The result also provides policy makers with the confidence they require in granting exemptions and benefits to the renewable industry.

Another way to examine the result would be to single out sources which are poorly performing. The sources oil and gas have become an integral part of the power sector in Pakistan: even though they have been proved unsuccessful, they are still being strongly encouraged for their immediate short-term gains.

6. Sensitivity Analysis

In multicriteria decision making, the sensitivity analysis pertaining to the different values and interests is of the utmost importance, since the solutions are judged as acceptable or unacceptable by considering different parameters. The sensitivity analysis was performed to find out how the system would behave if one criterion was given preference over another. However, the results showed very little deviation due to overall strong position taken by both solar and wind in the analysis.

The overall effect can be shown by changing one or more parameters of the criteria in the analysis. Figure 10 shows

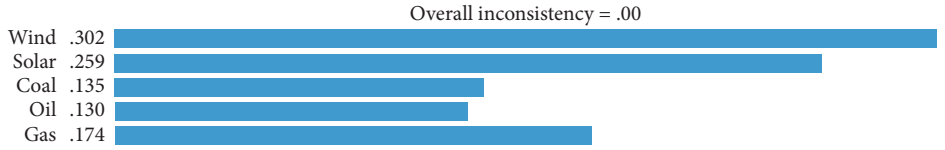

Figure 7: Synthesis with respect to goal: alternative to oil and gas.

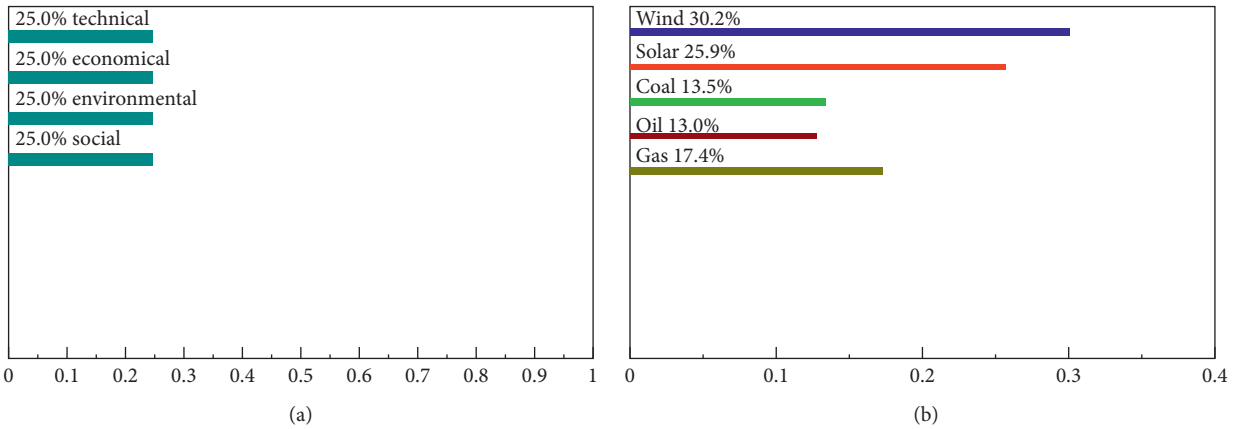

Figure 8: Ranking of technologies assuming equal weights of all criteria.

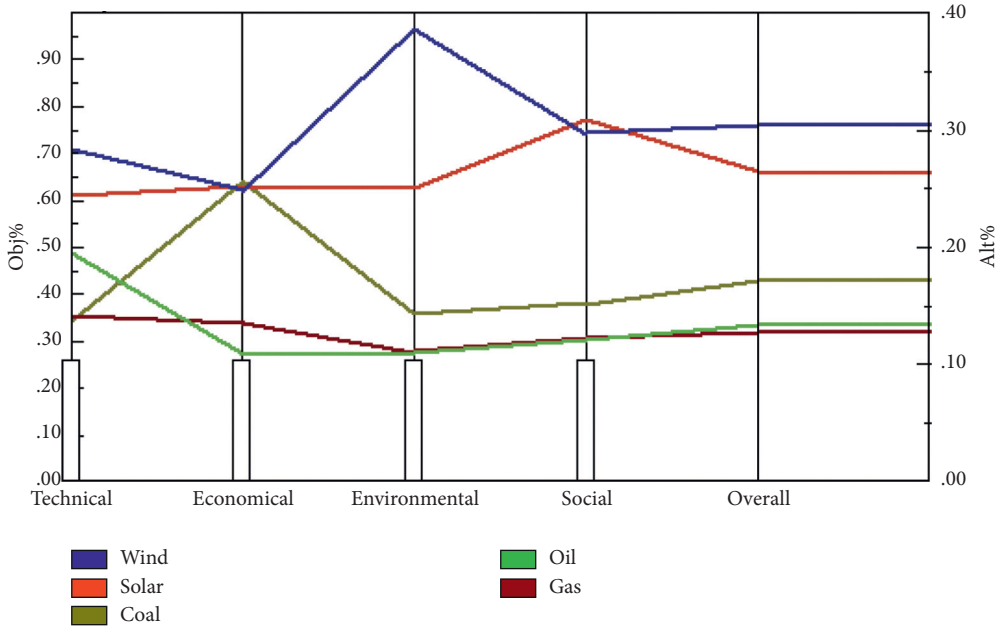

Figure 9: Performance sensitivity for each alternative against every criterion with equal weights.

almost similar results as those in Figure 11, even after the economic and technical criteria weights were increased to 45% each, and the environmental and social criteria were reduced to 5% each or 1/9 of the above value. Here, the stakeholder main emphasis is on the financial aspect, along with technical characteristics, i.e., efficiency, capacity factor, and availability of fuel for the power plants.

Wind and solar fell a little from the original result but showed an overall dominant position against nonrenewable resources. Similarly, gas was evenly good only in the economic criteria and was lagging in the rest. Both oil and coal showed poor results.

Pakistan's economy is evolving and has inadequate monetary assets. For most policy makers economic criteria would be the most significant. This means that a project's initial cost and tariff are given considerable importance. A similar result was obtained when the economic criteria weight was doubled to 0.4 compared to the other three all

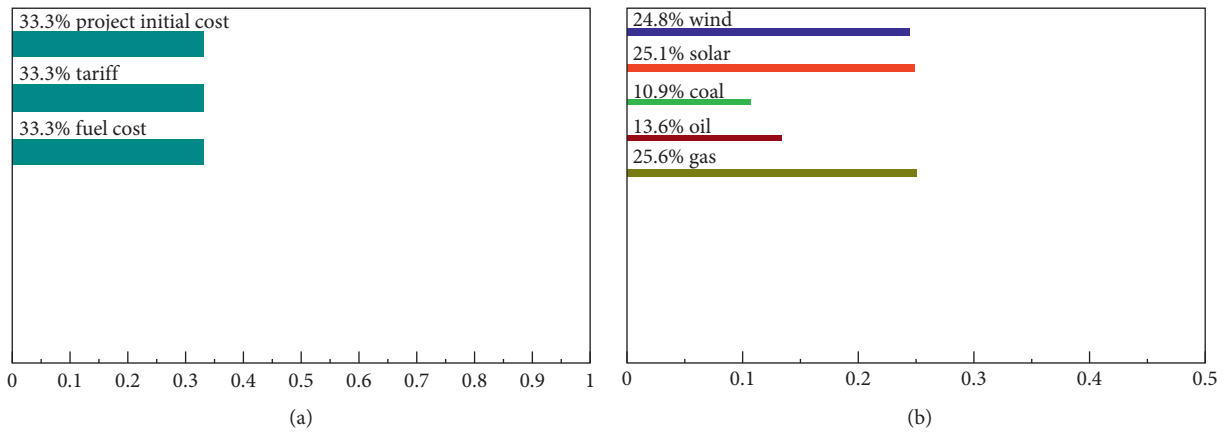

Figure 10: Result for economic criteria.

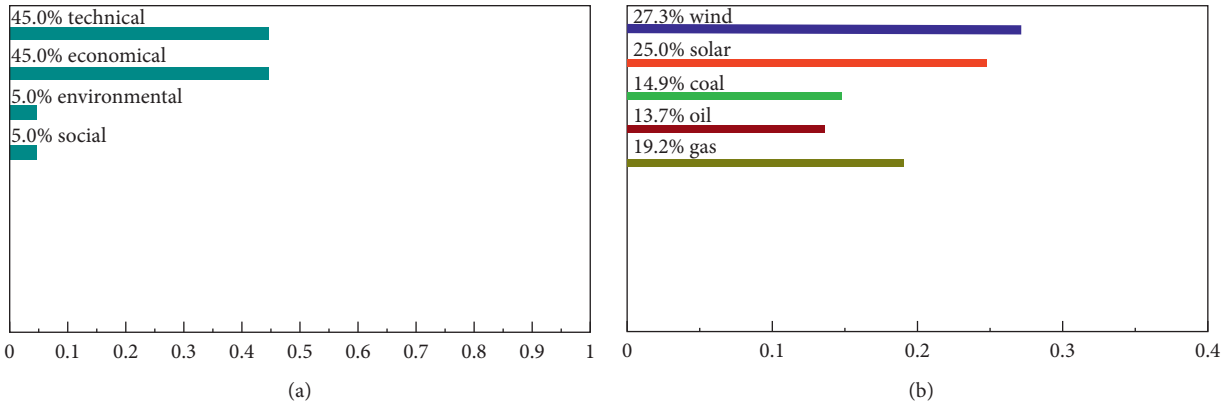

Figure 11: Ranking of all technologies assuming technical and economic criteria as extremely important to environmental and social criteria.

carrying weight of 0.2. Wind, oil, and gas showed similar results for the economic criteria, whereas wind and solar were better in the remaining three criteria. Wind again performed as the leading energy alternative for power generation in Pakistan, as shown in Figure 12.

By improving the weighing of economic criteria to extremely important, the overall position of gas resources improved, whereas that of wind and solar even after falling remained the best options as an alternative (Figure 13).

By improving the overall weighting of economic criteria to extremely important compared to the rest of the criteria, a steady decline is noted for RE sources, whereas gas improved significantly in its final result but remained behind RE sources (Figure 14).

For most environmentalists, environmental criteria would be the most weighted criteria. The emphasis is on reducing environmental degradation and improving the quality of life of the people, considering the environmental criteria as vital makes wind power a stronger alternative than the rest. Wind improved its proportion, whereas fossil fuel power plants sank down slightly more in the analysis, as shown Figure 15.

A huge difference has been observed in the environmental criteria of wind and solar, which are otherwise considered almost equal, since both are green sources of energy. This is due to the external cost of wind, which is three times lower than that of solar power. The overall result of environmental criteria of both wind and solar is much higher than that of the fossil fuel power plants, with coal and oil scoring just 11.8% and 11.7%, respectively, as shown in Figure 15.

Generally, renewable sources have been termed the best solution to the growing TWh of energy needs of the world but, due to the high initial setup cost of renewable sources, they have been avoided up till now. In recent years, due to immense R&D work, the cost has been brought down significantly and they have swiftly become the top priority among investors, as shown in Figure 16.

To answer "Can Pakistan completely rely on wind energy as one of the leading sources of power generation?" experts from different organizations in the wind sector were all of the same view: Pakistan can rely on wind energy as its leading energy source inside the country. But relying on it as a sole source is not technically and economically feasible.

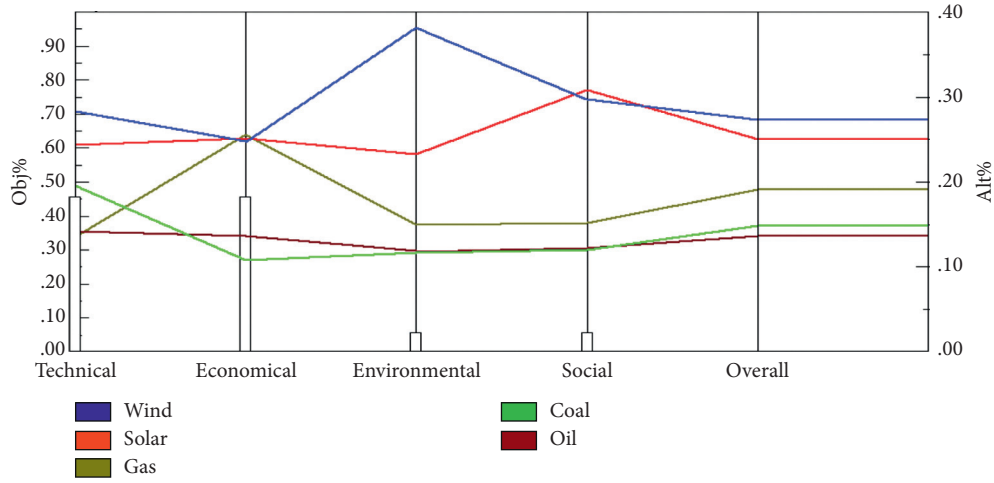

Figure 12: Performance sensitivity for each alternative against every criterion with economic and technical criteria being extremely important compared to social and environmental criteria.

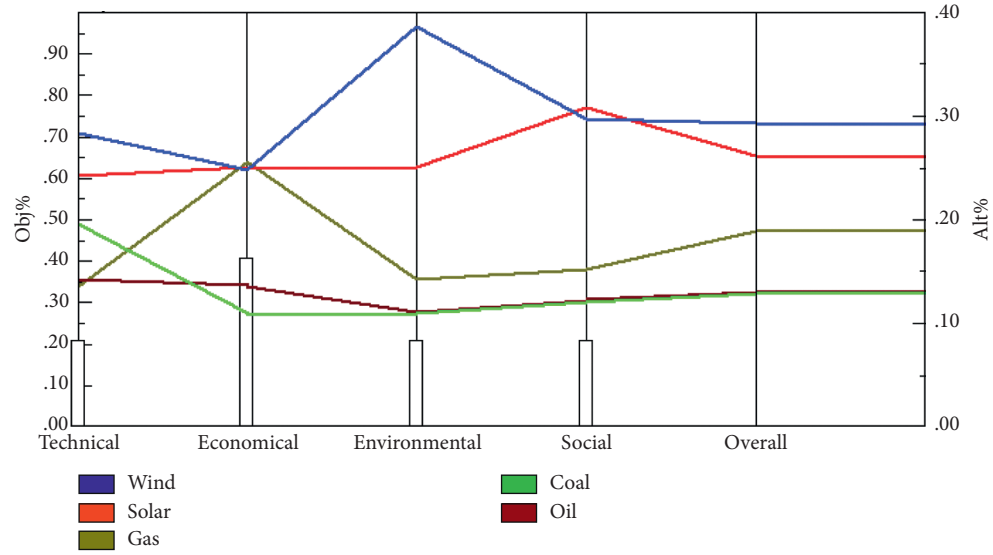

Figure 13: Performance sensitivity for each alternative against every criterion with economic criterion weighting twice compared to technical, social, and environmental criteria.

Due to variation in wind speed, power generated cannot be achieved at the desired capacity throughout the year. RE sources as primary sources of energy are best when coupled with nonrenewable energy sources for power generation. Two experts were of the opinion that decision makers can play a pivotal role in promoting it, if they are willing to accept wind as a source for power generation to tackle the energy crisis in the country for current and for future needs.

6.1. Comparison with Previous Research. The review of the literature reveals that studies of multicriteria decision making for selection among different sources were mainly based on the four main criteria of technical, economic, environmental, and social. This clearly shows that the criteria chosen are considered as a foundation for planning and evaluation of power projects. The analysis in this research was based upon these, along with 12 subcriteria carefully chosen after literature study. According to the findings, wind and solar emerge winners when it comes to a comparison with fossil fuel sources. Stein showed similar results in his studies; Amer and Daim [20] listed wind and solar as the best renewable sources for the energy needs of Pakistan.

Chatzimouratidis and Pilavachi [22, 29] revealed that RE was a preferable solution compared to conventional fuel power plants. While using AHP and later on PROMETHEE II to analyze the data, they used 13 criteria that were mostly related to environmental and social parameters and excluded economic and technical aspects of power plants. Their results showed minor variation from the results found here. The outcomes showed that wind, solar PV, and geothermal were the best alternatives for power generation.

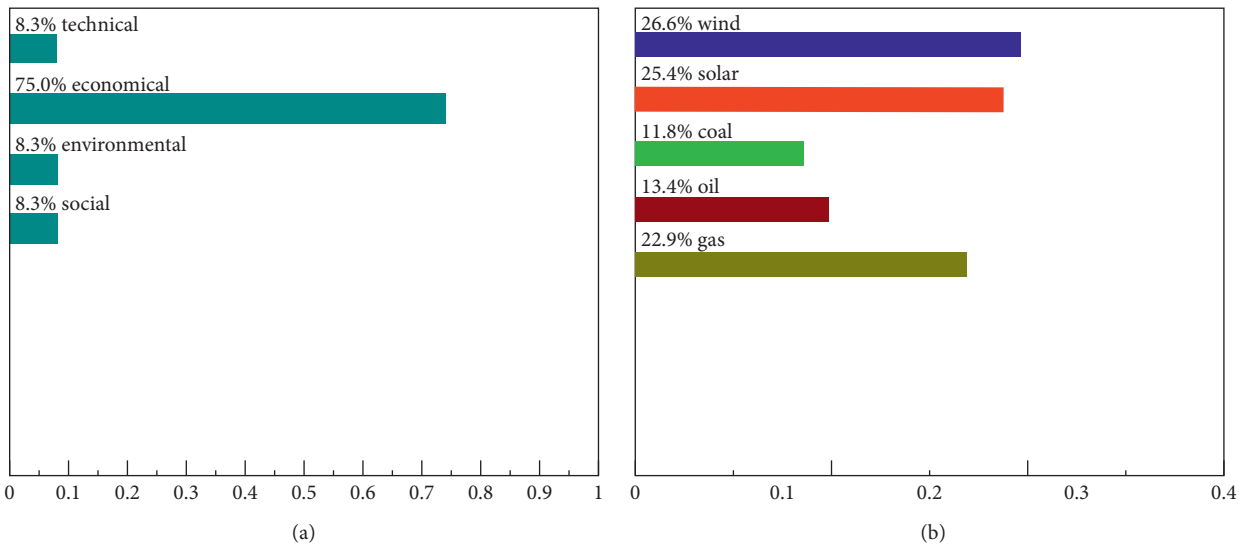

Figure 14: Ranking of all technologies assuming economic criteria extremely important compared to technical, environmental, and social criteria.

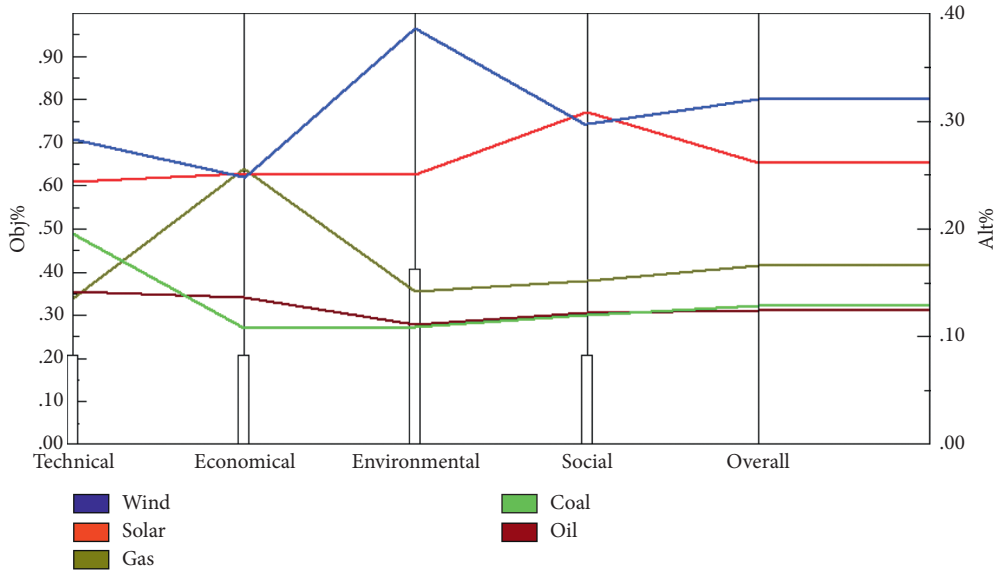

Figure 15: Ranking of all technologies assuming environmental criteria twice important compared to technical, economic, and social.

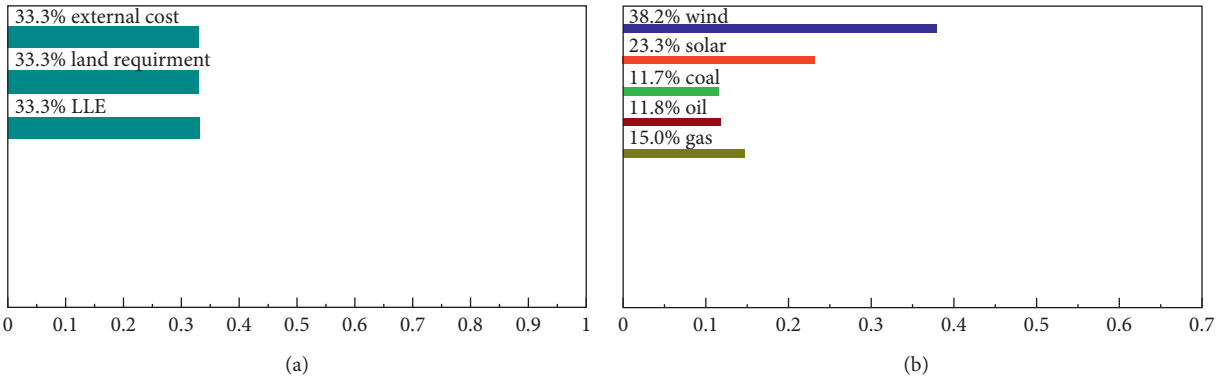

Figure 16: Environmental criteria overall weight when all the criteria were of equal weights.

They concluded that burning of oil and coal emissions for power generation add greatly to health disorders and mortality and therefore should be avoided.

Amer and Daim's study was based upon the comparison among renewable sources; the results showed that wind was the best alternative, followed closely by solar. They used AHP to analyze their data, which were mainly taken from US and EU data available on the Internet. Their results were similar, with wind topping the renewable list for alternative energy selection [20]. Stein's study was based upon nine alternatives, including renewables and nonrenewables. The power technologies were ranked by assuming equal weights. Wind took the top slot, followed closely by solar and hydro. Biomass was at the very bottom of the list, with coal, oil and gas; nuclear scored similar to fossil fuels [4].

7. Discussion and Conclusion

Pakistan's reliance on the use of fossil fuels for generation of electricity has worsened its position. Too much dependence on imports of foreign supplies has made it less energy-secure. The world changed its priorities regarding power generation long ago from fossil fuels towards much more reliable and environmental friendly RE sources. It is high time Pakistan found a consistent and well-designed policy to achieve a more sustainable, environmentally friendly, and affordable source for electricity generation as an alternative to fossil fuels. This will make the country less dependent on fossil fuels and protect it from energy insecurity.

This research gives us an insight into determining the best possible solution to our current energy crisis by considering future requirements. A multiperspective examination for technology appraisal has been used for a variety of available alternatives inside the country. Five alternatives were considered: wind, solar, coal, oil, and gas. The four most essential criteria (Technical, Economical, Environmental, and Social) for energy generation decision making were considered. Twelve subcriteria were measured to determine the four main criteria; all the criteria were equally preferred in their weights. This led us towards our final goal of finding the best solution for power generation in Pakistan.

For the first time, actual data from Pakistan's wind and solar sectors were used in order to prioritize among the energy alternatives inside the country. The data available on the NEPRA website were used for consideration of tariff and initial cost of power projects and subcriteria of economic criteria for wind, solar, and coal-based power plants. The capacity factor, a subcriterion of technical criteria for wind and solar, was taken from the upfront tariff determined by NEPRA.

The analysis revealed that RE easily outperformed fossil fuel power plants by a lengthy margin. Wind power as an alternative and RE source surpassed every other alternative. Gas showed good economic standing but the question remains: for how long? Gas is unable to tackle the energy crisis due to lower production capacity, and with meager resources, this can get worse. Unless more and abundant gas reservoirs can be explored, it will remain a bad choice for power generation. Thermal sources cannot be totally ignored but too much dependence on them should be avoided. The overall result calls for decision makers to focus on the RE sector, chiefly wind energy, as its driving force for future power generation. The policies devised to improve the share of RE mix must not only be maintained but expanded. Subsidies given to fossil fuels, if they remain necessary, must be truncated phase-wise to discourage the inclination towards them. Expenditure for fuel imports will be reduced and can be diverted towards operational cost and towards new investments prospects to drive more jobs. Wind power can improve the overall energy security of a country.

Pakistan as a country is highly insecure in terms of energy due to too-much dependence on fossil fuel power plants. Every now and then, there is fuel shortage supply to thermal power plants due to payment issues or problems faced due to poorer gas supply to the power plants. This in turn brings power outages, making the domestic and industrial customers suffer and affecting the whole business sphere. This has had a depressing impact on the industrial sector, and exports have suffered greatly due to high tariff rates along with high power outages. Focusing on wind and other renewables to improve the overall energy mix in the country will improve energy security. As the contribution of RE improves in the energy mix, the price of electricity will become more insensitive to the fluctuation in oil prices in the international market; thus, a steadier electricity price would be easily maintained. This gives investors and industrialists an incentive in the form of a cheaper and steadier tariff without affecting their productivity, which is usually very disturbed by power outages. Altogether, this will give confidence and investment security to customers to work inside the country.

The resources in Pakistan will not last forever, and so investing in RE and making the industry stronger will help in the long run to secure future employment. In addition, the health of the people can benefit from these technologies, which can in turn improve the savings and economic status of the people. Producing energy from renewable sources, especially wind, will prevent emissions of nonradioactive gases produced in Pakistan. This will evidence of the eagerness of the Government to improve its share of RE in the overall energy mix in accordance with the Kyoto Protocol.

The FFCEL wind farm project, which achieved a Commercial Operation Date (COD) on 16 May 2014, has successfully injected 129GWh of green energy into the National Grid in its first year of operation. The average availability factor for the first four months, i.e., from mid-May till mid-August 2014, was nearly 88%, which improved significantly and has been at 99% since October 2014 through to March 2015. If this trend of high availability was accomplished from the first day of COD, the power generated would have been significantly higher. The maximum availability factor can be easily managed with a quick response service team. The benchmark power for a complete year for the FFCEL wind farm was calculated to be 143GWh, which is achievable. It is assumed that the capacity factor can be above 31% or more if 98–99% of the wind farm availability factor is achieved. Hence, it can be concluded that the capacity factor for the wind farm in our sample area of

Jhimper is much higher than the one assumed by NEPRA for tariff determination.

Pakistan has vast land areas with wind potential, spread across all four provinces. The current focus in wind power is limited to the Gharro, keti Bandar, and Jhimper wind corridor, all near the coastal belt of Sindh Province, for utilizing all the wind power potential at a single place. But this focus should also be shifted to other parts of the country, especially towards the wind corridor near Mardan region and Islamabad. This will attract many investors who would find these places more desirable to invest in as being nearer to the federal capital. On the other hand, wind power supported with hydro electricity could be a good solution to tackle the power crisis. Even though hydro power has its own limitations, it still remains the best option as the most economical source of power generation. Wind at the southern region and hydro in the northern region of the country can be technically sound. By providing two nodes for the electricity supply system at the two far ends of the country, the distribution losses along the path can be reduced immensely.

Wind energy was followed by solar energy. Solar energy has been termed equally good, but, due to its higher cost, it has not enjoyed much success around the world. According to the Annual Energy Outlook 2011, the project initial cost for Solar PV has been around 4697 $/KW. This is the highest of all after nuclear power. The project's initial cost considered by NEPRA for tariff determination is around 1901 $/KW. This huge difference in cost remains a mystery in itself which needs to be cleared up. If this initial cost of solar power is true for Pakistan in all respects, then solar power projects can be much more economical than previously believed.

7.1. Limitations. Renewable energy offers many advantages in terms of copious free fuel and ease of use but there are also limitations to their availability all day long. Even though wind energy is one of the leading sources of power generation around the globe, wind power cannot be used as the only source of power generation and is only successful when supported by other sources of power generation, preferably nuclear energy in Pakistan's case. Wind as an energy source is never available around the clock. Wind turbine output varies with the temperature of the surroundings, and the speed, density, and intensity of wind. Wind is stronger and often available during summer, but in winter wind stops blowing hard and is not available as frequently as in summer. This makes the capacity factor of a wind farm much lower compared to other sources of power generation, creating many barriers to continuous supply of power.

Data Availability

The data used in this paper can be retrieved from Pakistan Energy Book.

Conflicts of Interest

The authors declare that they have no conflicts of interest.

Acknowledgments

The authors take this opportunity to thank the editorial board members Kai Wang, Wang Licheng, and Andrew Mendoza. This research was supported by the National Social Science Fund (19BGL127), the National Natural Science Fund (71572071), the China Postdoctoral Science Foundation Funded Project (2015M571708), and the Humanities and Social Sciences Fund of the Ministry of Education (18YJA630074).

References

[1] L. M. W. Leggett and D. A. Ball, "The implication for climate change and peak fossil fuel of the continuation of the current trend in wind and solar energy production," *Energy Policy*, vol. 41, pp. 610–617, 2012.

[2] G. A. Olah, "Beyond oil and gas: the methanol economy," *Angewandte Chemie International Edition*, vol. 44, no. 18, pp. 2636–2639, 2005.

[3] B. K. Savacool and M. A. Brown, "Competing dimensions of energy security: an international perspective," *Annual Review of Environment and Resources*, vol. 35, pp. 77–108, 2010.

[4] E. W. Stein, "A comprehensive multi-criteria model to rank electric energy production technologies," *Renewable and Sustainable Energy Reviews*, vol. 22, pp. 640–654, 2013.

[5] S. Shafiee and E. Topal, "When will fossil fuel reserves be diminished?" *Energy Policy*, vol. 37, no. 1, pp. 181–189, 2009.

[6] X. Long, Y. Chen, J. Du, K. Oh, and I. Han, "Environmental innovation and its impact on economic and environmental performance: evidence from Korean-owned firms in China," *Energy Policy*, vol. 107, pp. 131–137, 2017.

[7] A. W. Bhutto, A. A. Bazmi, and G. R. Zahedi, "Greener energy: issues and challenges for Pakistan-wind power prospective," *Renewable and Sustainable Energy Reviews*, vol. 20, pp. 519–538, 2012.

[8] REN21, "Renewable energy policy network for 21st century," 2013.

[9] Wharton, "University of pennsylvania," 2012.

[10] H. Sun, A. K. Kporsu, T. Farhad, and E. Bless Kofi, "Estimating environmental efficiency and convergence: 1980 to 2016," *Energy*, vol. 11, 2020.

[11] T. Muneer and M. Asif, "Prospects for secure and sustainable electricity supply for Pakistan," *Renewable and Sustainable Energy Reviews*, vol. 11, no. 4, pp. 654–671, 2007.

[12] H. Sun, B. K. Edziah, and A. K. Kporsu, "Institutional quality, green innovation and energy efficiency," *Energy Policy*, vol. 135, p. 111002, 2019.

[13] Z. Usman, R. Tanzeel, K. A. Abbas, and R. Muhammad, "An overview of implemented renewable energy policy of Pakistan," *Renewable and Sustainable Energy Reviews*, vol. 82, pp. 654–665, 2018.

[14] M. Shoaib, I. Siddiqui, Y. M. Amir, and S. U. Rehman, "Evaluation of wind power potential in Baburband (Pakistan) using Weibull distribution function," *Renewable and Sustainable Energy Reviews*, vol. 70, pp. 1343–1351, 2017.

[15] M. Kamran, "Current status and future success of renewable energy in Pakistan," *Renewable and Sustainable Energy Reviews*, vol. 82, pp. 609–617, 2018.

[16] M. A. Sheikh, "Energy and renewable energy scenario of Pakistan," *Renewable and Sustainable Energy Reviews*, vol. 14, no. 1, pp. 354–363, 2010.

[17] HDIP, "Pakistan energy year book," *Hydrocarbon Development Institute of Pakistan, Ministry of Petroleum and Natural Resources, Government of Pakistan*, vol. 14, 2012.
[18] S. N. Malik and O. R. Sukhera, "Management of natural gas resources and search for alternative renewable energy resources: a case study of Pakistan," *Renewable and Sustainable Energy Reviews*, vol. 16, no. 2, pp. 1282–1290, 2012.
[19] M. M. Qurashi and T. Hussain, "Renewable energy technologies for developing countries now and to 2023," 2005.
[20] M. Amer and T. U. Daim, "Selection of renewable energy technologies for a developing county: a case of Pakistan," *Energy for Sustainable Development*, vol. 15, no. 4, pp. 420–435, 2011.
[21] IEP, "Integrated Energy Plan 2009-2022," *Ministry of Finance, Government of Pakistan*, vol. 16, 2009.
[22] A. I. Chatzimouratidis and P. A. Pilavachi, "Decision support systems for power plants impact on the living standard," *Energy Conversion and Management*, vol. 64, pp. 182–198, 2012.
[23] C. Kahraman, İ. Kaya, and S. Cebi, "A comparative analysis for multiattribute selection among renewable energy alternatives using fuzzy axiomatic design and fuzzy analytic hierarchy process," *Energy*, vol. 34, no. 10, pp. 1603–1616, 2009.
[24] A. H. I. Lee, H. H. Chen, and H.-Y. Kang, "Multi-criteria decision making on strategic selection of wind farms," *Renewable Energy*, vol. 34, no. 1, pp. 120–126, 2009.
[25] J.-J. Wang, Y.-Y. Jing, C.-F. Zhang, and G.-H. Shi, "A fuzzy multi-criteria decision-making model for trigeneration system," *Energy Policy*, vol. 36, no. 10, pp. 3823–3832, 2009.
[26] S. D. Zhang and M. Ramachandran, "Application of multi-criteria decision making to sustainable energy planning-A review," *Renewable and Sustainable Energy Reviews*, vol. 8, no. 4, pp. 365–381, 2004.
[27] J.-J. Wang, Y.-Y. Jing, C.-F. Zhang, and J.-H. Zhao, "Review on multi-criteria decision analysis aid in sustainable energy decision-making," *Renewable and Sustainable Energy Reviews*, vol. 13, no. 9, pp. 2263–2278, 2009.
[28] S. Ahmad and R. M. Tahar, "Selection of renewable energy sources for sustainable development of electricity generation system using analytic hierarchy process: a case of Malaysia," *Renewable Energy*, vol. 63, pp. 458–466, 2014.
[29] A. I. Chatzimouratidis and P. A. Pilavachi, "Multicriteria evaluation of power plants impact on the living standard using the analytic hierarchy process," *Energy Policy*, vol. 36, no. 3, pp. 1074–1089, 2008.
[30] B. A. Akash, R. Mamlook, and M. S. Mohsen, "Multi-criteria selection of electric power plants using analytical hierarchy process," *Electric Power Systems Research*, vol. 52, no. 1, pp. 29–35, 1999.
[31] B. V. Mathiesen, H. Lund, and K. Karlson, "100% Renewable energy systems, climate mitigation and economic growth," *Applied Sciences*, vol. 88, pp. 488–501, 2011.
[32] M. Khalid Saeed, A. Salam, A. U. Rehman, and M. Abid Saeed, "Comparison of six different methods of Weibull distribution for wind power assessment: a case study for a site in the Northern region of Pakistan," *Sustainable Energy Technologies and Assessments*, vol. 36, 2019.
[33] M. H. Sahir and A. H. Qureshi, "Assessment of new and renewable energy resources potential and identification of barriers to their significant utilization in Pakistan," *Renewable and Sustainable Energy Reviews*, vol. 12, no. 1, pp. 290–298, 2008.
[34] U. Mirza, N. Ahmad, T. Majeed, and K. Harijan, "Wind energy development in Pakistan," *Renewable and Sustainable Energy Reviews*, vol. 11, no. 9, pp. 2179–2190, 2007.
[35] M. Asif, "Sustainable energy options for Pakistan," *Renewable and Sustainable Energy Reviews*, vol. 13, no. 4, pp. 903–909, 2009.
[36] W. Tong, *Wind Power Generation and Wind Turbine Design*, WIT Press, Boston, MA, USA, 2010.
[37] AEDB, "Alternative energy development board," 2014.
[38] F. Dincer, "The analysis on wind energy electricity generation status, potential and policies in the world," *Renewable and Sustainable Energy Reviews*, vol. 15, no. 9, pp. 5135–5142, 2011.
[39] NREL, "National renewable energy laboratory," 2012.
[40] S. K. Lee, G. Mogi, and J. W. Kim, "Decision support for prioritizing energy technologies against high oil prices: A fuzzy analytic hierarchy process approach," *Journal of Loss Prevention in the Process Industries*, vol. 22, no. 6, pp. 915–920, 2009.
[41] EIA, "Energy information agency," 2014.
[42] M. Z. Jacobson and M. A. Delucchi, "Providing all global energy with wind, water, and solar power, Part I: technologies, energy resources, quantities and areas of infrastructure, and materials," *Energy Policy*, vol. 39, no. 3, pp. 1154–1169, 2011.
[43] V. Fthenakis and H. C. Kim, "Land use and electricity generation: a life-cycle analysis," *Renewable and Sustainable Energy Reviews*, vol. 13, no. 6-7, pp. 1465–1474, 2009.
[44] ExternE, "ExternE-external costs of energy," 2006.
[45] Satty and L. Thomas, *The Analytic Hierarchy Process: Planning, Priority Setting, Resource Allocation*, McGraw-Hill, New York, NY, USA, 1980.
[46] K. v. Alphen, W. G. V. Sark, and P. Hekkert, "Renewable energy technologies in the Maldives-determining the potential," *Renewable and Sustainable Energy Reviews*, vol. 11, no. 8, pp. 1650–1674, 2007.
[47] M. Mohsin, J. Zhang, R. Saidur, H. Sun, and S. M. Sait, "Economic assessment and ranking of wind power potential using fuzzy-TOPSIS approach," *Environmental Science and Pollution Research*, vol. 26, no. 22, pp. 22494–22511, 2019.
[48] NEPRA, "National electric power regulatory authority," 2013.

Hindawi
Mathematical Problems in Engineering
Volume 2020, Article ID 3690564, 9 pages
https://doi.org/10.1155/2020/3690564

Research Article

Presynchronous Grid-Connection Strategy of Virtual Synchronous Generator Based on Virtual Impedance

Guanfeng Zhang, Junyou Yang, Haixin Wang, and Jia Cui

School of Electrical Engineering, Shenyang University of Technology, Shenyang 110870, China

Correspondence should be addressed to Junyou Yang; junyouyang@sut.edu.cn

Received 18 August 2020; Revised 28 September 2020; Accepted 15 October 2020; Published 9 November 2020

Academic Editor: Kai Wang

The virtual synchronous generator (VSG) technology of inverter is widely used to provide the inertia and damping support for power system. However, an additional measurement device PLL (phase-locked loop) is required in the virtual synchronous generator grid connection to track the voltage phase, amplitude, and frequency, which restricts the flexible output of the distributed power generation system. To tackle this challenge, a method for grid-connected control of virtual synchronous generator based on virtual impedance is proposed. It is assumed that there is a virtual power exchange between the synchronous machine and the power grid when the virtual synchronous generator is off-grid, the virtual impedance is developed to calculate the virtual current, and when the virtual current is zero, the output voltage of the VSG can be synchronized with the voltage of the power grid, thereby seamlessly switching between off-grid and grid-connected VSG. A semiphysical simulation platform is built based on RT-LAB; simulation and experimental results show that the proposed grid synchronization control strategy of the VSG can achieve seamless transform between different VSG modes, which is simpler than the conventional synchronization control, while having a good active and reactive power tracing performance.

1. Introduction

With the rapid economic development, the problems of energy crisis and environmental pollution have become increasingly prominent. Traditional fossil energy is supplemented or replaced by clean energy, which is an important means to ensure sustainable development in the energy field. Distributed power generation has gradually become a new mode of electricity production and renewable energy consumption due to its efficient, flexible, and friendly grid connection characteristics. However, a large number of intermittent and random distributed power sources are connected to the grid, which greatly increases the complexity and difficulty of management and control of the grid and has a major impact on the safe, reliable, and economic operation of the grid. The existing distributed power generation system uses power electronic devices to be integrated into the grid, which is more flexible than traditional power generation systems.

However, the conventional grid-connected inverter has a fast response speed, almost no moment of inertia, and is difficult to participate in grid regulation. Distributed power generation systems cannot provide the necessary voltage and frequency support for the distribution network with distributed power sources, nor can it provide the necessary damping effect for the relatively poorly stable microgrid.

The lack of a mechanism to effectively "synchronize" with the distribution network and microgrid affects the friendly compatibility of the distributed power generation system with the existing power grid. If the grid-connected inverter has the external characteristics of a synchronous generator, it will inevitably improve the operating performance of the distributed generation system and the microgrid with the grid-connected inverter. Based on this idea, researchers have proposed the virtual synchronous generator (VSG) technology [1]. By changing the external characteristics of the grid-connected inverter and absorbing the advantages of the synchronous generator, which ensures

the stable operation of the system. In 2007, the concept of virtual synchronization was first proposed by the European VCYNC project. The synchronverter algorithm was first proposed to realize the modeling of virtual synchronous generator [2]. In recent years, China has also made outstanding contributions in improving the stability of distributed generation systems with virtual synchronous generators [3].

At present, the technology of virtual synchronous generator has entered the practical stage. In 2016, the State Grid Corporation of China transformed the inverter of wind power generator and photovoltaic power generation system in the Zhangbei Wind-Solar Storage and Transmission Demonstration Project to become the largest virtual synchronous generator demonstration project in the world [4]. In the same year, the photovoltaic virtual synchronous generator developed by the China Electric Power Research Institute Power Distribution Institute was officially launched in the Sino-Singapore Tianjin Eco-City. The technical functions of the virtual synchronous generator are basically realized, and it has entered the optimization phase from preliminary development stage, but there is still room for further research at the system-level grid-connected transient control and application level.

A control strategy of VSG self-synchronous inverter is proposed to realize VSG no-load self-synchronization grid connection [5]. The microgrid frequency adjustment method based on virtual synchronous generator is studied to realize different operation modes of off-grid and grid-connected [6, 7]. Photovoltaics and energy storage are integrated based on virtual synchronous generator technology, realizing photovoltaic power generation friendly dissipation [8, 9]. The charge and discharge control method for DC unit of virtual synchronous generator was studied, and the optimized control method of the state of charge was given [10, 11]. Wind power grid-connected system based on virtual synchronous generator was proposed, which realized the goal of friendly grid connection with frequency response capability [12]. The abovementioned literatures all researched the application technology of the virtual synchronous generator in the existing distributed power generation system. In addition, the application of virtual synchronous generator technology for frequency modulation, voltage regulation, and fault was discussed in the context of microgrid operation [13, 14]. An electric vehicle charging method has been proposed based on virtual synchronous generator technology in [15]. A new seamless transfer method based on the second-order generalized integrator is proposed in [16], realizing switch from islanded mode to grid-connected mode smoothly. Single-PLL- and multi-PLL-based approaches are presented, and through the PLL presynchronization strategy, the voltage amplitude and phase angle before VSG grid connection are the same. However, PLL's participation in grid voltage lock-in not only makes the control structure more complex, but also makes it difficult to guarantee its accuracy and reliability in the weak grid environment [17–20].

These research results have the same basic principles at the level of the inverter-synchronous generator control strategy, the difference lies in the application. It can operate stably in both off-grid and grid-connected operation modes, and switch of operation mode can be realized without changing the controller structure. However, the synchronization time of off-grid seamless switch is long and lacks experimental verification.

In summary, an improved virtual synchronous generator grid-connection method is proposed to solve the problem that the extra measuring device in the traditional grid-connection restricts the flexible output of the distributed generation system, avoid the problems such as nonlinear, slow response and difficult parameter design of the PLL, and realize the more concise and effective VSG smooth grid connection; meanwhile, a semiphysical verification method is given.

This article is organized as follows. The equivalent model of virtual synchronous generator on-grid is given, the principle and the equations are illustrated and deduced in Section 2. The proposed synchronization control strategy of virtual synchronous generator based virtual inertia control is presented in Section 3. Simulations are carried out in MATLAB/Simulink to verify the validity of the proposed method in Section 4. In Section 5, RT-LAB hardware-in-the-loop simulation platform was built to verify the effectiveness of the control strategy mentioned in this paper. Various operating conditions with islanded mode, seamless switching, and grid-connected are presented. Finally, the conclusion is given in Section 6.

2. Equivalent Model of Virtual Synchronous Generator On-Grid

If the virtual synchronous generator is equivalent to a voltage source, the equivalent circuit of single-phase virtual synchronous generator grid connection system is shown in Figure 1, where e is the excitation voltage of a virtual synchronous generator, E is the virtual synchronous generator excitation voltage amplitude, i is the output current of virtual synchronous generator, X_S is the line impedance, u_g is the grid voltage, U_g is the amplitude of grid voltage, α_g is the phase angle of the grid voltage, and α is the phase angle of the excitation voltage of VSG.

The active power transmitted by the virtual synchronous generator is shown in the following equation:

$$\begin{cases} P = \dfrac{3U_g E}{2X_s}\sin\left(\alpha - \alpha_g\right), \\ \\ \delta = \alpha - \alpha_g, \end{cases} \tag{1}$$

where δ is the virtual power angle.

The transmission of reactive power by the virtual synchronous generator is shown by

$$Q = \frac{3U_g\left[E\cos\left(\alpha - \alpha_g\right) - U_g\right]}{2X_S}. \tag{2}$$

When the virtual synchronous generator is connected to the grid, the frequency, phase, and amplitude of the output

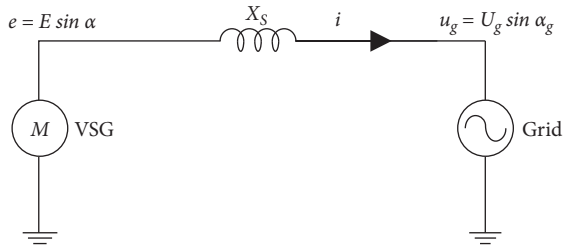

Figure 1: Equivalent circuit diagram.

voltage should be close to the grid voltage, which is expressed by

$$\begin{cases} \left|f - f_g\right| \le f_{\min}, \\ \left|E - U_g\right| \le U_{\min}, \\ \left|\alpha - \alpha_g\right| \le \alpha_{\min}, \end{cases} \tag{3}$$

where f, E, and α are the voltage frequency, amplitude, and phase of the virtual synchronous generator, respectively, g subscript is the grid side variable, min subscript is the set safety threshold, and the safety thresholds $f_{\min}$, $U_{\min}$, and $\alpha_{\min}$ in the optimal grid-connected case are zero.

From equations (1) and (2), it can be seen that the power transmission equation of virtual synchronous generator grid-connected mainly depends on the voltage amplitude and phase angle; that is, to meet the requirements of smooth grid-connected, the safety threshold should meet the requirements of the following equation:

$$\begin{cases} U_{\min} = 0, \\ \alpha_{\min} = 0. \end{cases} \tag{4}$$

Substituting equations (3) and (4) into equations (1) and (2), the following equation is obtained:

$$\begin{cases} P = 0, \\ Q = 0. \end{cases} \tag{5}$$

It can be seen that the synchronization of the virtual synchronous generator to the grid can be understood as that the active power and reactive power transmitted by the virtual synchronous generator to the grid are zero.

The output power of the virtual synchronous generator is deduced under the assumption that the virtual synchronous generator is connected to the grid, but the actual situation is that the virtual generator is off-grid and has no output power under the no-load state. In order to give the control strategy of virtual synchronous generator with zero output power, a virtual power exchange between a virtual synchronous generator and the grid is needed.

3. Synchronization Control Strategy of Virtual Synchronous Generator

The virtual synchronous generator is composed of DC power supply, DC/AC inverter, and filter circuit. The DC power supply can be regarded as the prime mover to provide the power required by the virtual synchronous generator. The control system of inverter is the core of VSG, which mainly includes VSG ontology model and control algorithm. The former mainly simulates electromagnetic relationship and mechanical motion of synchronous generator from mechanism, while the latter simulates active frequency modulation and reactive voltage regulation and other characteristics of synchronous generator from external characteristics.

The basic equation of virtual synchronous generator is shown in the following equation:

$$\begin{cases} u = -Ri - L_m\left(\dfrac{\mathrm{d}i}{\mathrm{d}t}\right) + e, \\ e = \omega M_f i_f \widetilde{\sin}\,\theta, \\ J\dfrac{\mathrm{d}\omega}{\mathrm{d}t} = T_m - T_e - D_p\left(\omega - \omega_{\mathrm{ref}}\right), \\ T_e = M_f i_f\left(i, \widetilde{\sin}\,\theta\right), \\ Q = -\omega M_f i_f\left(i, \widetilde{\cos}\,\theta\right), \end{cases} \tag{6}$$

where T_m is the virtual mechanical torque, D_p is the virtual damping coefficient, J is the virtual moment of inertia, M_f is the mutual inductance coefficient, u and i are the measured voltage and current, T_e is the virtual electromagnetic torque, i_f is the virtual excitation current, θ is the electrical angle, e is the excitation voltage, ω is the angular velocity, $\omega = \mathrm{d}\theta/\mathrm{d}t$, and ω_{ref} is grid synchronization angular velocity. $\widetilde{\sin}\,\theta$ and $\widetilde{\cos}\,\theta$ are defined as follows:

$$\begin{aligned} \widetilde{\sin}\,\theta &= \begin{bmatrix} \sin\theta \\ \sin\left(\theta - \dfrac{2\pi}{3}\right) \\ \sin\left(\theta + \dfrac{2\pi}{3}\right) \end{bmatrix}, \\ \widetilde{\cos}\,\theta &= \begin{bmatrix} \cos\theta \\ \cos\left(\theta - \dfrac{2\pi}{3}\right) \\ \cos\left(\theta + \dfrac{2\pi}{3}\right) \end{bmatrix}. \end{aligned} \tag{7}$$

The control part mainly includes power-frequency regulator, excitation regulator, and presynchronization unit, as shown in Figure 2. The output active power P of VSG is composed of the active power reference value P_{ref} and the frequency change difference ΔP as follows:

$$\begin{cases} D_p = -\dfrac{\Delta T}{\Delta\omega} \approx -\dfrac{\Delta P}{\Delta\omega \cdot \omega_{\mathrm{ref}}}, \\ P = P_{\mathrm{ref}} + D_p\omega_{\mathrm{ref}}\left(\omega_{\mathrm{ref}} - \omega\right). \end{cases} \tag{8}$$

The coefficient D_p is also commonly called the P-f droop control coefficient and is a set value that reflects the active

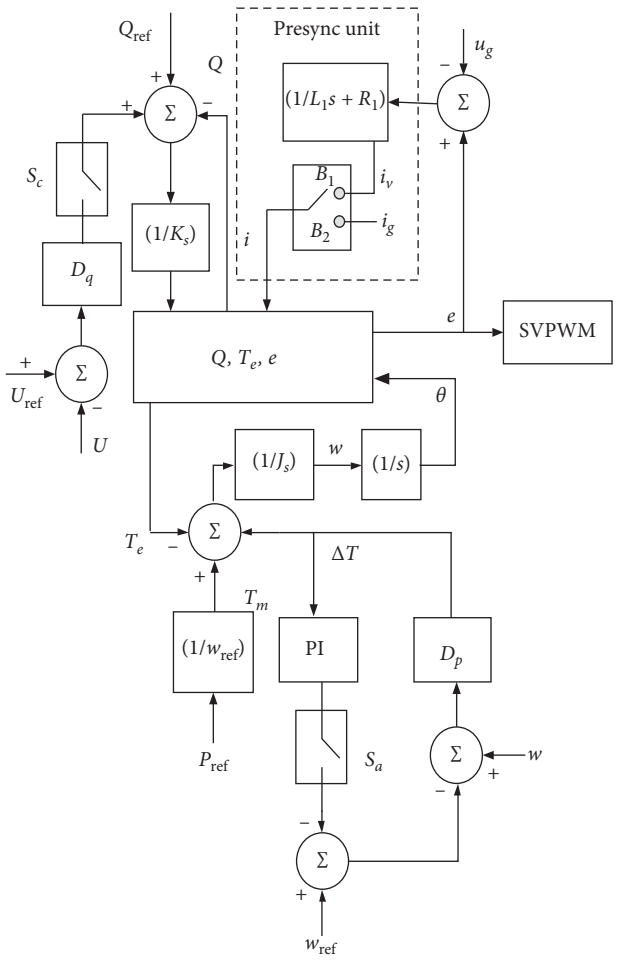

Figure 2: Control diagram of VSG based on virtual impedance.

power-frequency droop control characteristics. Due to the droop characteristic between active power and frequency, VSG has the self-synchronization characteristic of transmission generator. When the power grid frequency rate goes up (down), the VSG automatically reduces (increases) the active power injected into the grid and participates in the primary frequency modulation of the large grid.

Similarly, D_q is the reactive power-voltage droop control coefficient, which reflects the reactive power-voltage droop control characteristics ($Q - U$ characteristics). Due to the existence of reactive voltage droop control, the VSG can participate in the primary voltage regulation of large power grid; when the voltage amplitude of the power grid is lower than (higher than) the rated voltage U_{ref}, the reactive power Q of VSG output is higher than (lower than) the fixed value of reactive power rate Q_{ref}.

$$D_q = -\frac{\Delta Q}{\Delta U} = -\frac{Q_{ref} - Q}{U_{ref} - U}. \tag{9}$$

The basic control of virtual synchronous generator includes virtual speed regulation control and virtual excitation control. Based on the aforementioned mathematical model of virtual synchronous generator and typical active frequency drooping characteristic, virtual speed regulation control adopts the double-loop structure of power outer loop frequency inner loop to simulate the active power-frequency characteristic, inertia, and damping link of the synchronous generator. Virtual excitation control does not involve the abovementioned mathematical model, but mainly considers the external characteristics of virtual synchronous generator, so the traditional reactive power-voltage droop control structure is adopted [21].

In order to connect the virtual synchronous generator to the power grid smoothly, the traditional control method needs the special PLL to provide the voltage, frequency, and phase angle of the power grid to realize the synchronization, but the PLL is a nonlinear element and it takes time to adjust the parameters of the PLL. When there are multiple PLL in a system, these PLL will attempt to interlock, reducing the performance and stability of the system and increasing the complexity of the system.

Therefore, in the virtual synchronous generator island/grid switching process, this paper proposes a virtual synchronous generator presynchronization method based on virtual impedance; the virtual impedance designed by this method is to virtualize a power exchange between virtual synchronous generator and the grid.

Assuming that there is a virtual impedance X_V between the VSG terminal and the power grid, and $\alpha_g = 0$, the output virtual active power P_V of the VSG is

$$P_V = \frac{EU_g}{2X_V} X_V \mathrm{COS}\left(\varphi_V - \alpha_V\right) - \frac{U_g^2}{2X_V} \mathrm{COS}\varphi_V, \tag{10}$$

where the virtual impedance X_V and the virtual impedance angle φ_V satisfy

$$\begin{cases} X_V = \sqrt{\left(\omega L_1\right)^2 + R_1^2}, \\ \varphi_V = \arctan\left(\dfrac{\omega L_1}{R_1}\right). \end{cases} \tag{11}$$

The virtual current can be obtained by dividing the deviation between e and the grid voltage u_g by the virtual synchronous reactance:

$$i_V = \frac{e - u_g}{L_1 s + R_1}, \tag{12}$$

where i_V is the virtual current, L_1 and R_1 constitute the virtual impedance, R_1 is the virtual resistance, and L_1 is the virtual inductance. In theory, the smaller the L_1 is, the faster the system synchronizes. However, when L_1 is too small, the synchronous control process will be shaken, so L_1 is generally slightly smaller than the filter inductance L_S.

It can be seen from equation (10) that when the amplitude and phase of the VSG output voltage and the grid voltage are exactly the same, the virtual power P_V is equal to 0, so PI closed-loop control of the virtual power is needed to synchronize the VSG output voltage with the grid voltage. However, the premise of this method is that the amplitude and frequency of E and U_g are the same. Therefore, the presynchronization control unit based on virtual impedance

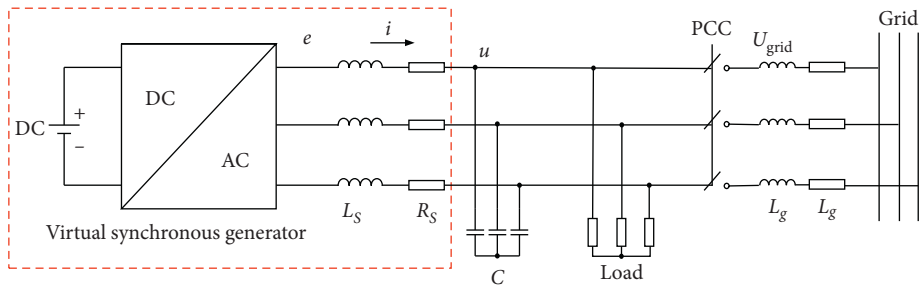

Figure 3: Simulation system.

and voltage frequency control is designed as shown in Figure 2, assuming a virtual impedance exists between virtual synchronous generator output voltage and the grid voltage, the virtual current can be calculated as shown in equation (12).

In off-grid state, switch S_a and switch S_c are closed to make the voltage amplitude and frequency of VSG consistent with the grid, the VSG, and load form a microgrid, which runs in the V/F mode. Then switch B_1 is closed to realize the synchronization of the VSG output voltage and the grid voltage. After the synchronization is completed, while closing the grid-connected switch, turn off the switch S_a and S_c, and then VSG is pulled into synchronization by the grid.

If VSG is running in VF state, S_a and S_c are already closed, the switch B_1 can be closed directly to synchronize the VSG output voltage with the grid voltage.

In the grid-connected state, the switch B_2 is closed, the real current i_g is routed into the controller for normal operation, and the virtual synchronous generator runs in grid-connected mode.

4. Simulation Analysis

Based on the above research, this paper uses MATLAB/Simulink software for simulation verification; the simulations are based on the microgrid configuration in Figure 3, which operates in islanded mode before $t = 0.04$ seconds. The values of relevant parameters in equations and block diagrams of this paper are shown in Table 1.

Comparing the grid connection control method proposed in this paper with the direct interconnection method of virtual synchronous generator, the simulation results are in Figure 4.

When the virtual synchronous generator is running with load, the voltage amplitude and frequency are consistent with the power grid, and there is a phase difference between the output voltage of the virtual synchronous generator and the power grid voltage, as shown in Figure 4. When $t = 0.04$ s, direct interconnection will generate a large inrush current. It adversely affects the stable operation of the virtual synchronous generator and cannot meet the requirements for smooth grid connection.

Adopting the presynchronization control method based on virtual impedance, the virtual synchronous generator tracks the voltage phase of the power grid through continuous adjustment, as shown in Figure 5, the output voltage of the virtual synchronous generator is kept in synchronization with the grid voltage, and there is no inrush current after the grid connection operation; the island/grid connection is realized seamlessly.

Table 1: Simulation parameters.

Symbol	Description	Values
u_{grid}	Grid voltage	400 V
e	Excitation voltage	380 V
C	Filter capacitor	40 μF
L_S	Filter inductance	0.45 mH
R_S	Filter resistance	0.2 Ω
L_g	Line inductance	0.1 mH
R_g	Line resistance	0.02 Ω
L_1	Virtual inductance	0.2 mH
R_1	Virtual resistance	0.05 Ω
P_{load}	Load power	10 kW
f_n	Grid rated frequency	50 Hz
f_c	Switching frequency	5 kHz

5. Experimental Verification

RT-LAB hardware-in-the-loop simulation platform was built to verify the effectiveness of the control strategy mentioned in this paper [22, 23], which includes a controllable load, a 10 kW·h lithium battery energy storage system, a 10 kW converter, RT-LAB, and a simulated power grid, as shown in Figure 6. Among them, RT-LAB is designed as a virtual synchronous generator controller, which simultaneously collects the voltage, current, frequency, etc., of the converter and the simulated power grid and sends out control pulses to form a closed loop. The lithium battery is used as a DC power source, and the lithium battery plus converter system is a virtual synchronous generator, which is directly connected to the controllable load and supplies power to the controllable load. First, the energy storage virtual synchronous generator and the controllable load form an isolated microgrid, which runs in the V/F mode with a frequency of 50 Hz. The controllable load suddenly increases by 0.5 kW at $t = 6$ seconds; then the virtual impedance strategy is started at $t = 9$ seconds. The isolated microgrid is connected to the simulated power grid through a control switch a $t = 10$ seconds and switches from off-grid to grid-connected mode. The experimental results of the VSG off-grid process are shown in Figures 7–12.

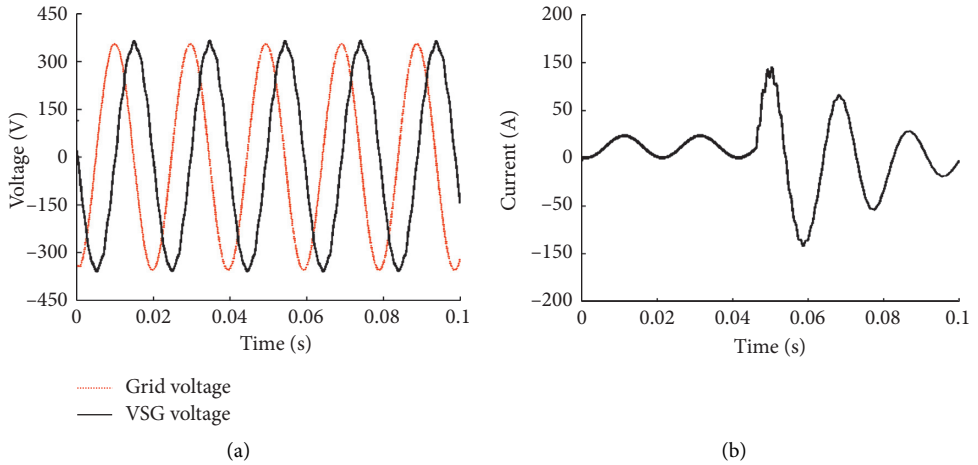

Figure 4: Voltage and current of the virtual synchronous generator.

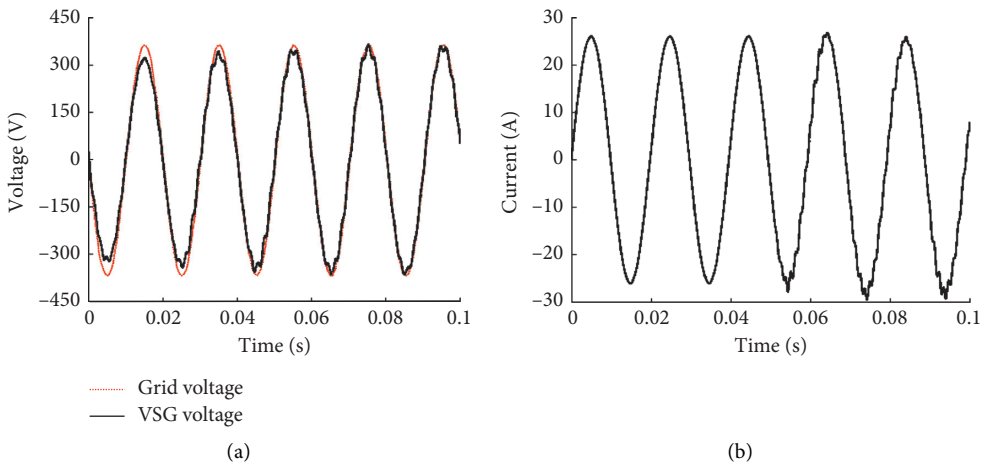

Figure 5: Voltage and current of virtual synchronous generator based on virtual impedance.

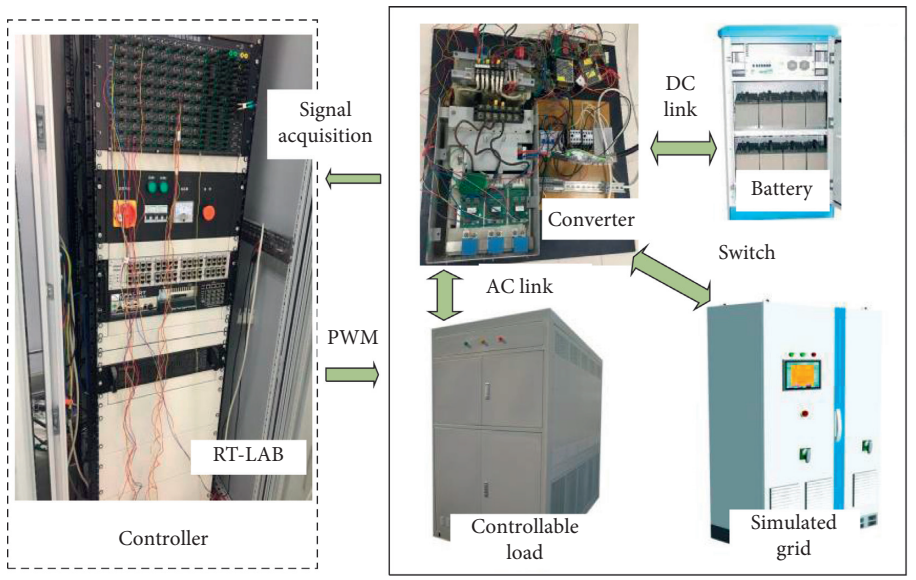

Figure 6: Experimental system.

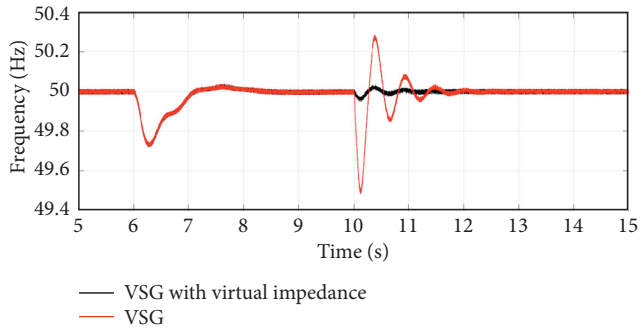

Figure 7: Frequency change of virtual synchronous generator at instant of grid connection.

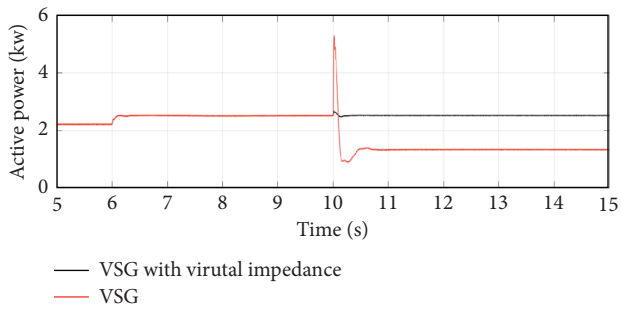

Figure 8: Comparison of active power response of virtual synchronous generator.

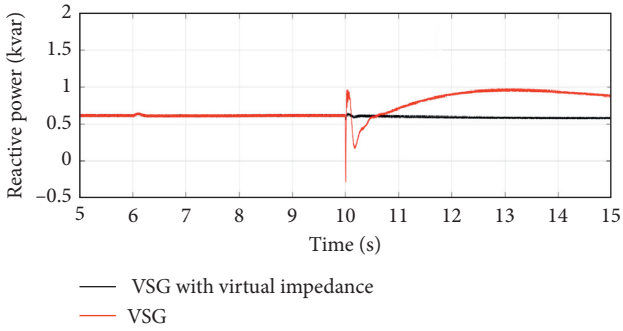

Figure 9: Comparison of reactive power response of virtual synchronous generator.

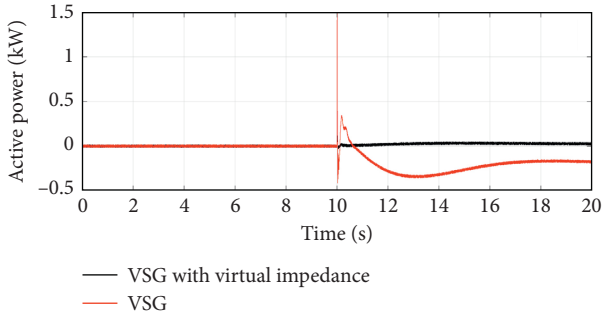

Figure 10: Comparison of active power response of the grid.

According to the test waveforms of the virtual synchronization machine during the off-grid connection, the control strategy proposed in this paper can achieve synchronization with the power grid before closing. When the virtual synchronous generator is running in island mode, the frequency is stable at 50 Hz, and the load power is suddenly increased, causing the frequency to drop at $t = 6$ s and quickly recover to 50 Hz, effectively reducing frequency fluctuations

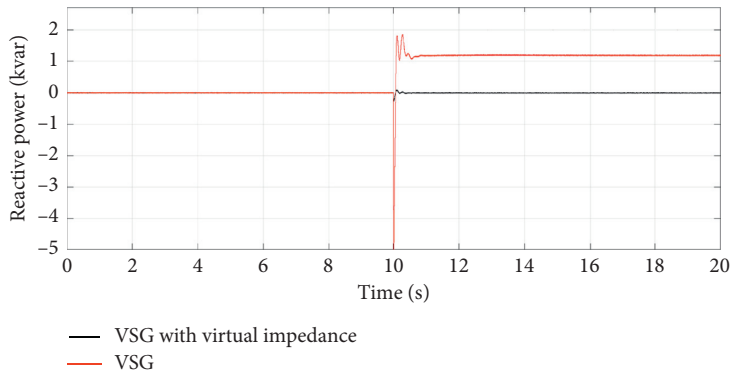

Figure 11: Comparison of reactive power response of the grid.

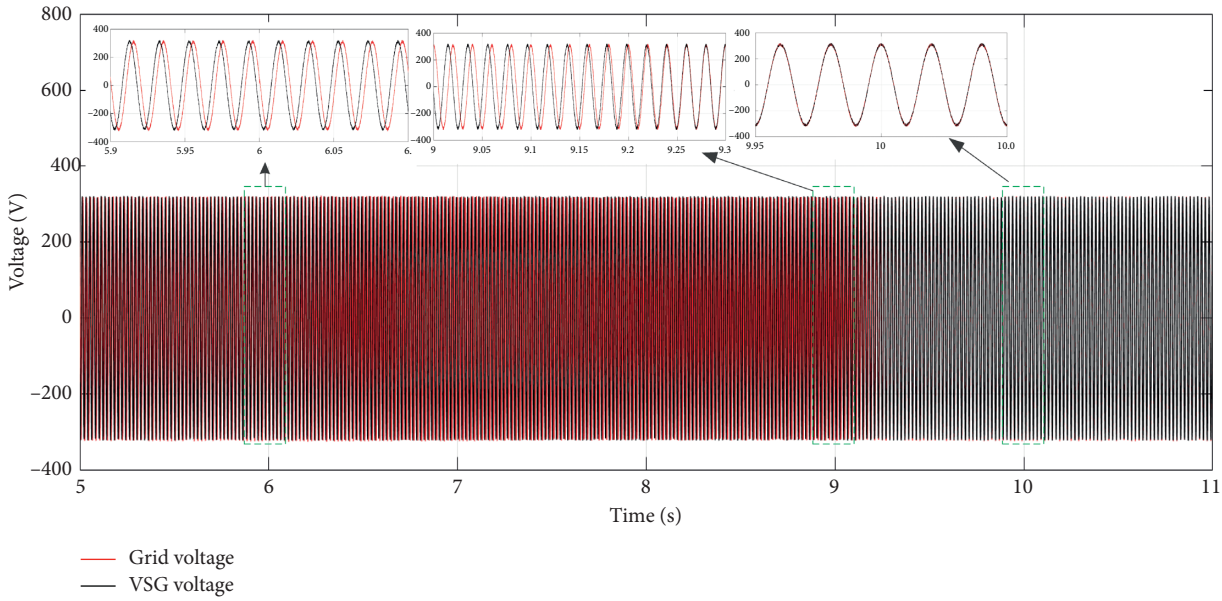

Figure 12: Voltage waveform based on virtual impedance.

during the switching process at $t = 10$ s, as shown in Figure 7. Figures 8–11 show that there is no obvious impact on active and reactive power of virtual synchronous generator and the grid when closing at 10 s.

The control strategy based on virtual impedance can achieve synchronization with the grid voltage in 0.25 s as shown in Figure 12, and the circuit breaker is turned on at $t = 10$ s, the frequency changes smoothly and then recovers. Actually, we can close the circuit breaker at any time after $t = 9.25$ s without obvious impact.

In the process of grid connection, the impact of active power and reactive power is significantly reduced, and the output power is smoothly transitioned to achieve a flexible grid connection of the distributed power generation system. At the same time, this paper builds a semiphysical simulation platform through RT-LAB, forms a hardware-in-the-loop real-time simulation system, completes the inspection of the controller algorithm strategy, and provides a reference for the control of the converter's virtual synchronous generator.

6. Conclusion

In this paper, a grid synchronization control strategy for virtual synchronous generator based on virtual impedance is proposed, which enables the grid-connected inverter to participate in the voltage amplitude and frequency adjustment of the large grid when it is connected to the grid, and can operate in V/F mode to supply power to the local load when off-grid. The power tracking and seamless switching capability of the control strategy are verified by RT-LAB semiphysical simulation platform.

The voltage of the virtual synchronous generator can be synchronized with the power grid by using the controller itself without the need of PLL, which is simpler and more effective than the traditional virtual synchronous generator grid connection method, which avoids the problems of nonlinearity, slow response, and difficult parameter design of the phase-locked loop.

As this controller solves the problem that the additional measurement devices restrict the flexible output of the

distributed power in the traditional grid connection, this improves the power grid's ability to accept distributed power generation units.

Data Availability

The data used to support the findings of this study are available from the corresponding author upon request.

Conflicts of Interest

The authors declare that they have no conflicts of interest regarding the publication of this paper.

Acknowledgments

This work was supported by the Postdoctoral Science Foundation Project of China under Grant no. 2019M651144 and the Liaoning Association for Science and Technology Innovation Think Tank Project under Grant no. LNKX2020ZD03.

References

[1] H. Bevrani, T. Ise, and Y. Miura, "Virtual synchronous generators: a survey and new perspectives," *International Journal of Electrical Power & Energy Systems*, vol. 54, pp. 244–254, 2014.

[2] Q. Zhong and G. Weiss, "Synchronverters: inverters that mimic synchronous generators," *IEEE Transactions on Industrial Electronics*, vol. 58, no. 4, pp. 1259–1267, 2010.

[3] L. Yang, J. Gan, C. Xia, Z. Hu, B. Gao, and L. Qu, "Research on the frequency regulation strategy of virtual synchronous generator based photovoltaic power plant," in *Proceedings of the 2018 IEEE 8th Annual International Conference on CYBER Technology in Automation, Control, and Intelligent Systems (CYBER)*, Tianjin, China, July 2018.

[4] B. Tian, X. Mo, Y. Shen, W. Lei, and P. Xu, "Prospect and key techniques of global energy interconnection zhangjiakou innovation demonstration zone," *Global Energy Interconnection*, vol. 1, no. 2, pp. 153–161, 2018.

[5] Q. Zhong, P. Nguyen, Z. Ma, and W. Sheng, "Self-synchronized synchronverters: inverters without a dedicated synchronization unit," *IEEE Transactions on Power Electronics*, vol. 29, no. 2, pp. 617–630, 2013.

[6] Y. Du, J. M. Guerrero, L. Chang, J. Su, and M. Mao, "Modeling, analysis, and design of a frequency-droop-based virtual synchronous generator for microgrid applications," in *Proceedings of the 2013 IEEE ECCE Asia Downunder*, Melbourne, Australia, June 2013.

[7] C. Andalib-Bin-Karim, X. Liang, and H. Zhang, "Fuzzy-secondary-controller-based virtual synchronous generator control scheme for interfacing inverters of renewable distributed generation in microgrids," *IEEE Transactions on Industry Applications*, vol. 54, no. 2, pp. 1047–1061, 2018.

[8] M. Mao, C. Qian, and Y. Ding, "Decentralized coordination power control for islanding microgrid based on PV/BES-VSG," *CPSS Transactions on Power Electronics and Applications*, vol. 3, no. 1, pp. 14–24, 2018.

[9] Y. Yu and X. Hu, "Active disturbance rejection control strategy for grid-connected photovoltaic inverter based on virtual synchronous generator," *IEEE Access*, vol. 7, pp. 17328–17336, 2019.

[10] J. Fang, Y. Tang, H. Li, and X. Li, "A battery/ultracapacitor hybrid energy storage system for implementing the power management of virtual synchronous generators," *IEEE Transactions on Power Electronics*, vol. 33, no. 4, pp. 2820–2824, 2018.

[11] T. El Tawil, G. Yao, J. F. Charpentier, and M. Benbouzid, "Design and analysis of a virtual synchronous generator control strategy in microgrid application for stand-alone sites," *IET Generation, Transmission & Distribution*, vol. 13, no. 11, pp. 2154–2161, 2019.

[12] Y. Ma, W. Cao, L. Yang, F. F. Wang, and L. M. Tolbert, "Virtual synchronous generator control of full converter wind turbines with short-term energy storage," *IEEE Transactions on Industrial Electronics*, vol. 64, no. 11, pp. 8821–8831, 2017.

[13] J. Liu, Y. Miura, H. Bevrani, and T. Ise, "Enhanced virtual synchronous generator control for parallel inverters in microgrids," *IEEE Transactions on Smart Grid*, vol. 8, no. 5, pp. 2268–2277, 2017.

[14] L. Chen, G. Li, H. Chen et al., "Investigation of a modified flux-coupling-type SFCL for low-voltage ride-through fulfillment of a virtual synchronous generator," *IEEE Transactions on Applied Superconductivity*, vol. 30, no. 4, pp. 1–6, 2020.

[15] K. Dhingra and M. Singh, "Frequency support in a micro-grid using virtual synchronous generator based charging station," *IET Renewable Power Generation*, vol. 12, no. 9, pp. 1034–1044, 2018.

[16] X. Li and G. Chen, "Synchronization strategy for virtual synchronous generator based energy storage system," in *Proceedings of the IECON 2019-45th Annual Conference of the IEEE Industrial Electronics Society*, Lisbon, Portugal, October 2019.

[17] I. J. Balaguer, Q. Lei, S. Yang, U. Supatti, and F. Z. Peng, "Control for grid-connected and intentional islanding operations of distributed power generation," *IEEE Transactions on Industrial Electronics*, vol. 58, no. 1, pp. 147–157, 2011.

[18] T.-V. Tran, T.-W. Chun, H.-H. Lee, H.-G. Kim, and E.-C. Nho, "PLL-based seamless transfer control between grid-connected and islanding modes in grid-connected inverters," *IEEE Transactions on Power Electronics*, vol. 29, no. 10, pp. 5218–5228, 2014.

[19] J. Wang, N. C. P. Chang, X. Feng, and A. Monti, "Design of a generalized control algorithm for parallel inverters for smooth microgrid transition operation," *IEEE Transactions on Industrial Electronics*, vol. 62, no. 8, pp. 4900–4914, 2015.

[20] J. Wu and C. Li, "Virtual synchronous generator control of VSC-HVDC system based on MMC of hybrid topology," *Mathematical Problems in Engineering*, vol. 2020, Article ID 6487135, 8 pages, 2020.

[21] K. Shi, W. Song, H. Ge, P. Xu, Y. Yang, and F. Blaabjerg, "Transient analysis of microgrids with parallel synchronous generators and virtual synchronous generators," *IEEE Transactions on Energy Conversion*, vol. 35, no. 1, pp. 95–105, 2020.

[22] Q.-C. Zhong, G. C. Konstantopoulos, B. Ren, and M. Krstic, "Improved synchronverters with bounded frequency and voltage for smart grid integration," *IEEE Transactions on Smart Grid*, vol. 9, no. 2, pp. 786–796, 2018.

[23] K. Wang, X. Feng, J. Pang, J. Ren, C. Duan, and L. Li, "State of charge (SOC) estimation of lithium-ion battery based on adaptive square root unscented Kalman filter," *International Journal of Electrochemical Science*, vol. 15, no. 9, pp. 9499–9516, 2020.

Hindawi
Mathematical Problems in Engineering
Volume 2020, Article ID 8971213, 11 pages
https://doi.org/10.1155/2020/8971213

Research Article

Optimization Control Strategy for Islanded Parallel Virtual Synchronous Generators

Hailin Hu,[1,2] **Fu Feng**,[1] **Tao Wang**,[1] **Xiaofeng Wan**,[3] **and Xiaohua Ding**[3]

[1]*School of Electrical Engineering and Automation, Jiangxi University of Science and Technology, Ganzhou 341000, Jiangxi, China*
[2]*Maglev Engineering Research Center, National University of Defense Technology, Changsha 410005, Hunan, China*
[3]*School of Information Engineering, Nanchang University, Nanchang 330031, Jiangxi, China*

Correspondence should be addressed to Hailin Hu; jackyhhl@163.com

Received 13 July 2020; Accepted 13 August 2020; Published 19 October 2020

Guest Editor: Kai Wang

Virtual Synchronous Generators (VSGs) can reduce the frequency and power oscillation in the grid. For parallel multi-VSGs in island microgrid, the differences of equivalent output impedance and line impedance affect the orderly sharing of reactive power and restraining of circulating current greatly. The power sharing and circulating current characteristics of VSGs are analyzed in this paper. To solve this problem, an optimization control method for parallel VSGs is proposed, which included the inner voltage and current loop and the outer reactive power loop. In the inner voltage and current loop, a virtual complex impedance including a resistive component and an inductive component is introduced. It reduces the coupling between active power and reactive power, and it reduces the disorderly distribution of power due to impedance differences. In the reactive power loop, the output voltage feedback and integrator links are adopted, which reduce the deviation of output voltage and restrain circulating current. The effects on the equivalent output impedance in the different control parameters and virtual complex impedance are analyzed, the effects on system stability in the different resistive components of virtual complex impedance are analyzed, and the proper parameters are selected. Simulation and experimental results show the correctness and validity of the proposed control method.

1. Introduction

By increasing the inertia and damping links in an active power control loop, the grid support capability in a weak grid of virtual synchronous generators (VSGs) is summarized in [1, 2]. When multiple VSGs are operated in parallel, there are differences in the output voltage, equivalent output impedance, and connection line impedance of the individual VSGs, which are caused by the different controller parameters, nonlinearities in the power devices, differences in filter parameters, and the distance from the grid connection point. These differences affect the accuracy of power distribution, increase the fundamental current circulation between the VSGs, and may cause overcurrent faults [3]. Therefore, it is of great value to study the power distribution and current circulation suppression between parallel VSGs. [4, 5].

Focusing on the power distribution problem of parallel VSGs, in [6], an integral controller is added in the reactive power loop to eliminate the influence of connection line impedance on reactive power distribution. However, the coupling of active and reactive power is not considered. In [7], a feedforward angular frequency is added to the power frequency link to realize switching under different operation modes. A small-signal model and several constraints are used to optimize the dynamic and static characteristics of the parameters, but the implementation method is complicated. In [8], function terms for the power and droop coefficient in traditional droop control are introduced. This improved the dynamic regulation performance, but it did not eliminate the steady-state error caused by the connection line impedance. In [9], a new multiloop control strategy is described, the virtual reactance can be selected according to the external inductance, but the conturation principle of virtual

impedance in parallel VSGs is not considered. In [10], a joint control method for the virtual inductor and external output inductor is proposed, which is used to improve the applicability of the inverter P-f and Q-V droop control in medium- and low-voltage networks. However, it is difficult to obtain the external output inductance accurately, and the method is not practical. In [11], a parallel VSGs control method based on virtual impedance is proposed. This approach improves the excitation link to achieve adequate control of the AC bus voltage, but the power coupling problem is not considered. In [12], a consistency-based parallel VSGs distributed control method is described. Although this enhances the system frequency and active power characteristics, it requires communication between the parallel VSGs.

This paper describes a method that improves the traditional virtual synchronous power generation technology, based on analysis of the parallel operation characteristics of multiple VSGs. The optimization control strategy includes the outer reactive power loop and the inner voltage and current loop. In the inner voltage and current loop, a virtual complex impedance including a resistive component and an inductive component is introduced. It reduces the effects on decoupling between active power and reactive power, and it reduces the effects on accurate power sharing due to the impedance difference. In the reactive power loop, the output voltage feedback and integrator links are adopted, which will reduce the deviation of output voltage and restrain circulating current.

2. Operating Characteristics of Parallel VSGs

Figure 1 shows the simplified structure of a traditional parallel VSGs system. For a single VSG, it connects to the AC bus through the connection line and grid-connected switch. Z_{line} is the impedance of the connection line, and K is the grid-connected switch. Z_{load} is the common load, L_1 is the filter inductance, and R_1 is the sum of the equivalent internal resistance of the filter inductance and the equivalent internal resistance of the power device. U_C is the VSG output capacitor voltage, also known as the terminal voltage. I_2 is the grid-side output current, and I_1 is the converter-side current.

A simple model with two parallel VSGs is shown in Figure 2. U_1 and U_2 are the voltage amplitudes of the VSG bridge arms' midpoint, E is the AC bus voltage amplitude, Z_o is the equivalent output impedance of the VSG ($Z_o = R_o + jX_o$), and Z_{line} is the connection line impedance ($Z_{\text{line}} = R_{\text{line}} + jX_{\text{line}}$).

The transmission impedance Z is equal to the sum of the equivalent output impedance and the connection line impedance, φ is the transmission impedance phase angle, and θ is the phase angle difference between the bus voltage and the voltage of the bridge arm's midpoint. I_o and I_L represent the output current of the VSG and load current.

2.1. Analysis of VSG Power Transmission Characteristics.

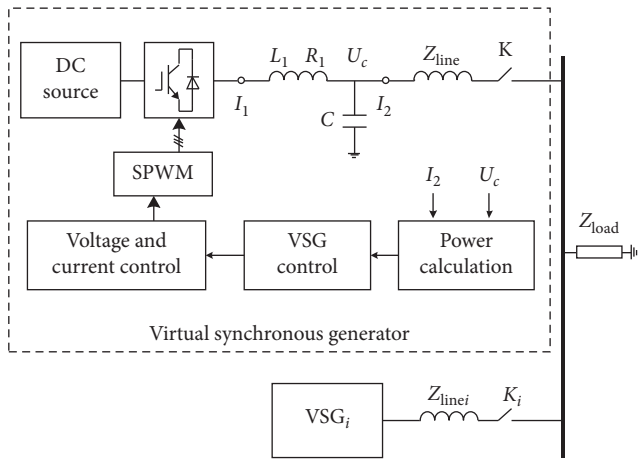

Figure 1: Structure diagram of parallel VSGs.

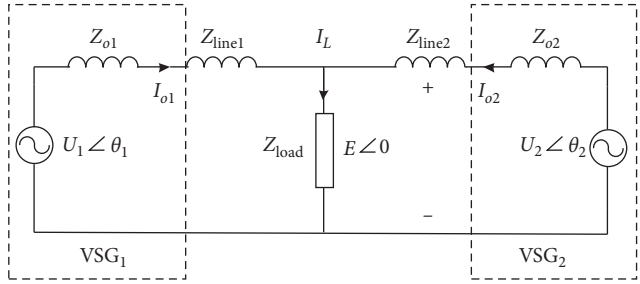

Figure 2: Two VSG parallel models.

The output active power and reactive power of VSG i ($i = 1, 2$) can be expressed as follows:

$$P_i = \left(\frac{U_i E}{Z_i}\cos\theta_i - \frac{E^2}{Z_i}\right)\cos\varphi_i + \frac{U_i E}{Z_i}\sin\theta_i \sin\varphi_i,$$
$$Q_i = \left(\frac{U_i E}{Z_i}\cos\theta_i - \frac{E^2}{Z_i}\right)sin\varphi_i - \frac{U_i E}{Z_i}\sin\theta_i \sin\varphi_i. \quad (1)$$

According to (1), the output active power and reactive power are related to the voltage amplitude and phase angle difference and are affected by the transmission impedance. By setting the voltage and current control loop parameters, the equivalent output impedance of the VSG can be controlled, so that the equivalent output inductive reactance is much larger than the equivalent output resistive impedance, $X_o \gg R_o$. The transmission impedance of different voltage levels has different impedance ratios. In low-voltage distribution networks, the resistive impedance is much larger than the inductive impedance, $X_{\text{line}} \ll R_{\text{line}}$. In medium-voltage distribution networks, $X_{\text{line}} \approx R_{\text{line}}$. This causes the transmission impedance to exhibit complex characteristics. To decouple the active power from the reactive power, the transmission impedance is set to be inductive using virtual impedance technology. The power transmission is approximately shown as follows:

$$P_i = \frac{U_i E}{X_{oi} + X_{\text{line}i}}\theta_i,$$
$$Q_i = \frac{E(U_i - E)}{X_{oi} + X_{\text{line}i}}. \tag{2}$$

From the abovementioned analysis, when the transmission impedance is inductive, the active power transmission is mainly affected by the voltage phase angle, whereas the reactive power transmission is affected by the voltage amplitude. [13] The active power and reactive power are approximately decoupled.

The VSG power control equation can be described as follows:

$$J\frac{d\omega}{dt} = \frac{P^*}{\omega_n} - \frac{P_i}{\omega_n} + D_p(\omega_n - \omega_i),$$
$$U_i = E_n + D_q(Q^* - Q_i), \tag{3}$$

where J is the virtual inertia, P^* is the reference value of active power, P_i is the actual output active power, D_P is the damping coefficient, ω_n is the rated angular frequency, and ω_i is the virtual angular frequency. U_i is the amplitude of VSG output voltage, E_n is the rated voltage amplitude, D_q is the reactive power droop coefficient, Q^* is the reference value of reactive power, and Q_i is the actual output reactive power. Combining equations (2) and (3), the VSG active power closed-loop control diagram is shown as Figure 3. The reactive power closed-loop control diagram is shown as Figure 4.

There is an integral link in the active loop of the virtual synchronous control strategy; when the VSG runs in the steady state, the input of the integral link is 0.

$$P_i = P^* + D_p(\omega_n - \omega_i). \tag{4}$$

According to (4), when the transmission impedance of the VSG is inductive, the active power distribution is related to the active power command value and the active-frequency droop coefficient, and active power distribution is not affected by transmission impedance.

For two VSGs with the same rated capacity, as long as the active power command value and the active-frequency droop coefficient are equal, the active power can be divided equally. Therefore, the active power transmission is highly robust.

Similarly, the VSG output reactive power equation can be obtained as follows:

$$Q_i = \frac{(E_n - E + Q^* D_q)(E/X_i)}{(1 + (E/X_i)D_q)}. \tag{5}$$

According to (5), the reactive power distribution is affected by the droop coefficient, the reactive power reference value, and the transmission impedance. When the reactive power of two VSGs with equal capacity is evenly distributed, the droop coefficients, reactive power setting values, and transmission impedances of each VSG must be equal. When the actual system is running, the system interference, the nonlinearity of the power device, the parameter offset, and the difference in connection impedance make it difficult to meet the conditions for the orderly distribution of reactive power.

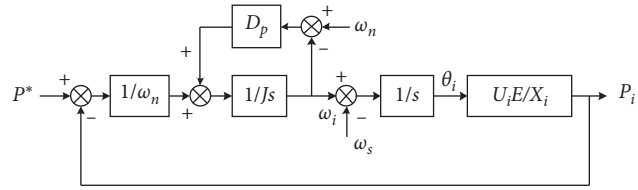

Figure 3: Active power closed-loop control diagram of the VSG.

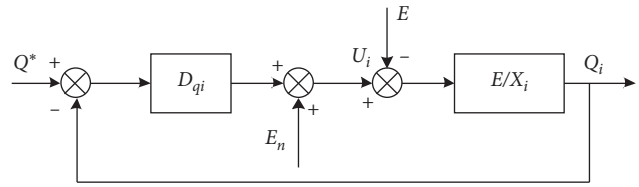

Figure 4: Reactive power closed-loop control diagram of the VSG.

2.2. Analysis of Current Circulation Characteristics of the VSG. The output current characteristics of parallel VSGs are analyzed in the fundamental wave frequency domain. Equation (6) can be obtained from Figure 2.

$$\begin{cases} U_1\angle\theta_1 - Z_{\text{line1}}I_{o1} = E\angle 0, \\ U_2\angle\theta_2 - Z_{\text{line2}}I_{o2} = E\angle 0, \\ I_{o1} + I_{o2} = I_L = E\angle\dfrac{0}{Z_{\text{load}}}. \end{cases} \tag{6}$$

In the abovementioned equations, the transmission impedance is the sum of the equivalent output impedance and the connection line impedance, $Z_i = Z_{oi} + Z_{\text{line}i}$. If the equivalent output impedance and connection line impedance of the two VSGs are equal, the following equation can be obtained:

$$\begin{cases} I_{o1} = \dfrac{U_1\angle\theta_1 - U_2\angle\theta_2}{2Z_1} + \dfrac{E}{2Z_{\text{load}}}, \\ I_{o2} = \dfrac{U_2\angle\theta_2 - U_1\angle\theta_1}{2Z_1} + \dfrac{E}{2Z_{\text{load}}}. \end{cases} \tag{7}$$

When the equivalent output impedance of the VSG is inductive and the connection line impedance is far less than the equivalent output impedance, the transmission impedance is approximately equal to the equivalent output impedance, $Z_i \approx X_{oi}$, and the following equation can be obtained:

$$\begin{cases} I_{o1} = \dfrac{U_1\angle\theta_1 - U_2\angle\theta_2}{2jX_{o1}} + \dfrac{E}{2Z_{\text{load}}} = I_{H1} + I_{oL1}, \\ I_{o2} = \dfrac{U_2\angle\theta_2 - U_1\angle\theta_2}{2jX_{o1}} + \dfrac{E}{2Z_{\text{load}}} = I_{H2} + I_{oL2}. \end{cases} \tag{8}$$

According to equation (8), as the equivalent output impedance of the two VSGs is inductive and equal and the connection line impedance is much smaller than the equivalent output impedance, the output current of the VSG includes two components: the load current I_{oL} and the circulation current I_H. The load current is distributed equally, and the circulating current is determined by the output voltage amplitude difference, phase difference, and equivalent output impedance of the parallel VSGs. [13].

The fundamental circulating current between two VSGs is defined as follows:

$$I_H = \frac{I_{o1} - I_{o2}}{2} = \frac{U_1\angle\theta_1 - U_2\angle\theta_2}{2jX_{o1}}. \tag{9}$$

If the virtual voltage amplitude of the VSGs is equal, there is only a phase difference, and the phase difference will cause active power circulation, which will transfer active current circulation from the advanced phase part to the delayed phase part in the parallel VSGs. If the virtual voltage phase of the VSG is equal, there is only an amplitude difference, and the reactive current circulation will flow from the high-voltage amplitude part to the low-voltage amplitude part. The output impedance of the VSG with high-voltage amplitude is inductive, and the output impedance of the VSG with low-voltage amplitude is capacitive. If both the amplitude and phase of the output voltages of the two VSGs are not equal, then the circulating current contains both active and reactive components [14].

From the analysis of the current circulation characteristics, it can be seen that the current circulation of the parallel VSGs is suppressed by achieving the output voltage and transmission impedance of the two VSGs is equal. The suppression of the current circulation can also be realized by increasing the equivalent output impedance.

3. Optimization Control Strategy of Parallel VSGs

3.1. Introduction of Virtual Impedance. From the analysis in the previous section, the active power and the reactive power are decoupled by setting the transmission impedance to be purely resistive or purely inductive, and this is the premise of independent control of active power and reactive power. Increasing the equivalent output impedance of the virtual synchronous generator can reduce the current circulation caused by the difference between the equivalent output impedance and the connection impedance. To change the transmission impedance characteristics of the VSG, the output current of the grid side is used as the feedback, and a virtual complex impedance consisting of resistance and inductive components is introduced. The negative resistive virtual impedance is used to reduce the resistive component of transmission impedance, and the transmission impedance is approximately purely inductive. It can reduce the coupling of active power and reactive power transmission. The positive inductive virtual impedance is introduced, the transmission impedance increases, and the current circulation caused by differences in the equivalent output impedance and connection line impedance is reduced. After introducing the virtual complex impedance, the voltage compensation is shown as follows:

$$\begin{cases} u_{vd} = R_{vd}i_{2d} - \omega L_{vd}i_{2q}, \\ u_{vq} = R_{vq}i_{2q} + \omega L_{vq}i_{2d}, \end{cases} \tag{10}$$

where R_{vq} and R_{vd} are the virtual impedances in the dq rotation coordinates. To reduce the resistive component of the equivalent output impedance, the virtual impedance R_v takes a negative value, and L_{vq} and L_{vd} are the virtual inductive resistances in the dq coordinates [13].

To increase the control precision and control the current circulation, the voltage-type VSG structure is adopted, and the terminal voltage control loop is added after the power control loop. The structure of the inner voltage and current control loop with virtual complex impedance is shown as Figure 5.

In Figure 5, k_{uP} and K_{ui} are the proportional (P) and integral (I) gains of the voltage-loop PI controller, k_{iP} is the proportional gain of the current inner loop, k_{Pwm} is the converter gain, $Z_v(s)$ is the virtual complex impedance ($Z_v(s) = R_v + L_v s$), u^* is the voltage-loop voltage command value, u_v^* is the voltage-loop reference value after introducing the virtual impedance, u is the output voltage, i_1 is the converter-side current, and i_2 is the grid-side output current. A mathematical model of the output voltage can be established according to Figure 5. When the virtual impedance is not introduced, it can be written as follows:

$$CsU(s) = \left\{ \left[\left(U^*(s) - U(s)\right)\left(\frac{k_{up} + k_{ui}}{s}\right) - \left(I_2(s) + U(s)Cs\right) \right] k_{ip}k_{pwm} - U(s) - \frac{\left(L_1 s + R_1\right)I_2(s)\}}{L_1 s + R_1} \right\}. \tag{11}$$

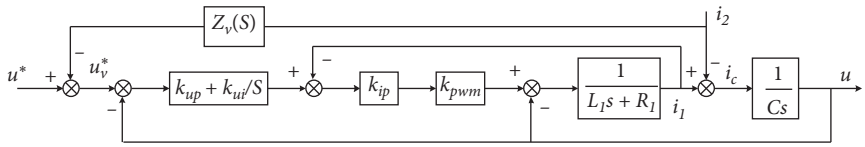

Figure 5: Voltage and current loop structure after adding virtual impedance.

Equation (11) can be transformed into the following equation:

$$U(s) = \frac{\left[k_{ip}k_{pwm}\left(k_{up}s + k_{ui}\right)\right]U^*(s)}{L_1Cs^3 + \left(k_{ip}k_{pwm} + R_1\right)Cs^2 + \left(k_{ip}k_{pwm}k_{up} + 1\right)s + k_{ip}k_{pwm}k_{ui}}, \\ - \frac{\left[L_1s^2 + \left(k_{ip}k_{pwm} + R_1\right)s\right]I_2(s)}{L_1Cs^3 + \left(k_{ip}k_{pwm} + R_1\right)Cs^2 + \left(k_{ip}k_{pwm}k_{up} + 1\right)s + k_{ip}k_{pwm}k_{ui}}. \tag{12}$$

It is equivalent to the following equation:

$$U(s) = G(s)U^*(s) - Z_o(s)I_2, \tag{13}$$

where $G(x)$ is the equivalent closed-loop voltage gain and $Z_0(s)$ is the equivalent output impedance. These terms can be written as follows:

$$G(s) = \frac{\left[k_{ip}k_{pwm}\left(k_{up}s + k_{ui}\right)\right]}{\left[L_1Cs^3\left(k_{ip}k_{pwm} + R_1\right)Cs^2 + \left(k_{ip}k_{pwm}k_{up} + 1\right)s + k_{ip}k_{pwm}k_{ui}\right]}, \\ Z_o(s) = \frac{\left[L_1s^2 + \left(k_{ip}k_{pwm} + R_1\right)s\right]}{\left[L_1Cs^3 + \left(k_{ip}k_{pwm} + R_1\right)Cs^2 + \left(k_{ip}k_{pwm}k_{up} + 1\right)s + k_{ip}k_{pwm}k_{ui}\right]}. \tag{14}$$

After adding the virtual impedance, the following equation can be obtained:

$$U_v^*(s) = U^*(s) - Z_v(s)I_2(s). \tag{15}$$

Substituting (16) into (13) gives

$$U(s) = G(s)\left[U^* - Z_v(s)I_2\right] - Z_o(s)I_2, \\ = G(s)U^* - \left[G(s)Z_v(s) + Z_o(s)\right]I_2, \tag{16}$$

where $G(s)Z_v(s) + Z_0(s)$ is the equivalent output impedance after adding the virtual complex impedance and $Z_0'(s)$ is shown as the following equation:

$$Z_0'(s) = G(s)Z_v(s) + Z_o(s). \tag{17}$$

According to equation (15) and the parameters in Table 1, the equivalent output impedance can be illustrated using a Bode diagram without the added virtual impedance. Figure 6 is the equivalent output impedance Bode diagram for $K_{ui} = 0$, 100, 500, and 1000. It can be seen that when $K_{ui} = 0$, the low-frequency equivalent output impedance is resistive, and it is the complex impedance characteristic at the fundamental frequency. When $K_{ui} = 500$, the equivalent output impedance is inductive at the fundamental frequency. The larger the value of K_{ui}, the wider the frequency band that belongs to the inductive output impedance. After the introduction of the virtual inductive impedance L_v, the equivalent output impedance is inductive at low and fundamental frequencies. The fundamental output impedance is approximately equal to the virtual inductive impedance L_v, which weakens the effect of changes in the filter inductance parameters on the output impedance. Therefore, the equivalent output impedance at the fundamental frequency can be designed by introducing a virtual complex impedance to match the impedance of the parallel VSGs, and the aim of improving power distribution accuracy and current circulation suppression can be achieved.

When selecting the virtual negative impedance R_v, the power decoupling and system stability requirements must be comprehensively considered. After introduction of the virtual impedance, the equivalent output impedance of the VSG at the fundamental frequency is approximately equal to the virtual impedance, so the transmission impedance at the fundamental frequency is given as follows:

$$Z(s) = Z_v(s) + Z_{\text{line}}(s) = \left(R_{\text{line}} + R_v\right) + s\left(L_{\text{line}} + L_v\right). \tag{18}$$

The formula $R_v = -R_{\text{line}}$ is established, and active power and reactive power transmission can achieve decoupling.

Table 1: VSG parameters.

Parameter/unit	Value
L_1/mh	5
R_1/Ω	0.1
C/uf	10
Z_{line}/Ω	$0.5 + 0.06j$
L_v/mh	1
k_{up}	0.3
k_{ui}	600
k_{ip}	2
k_{pwm}	250
R_v/Ω	−0.4

The resistive component of transmission impedance has a damping effect on nonfundamental frequency disturbances. In the resistive component of transmission impedance setting, both the power decoupling and the nonfundamental frequency stability should be taken into consideration. The equivalent output impedance of the VSG after introducing the virtual impedance can be expressed as follows:

$$\begin{aligned} Z(s) &= Z_o'(s) + Z_{\text{line}}(s), \\ &= G(s)Z_v(s) + Z_o(s) + Z_{\text{line}}(s). \end{aligned} \tag{19}$$

The relationship between the output harmonic current $i_d(s)$ and the voltage disturbance $u_d(s)$ is shown as follows:

$$\frac{i_d(s)}{u_d(s)} = \frac{1}{Z(s)} = Y(s). \tag{20}$$

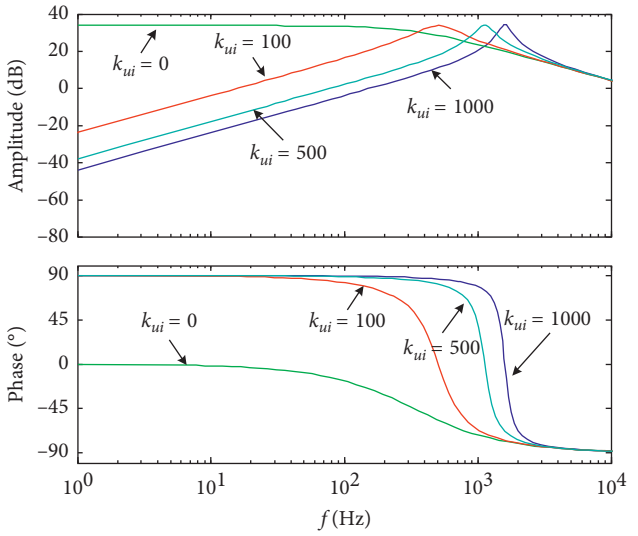

Figure 6: Equivalent output impedance Bode diagram with no virtual impedance.

Therefore, the stability of the system can be analyzed by identifying the distribution of the characteristic roots of the characteristic equation. Combining (17), (18), and (20), the following equation can be obtained:

$$\begin{aligned} Y(s) &= \frac{T(s)}{\left[(L_{\text{line}}s + R_{\text{line}})T(s) + k_{ip}k_{pwm}\left(k_{up}s + k_{ui}\right)\left(L_v s + R_v\right) + L_1 s^2 + \left(k_{ip}k_{pwm} + R_1\right)s\right]}, \\ T(s) &= L_1 C s^3 + \left(k_{ip}k_{pwm} + R_1\right)Cs^2 + \left(k_{ip}k_{pwm}k_{up} + 1\right)s + k_{ip}k_{pwm}k_{ui}. \end{aligned} \tag{21}$$

When $R_{\text{line}} = 0.5\,\Omega$ and $L_{\text{line}} = 0.4$ mh, according to the parameters in Table 1, the root locus of $Y(s)$ with respect to R_v is shown in Figure 7. The pole S_1 determines the stability of $Y(S)$. As R_v increases, S_1 moves to the right of the complex plane and reaches the origin when $R_v = -0.5\,\Omega$. Therefore, $|R_v|$ should not be too large, it should be kept at a certain difference with R_{line}, so as S_1 has a certain distance from the imaginary axis, and the system has a certain stability margin.

3.2. Reactive Power Loop Improvement. From the analysis in the previous section, it is known that the transmission of active power and reactive power is decoupled, when the transmission impedance of the VSG is inductive. Due to the integration link in the active power loop, the active power allocation of the parallel VSGs is related to the active power reference value and the active power droop coefficient, and it is not affected by the transmission impedance. The reactive power distribution is affected not only by the droop coefficient but also by the reactive power reference value and the transmission impedance. At the same time, the load voltage fluctuates because of the load fluctuation and the droop characteristics of the reactive power loop. The fluctuations of load voltage can be restrained, and the output voltage can be stabilized within a certain range by introducing a negative feedback link $K_e(E^* - E)$ in the reactive power loop (here, K_e is the feedback coefficient, E^* is the reference value of the load voltage, and E is the actual value of the load voltage). The integral link is introduced into the power loop, and it achieves the decoupling of reactive power and transmission impedance.

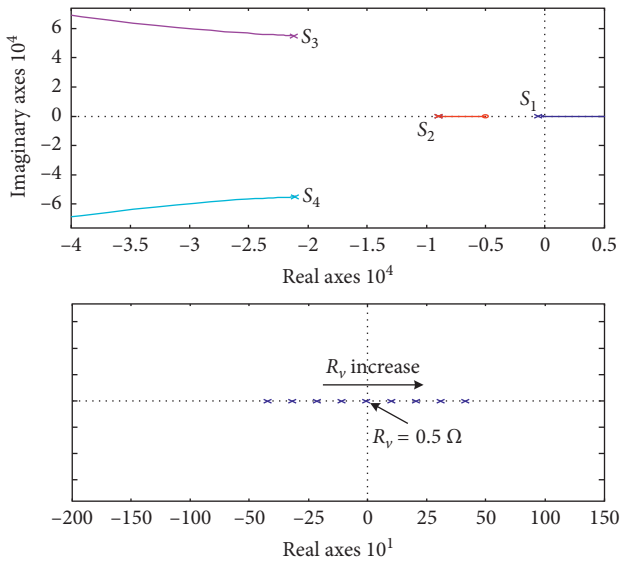

Figure 7: Root locus of $Y(s)$ for increasing R_v.

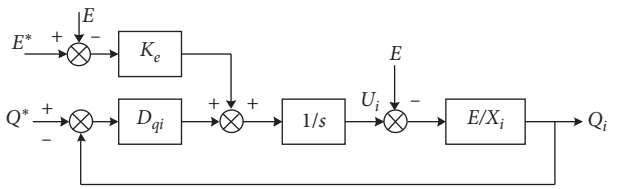

Figure 8: Improved virtual synchronous reactive power-voltage control block diagram.

The improved reactive power control loop structure is shown in Figure 8. When the system is stable, the input of the integration link is 0. The expression of power and voltage is shown as follows:

$$D_{qi}(Q_i - Q^*) = K_e(E^* - E). \tag{22}$$

From equation (22), it can be determined that the reactive power distribution is related to the droop coefficient, reactive power reference value, and voltage feedback coefficient.

It is independent of the transmission impedance. As long as the voltage feedback coefficients are equal and the reactive power reference value and droop coefficient are set in inverse proportion to the rated capacity, the ordered distribution of reactive power can be achieved [15, 16].

3.3. Structure of Optimization Control Strategy. A structure diagram of the inner voltage and current control loop is shown in Figure 9. The terminal voltage is controlled in the synchronous rotating coordinate system.

The terminal voltage loop adopts the PI regulator, the current loop adopts the P regulator, and the decoupling compensation is added to the controller to eliminate the cross coupling of the dq-axis voltage and current, and it

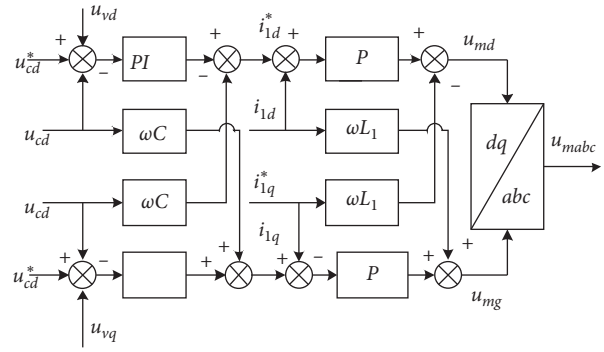

Figure 9: Structure of the inner voltage and current loop.

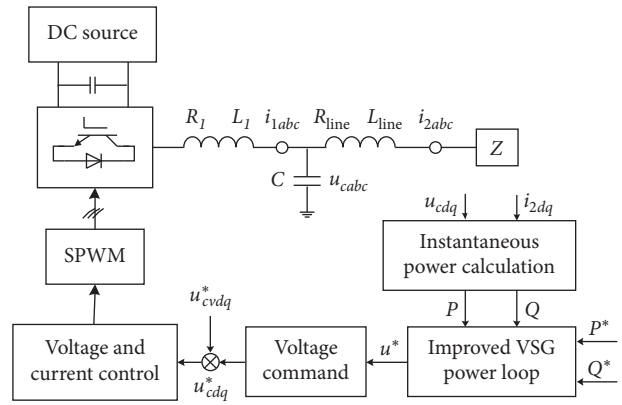

Figure 10: Improved parallel virtual synchronization control strategy.

improves the system dynamic performance. In the figure, the subscripts "d" and "q" indicate the synchronous rotation dq coordinates, $U_{c\,dq}$ and $i_{l\,dq}$ are the terminal voltage and

converter-side current in the synchronous rotation dq coordinate system, and ω is the virtual electrical angular frequency of the VSG [17, 18].

The improved control strategy of parallel VSGs is illustrated in Figure 10. In the figure, L_1 is the output filter inductor, R_1 is the sum of the internal resistance of the filter inductor and the internal resistance of the power device, C is the filter capacitor, and L_{line} and R_{line} are the connection line impedances. i_{1abc} is the inductor current on the converter side, i_{2abc} is the load current, and u_{cabc} is the voltage of capacitor.

The instantaneous power P and Q calculation formulas are shown as equation (23), and the reference value U^* of the midpoint voltage of the bridge arm is obtained by the improved power loop.

$$\begin{cases} P = 1.5\left(u_{cd}i_{2d} + u_{cq}i_{2q}\right), \\ Q = 1.5\left(u_{cd}i_{2\,d} - u_{c\,d}i_{2q}\right), \end{cases} \tag{23}$$

where $U_{c\,d}$ and U_{cq} are the d and q coordinate components of the filter capacitor voltage U_c, while $i_{2\,d}$ and i_{2q} are the d and q coordinate components of the load current i_2.

Ignoring the role of the filter capacitor C, the relationship among the bridge midpoint voltage, terminal voltage, and output current of the converter side is given by equation (24). The relationships between voltage and current in the dq coordinate system are given by equations (25) and (26) [11].

$$u_{cabc} = u_{abc} - R_1 i_{1abc} - L_1 \frac{\mathrm{d}i_{1abc}}{\mathrm{d}t}, \tag{24}$$

$$\begin{bmatrix} u_{c\,d} \\ u_{cq} \end{bmatrix} = \begin{bmatrix} u_d \\ u_q \end{bmatrix} - Y^{-1} \begin{bmatrix} i_{1\,d} \\ i_{1q} \end{bmatrix}, \tag{25}$$

$$\begin{cases} Y = \dfrac{1}{R_1^2 + X_1^2} \begin{bmatrix} R_1 & X_1 \\ -X_1 & R_1 \end{bmatrix}, \\ \begin{bmatrix} u_d \\ u_q \end{bmatrix} = \begin{bmatrix} E\cos\varphi \\ E\sin\varphi \end{bmatrix}, \end{cases} \tag{26}$$

where i_{1d} and i_{1q} are the output currents of the converter side in the dq coordinate system, U_d and U_q are the dq-axis components obtained by dq decomposition of the midpoint voltage of the bridge arm using the terminal voltage vector orientation, U_{cd} and U_{cq} are the dq-axis components of the terminal voltage, Y is the filter impedance matrix, and X_1 is the inductive reactance ($X_1 = \omega L_1$). The phase angle φ represents the phase angle difference between the bridge midpoint voltage vector and the terminal voltage vector, which is equal to the integral of the difference between the virtual rotor angular velocity ω and the terminal voltage electrical angular velocity ω_c of the virtual synchronous control [18].

The reference value of the terminal voltage under the synchronous rotation coordinates is shown as equation (25). The terminal voltage is sent to inner the voltage current control loop to get the modulation voltage, the control signals of power components are obtained through sinusoidal pulse width modulation, and power equipartitioning and circulating current suppression of the parallel VSGs are realized.

Table 2: System simulation parameters.

Parameter/unit	Value
U_{dc}/V	600
U/V	380
J, D_p	0.05, 15
D_q	480
P^*/kW	9
Q^*/kvar	6
L_v/mh	1
P_0/kW	4
Q_0Q_0/kvar	3
L_1/mh, R_1/Ω	5, 0.1
L_2/mh, R_2/Ω	4.8, 0.1
Z_{line1}/Ω	$0.45 + 0.06j$
Z_{line2}/Ω	$0.55 + 0.07j$
R_v/Ω	−0.2

4. Simulation and Experiment

The model of two parallel VSGs is constructed in the Matlab/Simulink environment to verify the effectiveness of improved control strategy. The main parameters are listed in Table 2. The total simulation time of the system is 2 seconds. From the start to 0.6 s, the first VSG runs alone, the other VSG is connected at 0.6 s, and the first VSG exits at 1.2 s.

Figure 11 shows the simulation results of the voltage, current, and circulating current when two parallel VSGs are running with the traditional control strategy and the improved control strategy.

Figure 12 shows the output power results of two VSGs with optimization control strategy.

Due to the influence of impedance differences, the circulating current of parallel VSGs with traditional control strategy is relatively large, and the reactive power equipartitioning cannot be achieved.

The dynamic current dividing response time of the improved control strategy is shorter, the amplitude of the circulating current is smaller in the steady state, and the effect of reactive power distribution is significantly improved.

The experimental platform of two parallel VSGs is shown in Figure 13, and the main parameters of the experiment are presented in Table 3. In the parallel VSGs experiment, the public load is 3 kW. During the experiment, an inverter works alone at the beginning, and another VSG is connected after a while.

Figure 14 shows the output current and circulating current waveforms of two parallel VSGs with the traditional control strategy and the improved control strategy. Compared with the traditional control strategy, the improved control strategy can respond more quickly, and the circulating current is smaller.

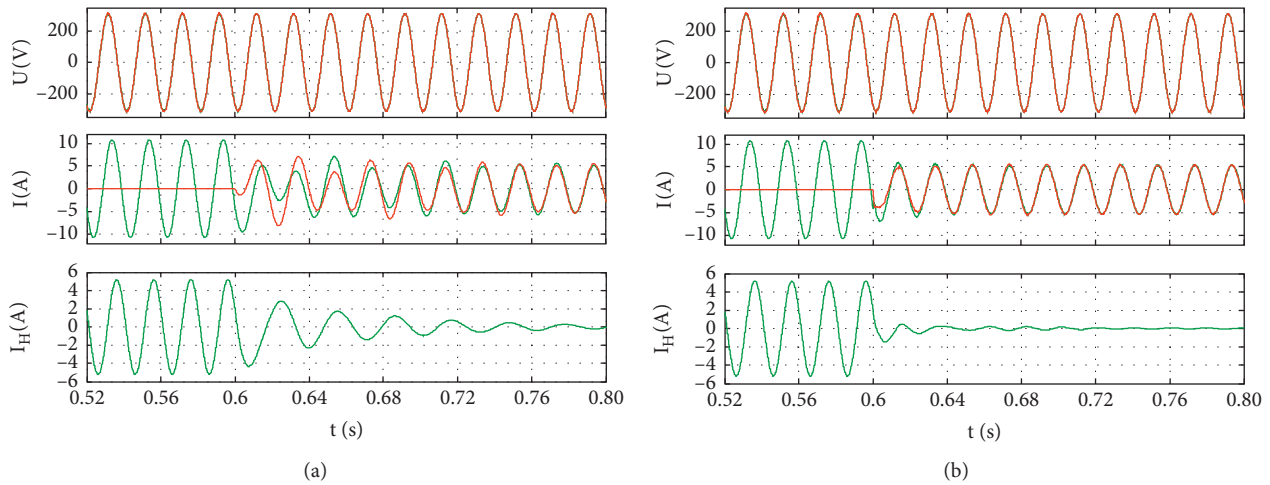

Figure 11: Output voltage, current, and circulating current of two parallel VSGs: (a) traditional virtual synchronization control strategy; (b) improved virtual synchronization control strategy.

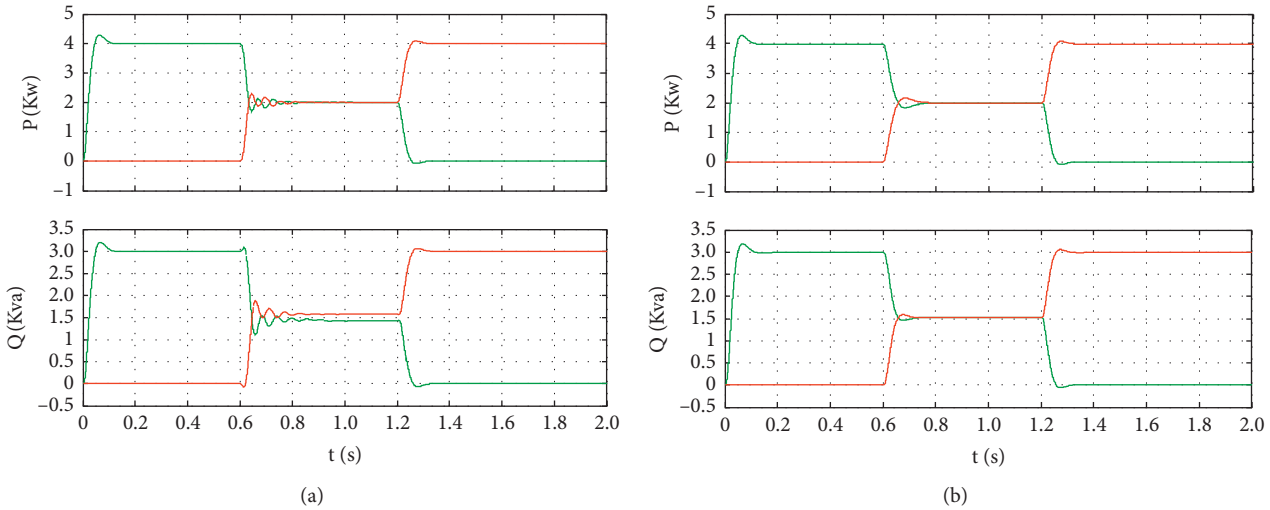

Figure 12: Output active power and reactive power of the parallel virtual synchronous control strategy: (a) traditional virtual synchronization control strategy; (b) improved virtual synchronization control strategy.

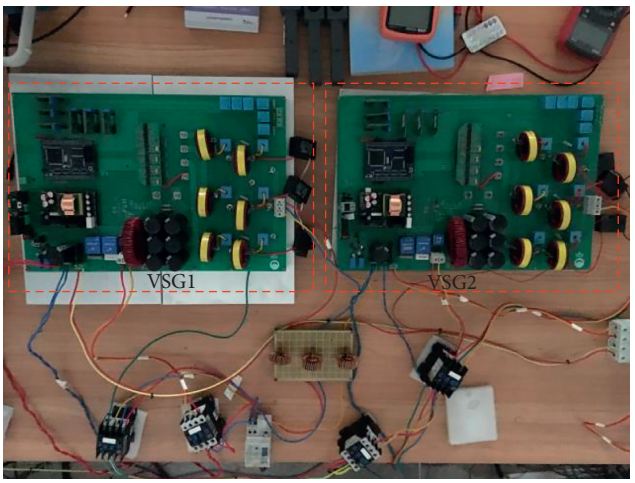

Figure 13: Pictures of the test platform.

Table 3: Experimental parameters.

Parameter/unit	Value
U_{dc}/V	600
k_{up}	0.07
k_{ui}	5
D_{qi}	190
Z_{line1}/Ω	$0.4 + 0.06j$
Z_{line2}/Ω	$0.5 + 0.07j$
L_1/mh, R_1/Ω	5, 0.1
L_2/mh, R_2/Ω	4.8, 0.1
L_v/mh	1
U/V	380
J, D_p	0.02, 6
k_{ip}	2
K_e	0.2
Q_0/kvar	1
P_0/kW	3
P^*/kW	4
Q^*/kvar	1
R_v/Ω	−0.2

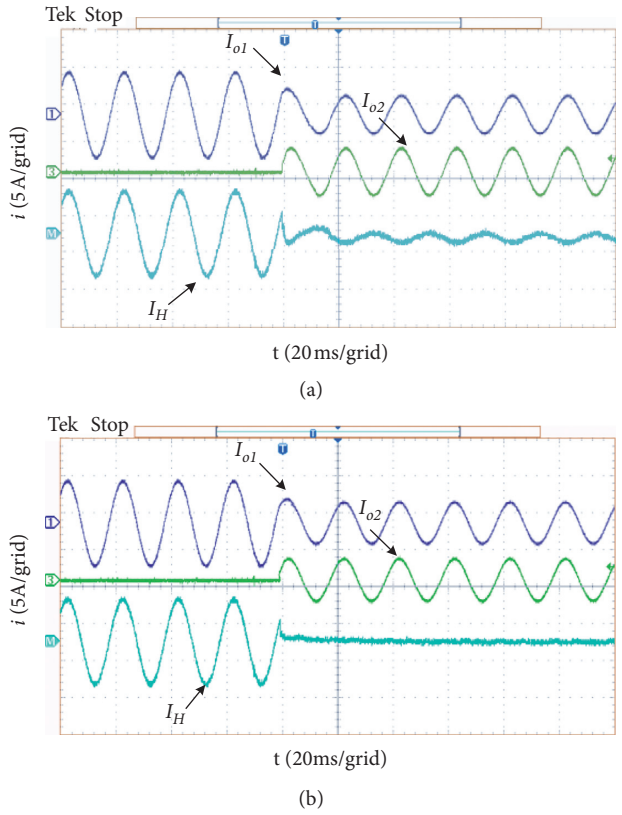

Figure 14: Output current and circulating current of two parallel VSGs: (a) traditional virtual synchronization control strategy; (b) improved virtual synchronization control strategy.

5. Conclusions

In this paper, the problems of power equipartitioning and circulating current suppression in the parallel operation mode of VSGs were studied. The conclusions and requirements for future work are as follows.

(1) When multiple VSGs are connected in parallel, the resistance and inductance characteristics of the transmission impedance cause the coupling between reactive power and active power. The reactive power distribution is affected by the droop coefficient, the reactive power reference value, and the transmission impedance. The current circulation of the parallel VSGs is affected by the deviation of output voltage and the value of transmission impedance.

(2) The virtual complex impedance including a resistive component and an inductive component is introduced into the inner voltage and current control loop. It reduces the coupling between active power and reactive power, and it reduces the disorderly distribution of power due to impedance differences. The load voltage control loop and integral part are introduced in the reactive power link of the VSG, which reduce the deviation of output voltage and restrain circulating current.

(3) According to the comparative analysis of the influence of control parameters and virtual complex impedance on the equivalent output impedance, the control parameters and virtual complex impedance are selected.

Data Availability

The data that support the findings of this study are included within the article.

Conflicts of Interest

The authors declare no conflicts of interest regarding the publication of this paper.

Acknowledgments

This work was supported in part by the National Natural Science Foundation of China with Grant no. 61563034, in part by the Youth Science and Technology Research Project of Jiangxi Provincial Department of Education with Grant no. GJJ180487, and in part by the Doctor Startup Fund of Jiangxi University of Science and Technology with Grant no. jxxjbs18030.

References

[1] T. W. Zheng, L. J. Chen, and S. W. Mei, "Review and prospect of virtual synchronous generator technologies," *Automation of Electric Power Systems*, vol. 39, no. 21, pp. 165–175, 2015.

[2] H. L. Hu, X. F. Wan, X. H. Ding et al., "An improved low voltage ride-through control strategy for distributed virtual synchronous generator," *Electric Machines and Control*, vol. 24, no. 1, pp. 145–155, 2020.

[3] Q.-C. Zhong and G. Weiss, "Synchronverters: inverters that mimic synchronous generators," *IEEE Transactions on Industrial Electronics*, vol. 58, no. 4, pp. 1259–1267, 2011.

[4] L. Y. Lu and C. C. Chu, "Consensus-based secondary frequency and voltage droop control of virtual synchronous generators for isolated AC micro-grids," *IEEE Journal on Emerging and Selected Topics in Circuits and Systems*, vol. 5, no. 3, pp. 443–455, 2015.

[5] K. Wang, L. Li, Y. Lan, and G. Xia, "Application research of chaotic carrier frequency modulation technology in two-stage matrix converter," *Mathematical Problems in Engineering*, vol. 2019, Article ID 2614327, 2019.

[6] Z. P. Lü, W. Z. Sheng, Q. C. Zhong et al., "Virtual synchronous generator and its applications in micro-grid," *Proceedings of the Chinese Society of Electrical and Electronics Engineers*, vol. 34, no. 6, pp. 2591–2603, 2014.

[7] Z. P. Lü, J. Su, R. Li, and H. Liu, "New power control strategy on paralleled micro-source inverters with different power levels," *Transactions of China Electrotechnical Society*, vol. 28, no. 7, pp. 191–198, 2013.

[8] Y. Du, J. H. Su, L. C. Zhang et al., "A mode adaptive frequency controller for microgrid," *Proceedings of the Chinese Society of Electrical and Electronics Engineers*, vol. 33, no. 19, pp. 67–75, 2013.

[9] J. Yao, H. B. Du, T. Zhou et al., "Improved droop control strategy for inverter parallel operation in micro-grid," *Power System Technology*, vol. 39, no. 4, pp. 932–938, 2015.

[10] M. R. Zhang, Z. C. Du, and S. B. Wan, "Research on droop control strategy and parameters selection for microgrids," *Transactions of China Electrotechnical Society*, vol. 29, no. 2, pp. 136–144, 2014.

[11] H. Zhang, F. Wan, X. Q. Li, and F. Yang, "Impedance matching strategy for parallel virtual synchronous generators," *Automation Electric Power System*, vol. 42, no. 9, pp. 69–74, 2018.

[12] L. J. Chen, Y. Y. Wang, T. W. Zhang, and T. Y. Chen, "Consensus-based distributed control of parallel-connected virtual synchronous generator," *Control Theory & Application*, vol. 34, no. 2, pp. 1084–1091, 2017.

[13] Q. H. Zhang, A. Luo, Y. D. Chen, and C. Peng, "Analysis of output impedance for parallel inverters and voltage control strategy," *Transactions of China Electrotechnical Society*, vol. 29, no. 6, pp. 98–105, 2014.

[14] Y. D. Chen and A. Y. Luo, "Circulating current analysis and robust droop multiple loop control method for parallel inverters using resistive output impedance," *Proceedings of the Chinese Society of Electrical and Electronics Engineers*, vol. 33, no. 18, pp. 18–29, 2013.

[15] Z. P. Lü and A. Luo, "Robust power control of paralleled micro-source inverters with different power ratings," *Proceedings of the Chinese Society of Electrical and Electronics Engineers*, vol. 32, no. 12, pp. 35–42, 2012.

[16] Q. C. Zhong, "Robust droop controller for accurate proportional load sharing among inverters operated in parallel," *IEEE Transactions on Industrial Electronics*, vol. 60, no. 4, pp. 1281–1290, 2012.

[17] S. Fan, T. J. Pu, G. Y. Liu et al., "Access technology of distributed power generation system in active power distribution network and its progress," *Transactions of China Electrotechnical Society*, vol. 31, no. 2, pp. 92–101, 2016.

[18] S. Fan, T. Pu, G. Liu, and Q. Chang, "Technologies and its trends of grid integration of distributed generation in active distribution network," *Transactions of China Electrotechnical Society*, vol. 31, no. 2, pp. 92–101, 2016.